UNIVERSIDAD COMPLUTENSE DE MADRID
FACULTAD DE CIENCIAS FÍSICAS
DEPARTAMENTO DE ASTROFÍSICA Y CIENCIAS DE LA ATMÓSFERA

TESIS DOCTORAL

Techniques for near-Earth interplanetary matter detection and characterisation from optical ground-based observatories

Técnicas de detección y caracterización de la materia interplanetaria próxima a la Tierra desde observatorios en tierra

MEMORIA PARA OPTAR AL GRADO DE DOCTOR

PRESENTADA POR

Francisco Ocaña González

DIRECTORES

África Castillo Morales
Jaime Zamorano Calvo

Madrid, 2018

UNIVERSIDAD COMPLUTENSE DE MADRID

FACULTAD DE CIENCIAS FÍSICAS
DEPARTAMENTO DE ASTROFÍSICA Y CIENCIAS DE LA ATMÓSFERA

Técnicas de detección y caracterización de la materia interplanetaria próxima a la Tierra desde observatorios en tierra

Techniques for near-Earth interplanetary matter detection and characterisation from optical ground-based observatories

Dirigida por:

Dr. África Castillo Morales
Profesor Contratado Doctor
UCM

Dr. Jaime Zamorano Calvo
Profesor Titular
UCM

Memoria presentada por
D. Francisco Ocaña González

para aspirar al grado de
Doctor en Astrofisica

Madrid, Abril 2017

Cover image: Cebreros TBT telescope at sunset.

You want fantasy? Here's one... There's this species that lives on a planet a few miles above molten rock and a few miles below a vacuum that'd suck the air right out of them. They live in a brief geological period between ice ages, when giant asteroids have temporarily stopped smacking into the surface. As far as they can tell, there's nowhere else in the universe where they could stay alive for ten seconds. And what do they call their fragile little slice of space and time? They call it real life.

Sir Terry Pratchett, *A Slip of the Keyboard*

A year ago astronomers across the Discworld had been puzzled to see the stars gently wheel across the sky as the world-turtle executed a roll. The thickness of the world never allowed them to see why, but Great A'Tuin's ancient head had snaked out and down and had snapped right out of the sky the speeding asteroid that would, had it hit, have meant that no one would ever have needed to buy a diary ever again.

(Sir and asteroid 127005) Terry Pratchett , *Thief of Time*

Agradecimientos

Sin lugar a dudas uno nunca quiere que su tesis quede incompleta y sin embargo estoy seguro de que me olvido de mucha gente a la que estoy agradecido porque he podido contar con ellos para hacer esta tesis. Principalmente no habría sido posible sin el trabajo de mis directores, África y Jaime. Su apoyo y confianza comenzó mucho antes que esta tesis y todo lo que he aprendido de ellos va mucho más allá de lo que queda en esta memoria. Gracias también a Jesús, que también ha estado presente en muchas partes de este trabajo y desde antes de que lo empezara.

Parte del equipo usado para este trabajo ha sido financiado por el MICINN (proyectos AYA2009-06330-E, AYA2009-10368), por la Comisión Europea y la Comunidad de Madrid (AstroMadrid CAM S2009/ESP-1496). Gracias también al Departamento de Astrofísica y Ciencias de la Atmósfera y al Ministerio de Educación por el premio del Certamen Arquímedes, cuyo importe fue empleado en instrumentos para la Estación de detección de bólidos del Observatorio UCM. A la gente del Departamento también quiero agradecerles no solo todo lo que he aprendido, sino también todos los buenos momentos (comidas en la sala entrecúpulas, cafés, charlas en los pasillos...).

No puedo más que estar agradecido a la Universidad Complutense de Madrid. Estudié la licenciatura y el máster en esta casa, cuyas instalaciones también han sido usadas para este trabajo. En especial el Laboratorio de Investigación Cientifica Avanzada, y el laboratorio al aire libre sobre la última planta, que nos acerca un poco más a las estrellas, pese a lo contaminado del cielo de Madrid. Además en la facultad he tenido grandes compañeros de despacho como Jaime, Álex, Cristina, Raúl, Alex y Lucía, entre otros. Con ellos he compartido grandes momentos (¡todos ellos serán doctores cuando lean esto!), y también los más pequeños del día a día. En la órbita de la facultad y alrededores, quiero dar las gracias a Toni y a Carlos (CETA), por muchas conversaciones muy interesantes.

Gran parte de las observaciones no habría sido posible sin la colaboración del Observatorio de Sierra Nevada (IAA-CSIC) y de los miembros del proyecto Daedalus, ellos saben que aprecio mucho su trabajo. Gracias también a la red SPMN, a todos sus miembros por su trabajo, y en especial a Jose María Madiedo y a Josep Maria Trigo, por su gran dedicación al estudio de los meteoros. Estoy agradecido también a los compañeros de la AAM, que me iniciaron en todo lo bello que tiene la astronomía.

Nunca pensé que mi trabajo de tesis sería tan teórico y tan ingenieril. Es por ello que estoy muy agradecido a todos aquellos que han creado las herramientas que he usado, especialmente de software (entre los que quiero destacar Python, Gnuplot, NEOPOP, LaTeX, SPICE, R , Astrometry.net, RTS2). En este apartado hago un hueco especial para Sergio, porque no sólo me inició en el software libre sino que me ha ayudado con la informática siempre que lo he necesitado. Gracias también a todos los investigadores y a sus resultados sobre los que se basa este trabajo, es especial a los que los han compartido en repositorios como ArXiV, SAO/NASA ADS, ResearchGate o SciHub, y a los que me los han facilitado directamente.

Gracias a todos los ‘compañeros’ y ‘jefes’ de la ESA. En especial a Jonathan McAuliffe y Detlef Koschny, por todo su apoyo, primero con los meteoros y después con los asteroides. Y en relación al proyecto TBT, a Tim Flohrer, Beatriz Jilete, Marco Micheli, Gian Maria Pinna e Igor Zayer. Quiero hacerlo extensivo a todos los compañeros de ESAC, por tantos buenos ratos. Y dentro de ellos, por su colaboración en esta tesis, a los miembros del Observatorio Virtual Español, en especial a Enrique Solano.

En el plano profesional, pero traspasado también al personal, quiero dar las gracias a todos los compañeros del proyecto TBT, sobretodo a Elena, Aitor y Ángel, por todas las noches de observación y los días de sueño que hemos pasado juntos. Gracias también a mis ‘jefes’ Vicente, Miguel y en especial a Daniel Ponz, que me apoyó desde el principio pero no pudo quedarse a ver el final. Parte del trabajo de TBT se realizó en la estación ESTRACK en Cebreros, y les agradezco a todos su colaboración, es especial a Rogelio que participó en varias fases del proyecto.

Más allá de la tesis, pero también cooperantes necesarios, están todos esos amigos que me han ayudado a mantenerme cuerdo. Es especial a mis amigos del barrio, Fer, Juanda y Jaime, que son los que más han sufrido esta tesis.

El agradecimiento más importante es para mi familia. Para Edu, y en especial para mis padres, María Ángeles y Paco, por su apoyo incondicional tantos años. Desde que me regalaron los primeros libros, luego unos prismáticos, para finalmente acompañarme en el mundo de la astronomía hasta que pude hacerlo por mí mismo. Hvala Maruša za vso tvojo pomoč, razumevanje in ukradeni čas, podnevi in ponoči.

Por último quiero expresar mi agradecimiento a los revisores externos y a los miembros del tribunal, por la dedicación desinteresada de su tiempo y su trabajo en esta tesis.

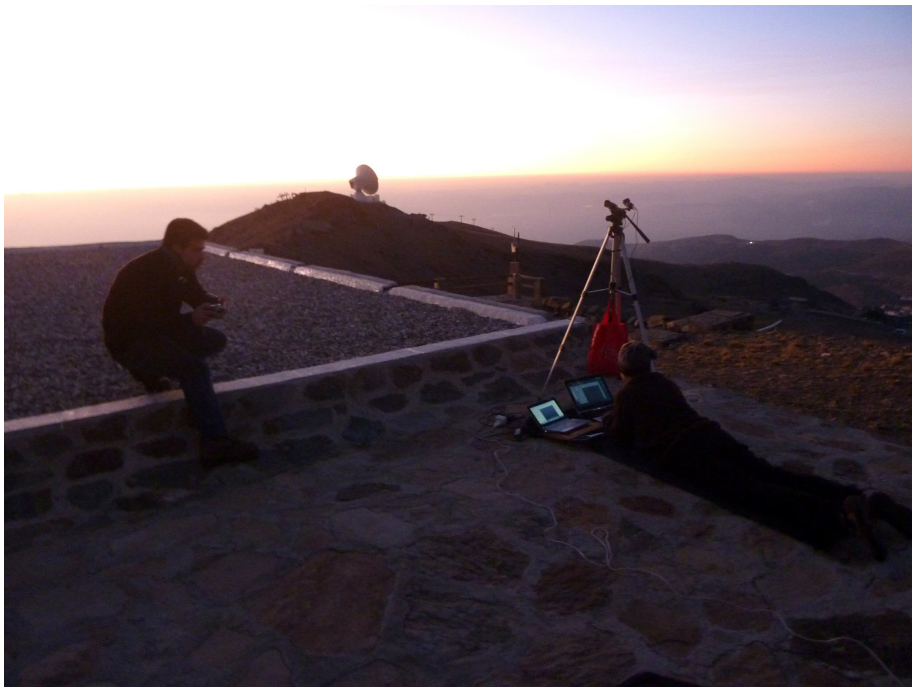

Figura 1: Jaime Zamorano (horizontal), Jaime Izquierdo (vertical, tras la cámara) y el autor (sentado) preparando los instrumentos para la observación de las Dracónidas 2011, en el Observatorio de Sierra Nevada. Álex Sanchez estaba lanzando el globo sonda a unos cientos de kilómetros. ¡Gracias a todos!

Madrid, 12 de abril de 2017

Contents

Resumen

Bajo el término de materia interplanetaria se engloban objetos en un gran rango de masas y tamaños en el Universo, desde el polvo micrométrico hasta los asteroides de centenares de kilómetros de diámetro. Esta materia toma parte de innumerables procesos en las ciencias planetarias. Además el polvo no sólo está presente en el espacio del Sistema Solar, sino también en una infinidad de sistemas extrasolares. Más aún, el polvo interplanetario es más brillante en el infrarrojo que los propios planetas y ya se han observado muchos de estos discos circunestelares de polvo caliente.

La materia interplanetaria en las cercanías de nuestro planeta es también relevante para el estudio de las ciencias de la Tierra y en la exploración espacial. El polvo extraterrestre participa en muchos procesos que tienen lugar en las capas más altas de la atmósfera. Asimismo los asteroides son una amenaza para la humanidad debido a la energía que pueden liberar en caso de impacto contra la Tierra. Se considera que los asteroides mayores de 1 km podrían provocar una catástrofe de proporciones globales y por ello el 90% de ellos ya han sido identificados. Actualmente los esfuerzos se centran en los objetos mayores de 140 m, con consecuencias sólo a nivel regional en caso de colisión. Fuera de la atmósfera terrestre estos cuerpos suponen un peligro para las naves espaciales, especialmente las partículas pequeñas que son las más numerosas y que pese a ello transportan energía suficiente como para comprometer su funcionamiento.

Esta tesis estudia la materia interplanetaria desde dos aproximaciones observacionales distintas. Por un lado se observa la luz solar reflejada por estos cuerpos. En este caso encontramos a los asteroides, cuerpos que se pueden observar con telescopios hasta cierto tamaño. Para la población de objetos próximos a la Tierra el rango de tamaños que podemos observar es mayor, hasta tamaños de apenas decenas de metros. Por ello esta población se considera como una muestra relevante a la hora de estudiar la población general de asteroides en el Sistema Solar. Especialmente cuando estudios recientes afirman que puede haber una diferencia estructural entre las poblaciones con diámetro mayor y menor a unos 200 m, donde los pequeños son objetos monolíticos mientras que los grandes son agregados de objetos. Los objetos menores sólo son accesibles a los instrumentos si se aproximan lo suficiente a la Tierra. La detección y caracterización de estos objetos próximos requieren redes de telescopios de tamaño moderado. En este trabajo presentamos el diseño de un sistema robótico (los telescopios TBT) para la Agencia Espacial Europea (ESA), como prototipos de una red futura. El primero de ellos se encuentra ya instalado en España y se incluyen los resultados del comisionado. Por otro lado hemos analizado el rendimiento que se espera de ellos con ayuda de una simulación de las observaciones de una población sintética de objetos. Consideramos que el sistema diseñado es una herramienta potente para el descubrimiento y seguimiento de estos objetos próximos a la Tierra. Es un sistema basado en componentes comerciales y que por tanto se puede replicar para desarrollar una red global.

Paralelamente los objetos más pequeños que los asteroides se pueden observar usando la atmósfera como detector. Cuando esas partículas colisionan con las moléculas atmosféricas se calientan, sufren un proceso de ablación en el que finalmente se vaporizan, y la luz emitida por esos vapores calientes es lo que denominamos meteoro. Por ello el estudio de los meteoroides se hace principalmente a través del análisis de los meteoros. En particular este trabajo se centra en dos propiedades distintas de los meteoroides. Por un lado hemos investigado la distribución de frecuencias en tamaño/masa usando como observable la densidad de flujo de meteoroides que entran en nuestra atmósfera. El método que hemos desarrollado emplea observaciones en vídeo y analiza las propiedades de los meteoros para optimizar la detección. El resultado son tres aproximaciones observacionales desde tierra que hemos transformado en tres desarrollos instrumentales. Primero hemos diseñado y construido una estación de vídeo de todo el cielo para el Observatorio UCM, y hemos analizado los datos de las Dracónidas de 2011 como ejemplo para demostrar la validez del sistema, con muy buenos resultados. Después hemos investigado la posibilidad de observar meteoros desde la estratosfera para salvar inconvenientes como la extinción o el tiempo atmosférico. Para ello hemos diseñado y probado en vuelo una instrumentación adecuada, y como demostración hemos medido la densidad de flujo de meteoroides para el vuelo en globo de las Gemínidas 2016. Este es un gran paso adelante en este campo al ser la primera vez que se usan datos tomados desde globo para medir la densidad de flujo de meteoroides.

Por otro lado, para la caracterización en composición de los meteoroides hemos diseñado un juego de filtros para un sistema fotométrico de banda estrecha, equivalente a un sistema espectroscópico de baja resolución. Haciendo uso de fotometría sintética sobre los espectros de un catálogo hemos reproducido algunos índices de clasificación de los meteoroides. Entre los resultados destacamos que el color V-R tiene una dependencia significativa de la velocidad y la composición de los meteoroides. Esto significa que los sistemas de detección sin filtro o con filtros anchos pueden tener un importante sesgo en la detección de las diferentes poblaciones de meteoroides.

Keywords: Materia interplanetaria, meteoroides, meteoros, asteroides, objetos próximos a la Tierra, telescopios robóticos, astronomía rango visible, instrumentación, observación astronómica desde globo, imagen de gran campo, sistemas fotométricos, fotometria sintética, caracterización observatorios.

PACS [2010] 92.60.-e, 94.20.Xa, 95.45.+i, 95.55.Cs, 95.75.De, 95.75.Fg, 95.75.Mn, 95.80.+p, 95.85.Kr, 96.30.Vb, 96.30.Ys, 96.30.Za, 96.50.Dj.

Summary

Interplanetary matter covers a wide range of mass and size in the Universe, from micrometric dust to multi-kilometre asteroids. This matter plays countless roles in planetary sciences. Dust fills the space in the Solar System, but also in a myriad of exoplanetary systems. Indeed, the interplanetary dust usually outshines the planets in infrared and these hot debris disks have already been observed in several exoplanetary systems.

The near-Earth interplanetary matter is also relevant for Earth sciences and space exploration. Extraterrestrial dust plays several roles in the upper atmosphere. Moreover the asteroids are a threat for humankind due to the energy they release in the case of impact against the planet. Asteroids larger than 1 km could produce global devastation and 90% of them are already catalogued. Current efforts are focused on the population larger than 140 m, able to produce an impact of regional proportions. Beyond Earth's atmosphere, these bodies pose a hazard to spacecraft, especially the small particles that are the most numerous but still carry enough energy to jeopardise their systems.

This dissertation undertakes the research of the interplanetary matter near the Earth using two different observational approaches. The first one is based on the detection of the sunlight reflected by the bodies. Individuals bodies can be observed with the use of telescopes, they are the asteroids. For objects close to the Earth the accessible range in size is wider, down to the decametre size and consequently this population are a probe to general population of asteroids in the Solar System. Especially if we consider that recent works suggest that objects larger and smaller than 200 m could be two different populations, being the smaller monolithic bodies while larger ones are more likely rubble piles. And we only have access to the smaller population if they come close enough to the be observable. The detection and characterisation of these nearby population require networks of medium-sized telescopes to survey and track them. We design a robotic system (the TBT telescopes) for the European Space Agency as a prototype for a future network. The first unit is already installed in Spain and we present the results of the commissioning. Additionally we evaluate the expected performance of such an instrument using a simulation with a synthetic population. We consider that the system designed is a powerful instrument for nearby asteroid discovery and tracking. It is based on commercial components, and therefore ready for a scalable implementation in a global network.

Meanwhile the bodies smaller than asteroids are observed using the atmosphere as a detector. When these particles collide with the atmospheric molecules they are heated, ablated, sublimated, and finally light is emitted by these hot vapours, what we call meteors. We conduct the investigation of these meteors to study the meteoroids. In particular we address two different topics. On one hand we explore the size/mass frequency distribution of meteoroids using flux determination when the collide into the atmosphere. We develop a method to determine this flux using video

observations of meteors and analyse the properties of meteors as an optical proxy to meteoroids in order to maximise the detection. It yields three ground-based observational solutions that we transform into instrumental designs. First we design and develop a meteor all-sky detection station for Observatorio UCM and use the Draconids 2011 campaign as a showcase for the flux determination, with successful results. Then we investigate the observation of meteors with instruments in stratospheric balloons, overcoming troposphere handicaps like weather or extinction. We have studied the practical implementation of the idea, designed and tested instrumentation for balloon-borne missions, and analysed the data of the Geminids 2016 campaign, determinating the flux of meteoroids in a moment close to the maximum. We consider this balloon-borne campaign for flux meteor flux determination a break-through in the meteor research.

On the other hand we design a filter set for narrow-band photometry for meteoroid characterisation, equivalent to low-R spectroscopy. We reproduce the classification of meteors using synthetic photometry over a spectra catalogue. We find the V-R colour to have a significant dependence to meteor speed and meteoroid composition, what implies a significant detection bias for unfiltered or broadband instruments.

Keywords: Interplanetary matter, meteoroids, meteors, asteroids, near-Earth objects, robotic telescopes, visible astronomy, intrumentation, balloon-borne astronomical observation, wide-field imaging, photometric system, synthetic photometry, site testing.

PACS [2010] 92.60.-e, 94.20.Xa, 95.45.+i, 95.55.Cs, 95.75.De, 95.75.Fg, 95.75.Mn, 95.80.+p, 95.85.Kr, 96.30.Vb, 96.30.Ys, 96.30.Za, 96.50.Dj.

1

Introduction

The estimation of the cosmic dust influx is a topic of importance for the planetary sciences and Earth sciences. The Earth is in constant interaction with the rest of the Solar System, including the infall of extraterrestrial matter. Indeed this accretion was very important in the first stages of the formation of the Solar System and shaped the planetary system into its current status (Stanley, 2005). The interplanetary matter comprises from dust particles to asteroids, what implies also violent impacts like the one that probably formed the Moon (Canup and Asphaug, 2001). Nowadays the impact and accretion rates are significantly lower but still relevant for many processes on Earth. These bodies are the source of metallic ions[1] in the upper atmosphere and thus responsible for ionospheric phenomena like the Polar Mesospheric Summer Echoes (Rapp and Lübken, 2004), the Sporadic-E (Mathews, 1998) and Polar Mesospheric Clouds (Hervig et al., 2012). This particulate matter affects the aeronomy of the upper stratosphere, and in general all the layers from the mesosphere (Gumbel and Megner, 2009) down to the tropospheric climate (Asher and Clube, 1993). For a full review of the interaction of the dust and the atmosphere see Plane (2012). The matter influx estimations range currently around $(5 - 500) \times 10^6$ kg per year (from 2 to over 200 tons per day) and therefore is a topic far from being closed. The modellers of the processes in which the dust is involved find this uncertainty quite deficient for their models (von Zahn, 2005), and often use as reference the classic value from Love and Brownlee (1993).

The dust is ubiquitous in the Universe and plays an important role in astrophysics from stellar to galactic fields, from interstellar medium to interplanetary medium. The research of the dust in the Solar System is essential to infer and understand dust properties beyond its boundaries. Moreover we are already able to observe the infrared dust emission of other planetary systems. Therefore its study is a proxy for the countless exoplanetary systems and their debris disks, being hot dust a tracer of planets (Nesvorný et al., 2010).

With regard to interplanetary matter as a hazard to the Earth, humankind has been aware of this problem at least for the last 50 years and has tried to find the objects with the largest destruction potential. In May 1998 NASA was committed to find at least 90% of the bodies larger than 1 km (global devastation in case of impact), what was achieved at the end of the last decade (Mainzer et al., 2011). In 2005 US President Bush signed the NASA Authorization Act of 2005 where the scope was increased to detect, track and characterise NEOs down to 140 m of diameter (regional devastation in case of impact). The goal was to complete the 90% of the catalogue by 2020, a deadline that NASA it is not going to meet (current achievement is in the 60% after 12 years). In October 2016 the 15000$^{\text{th}}$ NEO was discovered and 2016 set a new record with 1894 NEOs

[1] Note that they are essential for adaptive optics imaging as they are the input for the mesospheric sodium layer that is excited with lasers to create artificial stars.

discovered. Moreover at the end of the year the White House released the "National Near-Earth Object Preparedness Strategy", a strategy document to boost the preparation to address the hazard of these objects. In the near future the foremost milestone is expected in 2022 with the start of regular survey operations of the Large Synoptic Survey Telescope (LSST). LSST will find 80% to 90% of the NEOs larger than 140 m. Despite these efforts, unexpected impacts with smaller energy still happen (see figure 1.1). As recent as 2013 a decameter asteroid entered over Chelyabinsk releasing 2100 TJ and more than 1500 people were injured, mostly from broken glass (Borovička, 2015).

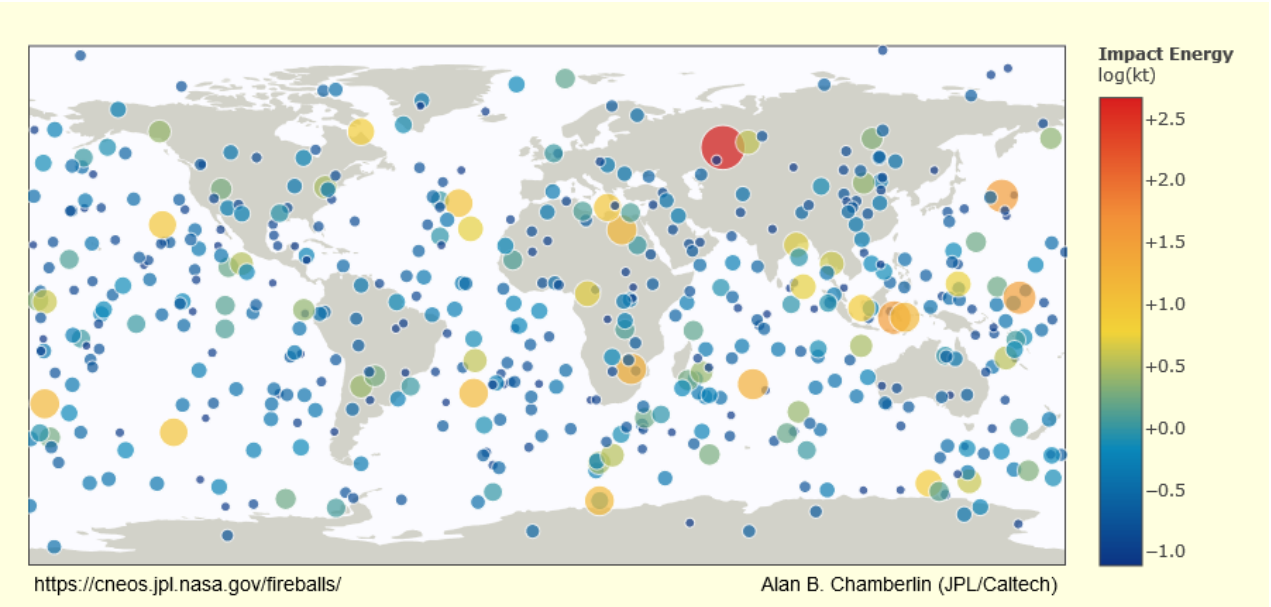

Figure 1.1: Geographical distribution of the impacts detected with IR sensors from satellites by the Department of Defense of the US from 1988 to March 2017. Colour circles represent the impact energy in kt. Plot adapted from CNEOS JPL website.

Apart from the strictly scientific relevance, the topic has further implications in the space industry and space exploration. The matter in the interplanetary space poses a risk for the spacecraft. The characterisation of its distribution (size frequency, mass frequency, velocity) and composition is essential for the evaluation of this risk.

1.1 Origin, distribution and properties of the interplanetary matter

The origin of the dust is found in the collisions of asteroids between Mars and Jupiter, and in the sublimation of comets close to the Sun. Each of them is subdivided into the two components according to their dominant dynamics, the Poynting–Robertson drag ($< 10^{-5}$ g) and collisional destruction at the origin ($> 10^{-5}$ g). The slope of the mass distribution of meteoroids changes at that point (Dikarev et al., 2005). Nesvorný et al. (2010) shows that comets are the main contributor to mm-sized particles at 1 AU. The peak of influx rate of particles into Earth's atmosphere is at 100 μm particle size.

Interplanetary matter falling to Earth, in the form of solid bodies, has a extremely wide mass distribution (figure 1.2). The masses span over 30 orders of magnitude from 10^{-16} g to 10^{15} g. The mass frequency distribution (MFD) is a fundamental quantity of the Solar System. It is essential for the estimation of the cosmic dust infall, the interpretation of observations of the zodiacal cloud and the models for meteoroid environment.

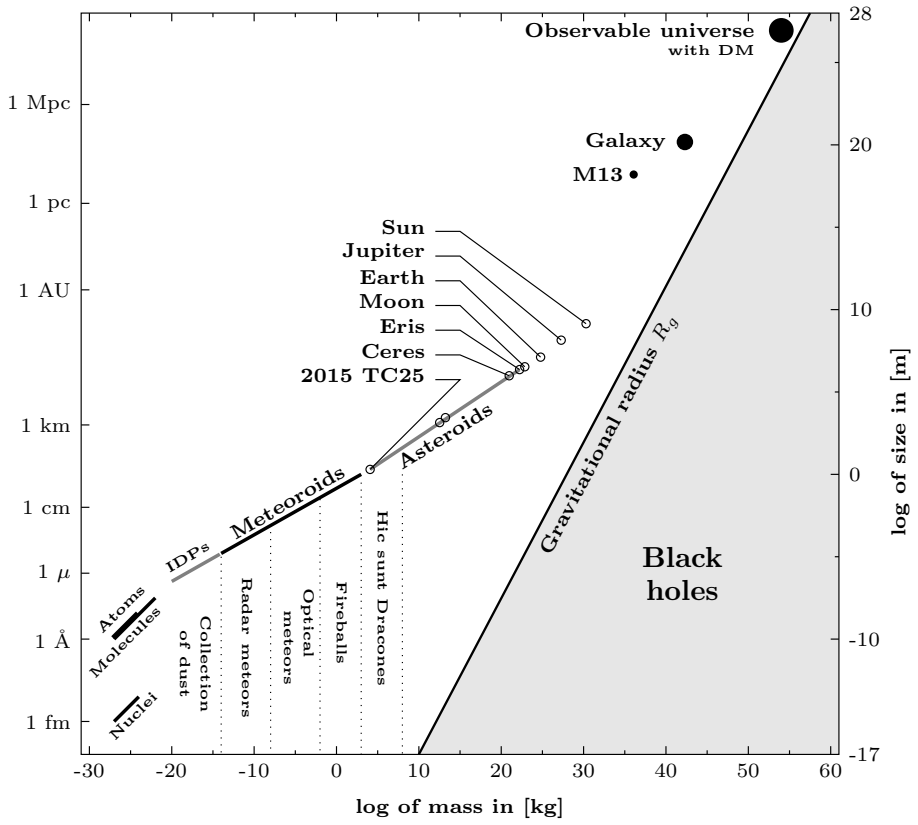

Figure 1.2: Mass and size distribution of the interplanetary matter and some other known objects of the observable Universe. Interplanetary matter comprises IDPs, meteoroids, asteroids and comets. Amongst the asteroids we have highlighted 2015 TC25, which is thought to be the smallest asteroid observed from telescopes on Earth (Reddy et al., 2016), Ceres, as the largest object in the main belt and Eris, as the most massive transneptunian object known to date. Note that Ceres and Eris are also considered dwarf planets. Figure after Ceplecha et al. (1998).

In the high-mass end of the distribution we find a big contribution to the total mass influx, although they are so rare that they play no role in atmospheric balance. However they pose a threat to human life and infrastructure. Awareness of the possibility of Earth encountering a dangerous asteroid/meteoroid in the near future was developed after the collision between fragments of comet Shoemaker-Levy and Jupiter in 1994, although the impact hazard was already known (Morrison, 1992). That impact against Jupiter acted as a reminder, as such collisions have already happened. In 1908 in the remote region of Tunguska (Russia), a 100-m asteroid impacted in the atmosphere. It disintegrated at an altitude between 5 to 10 km and the air burst released energy in the range of 10^{17} J (equivalent to 10 megatons of TNT) flatenning 2000 km^2 of Siberian Taiga forest (Chyba et al., 1993). A century later, in 2013 a $\sim$ 17 m asteroid produced an airburst over Chelyabinsk (Russia) and injured about 1500 people (Brown et al., 2013; Borovička et al., 2013).

1.2 Observation of the interplanetary matter

As MFD for interplanetary matter cover such a wide range of masses, the estimates are based on different methods and phenomena. The smallest dust particles are so numerous that they can be observed any dark night reflecting the sunlight in the ecliptic plane, is the zodiacal light. Zodiacal light brightness is related mainly to particles of mass $\sim 3 \cdot 10^{-7}$ g, in the range of 10 μm to 100 μm (Nesvorný et al., 2010).

Asteroids are also observed using reflected sunlight, and in the population that come close to us (Near-Earth Objects) we have access to the smaller part of their size distribution, that otherwise it is not detectable because of their distance. In chapter 2 we research the asteroid detection topic and present a design of an observatory based on commercial components that can be used for a worldwide network to cover the detection of these elusive objects.

On the contrary, there is a population of large particles that are not so numerous and therefore they are not easily detectable unless they enter into Earth's atmosphere. Particles under 0.05 mm in size are slowed down before the temperature reaches the evaporation point and the ablation does not start, emitting no light as a meteor. The particle cools down and sediments slowly through the atmosphere down to Earth's surface. While particles larger than 0.05 mm ablate and are sublimated (emitting light as meteors). Optical observation of meteors fill in the gap between the in-situ measurements from satellites and fluxes from lunar impacts, infrasound or infrared detection of large impacts on Earth's atmosphere.

Video observations of meteors cover a wide range of meteoroid sizes. From 100 μm using image intensifiers, to cm-sized meteoroids that are observed as fireballs with all-sky cameras. Assuming a meteor layer where they emit light, we can calculate the meteoroid flux crossing it. In order to combine fluxes from different cameras the data is reduced to an effective area up to a certain magnitude, assuming a mass index for the distribution of mass in the meteoroid stream under study. In chapter 3 we analyse this approach and study the meteoroid flux determination using video observation of meteors.

In chapter 4 we apply the analysis done to the design of some instrumental setups. The first one is a wide-camera meteor surveillance station, in order to join the SPanish Meteor and Fireball Network (SPMN) (Trigo-Rodríguez et al., 2004; Madiedo and Trigo-Rodríguez, 2008). Meteor surveys find meteoroids streams where the parent body is unknown. As meteors follow similar orbits than the parent body and they represent the impact of meteoroids, the parent bodies of the meteoroids streams are PHOs. Moreover as the release of meteoroids from asteroids is not common or efficient, the search of these meteoroids yield the finding of dormant comets amongst the Near-Earth Objects (Jenniskens, 2008; Ye et al., 2016). Dormant comets in the NEO population, as they are potential impactors, are relevant for the inflow to Earth of water and organic material, like the rest of the comets (Chyba et al., 1990). Then we carry out an analysis of the feasibility of meteor research as a by-product from large astronomical surveys, in particular applied to TBT telescopes, and conclude that the number of detections is not going to be significant unless for those surveys using short term exposures (in the order of seconds) and large pixels (several arcseconds), like the fast transients or space debris surveys. Finally in section 4.4 we present an innovative solution to observe meteors from the stratosphere and we design instrumentation to fly on board sounding balloons. We show that meteor observation over the troposphere have significant advantages.

1.3 Motivations and goals

The main motivation of this work is the study of the interplanetary matter to understand the evolution of the Solar System. Principally, we investigate the origin and distribution of the current nearby population across several orders of magnitude in mass/size. Particularly we focus on two size ranges: Near-Earth asteroids, especially those between 140 m and 1 km in size; and the mm-sized and cm-sized meteoroids.

The final goal for the Near-Earth objects is their discovery and the orbital determination, in order to calculate the size/mass frequency distribution and determine the origin and dynamics of the current population. For these goals we pursue an instrumental development for robotic telescopes in distributed networks. Secondly, the objective for mm-sized and cm-sized meteoroids is more ambitious. First we want to design an instrumental system for the characterisation of the meteoroid composition. On the other hand, we want to improve the methods for optical detection of meteors, focusing on the determination of the spatial number density of meteoroids. For that purpose we focus on some instrumental developments for meteoroid density flux determination.

Besides, the size/mass frequency distribution of asteroids and meteoroids are essential for the evaluation of impact threat against the Earth, and collisions with spacecraft respectively.

2

Near Earth Objects detection with optical ground-based telescopes

2.1 Detection and characterisation of asteroids in Earth's neighbourhood

As a result of the accretion and planet migration in the Solar System (Stanley, 2005), there is a significant asteroid population between Mars and Jupiter orbits, the so-called Main Belt. The asteroids in the main belt have stable orbits but in the long term they suffer non-gravitational thermal forces that makes them drift into resonant escape routes. These resonances are responsible for the expulsion from the main-belt onto planet-crossing orbits (Morbidelli and Vokrouhlickỳ, 2003; Granvik et al., 2017). When the asteroids are already in these orbits, the dynamics are dominated by close planet encounters. As the population is considered steady and the contribution from the main belt is constant, there are mechanisms of removal like collisions with Sun and planets, or the ejection out of the Solar System.

Hence these asteroids are a probe of the dynamical evolution of the planetary system, as well of the compositional evolution (DeMeo and Carry, 2014), including the collision between bodies. Indeed asteroids coming into the inner Solar System are mainly studied because of their hazard to the planet and their relation to the geological and biological evolution of Earth. Moreover, asteroids have also recently become of interests as targets for robotic and human exploration, as well as for mineral resource exploitation. Current research focuses on understanding if small asteroids (< 200 m) are monolithic while larger ones are more likely to be rubble piles. A difficulty is that we only have access to the smaller population if they are NEOs and consequently come close enough to be observable (Pravec and Harris, 2000). Furthermore the characterisation of NEOs using their spectral class and spin distribution is a test for current evolution models of the global asteroid population.

Near Earth Objects are the asteroidal and cometary bodies with a perihelion distance $q \leqslant 1.3$ AU. In this work we use interchangeably NEO and NEA (Near-Earth Asteroid) for the sake of simplicity, however, comets are also considered in the models we have used. Also, note that for modelling purposes the long period comets (LPC) have been excluded. Levison et al. (2002) argues that the risk of that populations is three orders of magnitude less than the other populations within NEO category. The limit is usually set with the Tisserand parameter $T_J > 2$. This parameter comes from the study of the restricted circular three-body problem, being T_J a pseudo-energy of the Jacobi integral that must be conserved (equation 2.1).

$$T_J = \frac{a_J}{a} + 2\,\cos i \sqrt{(1-e^2)\frac{a}{a_J}} \tag{2.1}$$

where a_J is the semimajor axis of Jupiter.

Amongst the NEOs there is a classification according to their orbital parameters: Amor ($1.017\,\text{AU} < q \leqslant 1.3\,\text{AU}$), Apollo ($a \geqslant 1.0\,\text{AU}$ and $q \leqslant 1.017\,\text{AU}$), Aten ($a < 1.0\,\text{AU}$ and $Q > 0.983\,\text{AU}$) and Atira ($a < 1.0\,\text{AU}$ and $Q < 0.983\,\text{AU}$). This division is reflected in the geometric observational conditions, for instance Amor asteroids never cross Earth's orbit and their close approaches are always at large elongation angles. While Atira asteroids always have small angular phase during their close approaches to the Earth, making them objects difficult to discover. According to a criterion for hazard in case of impact, the IAU adds an additional group: the Potentially Hazardous Objects (PHOs) are those NEOs with Minimum Orbit Intersection Distance $MOID < 0.05\,\text{AU}$ and $H < 22$.

Current NEO population can be described with the contribution from different source regions: the ν_6 secular resonance, the 3:1, 5:2 and 2:1 mean-motion resonances with Jupiter, the intermediate Mars crossing (IMC) region with Hungaria and Phocaea families and the Jupiter-family comets (JFCs). Each source produces NEOs with distinctive orbital distribution, albedo, SFD, etc.

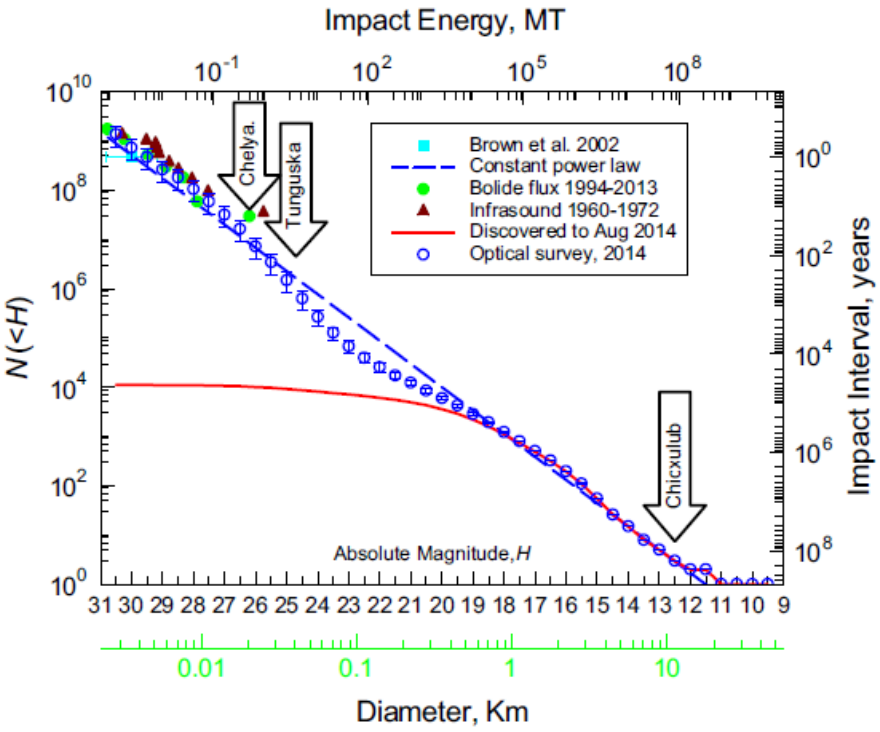

Figure 2.1: Cumulative number distribution of known Near-Earth Objects according to their absolute magnitude H or diameter. In a first approximation it can be fit by a constant power law assuming a dip between absolute magnitudes 19 to 25. Plot from Harris and D'Abramo (2015).

Most recent models (Harris and D'Abramo, 2015; Granvik et al., 2016; Tricarico, 2017) agree on a population of ∼1000 NEOs larger than 1 km and in the order of $\sim 10^8$ NEOs with absolute magnitude $H < 30$. The models are based on the characterisation of the detection efficiency of a survey comparing the input from the source regions and the effectively detected objects by that survey. The cumulative size frequency distribution (SFD) follows a power law distribution $N(D) \propto D^{-2}$, where N(0.5 km) $\sim 10^4$, from the largest known NEO (diameter $d \sim 30$ km) down to $d \sim 0.5$ km. For asteroids in the main belt the distribution this SFD follows a power law to the -2.5 of the diameter. On the other hand for the decameter objects, observed as bolides, that exponent is closer to -4 (Brown et al., 2002). The SFD shows a dip in the range from tens to hundreds of meters ($19 < H < 25$), probably due to a structural change, the transition from rubble piles to monolithic bodies (Harris and D'Abramo, 2015) (figure 2.1). Indeed rotational periods are always longer than 2 hours for the >200 m population, while the smaller NEOs could have periods as short as a minute (Warner and Harris, 2011). This change is relevant as the internal structure is a key parameter for the impact models in order to asses the potential damage.

For asteroids the absolute magnitude H is defined as the magnitude of an asteroid at zero phase angle and at 1 AU for heliocentric and geocentric distances. The diameter of an asteroid can be estimated from the absolute magnitude, using the value of the reflectance of its surface, the albedo p_V. Assuming a homogeneous spherical object (Chesley et al., 2002):

$$D = \frac{1329\, km}{\sqrt{p_V}} 10^{0.2\, H} \tag{2.2}$$

The conversion from brightness to mass involves an estimate of the albedo (known for some spectral types) and an estimate of a density (imprecisely known for some spectral types: $\sim 2 - 3$ g/cm^3 for S-type, ~ 1.5 g/cm^3 for C-type and up to ~ 6 g/cm^3 for M-type). Hence characterisation of NEOs is essential for elaborating the full picture of their nature. Albedo is only known for objects which have been observed in infrared or with radar. Therefore diameter estimations are usually given as a range, corresponding to albedos $0.05 < p_V < 0.25$, where most of the asteroids lay. We consider an average geometrical albedo $p_V = 0.14$ (Binzel et al., 2004). The absolute magnitude $H \leqslant 18$ corresponds to $\leqslant 140$ m, the size of the object which impact could cause regional or global devastation (see details in Morrison (1992) for conversion from size to impact effects).

The discovery of these nearby objects happened during the global search for asteroids in the Solar System, that started in the 18$^{\text{th}}$ century. The first asteroid was discovered in 1800, and the first NEA (most of the comets observed before fitted in the NEO category) to be discovered was 433 Eros, in 1898. With $34 \times 11 \times 11$ km^3 is the second largest, after 1036 Ganymed, which was discovered in 1924. The discovery rate stayed at < 10 per year until the 70's, when Helin and Shoemaker (1979) started a NEO survey looking for streaks in photographic plates. Afterwards the rates rocketed with the use of CCD for this task, which was pioneered by Rabinowitz (1991) for the Spacewatch survey. After them several surveys have searched these objects, and current discovery rate is over 1500 per year (figure 2.2). The discovery of these objects is mainly performed by wide-field ground-based telescopes, with typical exposure times between 30 to 60 s. Each field of view is visited 2 to 4 times with a cadence of 15 to 30 minutes, enough to show the high apparent movement of the NEOs. The surveys can be *Deep Surveys* and *Wide Surveys* (Farnocchia et al., 2012), depending on their selection in the trade-off between limiting magnitude and area covered.

In May 1998 NASA was committed by the House Committee on Science to find at least 90% of the objects larger than 1 km, goal that was achieved at the end of the last decade (Mainzer et al., 2011) and discovery rates since have declined with the progression of the task (figure 2.3). In 2005, in the NASA Authorization Act of 2005, the scope was increased to detect, track and characterise NEOs down to 140 m of diameter, becoming one of the seven major purposes for the agency. Models estimate there are $(10 - 20) \times 10^3$ objects larger than that size, but only 50% of them have been discovered so far (figure 2.3). The goal was to complete the 90% of the catalogue by 2020 and current figures do not suggest a fulfilment of the task in by that date. Note that we make a mention to these programs from the United States of America, as this country has provided 98% of the Near-Earth Objects observations since 1998[1] (figures 2.3 and 2.4). Current estimations show that more than 90% of NEOs larger than 1 km have been discovered, but this rate drops down to ∼25% for $D > 100$ m and to ∼0.001% for $D > 10$ m.

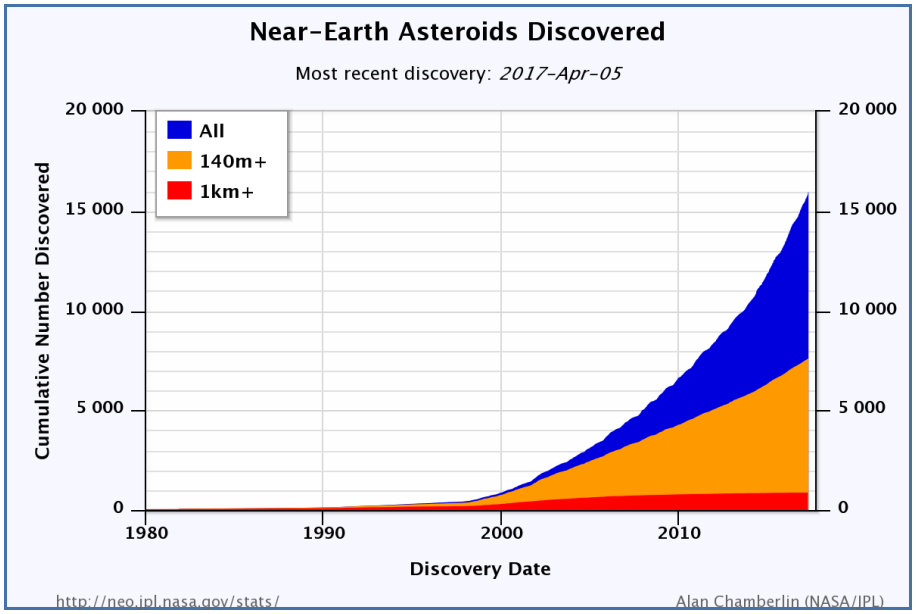

Figure 2.2: Cumulative number of known Near-Earth Asteroids (NEAs) versus time. Totals are shown for NEAs of all sizes, those NEAs larger than 140 m in size, and those larger than 1 km in size. Credit: JPL Near Earth Object Program.

After the discovery, the main task consists in astrometric follow-up to decrease the orbit uncertainty, essential for further observations. The first step is evaluate the impact risk to asses the need and urgency of new observations. The objects are classified according to the Palermo Scale (Chesley et al., 2002) and the Torino scale (Morrison et al., 2004). Palermo Scale is the base-10 logarithm of the relative risk, measured as the risk posed by an object compared to the background one. While the Torino Scale is intended for the general public and takes into account the predicted impact energy, the impact probability and depends upon the number of years until the potential impact.

[1]The Council of Europe issued the Resolution 1080 on the detection of asteroids and comets potentially dangerous to humankind in 1996, but the efforts in the European side have been more limited.

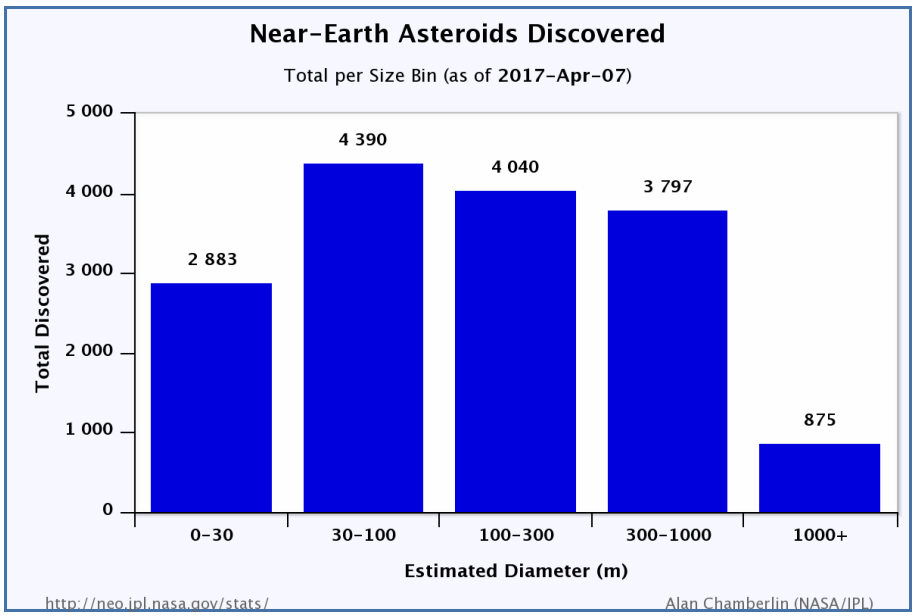

Figure 2.3: Current total number of known NEAs grouped according to their estimated sizes. Credit: JPL Near Earth Object Program.

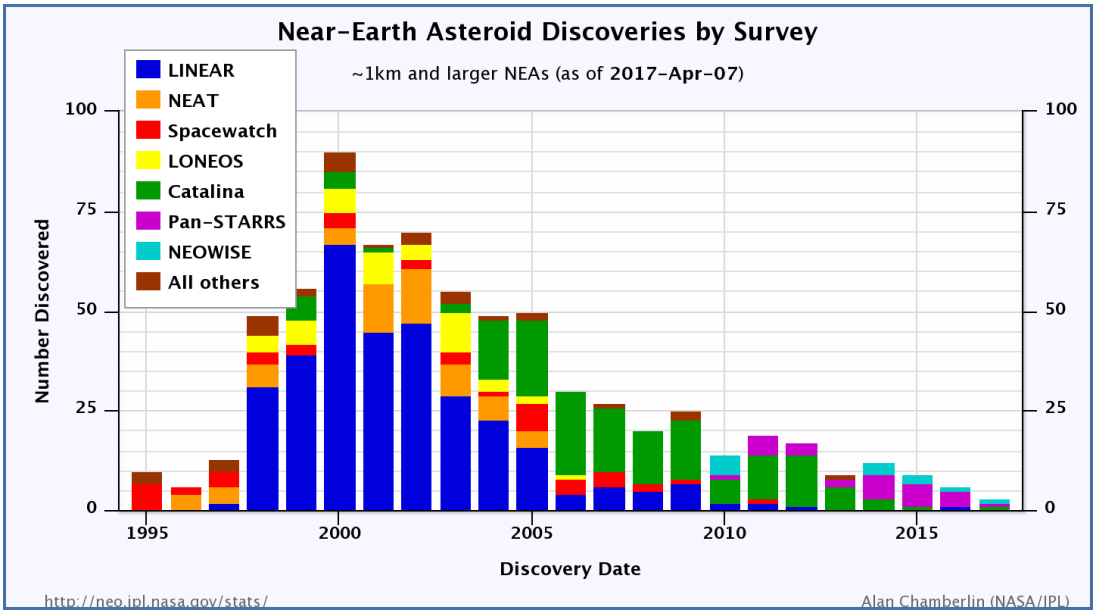

Figure 2.4: Number of NEA discoveries per year, by survey, for NEOs larger than 1 km. The discovery rates have declined as expected while getting closer to the completion of the catalogue. Credit: JPL Near Earth Object Program.

Moreover long-arc high-precision astrometry allows the determination of the area-to-mass ratio. Mass is a key property but it is usually not measurable, unless the asteroid is binary. Otherwise mass is estimated from shape and size, assuming a density and then constrained by the area-to-mass ratio. Further observations with radar or visible light curves are used to estimate rotation state and shape. Space-based IR measurements constrain better the albedo and therefore the diameter. Less than 10% of NEOs have a well-determined diameters and albedos, mainly performed by Mainzer et al. (2011) using the IR space telescope NEOWISE and ground-based radar observations.

We present here an instrument developed for this purpose of NEO observation, both for discovery and follow-up observation. We consider it a cost-effective robotic optical survey. The project is dubbed Test-Bed Telescopes (TBT) and is developed for the European Space Agency (ESA) by a consortium participated by the author. In section 2.2 we introduce the design from the high-level requirements provided by the agency, to the actual implementation in real hardware and software. In the sections 2.3 and 2.4 we evaluate the expected performance of the instrument. First we use a figure of merit for the survey capabilities and then we perform a simulation of the performance of the TBT telescopes with a realistic population in order to understand its capabilities and the biases inherent to its characteristics and strategy. Finally in section 2.5 we describe the commissioning of one of the TBT telescopes that is already installed in Spain.

2.2 Design of a NEO-detection observatory: TBT project

This part of the thesis has been done within the framework of a project for the European Space Agency (ESA), the Test-Bed Telescopes (TBT) project. The TBT project is being developed under ESA's General Studies and Technology Programme (GSTP), and shall implement a test-bed for the validation of an autonomous optical observing system in a realistic scenario, consisting of two telescopes, one located in Spain and another one in the Southern Hemisphere. The project is developed within the Space Situational Awareness (SSA) programme of ESA. The goal of the project is to provide two fully robotic telescopes, which will serve as prototypes for development of a future network.

The Space Situational Awareness program of European Space Agency foresees the deployment of several robotic telescopes to provide surveillance and tracking services for man-made as well as natural Near-Earth Objects (NEOs). These ground-based optical sensors are very efficient systems to detect and track faint objects in high altitude orbital regions. The requirements (table 2.1) for the project were stated by the agency and are partially based on the concept of dynamical observation for sensors network (Cibin et al., 2011). We copy here the description by ESA as the main high-level requirement: "*The observation system shall be a passive optical telescope with large aperture, with a wide field of view, and a attached highly-efficient CCD camera with moderately-large pixel scale, operating usually with 1 to 2 sec exposure time for space debris observations and 10 to 120 s exposure time for NEO observations, providing very fast read-out with low noise, and shall allow rapid readout during telescope repositioning; the observation system shall provide fast repositioning capabilities with short settling times, have a minimized duty cycle, and assure precise and reliable epoch registration.*"

	Requirement	**Value**
Detection magnitude for $t_{exp} = 2$ s	$m = 18.0$	$SNR = 4.6$ for $m = 18.0$
Field of view	minimum 2 deg x 2 deg goal 3 deg x 3 deg	2.5 deg $\times$ 2.5 deg
Telescope aperture	> 400 mm	560 mm
Pixel scale	< 3 arcsec/pixel	2.17 arcsec/pixel
Tube lenght	< 2 m	1400 mm long (f/2.5)
Spectral band	380 nm to 900 nm	380 nm to 1050 nm
PSF	diffraction limited, 80% of the energy from a point source encircled within one pixel	$D_{80} < 11.4$ μm (pixel size 15 μm)
Dark current	$\sim$ 0.1 e-/pixel/s	0.18 e- /pixel/s
Read-out noise	< 10 e- rms	7 e- @500 kHz 15 e- @1 MHz
Dynamic range	> 1:10000	average 1:12000
Non-linearity	< 1%	<1%
Peak QE	> 90%	92%
QE @ 550 nm	> 75%	$\sim$ 90%
Elevation angle	> 20 deg	> 15 deg
Mount slew rate	> 5 deg/s	12 deg/s
Tracking	Centroid of a point source within 1 pixel	rms RA: 0.41 arcsec Dec: 0.26 arcsec
Pointing	> 1/20th of the FoV purely by mechanical means > 1 pixel through processing of the data	mechanical 5 arcmin (1/30th FoV) model 26 arcsec rms (1/750th FoV) astrometric < 1 arcsec rms

Table 2.1: Summary of the hardware requirements and final values for the TBT telescopes provided by the manufacturers or measured during the HW testing and the observatory commissioning. The requirements were modified after the Preliminary Design Review, which included a market survey, in order to adjust them to the actual budget.

The project was contracted by ESA to the TBT consortium, which consists of companies and institutions from the countries funding the project. The prime contractor is the Spanish company ISDEFE, while other members of the consortium are Ixion Aerospace and Industry and the Fabra-ROA Telescope at Montsec[2]. The other partner is IGUASSU[3] from Czech Republic. The author worked for the packages led by ISDEFE and was in charge of the hardware selection, acquisition, integration, testing and validation. The author also led the commissioning and the testing of the image processing software (named Asteroid and Satellite Astrometric Processor - ASAP).

The project followed the standard ESA procedures and it comprises several work packages and milestones to be passed. The first part of the project consisted of a market survey and the definition of the baseline design. The design concept was closed in the Preliminary Design Review (PDR) and a detailed design was started. The project itself was driven by geographical return and based on Commercial Off-The-Shelf (COTS) components, both for hardware and software. According to the final selection in the Critical Design Review, the operation modes and strategies design were driven by the elements finally selected. All the elements were purchased, received, integrated, tested and validated by ISDEFE in Spain. Some of the hardware elements were tested in factory (FAT - Factory Acceptance Test) before delivery. The first unit was installed in Cebreros ($40°27'14.67''$ N, $04°22'09.55''$ W, altitude 719 m, see figure 2.6) and the full system functionality was tested in an internal Site Acceptance Test (SAT) after the commissioning period.

The telescopes are intended to be prototypes for testing strategies and detection modes. The final user of the TBT telescopes is going to be the Space Situational Awareness programme of ESA. The Near-Earth Objects (NEO) and Space Surveillance and Tracking (SST) segments will share the time of the telescopes. Therefore the telescopes will spend their observational times in both natural and artificial objects, and not only in survey but also in follow-up observations mode. Although the design, as they are prototypes, is not strictly scientifically driven, we have analysed the potential scientific cases in the field of this thesis, interplanetary matter, and especially the scientific capabilities of the telescopes related to the NEOs:

– NEO population survey and follow-up.
  It is the main objective within NEO segment, in order to warn for incoming objects and characterise the population of objects in Earth's environment. On one hand, in section 2.3, we evaluate the survey capabilities using a figure of merit. On the other hand, in section 2.4, we have analysed the TBT capabilities simulating its performance with a realistic NEO population. Other authors focus only on impactors, like Vereš et al. (2009). The distribution of impactors' orbits to smaller values for semi-major axis, eccentricity and inclination. Note that the instrument we design is focused not only in the Potentially Hazardous Asteroids (so-called potential impactors, with $H < 22$ and $MOID < 0.05$), but in the general NEO population. The study of the total population would allow us to infer the properties of the PHOs and a better estimate of its potential damage.

– NEO population characterisation.
  TBT telescope have colour estimation (B,V, R filters) and light-curve building capabilities, where such an instrument could have an impact as addressed by Warner and Harris (2011), who explicitly mention 0.5-1 m telescopes for this characterisation task. Broad-band colours

[2]TFRM http://www.am.ub.edu/bnc/
[3]Iguassu Software Systems (ISS), Prague

yield some level of discrimination amongst asteroid types (e.g., DeMeo and Carry (2013)). TBT project has soft photometric requirements and hence we have not studied this case in detail.

– Main-belt asteroids monitoring.
TBT will observe, detect and measure several asteroids in each field of view (figure 2.5). This monitoring is suitable, with 4 measurements per visit and a cadence of 6 days to return to the same field. It will eventually discover and/or recover asteroids in the main belt, although most of the discoveries nowadays are with magnitudes $m > 20$ and therefore beyond the TBT limiting magnitude.

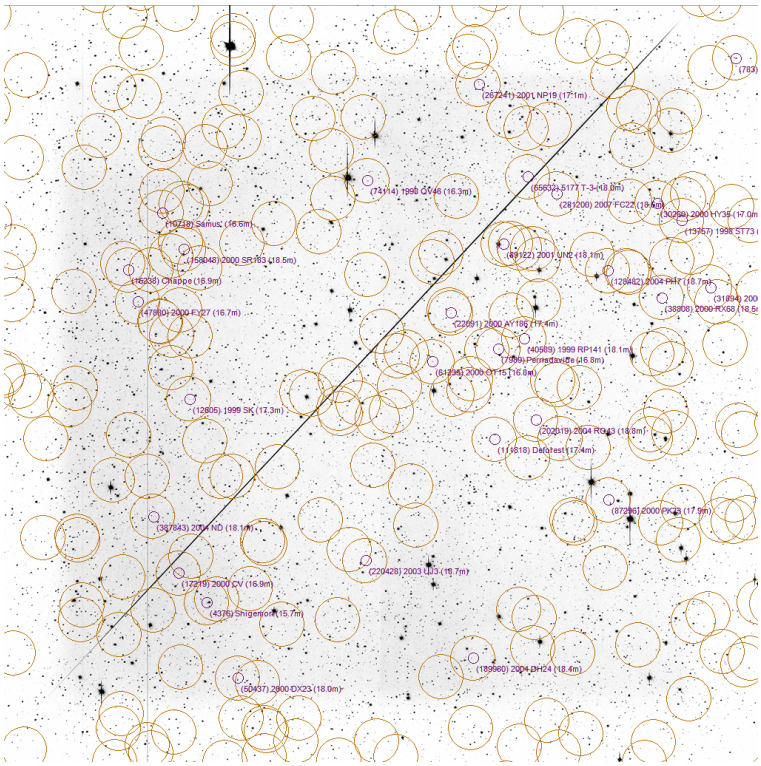

Figure 2.5: ASAP composite image (inverted colours) for the first survey performed by TBT telescope in Cebreros. ASAP found 38 known asteroids (purple circles) and discarded tens of fake detections (orange circles). Image is raw and shows vignetting and a diagonal line, which is an artefact caused by a nearby bright star.

– Transneptunian-objects (TNOs) observation.
TNOs must have an absolute magnitude $H < 4$ to be observable by TBT telescopes in the nominal mode ($t_{exposure} = 30$ s). Moreover the apparent movement is not compatible with the detection strategy for NEOs (field revisited 3-4 times, every 10-20 minutes). Study of TNOs is only accessible through the observation of star occulations by these objects.

In Winter 2015 the Cebreros telescope entered in the commissioning phase (section 2.5), led mainly by ISDEFE as the integrator of all the subsystems. After this phase, the second telescope will be installed[4] and both observatories will be tested as a complete autonomous and robotic system. For this Final Acceptance Test, the telescopes will be monitored from ESOC using the

[4]Second telescope is foreseen to be installed in Chile by the end of 2017

Figure 2.6: View of the Cebreros TBT Observatory at sunset. All the telescope equipment, control and processing computers are hosted inside of the 4.2 m diameter clamshell dome.

Human-Machine Interface HMI, implemented by Ixion, and programmed by the scheduler TRANSITO (Racero et al., 2015), developed by ISDEFE. The images are processed and the results sent automatically by ASAP, a software developed by M. Busch for the TOTAS project (Koschny and Busch, 2015) and tailored by IGUASSU for the TBT Project.

The final designed system consists of two telescopes, one in Spain and the second one in the Southern Hemisphere. The telescope is a fast prime-focus astrograph with a large Field of View (FoV) of 2.5×2.5 deg^2 and a plate scale of 2.2 arcsec/pixel. The tube is mounted on a fast direct-drive mount moving with speed up to 20 deg/s. The focal plane hosts a 2-port 4K x 4K back-illuminated CCD with readout speeds up to 1 MHz per port. All these characteristics ensure good survey performance for transients and fast moving objects. Each TBT telescope can cover up to a third of their visible sky each night while following a revisiting pattern for the search of asteroids. Detection software and hardware are optimised for the detection of NEOs and objects in high Earth orbits (objects moving from 0.1-40 arcsec/s). Nominal exposures are in the range from 2 to 30 seconds, depending on the observational strategy. Part of the validation scenario involves the scheduling concept integrated in the robotic operations for both sensors. Every night it takes all the input needed and prepares a schedule following predefined rules allocating tasks for the telescopes. Telescopes are managed by RTS2 control software, that performs the real-time scheduling of the observation and manages all the devices at the observatory (Kubánek, 2010). At the end of the night the observing systems report astrometric positions and photometry of the objects detected. Apart from the main hardware and software, there are many other ancillary elements that allow the observatory to be robotic. A detailed description can be found in Ocaña et al. (2016b). In the next paragraphs we describe the actual system, with all the hardware elements and their functionalities.

2.2.1 Main hardware elements

The telescope is a fast (f/2.5) prime-focus astrograph with a 3-lens Wynne corrector designed by Dr. V. Yu Terebizh (Crimean Astrophysical Observatory). It has a 56-cm diameter mirror and a

resulting unvignetted angular FoV of 3.5 degrees in diameter (see table 2.2 and figures 2.7 and 2.8 for further details). Mirror was polished by LOMO [5] and Wynne corrector manufactured by TEC[6]. The tube, mount and integration of the four of them were done by APM Telescopes[7]. The optical beam has an 80-mm shutter manufactured by BS [8], to ensure a 1 ms timing accuracy, with a homogeneity of 0.5% across the FoV. The shutter needs 150 ms to cover/uncover the whole beam, but the time across the chip can be mapped and corrected thanks to a high level of reproducibility.

Parameter	**Value**
Entrance pupil diameter	560 mm
Focal length	1415.5 mm
Image space f#	2.53
Plate scale	6.86 μm/arcsec
Angular field of view	3.5 deg
Linear obscuration	0.41
Effective aperture diameter	511 mm
Back focal length	121 mm
D_{80} (from centre to edge)	9.1 – 11.4 μm (1.3-1.7 arcsec)

Table 2.2: Optical parameters of the VT56s design from V. Yu. Terebizh for the TBT telescopes.

The mount is an APM GE-300 manufactured by Michael Knopf. It is able to load up to 300 kg, although our tube and accessories are significantly lighter. As the telescope is hosted in a clamshell dome, this mount was intentionally selected to perform better while tracking with moderated winds. The mount can move up to 20 degrees per second, but is limited at 12 degrees per second for TBT to increase slewing performance. This speed allows re-positioning in 2 seconds for neighbouring fields and maximum 20 seconds between any two locations in the sky. TBT telescopes' mounts are controlled by Sitech[9] Telescope Control Systems. The mount has Renishaw absolute encoders with a resolution better than a tenth of arcsecond. The servo controller system actuates over two direct driver motors in a close-loop at 2000 Hz. It has a proportional-integral-derivative (PID) controller which has different slewing and tracking modes. These PID parameters were fine-tuned for the requirements of the project. The mount is set on a pier that is tilted according to the latitude of the site. This design allows the movement of the tube under the mount, removing the collision risk. The position of the tube under the head of the mount is only used to point to the flatscreen hanging on the wall of the dome. Factory acceptance test, site acceptance test and commissioning were carried out by the author and the final results are summarised in the section 2.5.

[5]Leningrad Optical Mechanical Association, Saint Petersburg, Russia
[6]Telescope Engineering Company, Colorado, USA
[7]Amateur- und Präzisionsoptik Mechanik, Germany
[8]Bonn Shutter, Bonn, Germany
[9]Sidereal Technology, Oregon, USA

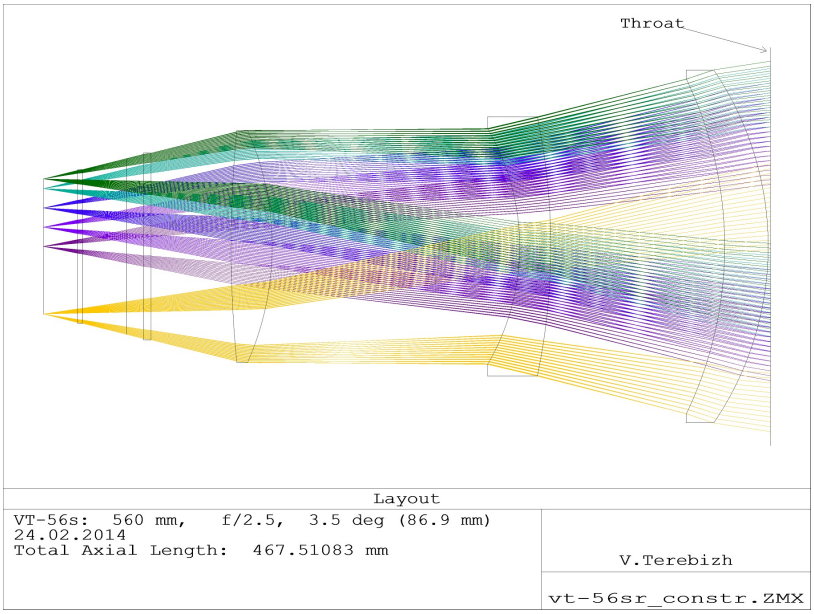

Figure 2.7: Detail optical layout of the VT56s design from V. Yu. Terebizh for the TBT telescopes: from the first lens of the Wynne corrector (right) to the focal plane (left). It includes the shutter, filter and the camera window.

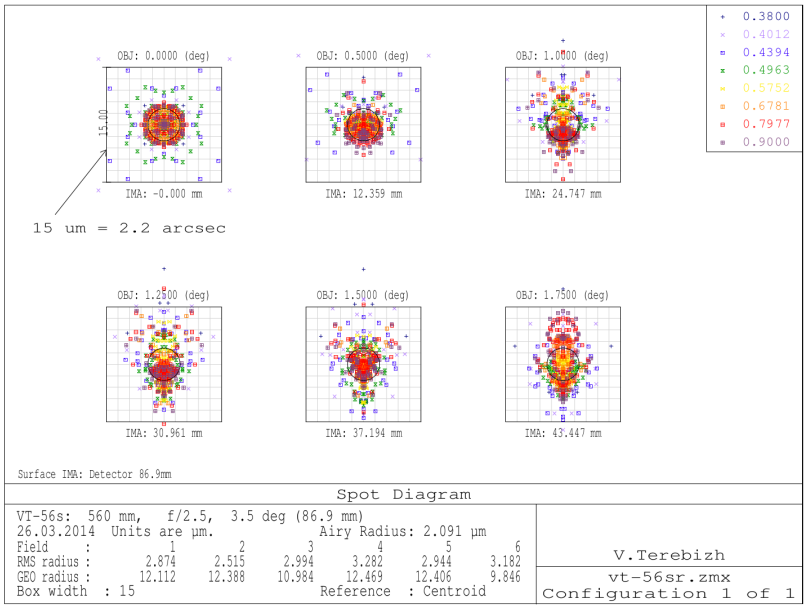

Figure 2.8: Spot diagram in the integral light between 380 nm and 900 nm. Star images correspond to the following field angles (in degrees): 0, 0.5, 1.0, 1.25, 1.5 and 1.75. Box size is 15 microns (2.2 arcsec). Diffraction Airy spot is shown by the circle.

TBT telescopes are equipped with Spectral Instruments 800S cameras. This model has two 16-bit outputs, with readout values between 500 kHz and 1 MHz. Each camera hosts an e2V 231-84 chip with a midband astronomical coating and a quantum efficiency QE peak >95%. It is a 4K $\times$ 4K chip with 15 μm pixels, covering up to 61 mm $\times$ 61 mm. The resulting plate scale is 2.17 arcsec/pixel, and the FoV is 2.5 deg$\times 2.5$ deg. The camera reads the image from these chips in 12 seconds in the fastest mode (read-out speed 1 MHz). The read-out noise is less than 16 electrons for this mode, while the dark noise is always under 0.2 electrons per second and pixel, at -20 degrees Celsius. For the 500 kHz readout speed, the readout time is 22 s, but the readout noise is under 8 electrons. Linearity and CTE are better than 99% and 0.999999 respectively. We have estimated the expected sensitivity for TBT. We have input the TBT characteristics and expected values for Cebreros (table 2.3) to the exposure-time calculator software Signal (Benn, 1992) and calculated the values that correspond to the requirements (table 2.4).

Parameter	Value
Diameter	56.0 cm
Obstruction	26.6 %
Sky brightness V	20.6 mag/arcsec^2
Extinction k_λ	0.15
Gain	1.7 e$^-$/ADU
Read-out noise	11 e$^-$ (800 kHz)
CCD QE	90 %
Mirror reflectivity	0.85
Throughput	0.9
Plate scale	2.17 arcsec/pixel
FWHM	4 arcsec

Table 2.3: Input parameters fed to the Signal ETC for the TBT telescope. Observing conditions are conservative values for the V band at Cebreros observatory.

For survey the use of binning could reduce the readout time to 2 s and thus matching it with the repositioning dead time of the telescope, leading to more than 350 deg^2 surveyed per hour (for 30 s exposure, magnitude V$\sim$19.5 depth). For follow-up the use of windowing could also reduce the read-out time under 1 s, that is interesting for fast objects.

Time [s]	Limiting magnitude (V)
0.2	16.3
1	17.7
2	18.2
5	18.8
30	19.5

Table 2.4: Limiting magnitude estimated for different exposure times for a signal-to-noise ratio 3, with the camera Spectral Instruments 800S hosting an e2V 231-84 chip read 800 kHz under expected conditions for Cebreros (4-arcsec FWHM and sky brightness 20.0 mag/arcsec^2).

2.2.2 Ancillary equipment

Apart from the main systems described here, the TBT project consists of many other elements that we describe briefly in this section. In order to avoid hardware failures due to hard shutdowns, all the computers and sensitive electronics rely on a 3000 VA Uninterrupted Power Supply. This UPS is monitored by RTS2 in order to shut down properly all the equipment in case of a prolonged power outage. However the observatory relies on a short-break line, that is never down for more than a few seconds during the automatic start of the station backup diesel generators. For the event of a major failure the TBT project has the Autonomous Emergency System (Ocaña et al., 2015) running in parallel to the nominal systems. It is an Arduino-based system that monitors the environment with redundant sensors (rain, wind, light, power) and closes the dome in case of risk for the operations. It is designed to override the nominal system, although its safety parameters are more relaxed and it only takes control when the nominal system fails to react to the change of conditions. The system relies on two 12 V batteries that are able to close the dome even at 25% of charge when there is a shutdown. For nominal operations the control system takes the weather input from a Davis Vantage Pro 2 weather station. The outdoor sensors are located on a pole next to a nearby building, 4 meters away from the dome. The station is equipped with instruments to measure humidity/temperature (inside and outside the dome), rain and wind speed (gust and averages).

The calibration of the images includes the use of flat images. The use of dusk/dawn sky images was discarded due to the large gradient present in the FoV. Therefore we use an electroluminiscent flatscreen with a smooth flat spectra covering from 400 nm to 1100 nm. The results are good, but the use of night images is promising. When the telescope archive have enough images, the use of night-sky flats is foreseen.

The camera has a two-stage refrigeration system, where the hot plate of the peltier is cooled down by a 15 degrees Celsius water flux. We use a Thermocube chiller to circulate 2 liters of water per minute. The chiller is controlled and monitored by RTS2. Alarms for low/high temperature and low level of water are active, although in case of a temperature increment in the peltier, the camera is automatically shutdown for protection.

2.2.3 Software and operations

Apart from the hardware it is worth to mention the software modules developed by ISDEFE and IGUASSU for this project, and how they define the strategies to be used for NEOs and the final operation. The scheduling tool TRANSITO (Racero et al., 2015) implements two general observing strategies for space objects, that is Survey and Follow-Up. The Survey strategy aims at the detection of new objects for different target population speeds, whereas the Follow-Up goal is the detection of objects in need of revisit (table 2.5). TRANSITO is conceived as a high-level web planning tool for the manual and automatic planning to be executed by the telescope control software or RTS2. This software will generate the Short Term Plan for the night, thus it will be responsible for the definition and management of the global strategy for the SSA-TBT observatories. It relies on the RTS2 internal meta-queue system for the real-time response and monitoring of the system. RTS2 is an open source package with the aim to create a modular environment for complete observatory control (Kubánek et al., 2004) and is oriented to distributed telescope networks (Kubánek, 2008). It allows automatic fast reaction to emerging targets of opportunity.

The data processing is done on-site in two different machines. The basic postprocessing is done in the control server, using RTS2 built-in scripts. The images are bias and flat corrected, while the dark is considered negligible. The two channels read are merged in one single image, adding all the keywords needed (based mainly in FITS keywords requirement coming from NEO and SST segments). Astrometric reduction is done using `Astrometry.net` routine (Lang et al., 2010). The TBT Consortium made a trade-off analysis with all the European commercial detection software. In the selection, amongst other parameters, were taken into account the performance, availability, license and price. This led to the selection of the software from the Teide Observatory Tenerife Asteroid Survey (TOTAS) (Koschny and Busch, 2015). This software was written by Matthias Busch for the TOTAS project, a survey performed by ESA's telescope: Optical Ground Station (OGS). TOTAS was modified for the TBT project in order to detect and measure objects in GEO and MEO orbits, thus renamed Asteroid and Satellite Automatic Processor (ASAP). The modification was done by IGUASSU and is based on masking the trailed stars in images taken with on-object tracking. According to high-level requirements from ESA, and the hardware and software selected at the CDR, the TBT Project has defined 4 different observation modes that have defined the approach for the Scheduler and Control System (table 2.5).

Mode	**Description**
Asteroid survey	30 s exposure 4×4 pattern, 4 revisits, every 15 minutes
Asteroid follow-up	Individual strategy for each object
Satellites survey	2 s exposure, 5 to 9 exposures, depending on the object apparent speed
Satellites follow-up	2 s exposure, 5 to 9 exposures, depending on the object apparent speed

Table 2.5: Nominal observing modes supported by TRANSITO and implemented in ASAP.

Part of the validation scenario involves the scheduling concept integrated in the robotic operations for both sensors. At the moment TRANSITO depends on external services to gather all needed information for the generation of the Short Term Plan for the night. This information will mainly be provided for NEOs by the NEO Confirmation Page and Sky Coverage services from the Minor Planet Centre and by the NEO Priority List from ESA's NEO Coordination Center. For the satellites, ESA's Space Debris Office will feed Tracking Data Messages and Orbital Data Messages with the objects of interest. According to predefined selection parameters, TRANSITO will choose and schedule the objects for the night. RTS2 will receive them and execute the plan, managing the real-time response to change in environmental conditions.

2.3 TBT performance for moving objects' survey

Although the general design envelope was set by the agency, in the framework of this thesis we have performed a comparison to other competitors using the actual-design values for TBT. The comparison is based on the calculation of figures of merit for only a sample of relevant similar surveys and do not pretend to be a comparison of all the NEO surveys. See Jedicke et al. (2015) for a full review of current and future NEOs survey and astrometric follow-up projects. Please note that TBT telescopes are meant to be prototypes and may be used only for testing purposes. For an evaluation of the capabilities of the system for discovery but also follow-up in the next section we carry out an analysis of the expected performance using a simulation with a real population.

For a survey telescope the *etendue* is usually considered a figure of merit as it is the capability to collect information. It is defined as the product of the aperture of optical system and the solid angle subtended: $etendue = A \cdot \Omega$. However for the search of NEOs we face a more complex problem as they are fast moving objects, randomly placed and they have heterogeneous properties. Myhrvold (2016) proposes the definition of a search volume, as the volume where a telescope can observe a certain object. Therefore for larger absolute magnitudes H the volume is going to be smaller than for brighter objects. We go deeper in that idea in the simulation (section 2.4). For a more general view we select a parameter that is based on the survey characteristics and not so much in the target population. Tonry (2011) defines the overall capability of a survey telescope for moving telescopes M:

$$M = \frac{A\,\Omega\,\epsilon\,\delta}{\omega} 10^{0.4(\mu+m_0)} = \frac{SNR^2\,\Omega}{\delta/t_{exp}}\,10^{0.8m} \tag{2.3}$$

where in the left side are direct observational parameters: $A\,\Omega$ is the *etendue*, ω is the solid angle of the source till the edge where it equals to background noise, ϵ is the throughput, δ is the net fraction of shutter open time (in the best case is the exposure time divided by the sum of exposure time plus overheads), μ is the sky brightness in magnitudes per square degree per second and m_0 is the reference magnitude. Tonry uses AB magnitude $m_0 = 25.10$ for a photon per square meter and second for a wide-band filter ($\log \Delta\lambda = 0.2$). And on the right side you find the survey operational parameters, as m is the magnitude of the faintest object that can be observed with a signal-to-noise ratio SNR that is a threshold related to the detection software and δ/t_{exp} is the cadence of the survey to revisit the field to check for moving objects.

Thus the problem is studied as the trade-off of two independent parameters. Taking a logarithm we can find a surface of SNR vs δ/t_{exp}, where magnitude m and solid angle Ω are descriptive of the telescope. We find two regimes: for short t_{exp} the $SNR \propto t_{exp}$ is limited by the read-out noise, where after the point where flux of the source equals the flux of the background the $SNR \propto {t_{exp}}^{1/2}$, i.e., the photon limited regime. Tonry also proposes a formula to calculate the SNR in the undersampled regime, where we may expect a NEO survey telescope with large FoV and a limited amount of pixels. We adapt it to calculate the expected PSF in that regime:

$$FWHM_{PSF} = (3.5\,d^2 + 0.4\,dp + p^2)^{1/2} \tag{2.4}$$

where d is the physical FWHM and p is the pixel size. For TBT project $p = 2.17$ arcsec/pix and $d = 2$ arcsec, yielding an expected $FHWM = 3.0$ arcsec.

The TBT nominal survey design calls for the following survey parameters:

- Exposure time $t_{exp} = 30$ s with an overhead $t_{OH} = 12$ s and a read-out noise of 12 e^-. Observations will be carried in *clear* mode, only with a filter cutting IR to avoid fringing, equivalent to B+V+R.

- Both telescopes cover up to 6000 deg^2 per night, one third of the visible sky. Observatories in Northern and Southern Hemisphere will be coordinated, covering the whole sky in less than 3 nights.

For each of the TBT telescopes, the rest of the values for the calculation of the figure of merit M are $A = 0.18$ m^2, $\Omega = 6.25$ deg^2 and the software is able to detect objects with $SNR = 3$, that is down to magnitude $m = 20.0$. In the range of telescopes < 1 m, the current most successful NEO survey is Catalina (Larson et al., 2003) and TBT has a figure of merit slightly worse than it (see table 2.6). Over them it is ATLAS (Tonry, 2011), a project similar to TBT but with four telescopes combined and hence covering a much wider area up to a similar magnitude.

Survey	***etendue***	**SNR**	**m**	Ω	**log M**
TBT	1.10	3	20.0	3125	20.6
Catalina 0.7m	7.31	4	19.5	3000	21.0
ATLAS	5.80	5	19.9	20000	21.8
Spacewatch	1.48	3	21.7	150	20.8
LINEAR	2.40	4	19.0	2400	20.4

Table 2.6: Survey design parameters and performance. *Etendue* is in m^2 deg^2, SNR is the signal to noise ratio achieved for magnitude m and Ω is the total are surveyed each night in deg^2. Apart from the projects mentioned in the text, we include the two leading projects in the previous decade: Spacewatch (McMillan, 2006) and LINEAR (Stokes et al., 2000). Values are updated from Tonry (2011) according to current status of the projects.

Note that the apparent brightness of an asteroid does not only depend of the absolute magnitude H but in geometric observational conditions like the phase ϕ and associated phenomena (opposition effect, asteroid shape, etc.). In general we can calculate it as:

$$m_V = H + 5\log(d, p_V) + 5\log(d_{Sun}, d_{\oplus}) - 2.5\log(\phi(\alpha, G)) \tag{2.5}$$

where m_V is the apparent magnitude, H is the absolute magnitude (function of diameter d and albedo p_V), d_{Sun} and $d_{\oplus}$ are the distances from the asteroid to the Sun and Earth respectively and ϕ is the phase, that depends on the phase angle α and the G parameter (from the HG model, by Bowell et al. (1989)).

Moreover for the estimation of the final SNR of the observed object we have to take into consideration the trailing losses. Asteroid movements cause the spread of photons across multiple pixels. The trailing effect could be used by software to find lower SNR streaks. However TBT uses ASAP software, that is able to find only point-like moving objects. Therefore the best way to estimate the performance of the TBT as a NEO detection survey is to simulate the detections of a synthetic population.

2.4 Simulating the performance of the TBT telescope

In order to evaluate the performance expected for the TBT telescopes we can simulate observations of the realistic population created before. We expect some biases due to the characteristics of the observations, which we can quantify with the simulation. For the simulation we use an ESA tool that is freely available, called NEOPOP. Near-Earth Object Population Observation Program (NEOPOP) is a sensor system simulation software tool developed for ESA by the Institute of Aerospace Systems (Technische Universität Braunschweig, TUBS, Germany) and the Institute of Planetary Research (German Aerospace Center, DLR, Germany) with support of Observatoire de

la Côte d'Azur (OCA, France), under the contract ID AO/1-7015/11/NL/LvH. The description, user manual and all the technical information can be found in the NEOPOP webpage (ESA-SSA, 2015). Here we present a description of our approach to execute the performance analysis of the TBT telescopes.

The first module of NEOPOP is the Population Generator. It generates the NEO population that we are going to use to analyse. It uses a set of files that comprise properties for the objects sources. Based on those properties it generates a certain number of objects that shape a synthetic population for analysis. NEOPOP offers a couple of models already built for population generation. The first one is the so-called "old" model by Bottke et al. (2002). The model was based on only 120 NEOs, calibrated to $H = 22$ and it is not accurate for larger values, thus it is considered outdated. The software developers suggest using a new model based on 4000 NEOs observed by Catalina Sky Survey between 2006 and 2011. The model is not named yet, so we term it as *default* model for this work. It is calibrated in the range $15 < H < 25$. Beyond that range (H=25 is 25 m to 60 m) one can choose between two different datasets, a user-defined one or one based on bolide observations by satellites (Brown et al., 2002) with $\alpha = 0.6434$, which we selected for our simulation. It includes seven source regions using a different absolute magnitude distribution for each source, and different albedo distribution (e.g., all JFC have albedo < 0.1 while most of the Hungaria members have albedo > 0.3). For objects brighter than $H = 15$ it uses the current population of known NEOs as it is supposed to be complete. As an output it gives the numbers of asteroids for the four NEO subgroups (Amor, Apollo, Aten and Atira).

As the software offers the option to implement user-defined models, we tried to introduce a new model based on Schunová-Lilly et al. (2017). This model is based on observations by Pan-STARRS PS1 NEO observations and is in good agreement with the new model of Granvik et al. (2016), based on Catalina Sky Survey and which could be considered an updated of the one implemented by default in NEOPOP. Unfortunately this new model by Granvik is not yet published. The agreement between Schunová-Lilly et al. (2017) and the *default* model are very good so we perform all the simulations with the default one, as the option with user-defined models appeared to have some bugs.

Once the population is built, the objects orbits are propagated to the Analysis Epoch. The NEOPOP software uses the methods in the SPICE software library (Acton, 1996). NEOPOP offer also a Close Approach Analysis. It uses a constant time step of 30 days that is adjusted dynamically for objects coming closer to the Earth. This routine is also based on the SPICE library.

The second module of NEOPOP is the Observation Simulator that performs a simulation of the behaviour of a real sensor, especially suited for optical ground-based observations. It takes into account the usual observing constraints and allows the input of observation strategies. The population generated in the previous step is read and propagated to the observation. For the statistical analysis the population is modified instead of propagated for each of the Monte Carlo runs. In order to save computation time the objects are pre-filtered, removing the ones that will never be observed by a certain sensor. This filtering is based on geometric constraints, calculating the volume that is accessible to the sensor from its position. For a ground-based sensor, like TBT, the analysis of long term observations (> 2 months), the step size is month and extra 25 steps in the last 24 hours at the end of the period.

The detections of the objects that pass the filter are investigated with a crossing analysis of the field of view. Afterwards these ones are analysed according to the crossing geometry to determine whether they can be detected by the sensor or not. For each time an object is in the line of sight of the sensor, the system calculates and stores some parameters that define the crossing: time of closest approach (TCA), range at TCA, range rate at TCA, FOV dwell time, minimum path offset (closest angler to the centre of the FoV), mean angular velocity through the FoV and mean phase angle.

The detection analysis is carried out by an optical performance model. The model covers the visual spectrum (up to $1\ \mu\mathrm{m}$) of light for ground-based sensors. Apart from the observation details of the simulation, it includes the information of the population generated, the crossing geometry just created and the sensor parameters. For TBT we have used the parameters (table 2.1) calculated by us and the requirements provided by ESA. For TBT survey we input the data summarised in table 2.7. For the nominal strategy, with $t_{exp} = 30$ s, a gap time $t_{OH} = 12$ s and require the detection in 3 consecutive frames with $SNR > 2.5$ to consider it to be positively detected. The optical response curve is the one we calculated and an average throughput of 0.7.

Parameter	Value
Diameter	56.0 cm
FoV	2.5×2.5 deg^2
Exp.time	30 s
Gap time	12 s
# detections	3
m_{limit}	19.5
Pixel size	15 μm
Pixel scale	2.17 arcsec/pixel
FWHM	2 pixel
Threshold	1.5
Read-out noise	12 e$^-$
Dark current	0.2 e$^-$
Throughput	0.7

Table 2.7: Input parameters for TBT Cebreros in the NEOPOP simulator.

The output of the model after the simulation of the observation are several observational values that determine if an object crossing the FoV could result in a detection. The parameters for each crossing are: detection flag, mean object irradiation, mean object apparent magnitude, mean sky background magnitude and maximum SNR. We used them to study the detection of each object.

The model includes atmospheric components with airglow contribution from Daniels (1977), atmospheric extinction based on a user-provided table values fitted with an exponential law. The instrument spectral response is calculated as the convolution of the quantum efficiency $QE(\lambda)$, the optical system transmission $OT(\lambda)$ and the optical filter transmission $OF(\lambda)$. For the calculation of the zodiacal light, background signal of Galaxy stars in the galactic plane, scattered sunlight, scattered moonlight it also uses the data from Daniels (1977).

The model calculates all these background contributions for each CCD frame. Then it calculates the trace on the CCD and the pixel dwell times, that are essential for estimating the objects signal. For each frame the models adds the sensor contributions of dark noise and the read-out noise. The detection decision is taken based on the background and object signals and is considered a positive detection when:

$$S_{obj} > S_{bkg} + a \cdot \sigma_{S_{bkg}} \tag{2.6}$$

where S_{obj} and S_{bkg} are the signal of object and background respectively, $\sigma_{S_{bkg}}$ is the noise of the background signal according to Poisson statistics $\sigma_{S_{bkg}} = \sqrt{S_{bkg}}$ and a is a user-defined threshold factor that depends on the detection software.

The observing strategy must be defined for each telescope. Basically it consists on the movement of the sensor pointing into different orientations following a pre-defined pattern that prepares the input needed for the detection software (a series of n images of the same FoV revisited every m minutes). As a first approach for TBT we use a fixed location as an average position for observing NEOs at the opposition. After some years of opposition we can repeat the exercise with the actual pointings and compare the simulation to the observed objects.

First we perform a population analysis in order to fully understand the observation simulation. For this analysis we have divided it into two groups according to their absolute magnitude H, choosing the limit at $H = 22$, an average diameter 140 m. For objects with $H < 22$ the model generates a total population of 25653 objects (9427 Amors, 14895 Apollos, 919 Atens and 412 Atiras). The 3D distribution shows the position of each object at the moment of this analysis (figures 2.17 and 2.18). In the plane (a,e) and (e,i) we can recognise the features of the sources in figures 2.9, 2.11 and 2.13, being the largest contributor the ν_6 and 3:1 resonances (figure 2.10). It is interesting to note that the orbits are close to the plane of the ecliptic ($i < 10°$), indeed less than 0.2% of the objects has $i > 90\%$ (see figure 2.19), but the distribution has axial symmetry (figure 2.17). The SFD, in terms of absolute magnitude H, fits a power law, but the contribution of each source has a different exponent (figure 2.14) and at $H = 22$ the objects from ν_6 and 3:1 resonances are 45% and 38% respectively (when at $H = 15$ they accounted for only 28% and 19% respectively). For the purpose of the search it is worth to show the MOID distribution of object (figure 2.15). At any moment at least 40% of the NEOs are closer than 2 AU (figure 2.12), but 80% of the NEOs has a MOID smaller than 0.2 AU and eventually they will be at that distance, after some synodic periods[10]. The larger MOIDs corresponds to the higher values of inclination (figure 2.16), and thus a wide survey like TBT will be biased to lower inclinations.

[10]Synodic period S is the time between to similar consecutive apparitions: $S = |1 - \frac{1}{P}|^{-1}$ years , with P being the period of the orbit in years. 80% of known NEAs has $S < 3$ years (Galache et al., 2015).

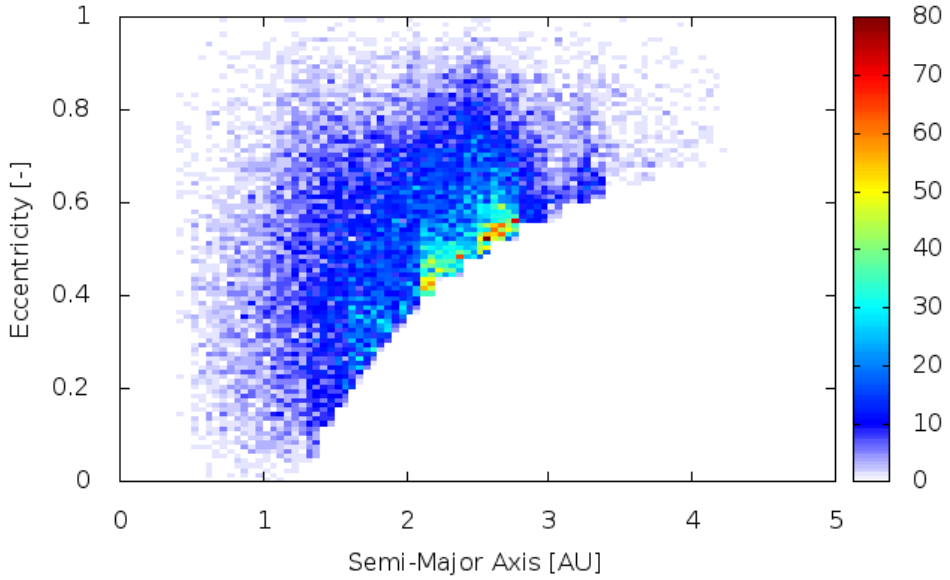

Figure 2.9: Distribution in semi-major axis and eccentricity (a,e) plane for the population with $5 < H < 22$.

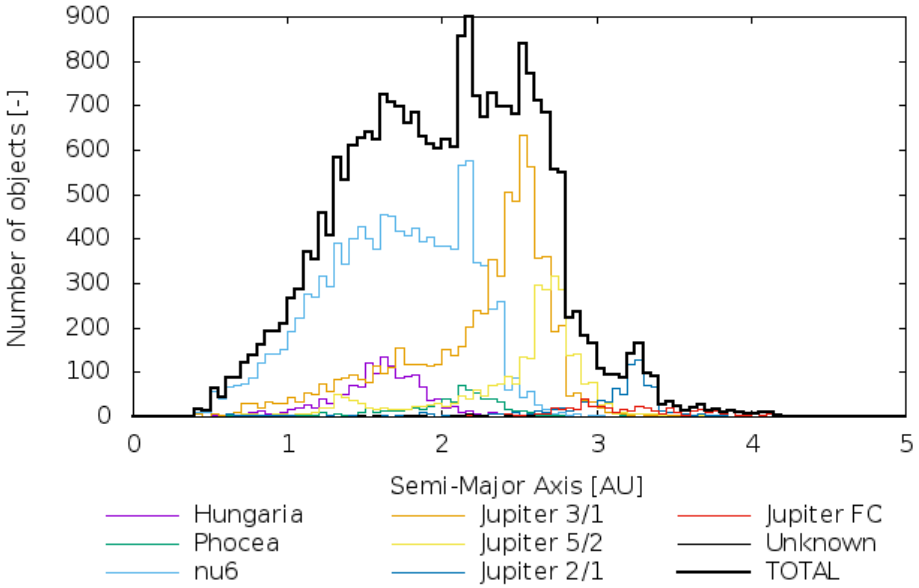

Figure 2.10: Histogram of the semi-major axis distribution of the population with $5 < H < 22$. The model describes the contribution of each of the 7 sources comprised.

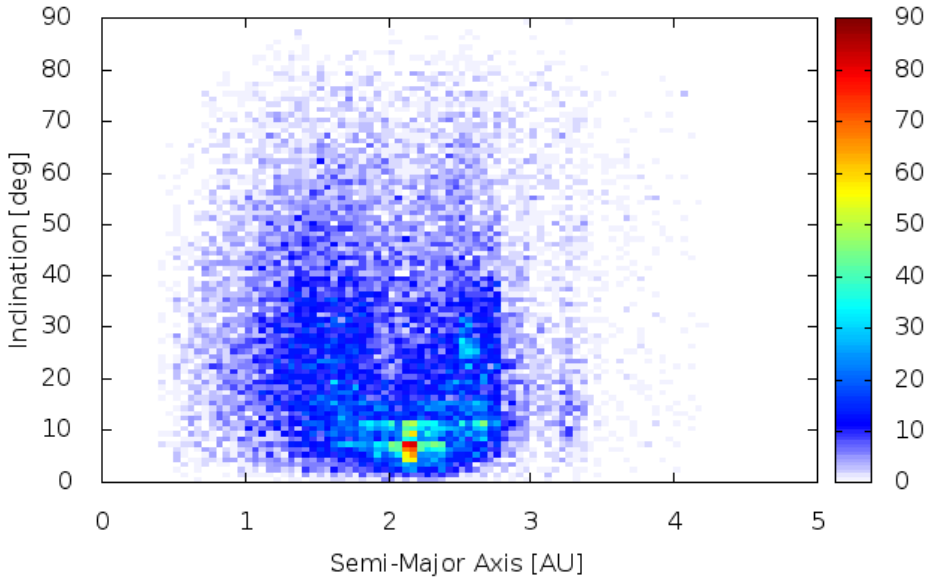

Figure 2.11: Distribution in semi-major axis and inclination (a,i) plane for the population with $5 < H < 22$.

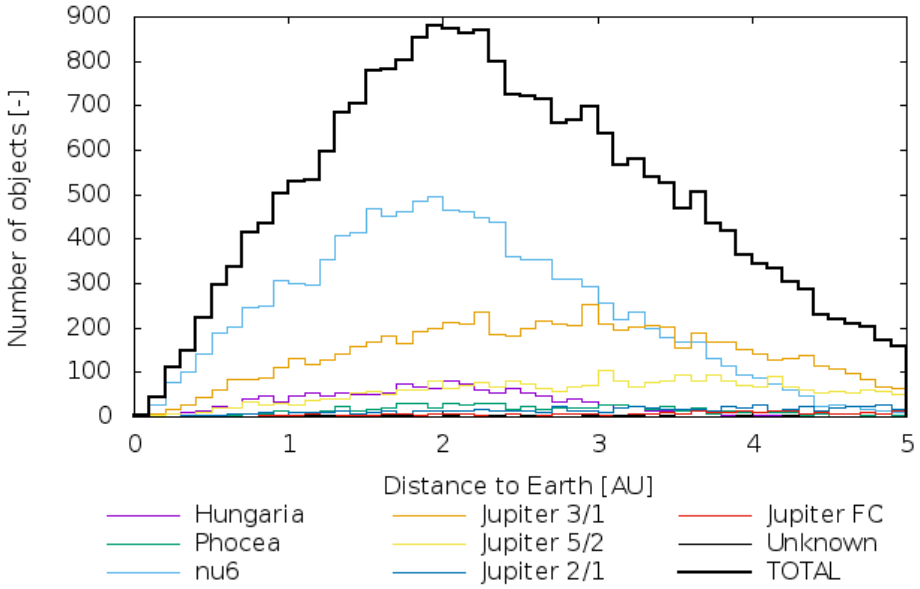

Figure 2.12: Distribution of the objects, with $5 < H < 22$, according to their distance to the Earth at the epoch of the analysis for the population. The distribution of the objects from each source and their characteristics (e.g., albedo) are essential for a proper simulation.

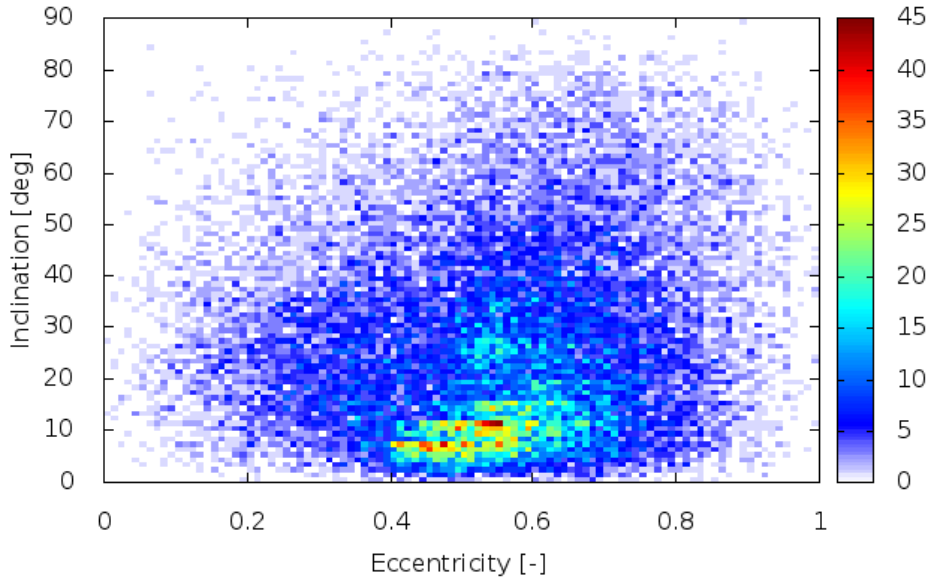

Figure 2.13: Distribution in eccentricity and inclination (e,i) plane for the population with $5 < H < 22$.

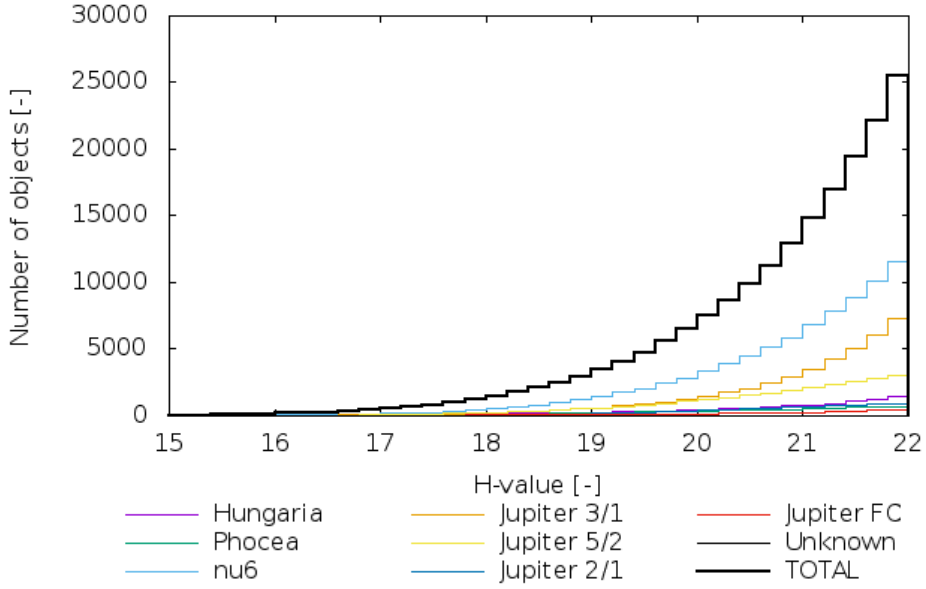

Figure 2.14: Cumulative distribution histogram of the number for each class of absolute magnitude H, for the population with $5 < H < 22$.

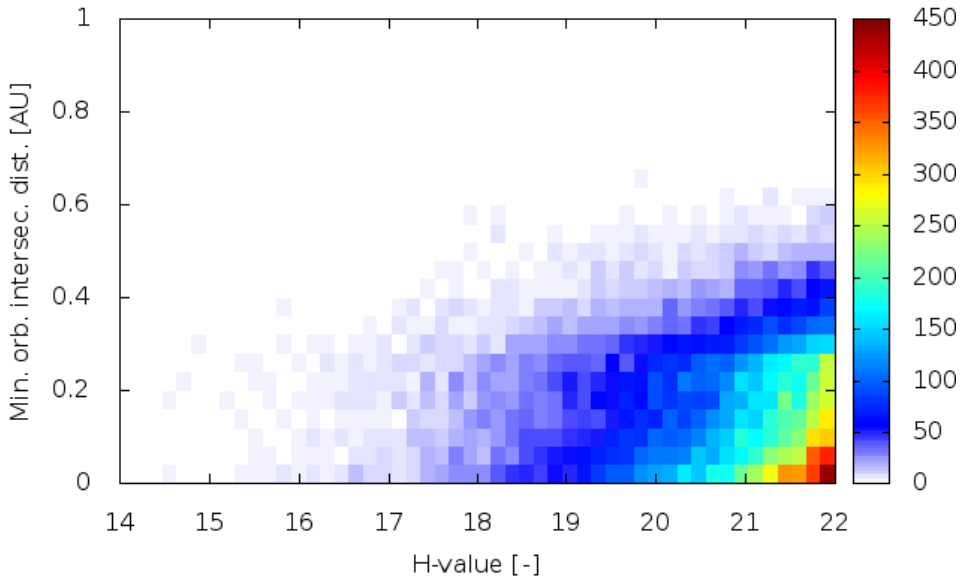

Figure 2.15: Distribution of the MOID for the values of absolute magnitude H, for the population with $5 < H < 22$. MOID is a key parameter for detection, as it will be biased to objects with smaller inclination, what is confirmed by the simulation.

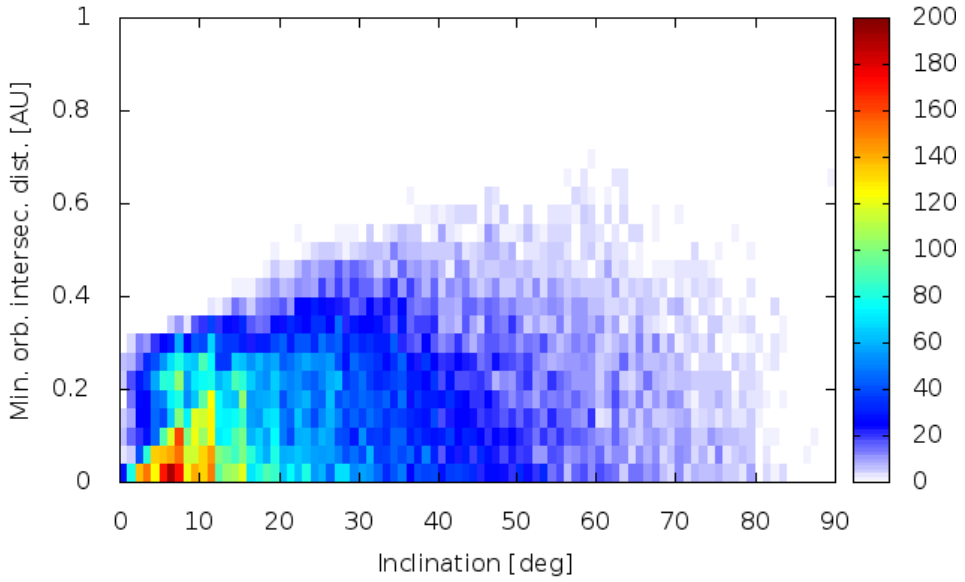

Figure 2.16: Distribution of the MOID for the values of inclination i, for the population with $5 < H < 22$.

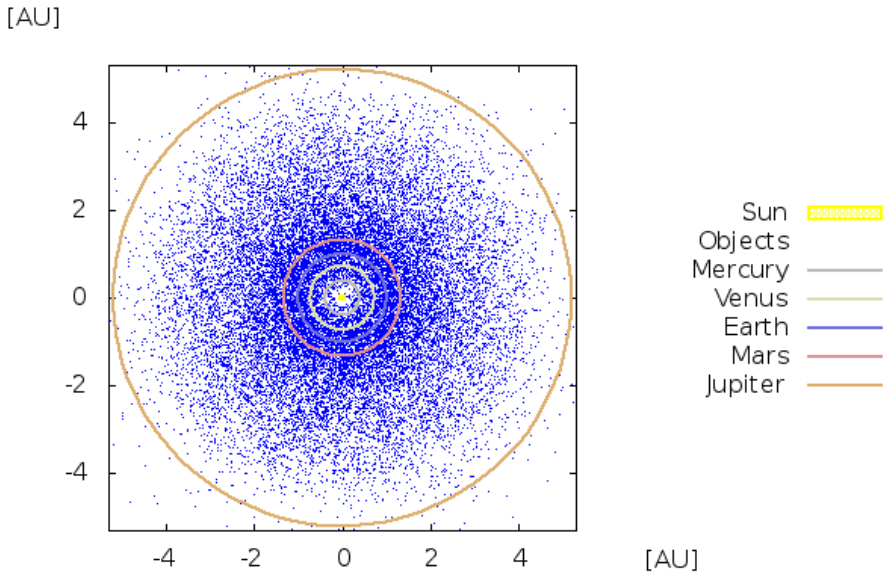

Figure 2.17: Solar System polar view of the simulated population with $5 < H < 22$. Distribution shows radial symmetry

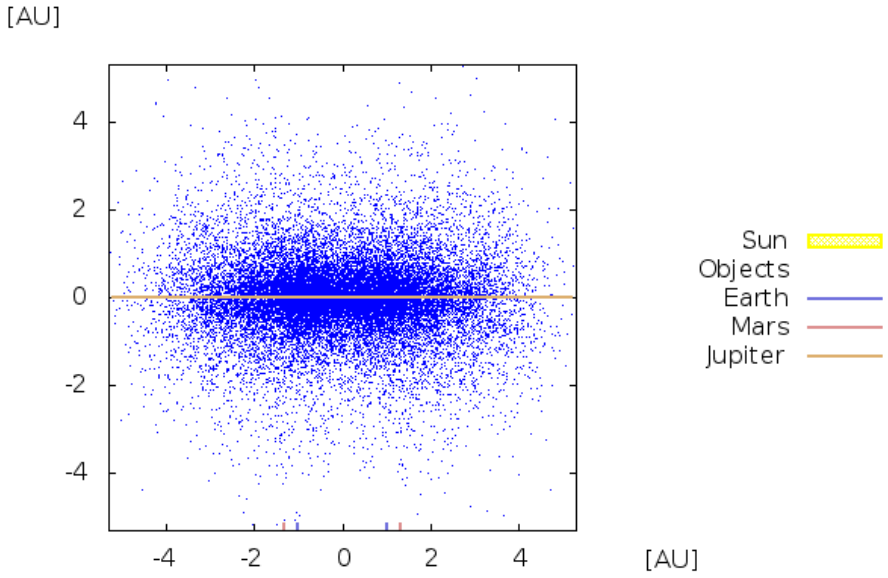

Figure 2.18: Solar System side view of the simulated population with $5 < H < 22$. Distribution shows larger spatial number density in the plane of the ecliptic.

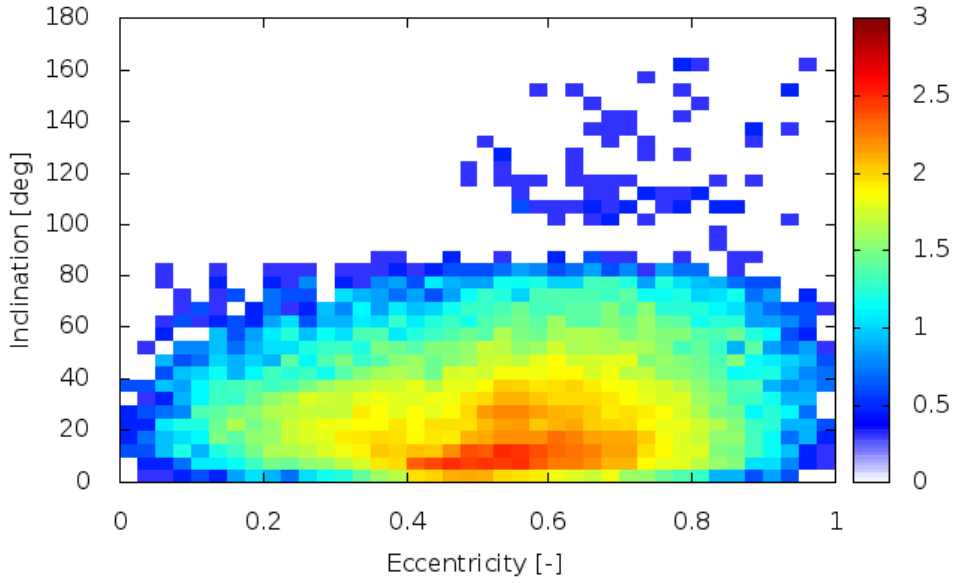

Figure 2.19: Scatter plot of eccentricity versus inclination for all the objects of the simulated population with $5 < H < 22$. Less than 0.2% of the NEOs have inclination $i > 90°$ and all of these have eccentricity $e > 0.5$ as they have their origin in the JFC source.

For objects with $22 < H < 28$ the model generates a total population of 6.8×10^7 NEOs. The number is too large to be handled by NEOPOP and the distribution is sampled to the 0.1% and 68281 NEOs are generated (26370 Amors, 38608 Apollos, 2328 Atens and 975 Atiras). NEOPOP no longer assigns the source for objects with $H > 25$ (figure 2.21), but in the plane (a,e) we can still recognise the feature of the sources (figures 2.20, 2.23 and 2.25). In comparison to the population $H < 22$ (in figures 2.11 and 2.13) this one shows a stronger contribution from Hungaria source ($a < 2$ and $15° < i < 35°$) and from 3:1 resonance ($2.4 < a < 2.6$), however the contribution from the 2:1 resonance ($3.0 < a < 3.3$) is reduced significantly. It is interesting to note that the orbits are close to the plane of the ecliptic ($i < 10°$) but the orbit distribution has axial symmetry, as seen in figure 2.22. The SFD, in terms of absolute magnitude H, fits a power law (figure 2.26). For $H > 25$ the exponent used is $\alpha = 0.6434$ (Brown et al., 2002). For the purpose of the search it is worth to show the MOID distribution of objects (figure 2.27). For this distribution at any moment at least 50% of the NEOs are closer than 2 AU (figure 2.24), but in this case only 40% of the NEOs has a MOID smaller than 0.2 AU. The larger MOIDs corresponds to the higher values of inclination (figure 2.28) and again a wide survey would suffer a bias to smaller inclinations.

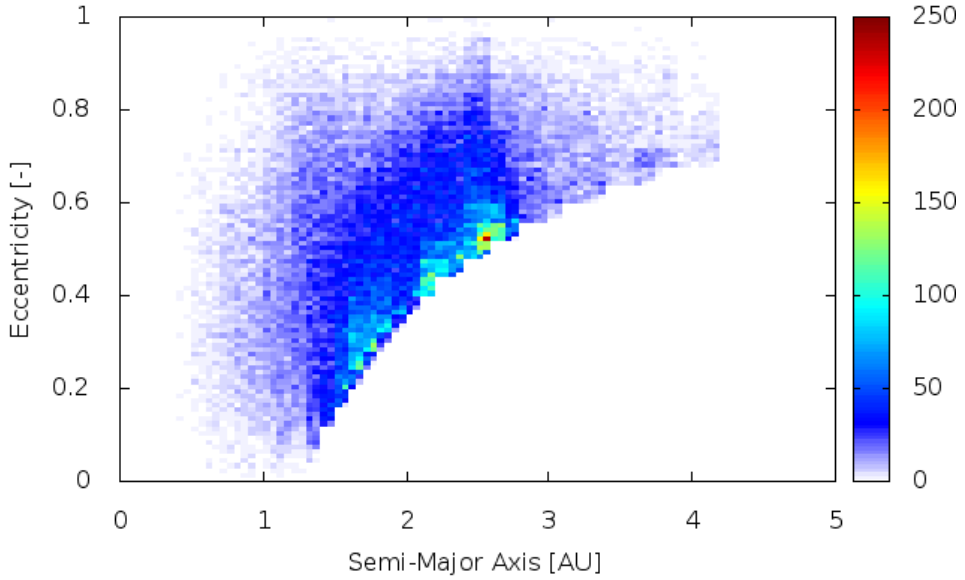

Figure 2.20: Distribution in semi-major axis and eccentricity (a,e) plane for the population with $22 < H < 28$. NEOPOP does not assign a source to the vast majority of them objects.

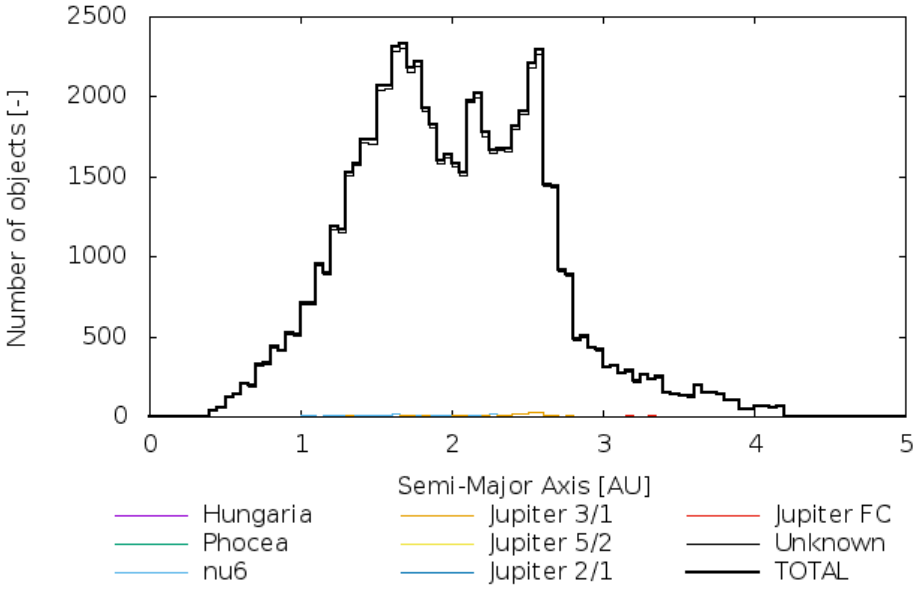

Figure 2.21: Histogram of the semi-major axis of the population with $22 < H < 28$.

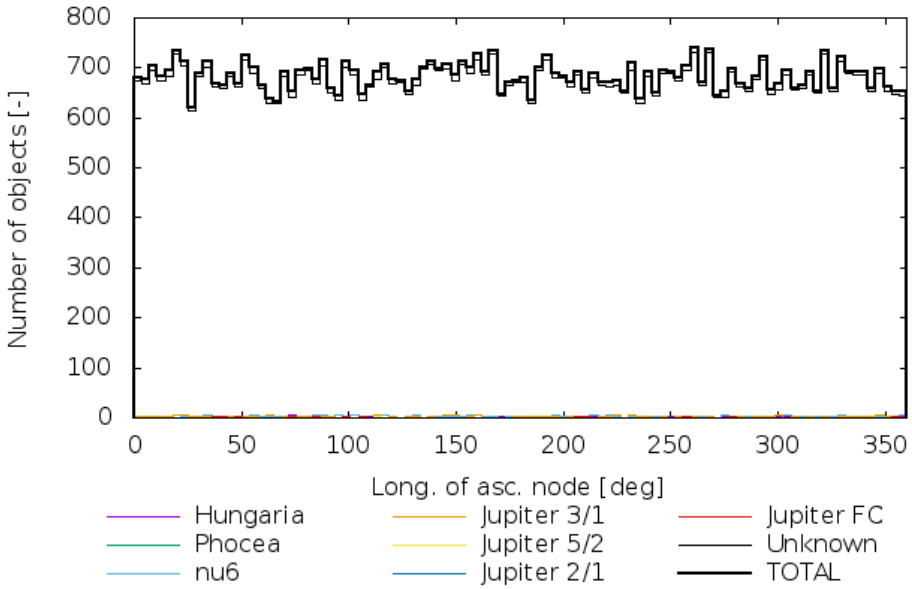

Figure 2.22: Histogram of the longitude of the ascent node of the population with $22 < H < 28$.

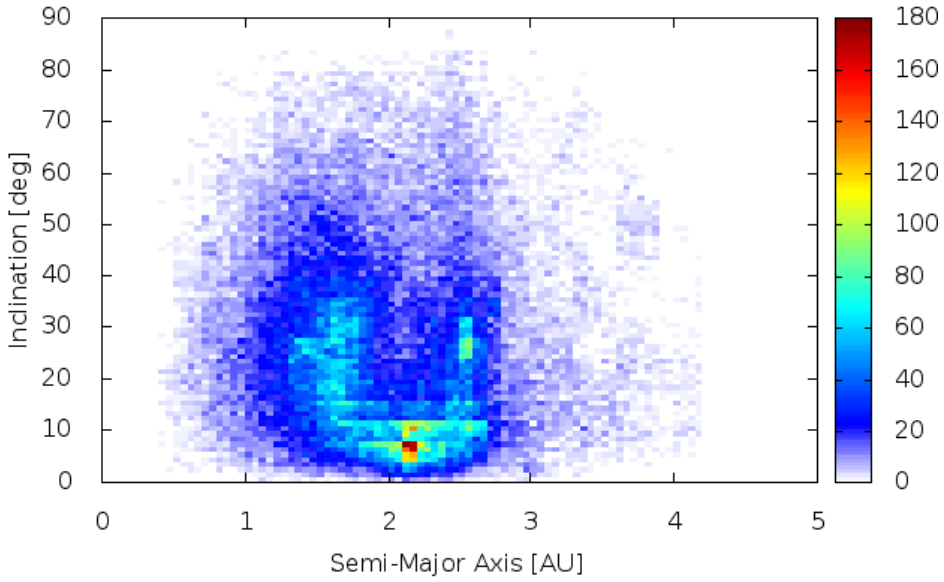

Figure 2.23: Distribution in semi-major axis and inclination (a,i) plane for the population with $22 < H < 28$.

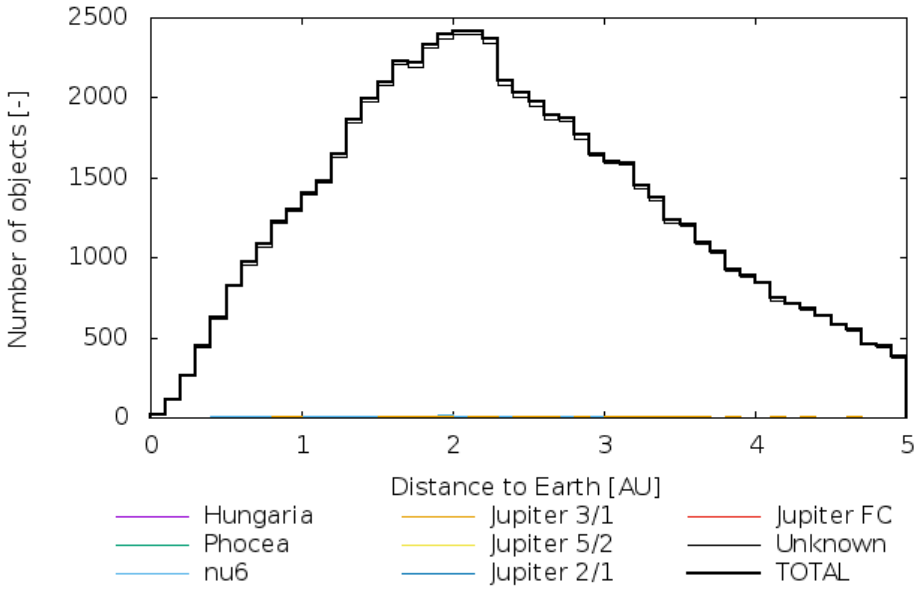

Figure 2.24: Distribution of the objects, with $22 < H < 28$, according to their distance to the Earth at the epoch of the analysis for the population.

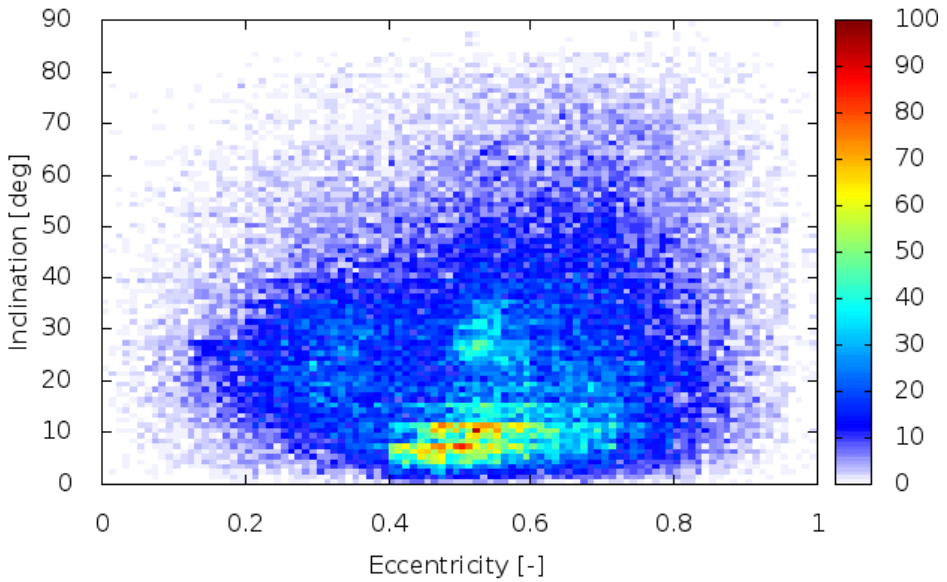

Figure 2.25: Distribution in eccentricity and inclination (e,i) plane for the population with $22 < H < 28$.

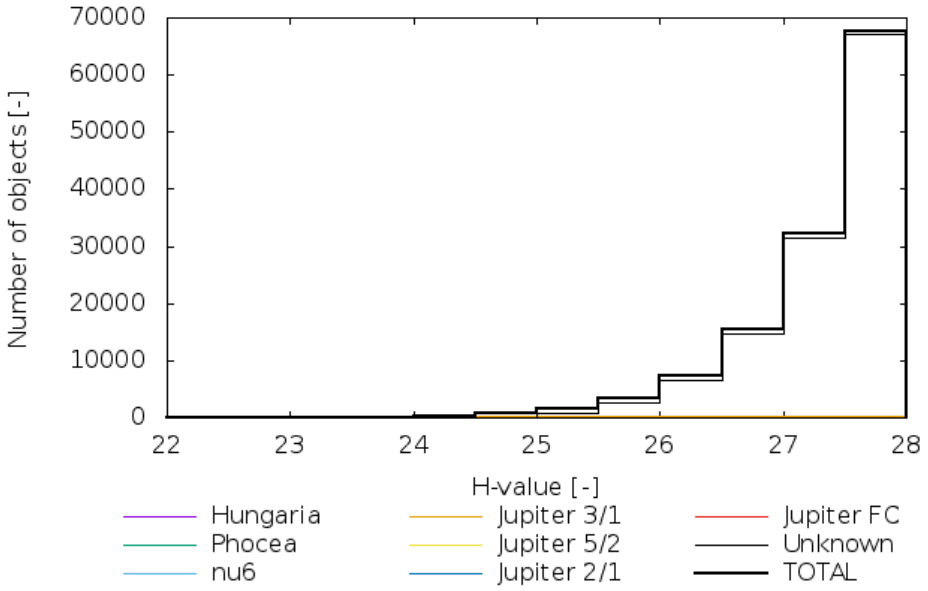

Figure 2.26: Cumulative distribution histogram of the number for each class of absolute magnitude H, for the population with $22 < H < 28$.

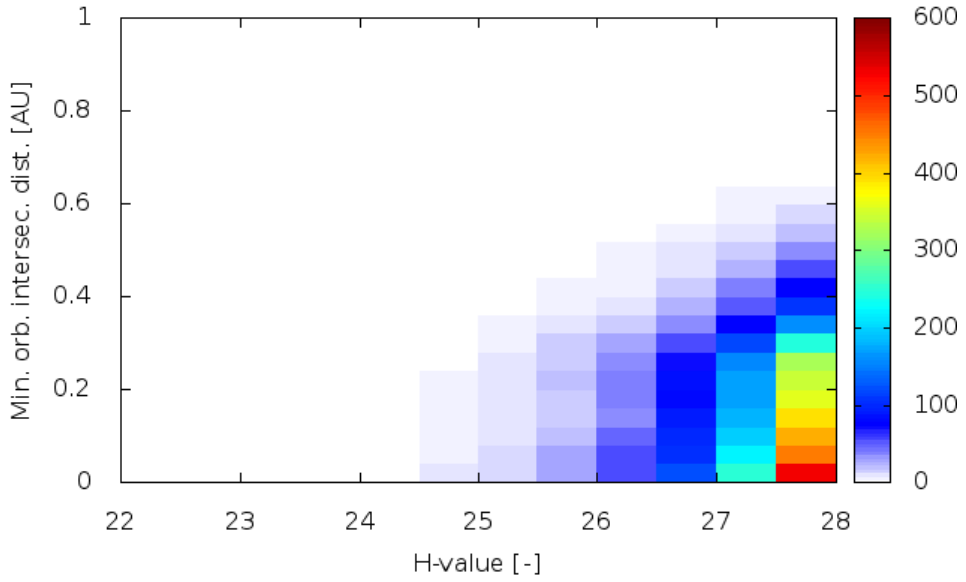

Figure 2.27: Distribution of the MOID for the values of absolute magnitude H, for the population with $22 < H < 28$.

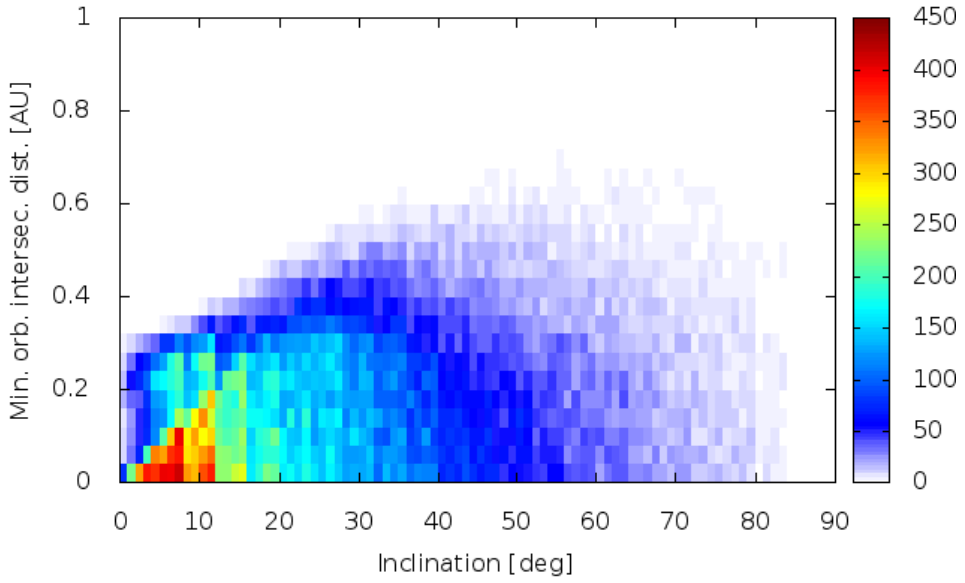

Figure 2.28: Distribution of the MOID for the values of inclination i, for the population with $22 < H < 28$.

For the first simulation we have used the bright population $5 < H < 22$, down to the limit of 140 m, and simulate the performance of a TBT telescope located at Cebreros (MPC code Z58) pointing to an average position (azimuth 180° (S) and elevation 60°). Most of the population has $H > 20$, therefore we constrain the range of the objects to 1 AU from the telescope in order to save computing time. The results show that 23623 objects crossed the FoV of the telescope under those constraints (figure 2.38). Out of them 121 objects were detected. We analyse the performance comparing the base population with all the objects selected, the ones that were potentially detectable and the ones that were eventually detected. As the simulation period is one year we see better performance for objects with smaller semi-major axis (shorter periods on average), as seen in figure 2.30. TBT is designed for wide survey, and therefore most of the objects are detected in a close range (figure 2.39). Indeed for objects with $H > 17$ (the vast majority in this population) the detection is only possible when they are closer than 0.3 AU. That means a bias to objects with smaller semi-major axis, smaller eccentricity and smaller inclination than average NEO population (figures 2.30, 2.33 and 2.35). Indeed the best performance is achieved for objects with $e < 0.3$ and $i < 40^\circ$. The objects detected have therefore similar properties to the impactor population (Vereš et al., 2009; Farnocchia et al., 2012) (figures 2.29, 2.31 and 2.36). With regard to the diameter, it spans the range from 400 m to 10 km, and the detection performance is better for largest objects as expected, being less than 1% for objects smaller than 400 m (figure 2.34). In terms of absolute magnitude (figure 2.32), 90% of objects are detected if $H < 16$ and then this performance sinks down to 0 for $H > 19.5$. In the second simulation we investigate further the detection of this dim population. We can constrain the range of search for objects closer than 0.1 AU (figure 2.37).

The second simulation is limited to the objects dimmer than absolute magnitude 22. For computational reasons we have limited it to magnitude 28 (diameter ~ 10 m). The model generates a total population of 6.8×10^7 NEOs. The number is beyond the limit of NEOPOP, so we scale down the population one thousandth to 68281 NEOs. Again we simulate the performance of a TBT telescope located at Cebreros (MPC code Z58) pointing to an average position (azimuth 180° (S) and elevation 60°). In this case we constrain the range of the object to 0.3 AU, but the duration of the simulation is extended up to 5 years to search for these rare cases. As expected the results are negative, with no detection despite the crossing of 11171 objects. The objects that reach a brighter magnitude than the survey limit $m_{obj} < m$ are only the ones that are at a very close range and therefore the apparent speed produces significant trailing losses. The survey performance could be increased using binning or a different detection software that could deal with streaked objects.

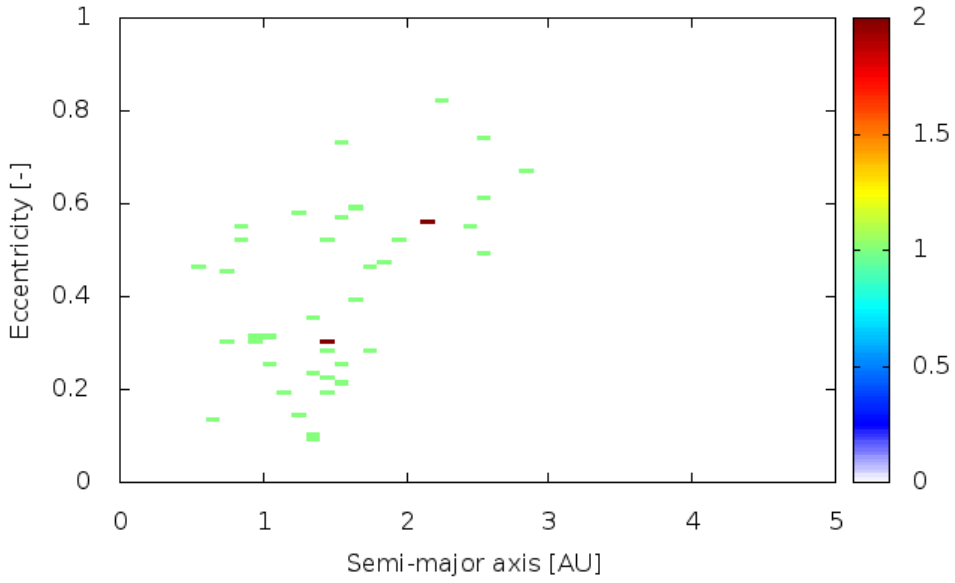

Figure 2.29: Distribution of the detected objects in semi-major axis and eccentricity (a,e) plane for the simulated observation with the population with $5 < H < 22$.

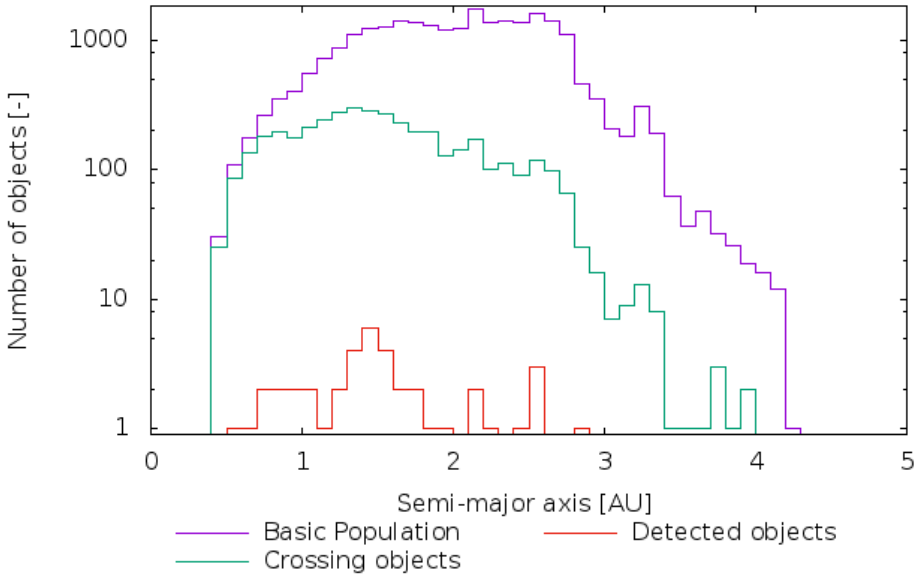

Figure 2.30: Histogram of the detected objects according to their semi-major axis for the simulated observation with the population with $5 < H < 22$.

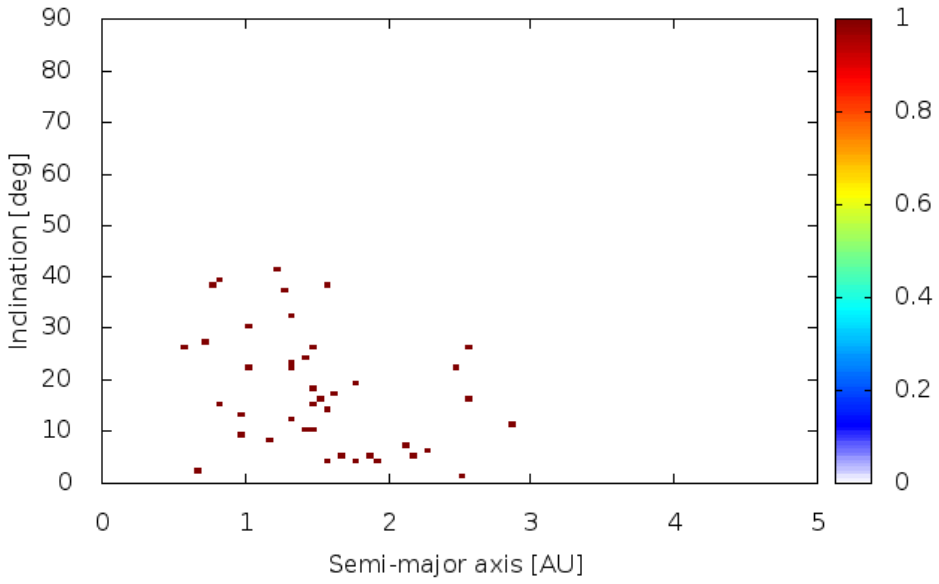

Figure 2.31: Distribution of the detected objects in semi-major axis and inclination (a,i) plane for the simulated observation with the population with $5 < H < 22$.

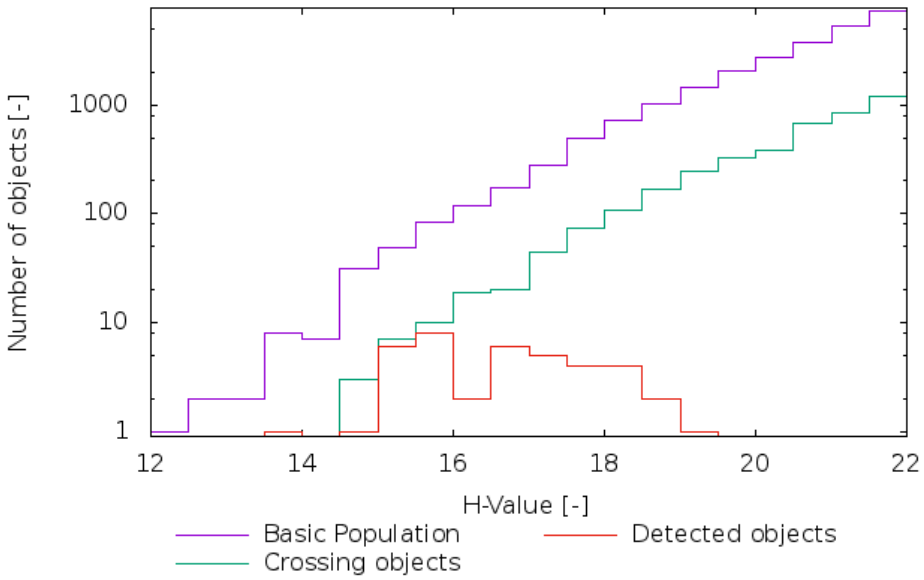

Figure 2.32: Histogram of the detected objects according to their absolute magnitude H for the simulated observation with the population with $5 < H < 22$.

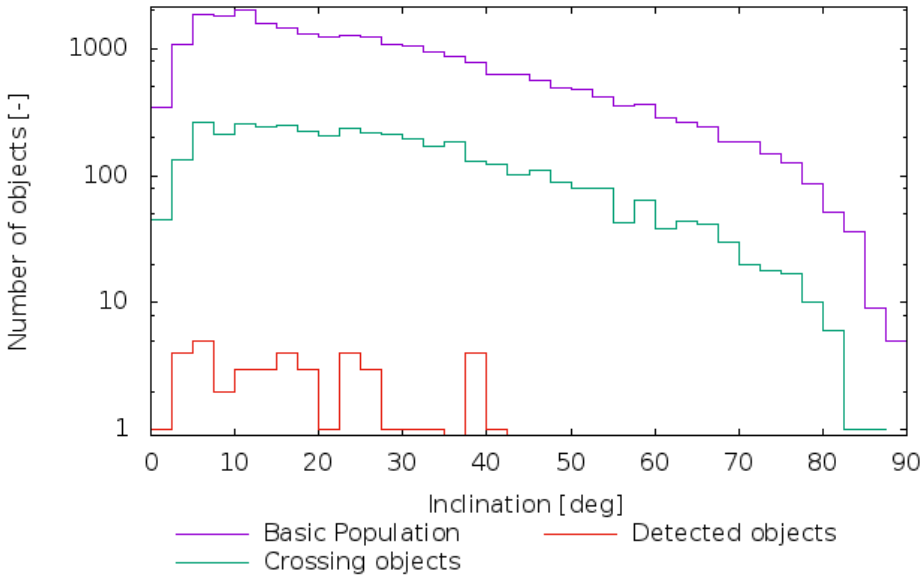

Figure 2.33: Histogram of the detected objects according to their orbit inclination i for the simulated observation with the population with $5 < H < 22$.

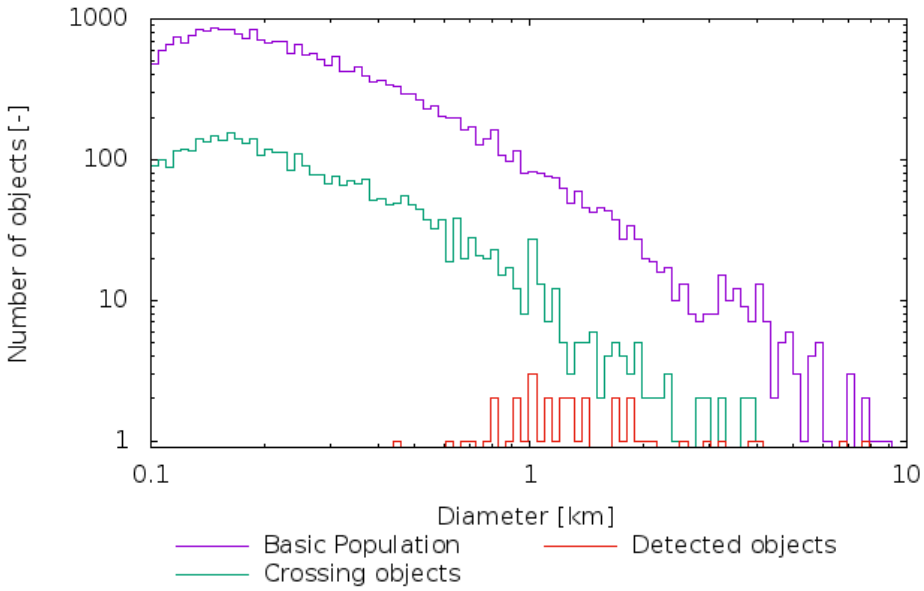

Figure 2.34: Histogram of the detected objects according to their diameter for the simulated observation with the population with $5 < H < 22$.

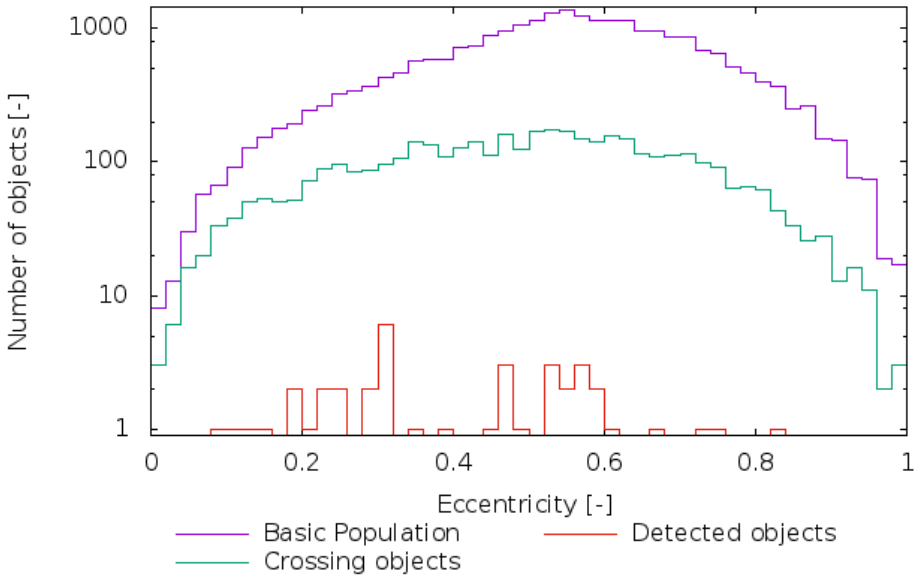

Figure 2.35: Histogram of the detected objects according to their orbit eccentricity for the simulated observation with the population with $5 < H < 22$.

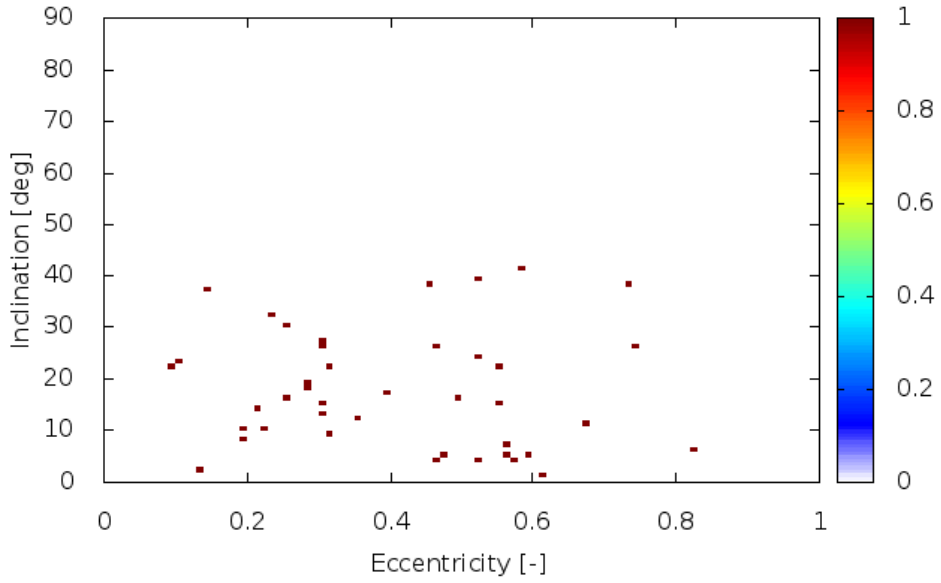

Figure 2.36: Distribution of the detected objects in eccentricity and inclination (e,i) plane for the simulated observation with the population with $5 < H < 22$.

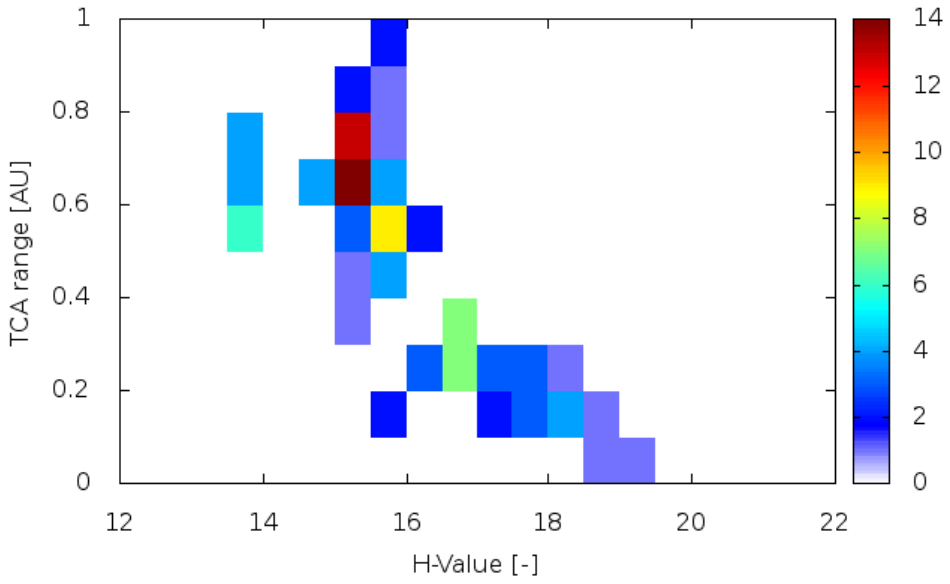

Figure 2.37: Distribution of the detected objects in the plane of the absolute magnitude H and the distance at the moment of observation (TCA range) for the simulated observation with the population with $5 < H < 22$.

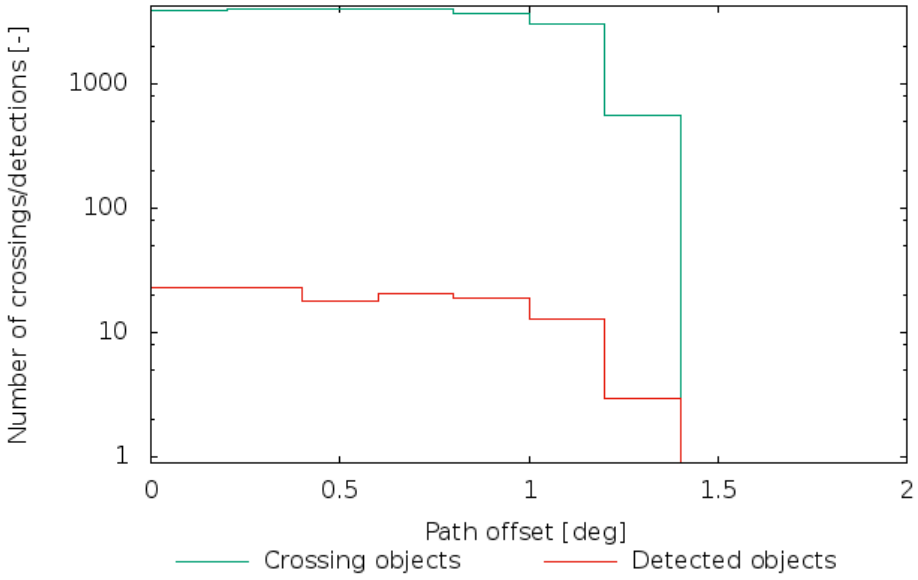

Figure 2.38: Histogram of the detected objects according to their distance to the centre of the FoV for the simulated observation with the population with $5 < H < 22$. It defines an effective FoV with radius 1.2 deg, as objects that do not get any close do not stay the required time in the FoV for a detection.

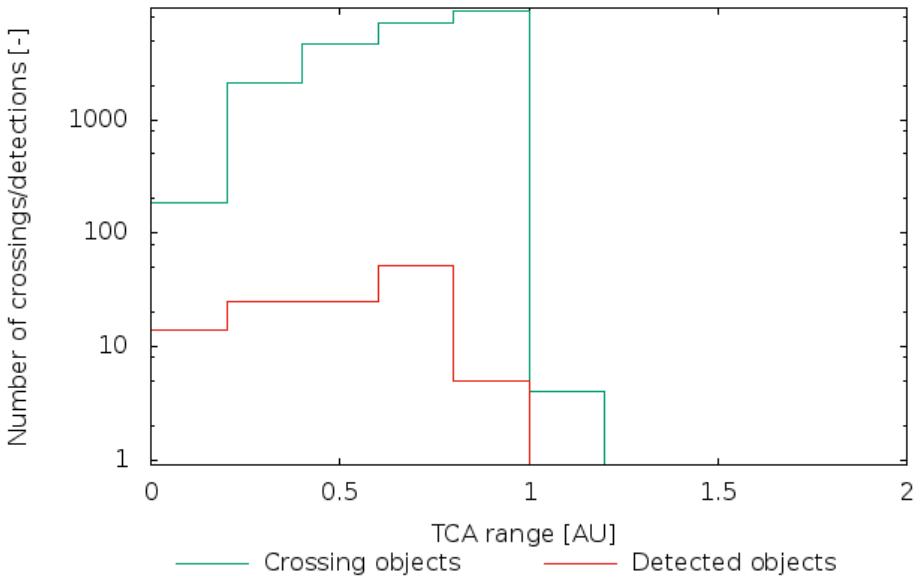

Figure 2.39: Histogram of the detected objects according to their distance to the telescope (TCA range) for the simulated observation with the population with $5 < H < 22$. Detection performance sinks beyond 0.8 AU as the objects are not bright enough to be detected. Note that simulation is limited to a range of 1 AU but the histograms shows the objects that cross that limit after the first detection.

2.5 Commissioning of the Cebreros TBT telescope

The first telescope was installed in Cebreros Satellite Tracking Station in mid-2015. During 2016 it passed the commissioning phase and we present here the results of this process (presented preliminarily in Ocaña et al. (2016b)). We evaluate the site characteristics (figure 2.40) and the performance of the TBT Cebreros telescope in the different modes and strategies. We include here the part of the commissioning performed by the author of this thesis. All the requirements for the project are achieved, with average residuals for asteroids under 0.5 arcsec, and around 1 arcsec for upper-MEO and GEO satellites. The survey depth is dimmer than magnitude V 19.5 for 30-s exposures with the usual star FWHM around 4 arcsec.

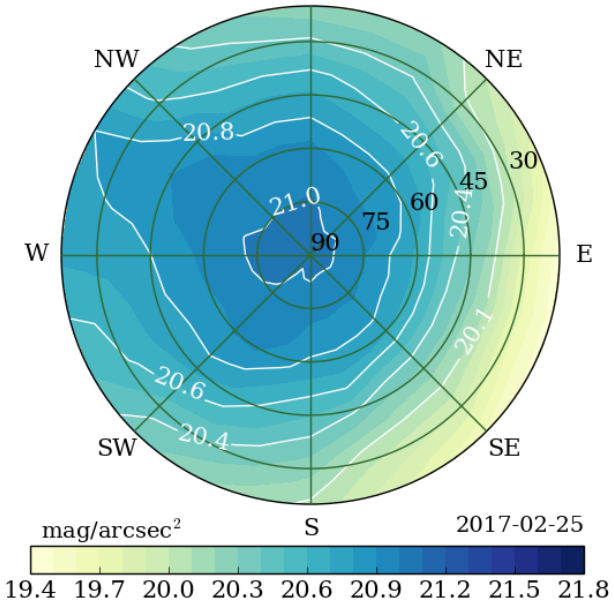

Figure 2.40: All-sky sky brightness map for Cebreros (Z58) in $mag/arcsec^2$ for the SQM band. Zenithal value is 21.0 $mag/arcsec^2$. The brightest value is 19.4 $mag/arcsec^2$ in the horizon in the direction to Madrid. Plot generated by the NixNox project (Zamorano et al., 2011).

2.5.1 Pointing model and tracking

TBT project uses the RTS2 built-in pointing model: Gpoint, that stands for GPLed Telescope Pointing model fit (Buie, 2003; Spillar et al., 1993). This model is intended for equatorial mounts and includes terms to account for non-orthogonality between axis, tube flexure, misalignment of optics and mechanics, zero-point offset, misalignment between instrumental pole and true pole, misalignment to the true meridian, flexure of the declination angle, refraction and hour angle scale error. Some of them are negligible for our system, like the ones associated with periodic gear terms as we use a direct-drive mount.

The data acquisition is done automatically by a script that makes pointings evenly spaced. The result for TBT Cebreros telescope is a model with 26 arcsec rms pointing quality, and a maximum value of 79 arcsec over the whole sky. Those values are 12 and 36 pixels respectively, or in terms of FoV, 1/750th and 1/250th. These values are accurate enough for normal operation of the software, and are an order of magnitude better than the requirements.

We have also evaluated the tracking performance of the telescope. In principle the telescope is going to take short exposures, but we tested it for larger times. Over 90 minutes (90 exposures of 48 s) the range of the values was below 7 arcsec, with rms 0.9 arcsec in right ascension and 1.4 arcsec in declination. These values are in good agreement with the model quality, and are within the requirements of the project and expected accuracy with 4-arcsecond star FWHM.

For 20-minute tracking (20 exposures of 48 s), the range of values is 1.8 arcsec in RA and 1.0 arcsec in Dec, being the rms 0.41 arcsec and 0.26 arcsec respectively.

2.5.2 Astrometry

Plate solving is performed with `Astrometry.net`, using a TAN projection third order polynomial, stored in FITS World Coordinate System (WCS) with the Simple Imaging Polynomial (SIP) convention. This convention represents the distortion of the image by polynomials. The SIP convention is described in Shupe et al. (2005) and defines the relation between u, v, the relative pixel coordinates with origin at `CRPIX1` and `CRPIX2` and x, y, intermediate world coordinates in degrees, with origin at `CRVAL1`, `CRVAL2`:

$$\begin{pmatrix} x \\ y \end{pmatrix} = CD \begin{pmatrix} u + f(u,v) \\ v + g(u,v) \end{pmatrix} \tag{2.7}$$

where $f(u)$ and $g(u)$ are the quadratic and higher-order terms of the distortion polynomial.

The $\texttt{CD}_{ij}$ keywords store skew as well as rotation and scaling. The information about the distortion is encoded in the polynomial coefficients A_p_q and A_p_q as for polynomial terms $u^p v^q$. For the TBT telescopes we found that a second-order polynomial is enough:

$$\begin{aligned} f(u,v) &= \texttt{A\_2\_0}u^2 + \texttt{A\_0\_2}v^2 + \texttt{A\_1\_1}uv \\ g(u,v) &= B\_2\_0u^2 + B\_0\_2v^2 + B\_1\_1uv \end{aligned} \tag{2.8}$$

Reciprocally there is the reverse transformation to the corrected pixel coordinates `U`,`V` from world coordinates with the inverse matrices $\texttt{CD}^{-1}$, `AP` and `BP`:

$$\begin{pmatrix} x \\ y \end{pmatrix} = CD \begin{pmatrix} u + f(u,v) \\ v + g(u,v) \end{pmatrix} \tag{2.9}$$

All the images are processed with `Astrometry.net` and they receive a WCS header (see example in figure 2.44). We have analysed the average of these headers to calculate the distortion of the TBT images up to a second-order polynomial in relative sensor coordinates u, v (figure 2.41) and the total distortion per pixel (figures 2.42 and 2.43). The maximum distortion is 7.4 arcsec, less than 0.1% of the FoV, thus within requirements.

The skew (non-orthogonality) between the two axes of the planes (object and projection) is calculated as the difference of the rotation angles. We consider the rotation angle the average of both: `CROTA2`= 92.77 deg.

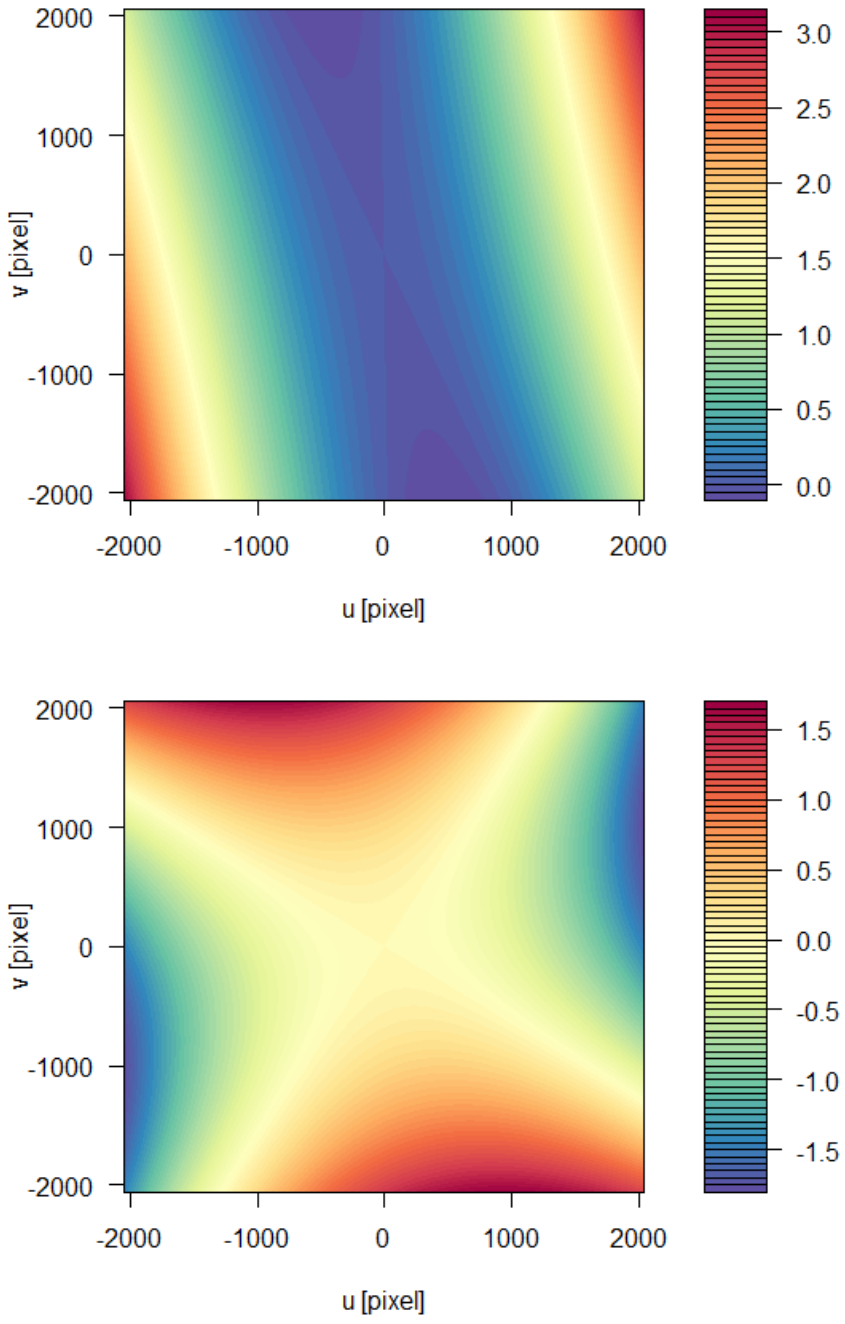

Figure 2.41: Distortion heatmap (colour scale in pixels) separated by coordinates. Top: f(u,v). Bottom: g(u,v).

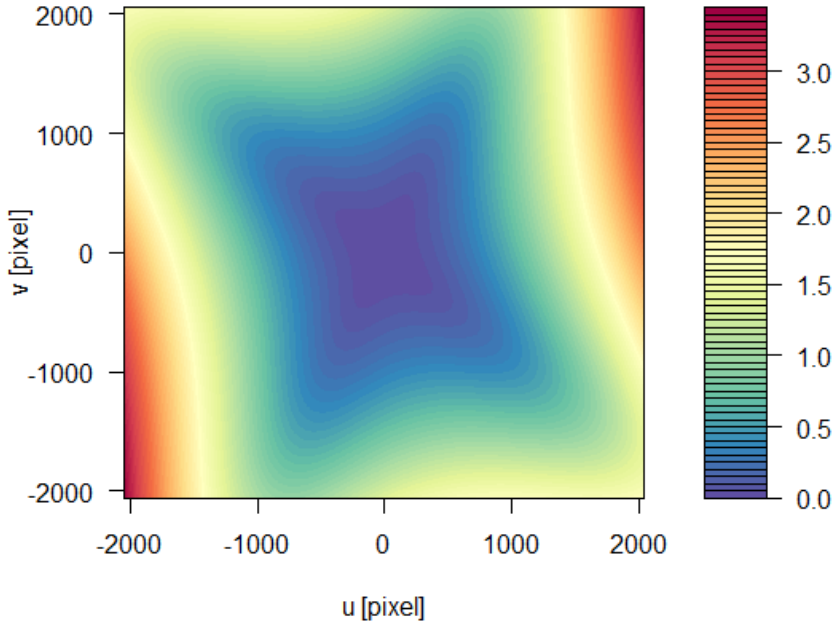

Figure 2.42: Total distortion heatmap (colour scale in pixels). The maximum distortion is up to 3.4 pixels, or 7.4 arcsec.

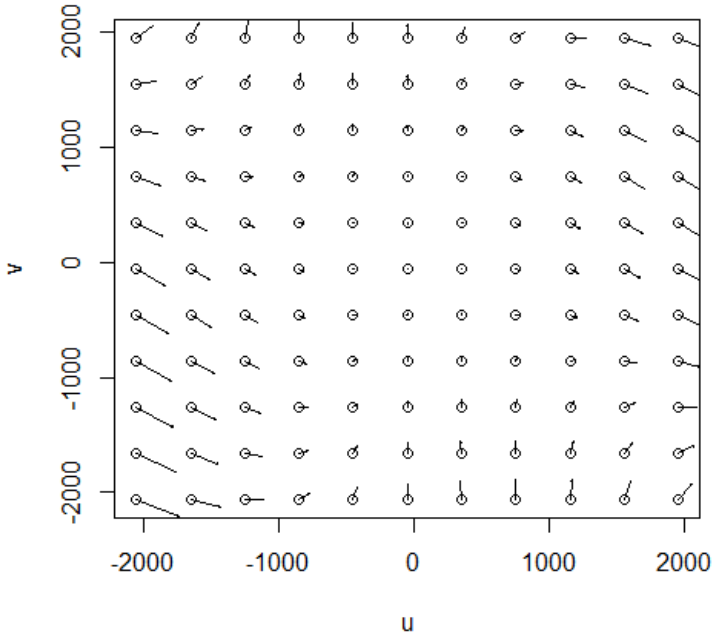

Figure 2.43: Distortion at the sensor plane, u, v coordinates, in pixels. Length of arrows not to scale. The maximum distortion is up to 3.4 pixels, or 7.4 arcsec.

```
WCSAXES =                    2 / no comment
CTYPE1  = 'RA---TAN-SIP' / TAN (gnomic) projection + SIP distortions
CTYPE2  = 'DEC--TAN-SIP' / TAN (gnomic) projection + SIP distortions
EQUINOX =               2000.0 / Equatorial coordinates definition (yr)
LONPOLE =                180.0 / no comment
LATPOLE =                  0.0 / no comment
CRVAL1  =        225.663664634 / RA  of reference point
CRVAL2  =        40.2414923446 / DEC of reference point
CRPIX1  =               2048.5 / X reference pixel
CRPIX2  =                 2056 / Y reference pixel
CUNIT1  = 'deg     ' / X pixel scale units
CUNIT2  = 'deg     ' / Y pixel scale units
CD1_1   =    2.89906535346E-05 / Transformation matrix
CD1_2   =   -0.000602168358812 / no comment
CD2_1   =    -0.00060232180406 / no comment
CD2_2   =   -2.92819755682E-05 / no comment
IMAGEW  =                 4096 / Image width,  in pixels.
IMAGEH  =                 4111 / Image height, in pixels.
A_ORDER =                    2 / Polynomial order, axis 1
A_0_0   =                    0 / no comment
A_0_1   =                    0 / no comment
A_0_2   =    5.02961513573E-07 / no comment
A_1_0   =                    0 / no comment
A_1_1   =    3.59612531443E-09 / no comment
A_2_0   =    2.31745233994E-07 / no comment
B_ORDER =                    2 / Polynomial order, axis 2
B_0_0   =                    0 / no comment
B_0_1   =                    0 / no comment
B_0_2   =   -3.45800127315E-07 / no comment
B_1_0   =                    0 / no comment
B_1_1   =    3.19975382026E-07 / no comment
B_2_0   =    -3.2345751575E-07 / no comment
AP_ORDER=                    2 / Inv polynomial order, axis 1
AP_0_0  =   -3.97138192613E-06 / no comment
AP_0_1  =   -1.41714903238E-06 / no comment
AP_0_2  =   -5.02960430196E-07 / no comment
AP_1_0  =    1.11907056554E-06 / no comment
AP_1_1  =   -3.59711415073E-09 / no comment
AP_2_0  =   -2.31744477638E-07 / no comment
BP_ORDER=                    2 / Inv polynomial order, axis 2
BP_0_0  =    4.73341184689E-06 / no comment
BP_0_1  =    1.67727252878E-06 / no comment
BP_0_2  =    3.45798860004E-07 / no comment
BP_1_0  =   -1.66856243885E-06 / no comment
BP_1_1  =   -3.19974267432E-07 / no comment
BP_2_0  =    3.23456798661E-07 / no comment
```

Figure 2.44: An example of WCS coordinates extracted from an actual TBT FITS header.

```
COD XXX
OBS F. Oca\~na, A. Montero, A. Ibarra
MEA F. Oca\~na, J. Doubek, M. Micheli, D. Koschny
TEL 0.56-m f/2.52 astrograph prime-focus corrector + 4K CCD
COM ESA Cebreros TBT Observatory
COM Long. 4 22 09.55 W, Lat. 40 27 14.67 N, Alt. 719m, Google Earth
NET UCAC-4
ACK MPC code batch
AC2 francisco.ocana.gonzalez@gmail.com,Marco.Micheli@esa.int


04673         C2016 05 19.87769 09 55 15.26 +28 18 30.4          16.9 V      XXX
04673         C2016 05 19.89089 09 55 16.11 +28 18 23.5          16.7 V      XXX
04673         C2016 05 19.90500 09 55 17.09 +28 18 16.5          16.8 V      XXX

00943         C2016 05 19.87707 11 23 20.67 +18 51 34.3          15.0 V      XXX
00943         C2016 05 19.89028 11 23 21.04 +18 51 28.9          15.0 V      XXX
00943         C2016 05 19.90439 11 23 21.43 +18 51 23.2          14.8 V      XXX

04673         C2016 05 20.90042 09 56 25.98 +28 10 03.8          17.1 V      XXX
04673         C2016 05 20.91416 09 56 26.95 +28 09 57.3          17.2 V      XXX
04673         C2016 05 20.92797 09 56 27.88 +28 09 50.2          17.1 V      XXX

00943         C2016 05 20.91077 11 23 51.36 +18 44 32.8          14.9 V      XXX
00943         C2016 05 20.92463 11 23 51.76 +18 44 26.9          14.7 V      XXX
00943         C2016 05 20.93837 11 23 52.17 +18 44 21.3          14.8 V      XXX
----- end -----
```

Figure 2.45: First observation batch from TBT Cebreros telescope sent to the Minor Planet Center to obtain the MPC code.

Using stars with magnitudes in the range from 12 to 18 in UCAC-4 catalogue, we match more than 2000 objects (up to 12000 in crowded galactic plane fields). The average astrometric residuals are under 0.1 arcsec in both right ascension and declination axis, with no spatial dependence, having a random error distribution across the image. Photometry fitting shows random distribution, with average residual of 0.1 magnitudes in V band. The astrometric results for asteroids observations are in section 2.5.3.

2.5.2.1 MPC code assignment

ESA requests asteroid observations by TBT to be reported to the Minor Planet Center (MPC). This centre requires a code to accept these observations. The MPC assigns such code upon receipt of acceptable observations of low-numbered minor planets each on pairs of nearby nights. The observations are processed by MPC what confirms all the data provided (coordinates of the observatory) and the quality of the observations, as low-numbered objects have well determined orbits.

In May 2016 we sent the observations required and the code assigned was Z58. For the sake of completeness we include in figure 2.45 the first observation batch from TBT Cebreros telescope sent to the Minor Planet Center.

2.5.3 Asteroid observation

During the months of commissioning, the Cebreros TBT telescope performed survey campaigns every night that the weather conditions were good and the telescope was available and functional (no other tests running). We have analysed the data for 4 fields observed in 4 different nights (20

minutes effective time). The average star FWHM for those nights was 4-4.5 arcsec. We took 324 positions of more than 80 different objects ranging between magnitudes 12 and 19, and measured their astrometric positions and calculated the residuals (figures 2.46). The average residual in RA was 0.04 ± 0.43 arcsec and in Dec it was -0.06 ± 0.43 arcsec. The average total residual was 0.46 ± 0.42 arcsec, with less than 7% of the measurements worst than 1 arcsec. All of the objects were slow compared to NEO category. The fastest of these 80 objects was around 1 arcsec/min.

We have observed that the depth of the survey in Cebreros is usually magnitude 19 to 19.5 for exposures of 30 to 60 seconds depending on sky brightness and seeing conditions. Astrometric precision according to Birney et al. (2006):

$$\sigma = \frac{1}{2.355}\frac{FWHM}{SNR} \tag{2.10}$$

for the usual conditions at Cebreros, at the limit of detectability (SNR=3) it is 0.6 arcsec, that is in agreement with the residuals we have found for the asteroids measurements.

Fast NEOs and satellite observations are very sensitive to timing uncertainties, consequently part of the efforts of the commissioning has been employed in this topic. The control server is the one stamping the time in the image file. This server is connected to an NTP time server inside ESA's network. We have tested the timing of the images down to the level of uncertainty of the shutter. The shutter has a travel time of 0.15 s across the FoV. For NEOs we have observed up to a maximum of 35 arcsec/min, with residuals under 1 arcsec.

2.5.4 Satellites and space debris survey and follow-up

Apart from the NEO related activities, during the commissioning period the Cebreros TBT telescope has also performed satellite observations every available night. Most of the observations have been done for satellites in GEO orbital regime reaching magnitude 18 in 5-second exposures. For calibration purposes we observe regularly Galileo, GLONASS and GPS satellites.

For GEOs (moving around 15 arcseconds per second) the residuals are also better than 1 arcsecond, using the star trails as astrometric reference (measured by our collaborators from the TFRM telescope (Montojo et al., 2011; Fors et al., 2013), that are part of the TBT consortium). The formal commissioning satellite observations have been sent to ESA and they are analysing the performance of TBT.

The fastest object observed until the moment has been Exomars. On March 14$^{\text{th}}$, the European Space Agency launched Exomars. The probe was sent to Mars using different rocket stages. Cebreros TBT telescope was well located to observe Exomars after the last boost. The spacecraft was first imaged at 20:10 UTC, located less than 5000 km above Earth's surface, already with escape velocity. The last image was at 20:16 UT with the object below 15 degrees of elevation and still moving over 40 arcsec/s. In spite of this speed being beyond the requirements, the TBT could observe Exomars using non-nominal strategy tracking on sky. The images were not measured with ASAP but sent to ESA. Their preliminary measurements show residuals of ~ 1 arcsec.

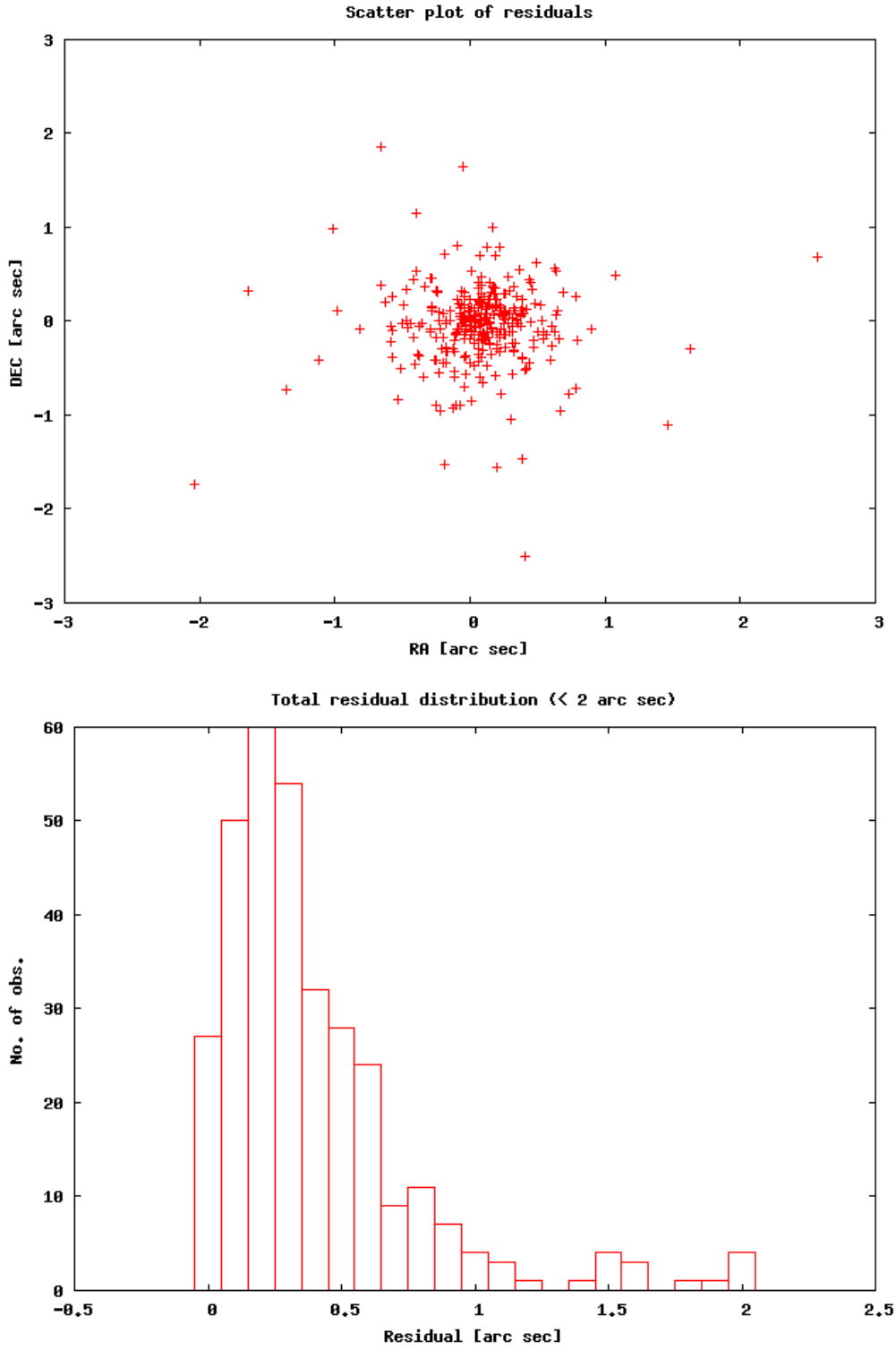

Figure 2.46: Up: Scatter plot of the residuals of 324 positions of asteroids. All the residuals larger than 1 arcsecond are for objects of magnitude 18 and dimmer. Bottom: Distribution plot of the asteroid observations residuals, with the peak in 0.2 arcseconds. Plots made by the Calculations of residuals service (Fitsblink.net), by Jure Skvarč.

3

Determination of meteoroid influx towards the Earth with optical meteor observation

Ever since the dawn of time humans have observed meteors. These light trails, often observed in mass numbers as meteor showers, appear in records as early as 7th century in oriental chronicles from China, Japan and Korea (see the work of Imoto and Hasegawa (1958)). In ancient times, their appearance was related to superstition, gods or simply meteorological phenomena. It was only at the end of the 17th century that a cosmic origin was suggested by E. Halley. He estimated the limit of atmosphere at 65 km high and located the meteors between 65 and 80 km high, with speeds larger than 4 km/s (Beech, 1990). During the 18th century several observations located meteors in the range from 60 km to 100 km and the fall of several meteorites established the grounds for the extraterrestrial origin of meteors and meteorites.

The first systematic study was carried out by Benzenberg and Brandes (1800) who established double station observations from two points located several kilometres apart to calculate meteor trajectories from triangulation and parallax. They estimated speeds between 29 and 44 km/s, and altitudes between 30 and 170 km, not far from the values we know now.

It was realised that meteor storms observed in November 1799 and November 1833 were connected as both had the same radiant point in the constellation of Leo. Several researchers noticed the periodicity and found previous displays of Leonids, and calculated a 33.25-year period. However it was not until 1861 when Kirkwood proposed that meteors were debris from comets. In 1867 Schiaparelli linked the Perseids stream to comet 109P/Swift-Tuttle and Peters linked the Leonids to comet 55P/Temple-Tuttle. Note also that H.A. Newton (1865) was the first one to use the word meteoroid in 1864.

The basis for modern meteoric science was set in 1885 when the first photograph was taken (Weinek, 1886). By the end of the century Yale Observatory and Harvard Observatory had set up systematic programmes to calculate the atmospheric trajectories of the meteors, their speed and the orbit of the meteoroids. After the World War II, military radar were available for civilian use and astronomers soon observed meteors with radar, including the storm of Draconids in 1946. Whipple (1950, 1951) proposed a model of a comet as an icy nucleus with embedded dust grains, and a model for the ejection of these dust grains as meteoroids, moving in an orbit similar to the one of the comet and creating a stream. Currently we also know that comet catastrophic break-up is common and up to 10 major meteoroid streams have such origin (Jenniskens and Vaubaillon, 2008). This second method is important for larger meteoroids, as gas drag has a limit of around 20 cm for the ejection model (Napier, 2001). However since the 1960's several automatic photographic networks have been systematically recording fireballs produced by multi-

kg meteoroids and calculating their trajectories in order to recover the meteorites on ground. Most of them have their origin in asteroid collisions, but meteorites from comets are possible and they would provide an insight of comet interiors.

Nowadays most of the research on the meteoroids is focused on their chemical characterisation in order to understand the global chemistry of the Solar System and specially the role of interplanetary matter in the spread of organic matter and its delivery to Earth (Anders, 1989). Moreover the observation of meteor outbursts from recent ejecta provide clues about comet mass loss and meteoroid stream dynamics (Jenniskens, 1999b). Models of the Leonid meteoroid stream (Asher, 1999; McNaught and Asher, 1999) consider individual ejecta for each return of the comet, representing a view in the activity of a comet tens or hundreds of years ago.

Current lines of research also work on the determination of the flux density of meteoroids, as the interplanetary matter in this size/mass range is the largest threat for spacecraft and mid-term manned spatial exploration. Meteoroid impacts pose a threat to spacecraft. The characteristics of the meteoroids in the Earth environment are the major input for spacecraft hazard estimates. These estimates rely on mass distributions of the background meteoroid component and the different meteoroid streams that Earth encounters along the orbit. Particles smaller than a microgram routinely hit satellites with no consequence, however larger meteoroids ($> 100mg$) could cause mechanical or electromagnetic damage. Many satellites are turned away from the oncoming stream when the risk is enhanced in order to present a minimal target area.

In this thesis we present the state of the art and knowledge about the observations of meteors and fireballs in section 3.1. In section 3.2 we describe a method for analysing optical video observations of meteors in order to measure the meteoroid influx and determine some instrumental parameters to optimise meteor detection. Finally in section 3.3 we present meteor spectroscopy as a method of the characterisation of meteors and introduce narrow-band photometry to overcome some of the difficulties of the spectroscopic analysis.

3.1 Using the atmosphere as a detector: meteors and fireballs

The observation of meteors represents the detection of the interplanetary matter at its closest to the Earth. The Earth's atmosphere is used as a detector to derive meteoroid properties from the light emitted by the meteor. Meteoroids are defined as solid bodies that produce meteors when entering into Earth's atmosphere. This definition sets a lower limit as meteoroids with masses below $\sim 10^{-8}$ g (diameter $< 30 - 100$ μg) experience no ablation (Bronshten, 1983), and therefore emit no light (Jones and Kaiser, 1966). Meteoroids lighter than $\sim 10^{-8}$ g lose kinetic energy through radiation instead of through ablation process. But this limit depends on the meteoroid composition and speed, and has been idealised as a round diameter value. Moreover the smaller particles are not in bound orbits as their dynamics is dominated by Sun's radiation pressure. On the other hand, the upper limit is set by asteroids. It is a complete arbitrary limit that currently is assumed between 1 m to 10 m based on the capabilities of telescopes to detect asteroids, when meteoroids are only detected because of the meteor light. Current IAU definition is ambiguous and obsolete[1]. The topic has been extensively debated in the literature, see the reviews by Beech and Steel (1995); Rubin

[1]IAU definition for meteoroid (Millman, 1961): a solid object moving in interplanetary space, of a size considerably smaller than an asteroid and considerably larger than an atom or molecule.

and Grossman (2010). For this thesis we consider the current proposition from the IAU Division F (Borovička, 2015), to be voted in the next IAU General Assembly: *"Meteoroid is a solid object of a diameter between 30 μm and 1 meter moving in, or coming from, interplanetary space"*. Therefore meteoroids cover 6 orders of magnitude in size, or 17 orders of magnitude in mass, from 10^{-11} g to 10^{6} g.

For meteoroid streams, the cumulative mass distribution N(m) can be described by a power law of the form:

$$N(m) = K \cdot m^{-a} \tag{3.1}$$

where $N(m)$ is the cumulative influx into Earth's atmosphere of mass equal to or larger than m. K is a constant and a is the cumulative mass distribution index. Usually this is treated as differential mass distribution,

$$dN(m) = C \cdot m^{-s}\, dm \tag{3.2}$$

where $dN(m)$ is the differential flux of meteors with masses between m and $m + dm$, and s is the differential mass index, that is related to the nature of the ejection process and the dynamic evolution of the meteoroid stream.

This mass distribution (figure 3.1) is modelled and calibrated with the observational data we have available about meteoroid fluxes with different techniques. There are two models that are widely used. One is the NASA's Meteoroid Engineering Model, MEM[2] (Jones, 2004; McNamara et al., 2005), which is heavily based on observations at 1 AU: sporadic meteor observations from the Canadian Meteor Orbit Radar (CMOR), lunar crater size distribution and zodiacal light observations. The other one is the ESA's Interplanetary Micrometeoroid Environment Model, IMEM[3] (Dikarev et al., 2005), which is a physics-based model. It assumes a parent source population (comet and asteroids) and injection methods (collision and ejection) to create a model applicable from 0.1 AU to 5.0 AU at mass range from 10^{-18} g to 1 g. The population of meteoroids created is weighted with lunar crater statistics, data from dust detector on the Galileo and Ulysses spacecrafts, and the IR observations of the COBE observatory. Propagate until encounter with Earth. The comparison (Grün et al., 2013) between current meteoroid models of ESA (IMEM) and NASA (MEM) yields flux differences up to 2 orders of magnitude at some heliocentric distances and meteoroid sizes. It reflects the need for further studies to obtain a reliable model, which would benefit from more flux estimations to improve the models.

Taking the data from the models at 1 AU we can calculate the mass that our planet receives. The mass influx at Earth has a maximum at 10^{-5} g, around 200 μg and a total mass influx of $(40 \pm 20) \cdot 10^{6}$ kg/yr or around 110 ± 55 tons per day (Love and Brownlee, 1993).

Meteoroids at 1 AU are usually studied with ground-based observations of meteors, which requires sophisticated modelling to convert from meteor parameters to meteoroid properties. Direct in-situ measurements are possible with sensors on-board satellites, interplanetary dust particles (IDPs) collected in the stratosphere and the analysis of returned spacecraft surfaces that has been exposed to meteoroid influx. Unfortunately these in-situ methods prevent decoupling velocity from mass and have a very limited collection area, detecting only the smallest meteoroids.

[2]MEM is available for US Release only.

[3]Note that IMEM is going to be complemented with the Interplanetary Meteoroid Environment for eXploration (IMEX), including meteoroid streams from 400 short-period comets in the inner Solar System to asses the specific risk arising from these dusts trails (Soja et al., 2014).

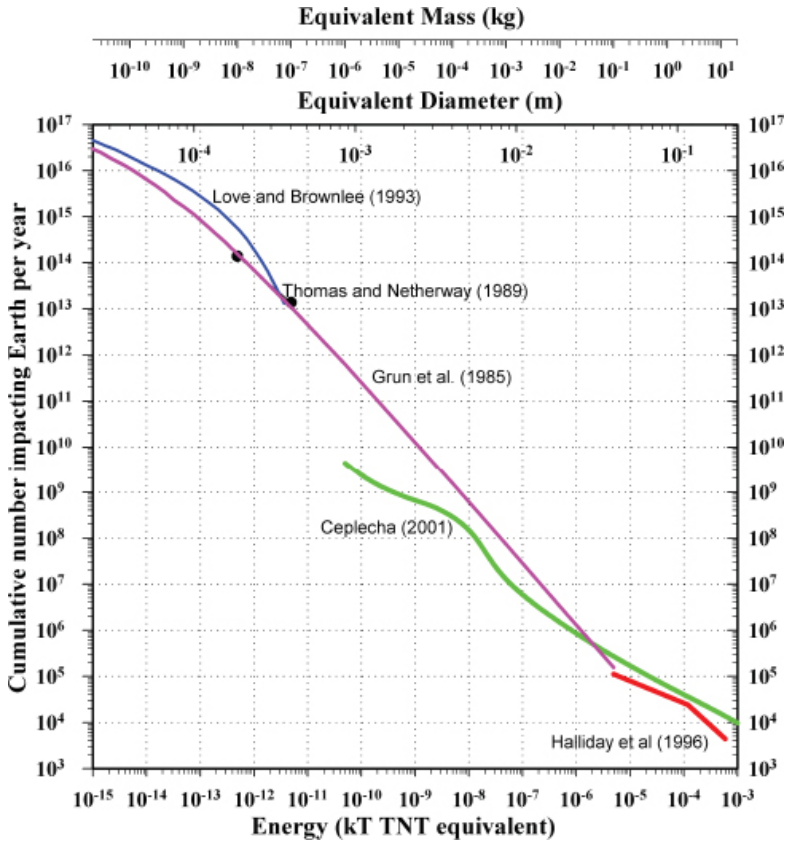

Figure 3.1: Influx of meteoroids to the Earth. Note the discrepancies between the different sources in the literature. Figure from National Research Council (2011).

When a meteoroid collides with the Earth it produces heat, light and ionization. Likewise these phenomena associated with a meteoroid impacting any planetary atmosphere are named a meteor, whilst the collision against a planetary surface with no atmosphere is termed *impact flash*. Ablation is the term for the process of mass loss from the meteoroid in any form and phase: solid fragments, liquid droplets and eventually the hot gas, that is what one observes as a meteor. Optical measurements of meteors provide flux and velocity distributions. Density and mass can be estimated with modelling. The main constrain comes from the conversion factor between total initial kinetic energy, and the amount of radiation measured by the instrument, the luminous efficiency. This parameter shows wide variation depending on the author and method of estimation (Subasinghe et al., 2017). Also the velocity distributions differ depending on the study and the mass limit. It may indicate a change in the velocity distribution with mass, as predicted for instance by Wiegert et al. (2009).

Knowledge of meteoroids also results from plasma ionization observations at radio and radar wavelengths. This includes both the plasma formed around the meteoroid and the plasma that extend behind the particle, sometimes for kilometres. Radar observations are based on the return of electromagnetic waves scattered from the meteor plasma. Again modelling requiring significant assumptions is needed. Apart from meteors in our planet, we can observe meteors in other planets' atmospheres, like Mars (Selsis et al., 2005) or impact flashes in Jupiter (Hueso et al., 2013). Also relevant for the flux at 1 AU are the observations of the impact flashes on the Moon (Ortiz et al., 2000). Each technique and phenomenon has different constraints and refer to different mass regimes. In this work we focus on optical techniques for meteor detection and characterisation.

Meteoroids encounter the Earth's atmosphere with a velocity V_∞ (*entry velocity* or *at infinity*) that is the vectorial sum of the heliocentric velocity V_h and the Earth's velocity $V_\oplus$. Both quantities are constrained for meteoroids from the Solar System, as the maximum heliocentric speed near the Earth is 42 km/s and the Earth's speed is 30 km/s. Therefore, in a geocentric reference system, we get *geocentric velocities* V_g in the range within 0 km/s to 72 km/s for a catch-up and head-on collision respectively. In order to obtain the velocity V_∞ we have to add the influence of Earth's gravity, usually considered as a free fall from infinity with a resulting velocity of 11.2 km/s. Hence the range for the velocity V_∞ is from 11.2 km/s to 72.8 km/s. Unless otherwise noticed, in this work we refer to the velocity at infinity V_∞.

Meteors are typically produced by meteoroids in size range between 0.05 mm to 20 cm. In the higher parts of the atmosphere meteoroids start to be heated up, although usually only a layer of around 0.5 mm is heated. At a height around 100 km the surface of the meteoroid reaches ~ 2200 K and starts to sublimate, creating a shell of hot vapours that de-excite by radiative emission, what we see as a meteor. The meteoroid is slowed during the ablation process and usually it consumes all the mass. When the size is larger than ~ 20 cm the meteoroid is slowed down to a critical $\sim 3\,\mathrm{km/s}$ and the ablation stops because the temperature drops below ~ 2200 K, ending the luminous path as meteor. The surface of the meteoroid solidifies and creates the crust that is characteristic of meteorites. The remaining mass enters in the dark-flight phase and falls at the free fall velocity of the atmosphere from that height. This fall lasts several minutes and the meteorite reaches the ground at a velocity in the range of tens of meters per second, making a small impact pit if the ground is soft. When the body is larger than several meters, slow and strong enough, the body hits the surface before it is decelerated from hypersonic velocities creating a crater. In the the case of an impact we would more likely talk about an asteroid rather than a meteoroid.

The brightness of meteors is usually expressed in Pogson magnitudes as for most of the astronomical observations. However the standard reference distance considered for meteors is 100 km. Thus the relation of the absolute magnitude M and the apparent magnitude m is

$$M = m - 5 \log \frac{d}{100} \tag{3.3}$$

This difference between absolute and apparent magnitude due to the distance is 0.75 magnitude for a zenithal distance of 45 degrees and rises up to 5.3 magnitudes close to the horizon, when meteors are farther than 1000 km. Absolute magnitude corrections are in the same range as extinction magnitude losses in the visible wavelengths.

A fundamental property of a meteoroid is its mass. However the determination of the mass is difficult as it is never direct but through observations. The most common method is studying the relationship between the luminous intensity and mass. This relationship is quite complex, and depends on the meteoroid properties (luminous efficiency, speed) and geometric observational conditions (entry angle), amongst others. For a review of the topic please see Subasinghe et al. (2017). As a first approach we consider an approximation that takes into account only the geocentric speed V_g and the absolute magnitude in the visual band m_V from (Verniani, 1973; Hughes, 1987) (adapted by the author for a input of the speed in km/s, and an output of the mass m in grams):

$$0.92 \log m = 5.56 - 0.4\, m_V - 3.91 \log V_g \tag{3.4}$$

Meteor shower	IAU Code	$\lambda_o(max)$	V_g	ZHR	r	Parent body
Quadrantids	010 QUA	283	40.7	130	2.2	2003 EH1
Lyrids	006 LYR	32	46.7	13	2.9	C/1861 G1 (Thatcher)
η Aquariids	031 ETA	46	65.7	28	2.7	1P/Halley
Perseids	007 PER	140	59.1	85	2.5	109P/Swift-Tuttle
Draconids	009 DRA	195	20.7	var	2.6	21P/Giacobin-Zinner
Orionids	008 ORI	209	66.3	23	2.9	1P/Halley
Leonids	013 LEO	235	70.2	15	2.5	55P/Tempel-Tuttle
Geminids	004 GEM	262	33.8	120	2.0	(3200) Phaethon

Table 3.1: List of selected major showers. $\lambda_o(max)$ is the solar longitude (in degrees) at the time of the maximum activity of the shower, V_g is the geocentric speed, where var stands for variable, ZHR is the zenithal hourly rate and r is the population index (or magnitude distribution index). Information compiled from (Jenniskens, 2006; Jenniskens et al., 2016). See Jenniskens (2017) for a full review about the current knowledge of meteor showers. For a complete list please refer to the IAU Meteor Data Center.

The relationship shows the strong dependence on the speed, as expected since the kinetic energy is proportional to v^2. Indeed, in order to get a meteor of magnitude 6.5, one needs a 22 μ g meteoroid if the geocentric speed is 71 km/s (e.g, Leonids), while at 20 km/s (e.g, Draconids), the meteoroid should be of 10 mg, i.e, almost 500 times more massive.

Over a certain value of brightness, meteors are categorised as fireballs or superbolides. They are the same phenomena as meteors, although their physics is more interesting as they could penetrate deeper and occasionally produce a meteorite fall. The possibility of it depends strongly on the meteoroid speed. Due to ablation, there is an asymptotic limit at ~ 30 km/s as the terminal mass varies at V_∞^{-6}. As brightness is proportional to mass, fireballs and superbolides are meteoroids with masses closer to asteroids. Moreover in the case of superbolides the deep penetration is associated to a big energy release from an explosion. The associated airblast (shock wave travelling through the air) could produce damage at the ground at city-level extension. In 2013 the Chelyabinsk event released an energy equivalent of about 2100 TJ ($\approx$ 500 kt of TNT) and broke several windows and fragile structures (Brown et al., 2013).

Stream meteoroids are particles with a common origin, usually within the last 10^5 years. They are usually ejected by comets and asteroids and follow similar orbits to their parent bodies, and when these meteoroids encounter the Earth, they all follow nearly parallel trajectories across the atmosphere. The observational effect is called *radiant*, the region where they seem to emanate, and is a consequence of perspective. The direction of the radiant is determined by the vectorial addition of Earth's velocity and meteoroid velocity. The meteor shower resulting of the encounter takes the name of the location of this radiant area, following certain IAU rules (Jenniskens, 2006) (table 3.1).

Thus sporadic meteors are meteoroids not found in streams. Nevertheless they are not randomly distributed but have clear sources in ecliptic reference frame: the helion/antihelion, apex and toroidal sources (Campbell-Brown, 2008). This distribution is a result of the collisional lifetimes and collision probabilities of the meteoroids.

The meteoroid hazard for artificial satellites has been thoroughly studied and it is small but not negligible. During the Perseids 1993 outburst astronauts at Mir station reported audible me-

teoroid impacts, that were later confirmed (Beech et al., 1995), and ESA's Olympus-1 satellite suffered a major failure, likely due to the impact of a Perseid (Caswell et al., 1995). Other spacecraft failures have happened during large meteoroids influxes, but the impact of artificial debris can not be discarded: for instance two spacecraft suffered power failures during the 2003 Orionid shower ,the ADEOS-II satellite, the Landsat 5 spacecraft during the 2009 Perseids outburst and the ALOS spacecraft during the 2011 Lyrids shower (National Research Council, 2011). Moreover Carpenter et al. (2006) reports at least two impacts in sensors of XMM-Newton and SWIFT incidence-grazing telescopes.

The impact probability of a space platform with an area A to suffer an impact, during a time t, from a meteoroid stream is proportional to the spatial number density $\rho(m)$ of meteoroids of mass larger than m (Beech et al., 1995):

$$I = \rho(m)\, V_\infty\, A\, t \tag{3.5}$$

Note that apart from the momentum transfer, in a hypervelocity impact, part of the meteoroid is vaporised and even ionised. This plasma cloud poses a risk of satellite malfunction in the form of electrostatic discharge or electromagnetic pulse. The electric charge produced is proportional to the collisional speed $V^{3.48}$ (McDonnell et al., 1997). Therefore the damage suffered from meteoroid impacts is significantly dependant on the speed. It depends on the meteoroid density for mechanical damage, but also the chemical composition is relevant. Plasma production is related to the composition of the meteoroids because of the different level of ionization of the elements.

Therefore, knowledge of the velocity and the spatial number density $\rho(m)$ of the meteoroid streams is essential in order to estimate the hazard to spacecraft caused by meteoroid streams. But it is also important to characterise the meteoroids in term of chemical composition, density, tensile strength, etc.

The risk of collision with meteoroids is not the only threat, as space debris has also hit artificial satellites. Beyond Low Earth Orbit (LEO), meteoroids constitute the the dominant impactor population, while orbital debris dominates in LEO for sizes larger than 1 mm, and is of similar importance in the range from 10 μm to 1 mm (Laurance and Brownlee, 1986; National Research Council, 2011). Apart from the number, the risk differs in the collisional parameters: the average velocity is higher for meteoroids, and the bulk density is different between the two populations.

3.2 A method to determine meteoroid influx towards the Earth with optical video observation of meteors

The spatial number density is a key parameter when studying a meteoroid stream or the sporadic meteoroid background. In the Space Situational Awareness field, there is a need for knowledge of the number and masses of particles in our neighbourhood (McNamara et al., 2005; Grün et al., 2013). The meteoroid spatial density at 1 AU can be studied as the meteoroid influx towards the Earth observed as meteors.

When observing meteors, the Earth's atmosphere is used as a detector of the meteoroids in the near Earth environment. With growing video meteor observing networks around the world

(Molau, 2001; Weryk et al., 2008; SonotaCo, 2009; Trigo-Rodríguez et al., 2004; Madiedo and Trigo-Rodríguez, 2008) there is continuous and automatic coverage of several thousands of cubic kilometres of atmosphere, like a very unique cloud chamber. Various observational geometry effects need to be corrected in order to standardise all the different viewing location geometries to get the physical magnitudes of the observed phenomena.

Several methods for flux calculations have already been developed. First Koschack and Rendtel (1990) did it for visual observation. Later it was adapted for photography by Trigo-Rodríguez and Bellot Rubio (1994b). They lack the treatment of data coming from video techniques and can be used only for ground-based observations. This work seeks to extend these methods to video techniques under non-standard observing conditions. The algorithm we present here is based on that of Bellot Rubio and adapted to video observations and generalised for different observatory elevations. Many other authors have already used video observations to calculate fluxes. Koschny and Zender (2000) estimated a flux through a volume, while others have estimated the flux through an area (Brown et al., 2002; Trigo-Rodriguez et al., 2009) or a simulation approach (Gural, 2002). We reproduce their results with a different algorithm and extend its application to observations out of the troposphere.

This work was started as a collaboration with D. Koschny and J. McAuliffe during a stay of the author in the European Space Astronomy Center (ESAC). The aim of the project was to develop an algorithm to deal with video observations and develop a code to serve as a tool at the Virtual Meteor Observatory (VMO) (Ocaña et al., 2011). All of the calculations are sensitive to the number of events, so it is important to gather as many observations as possible around the globe.

The algorithm written is based in the Bellot Rubio's paper for photography observations. However, some aspects make little sense for video observations (CCD based, several frames per second). We have adapted the method and introduced new variables to account for it. For instance, the limiting magnitude concept is different, as now it is easy to find the relationship between the faintest star visible and the faintest meteor recorded.

The main idea is to calculate the number of meteors that will be seen in certain conditions (vZHR, see 3.2.1) in the volume that the camera is monitoring. Distance and the extinction diminish the light received from the meteor, which results in the need of using a reduced or effective area. There is a loss of magnitude due to the distance, therefore we must correct to the absolute magnitude (equation 3.3). In most of the cases, the same area (not FoV) in the zenith gives more meteors than closer to the horizon.

3.2.1 vZHR

The first observational parameter that one can associate to a meteor shower is the hourly rate. However the amount of meteors seen depends on the elevation of the radiant h_R and the darkness of the sky, measured by the faintest star observed and thus called *limiting magnitude* lm. For visual observers this approach derives into the zenithal hourly rate (ZHR) (Arlt and Barentsen, 2006), a standardised hourly rate:

$$ZHR = \frac{N+1}{T} \sin^{-\gamma} h_R \cdot r^{6.5-lm} \tag{3.6}$$

where N is the number of meteors observed, T is the effective time of observation, r is the population index and γ is the exponent that summarises the geometrical and non-geometrical effects of the elevation of the radiant h_R, the so-called zenith correction factor (Zvolankova, 1983). Therefore ZHR is an attribute of a shower and different observers should determine the same value, differing only in an individual perception coefficient C_p.

The population index r is an observational parameter of the meteor shower that describes the relationship between the numbers of meteors of different magnitude classes m:

$$r = \frac{N(m+1)}{N(m)} \tag{3.7}$$

The population index is directly related to the mass index s, that describes the relationship between the numbers of meteoroids of different mass clases M:

$$s = \frac{N(M+dM)}{N(M)} \tag{3.8}$$

Using the mass-luminosity conversion from Verniani (1967) and assuming that the shape of the light curve does not change within the magnitude range, the relation between both is:

$$s = 1 + 2.3 \log r \tag{3.9}$$

For video observations we follow a similar approach and define the video ZHR. The $vZHR$ is the hourly rate of meteors recorded by the camera, assuming a radiant in the zenith and a video limiting magnitude vlm. It is the number of meteors N, divided by the time T (in hours) and corrected with the radiant elevation h_R and the limiting magnitude (6.5 is merely a convention for an average dark sky).

$$vZHR = \frac{N+1}{T} \sin^{-\gamma} h_R \cdot r^{6.5-vlm} \tag{3.10}$$

Note: vZHR or video ZHR must not be mistaken with the ZHR of visual observations. While we all have essentially the same eyes, the ZHR can be considered characteristic of a shower; but vZHR depends significantly on the system used.

3.2.2 Spatial Number Density and Flux Density

The end goal of meteor observations is to determine physical quantities that characterise a stream over a given time. The number of meteors detected is proportional to the number of particles in a meteoroid trail. This number could be calculated as a flux of meteoroids entering the Earth's atmosphere, or taking into account the characteristics of the encounter, as the spatial number density of the trail crossed by the Earth.

Flux density is the number of meteoroids larger than a given mass passing through a unit area in a unit time.

$$[Q] = \frac{meteoroids}{km^2\, hour}$$

While the spatial number density is the number of meteoroids larger than a given mass in a unit volume. It is calculated with the flux density and the geocentric velocity of the particles.

$$[\rho] = \frac{meteoroids}{km^3}$$

In order to calculate the flux of meteoroids through a given area, a 'meteor layer' is defined, located at a height H. The value H is assumed to be 100 km, as an average between different values observed for the middle point of meteors and in general it has an impact of less than 10% of deviation in the final flux calculation (Koschack and Rendtel, 1990).

The area surveyed by a sensor is calculated as the projection of the field of view onto the meteor layer. The method explained here is a generalization of the method defined by Koschack and Rendtel (1990) and later applied for cameras by Bellot Rubio (1994b). It includes the height of the observer, h_b, as an extension for airborne and balloon-borne observations.

The lens is selected as the origin for a rectangular coordinate system, where the meteor layer is described as an spherical surface with radius $r = (R_\oplus + H)^2$ and centred in $z_0 = -(R_\oplus + h_b)$:

$$x^2 + y^2 + (z + R_\oplus)^2 = (R_\oplus + H)^2 \tag{3.11}$$

Following Bellot-Rubio's notation (figure 3.2), a point P in the CCD sensor is characterised by two angles that describe the position in the sky (α,β). The projection of that point in the meteor layer surface can be parametrised as:

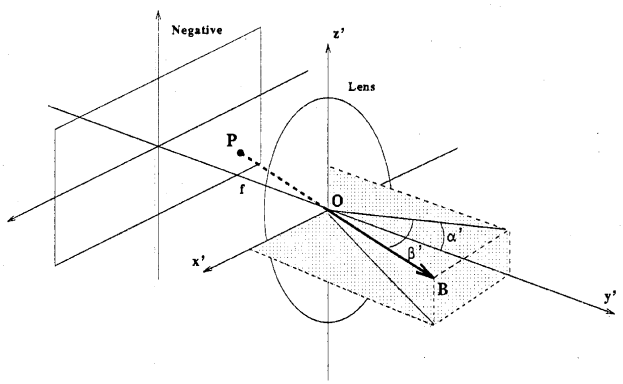

Figure 3.2: Camera diagram. The point P, on the focal plane, is described by the two angles (α,β) which define a direction in the sky. Figure from Bellot Rubio (1994b).

$$\begin{aligned} x' &= p\, sin\beta' \\ y' &= p\, cos\beta' cos\alpha' \\ z' &= p\, cos\beta' sin\alpha' \end{aligned} \tag{3.12}$$

with p being the parameter.

Then generalised for a point with an elevation over the horizon h :

$$\begin{aligned} x' &= r\, sin\beta' \\ y' &= r\, cos\beta' cos(\alpha' + h) \\ z' &= r\, cos\beta' sin(\alpha' + h) \end{aligned} \tag{3.13}$$

And writing $h' = \alpha' + h$:

$$\begin{aligned} x' &= p\, \frac{tan\beta'}{cosh'} \\ y' &= p \\ z' &= p\, tanh' \end{aligned} \tag{3.14}$$

The system of equations 3.11 and 3.14 is solved to calculate the value of the parameter p. Since it is a quadratic equation it could be bivalued and we take the positive root as the only one with a physical meaning. The solution is real (positive discriminant) only if $h_b < 100km$, therefore the method is constrained for observations below the meteor layer.

Solving equations 3.11 and 3.14 gives the values of coordinates x_i, y_i and z_i for every point of the sensor projected onto the meteor layer. In order to evaluate the area covered by the field of view of the instrument the sensor could be discretised on a mesh of these points. Each square is projected as a trapezoid with an area A_i.

However the flux of meteors observed through this geometric area does not correspond to the flux of meteoroids through it. The apparent magnitude of a meteor depends on the distance to the observer. Therefore the lower the elevation over the horizon, the farther the meteor is and the dimmer it appears to be. Thus using the same unit area at lower elevations will result in fewer meteors detected.

The correction to an absolute magnitude requires the further correction of the geometric area to an effective or reduced area A_{red}. This correction means a reduction of the area to correct the effect of the loss of meteors due to distance. It corrects the fact that a camera covering a given area pointing to lower elevation would detect fewer meteors than another camera monitoring the same given area but closer to the zenith. Therefore the camera pointing lower needs to be standardized as if it was observing through an effective area, smaller than the geometric one.

$$A_{red} = \sum_i A_i \cdot r^{5 \log \frac{H}{d_i} - \varepsilon_i} \tag{3.15}$$

Where A_i, ε_i and d_i are calculated for each of the elements of the mesh in which the field of view of the instrument is divided. The sum of the corrected areas is the reduced or standard area. A_i is the area of each individual tile projected into the meteor layer, ε_i is the extinction in each individual direction and d_i is the distance from the observer to the point projected onto the meteor layer.

This correction to an absolute magnitude is based on the assumption that the population index r is constant within the range of masses. Moreover it implies that the mass index s of the

meteoroid stream is constant within the range of masses correspondent to that brightness. As an example, note that a 6.5 magnitude Leonid is a 22 μg particle, but a 6.5 magnitude Draconid has a mass of 4.9 mg.

The calculation of the distance is adapted from the formulae from Koschack and Rendtel (1990) and generalised for airborne and balloonborne observations, according to the figure 3.3:

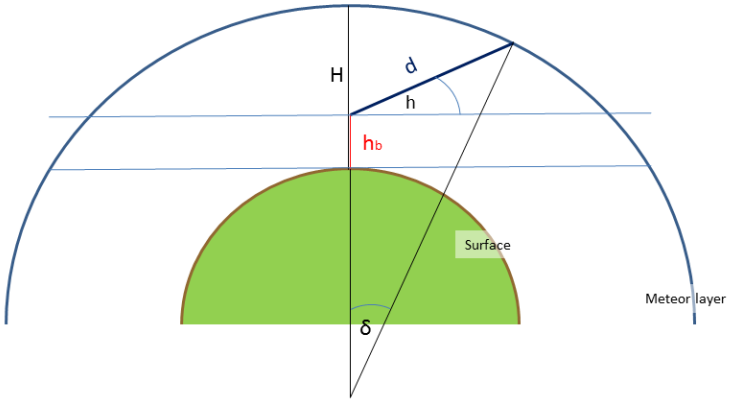

Figure 3.3: Diagram to calculate the distance d to an observer located at an altitude h_b above the ground to the meteor observed at an elevation angle h.

$$d = (R_\oplus + H - h_b)\frac{\sin\delta}{\cos h} \tag{3.16}$$

where δ is:

$$\delta = arccos\frac{(R_\oplus + h_b)\cos h}{R_\oplus + H} - h \tag{3.17}$$

After calculating the vZHR and the reduced area, the flux density Q and spatial number densities ρ are determined as the meteor rate divided by the area being monitored.

$$Q = \frac{vZHR \cdot Cr}{A_{red}} = 3600 \cdot V_\infty \cdot \rho \tag{3.18}$$

Q, ρ represent the same physical magnitude except the time factor and geocentric velocity, which gives to the flux a 3rd dimension in order to get a spatial density.

The software is a short piece (500 lines) of C++ code. It uses basic libraries and follows the C++ standard. Apart from the main function, each of the processes mentioned above is an independent routine. The main routine reads the data from input files written by the user, and calls the different processes (figure 3.4). The input is the number of meteors N, the duration of the observation T, and the details of the camera (FoV) and session (limiting magnitude, radiant elevation...). There is a constants file where the user can change the assumed values for some variables, such as the height H, the gamma exponent, etc.

Afterwards the code has been transformed into a Python code, overcoming some of the constrains of the C++ version in terms of memory allocation and maximum number of elements

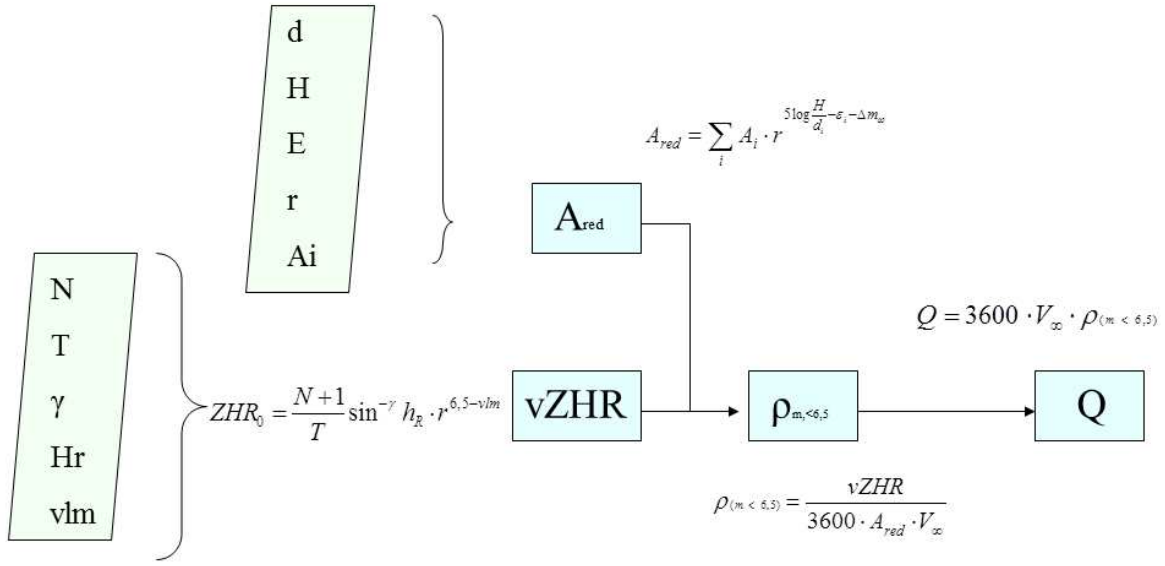

Figure 3.4: Schematic diagram of the calculation of flux density Q.

in the grid. Moreover we included the generalisation to different observers heights h_b. In the next section we discussed the approach used for the calculation of some parameters needed for the practical implementation of the method.

3.2.3 Extinction and constraints in air mass calculations

Apart from the calculation of the distance, in order to make a correction to the absolute magnitude, the other main correction is due to the atmospheric extinction. The extinction is the loss of light intensity produced by the absorption and scattering by aerosols and by atmospheric particles. The main contributors are the Rayleight scattering and absorption by atmospheric molecules, and the Mie scattering by atmosphere aerosols. The proportion of them are variable across space and time, so we use the quadratic fit to the tables found in Roth et al. (1994) by Gural and Jenniskens (1998).

$$\Delta m_v = -0.003X^2 + 0.228X - 0.225 \qquad X < 35 \text{ air masses} \tag{3.19}$$

The air mass is calculated as the integral of the air density along the path of the radiation. This dependence on the air mass X is the main restriction for our method because the air mass determination is very sensitive to the local conditions. Specially for low elevation angles where the refraction plays an important role and the difference between the atmospheric models (Standard Atmosphere USSA-76, exponential profile, quartic profile) is larger (Rapp-Arrarás and Domingo-Santos, 2011). Moreover for airborne and balloon-borne observers observations below the true horizon are possible. However the air masses could double as the light path could even cross twice the lower layers of the atmosphere. Therefore we limit the calculations to elevations over the true horizon and we apply a functional form for the airmass calculation, the five-parameter form of Dogniaux (1975), as adapted by Rapp-Arrarás and Domingo-Santos (2011) ,

$$
\begin{aligned}
X &= \frac{a_1 z^2 + a_2 z + a_3}{z^2 + a_4 z + a_5} \\
a_1 &= 0.450136 \\
a_2 &= -2.16910 \\
a_3 &= 2.48596 \\
a_4 &= -3.28380 \\
a_5 &= 2.69572 \\
\text{where } z &= 90^\circ - h_f, \text{ z in radians}
\end{aligned}
\tag{3.20}
$$

On the other hand for balloon-borne observations, at height larger than 20 km, the extinction could be considered negligible compared to other magnitude losses, especially for low elevation observations (figures 3.5, 3.6). Using the exponential-profile atmosphere we calculate that an instrument at mountaintop (3 km height) is over 31% of the atmosphere, and that raises up to 74% for airborne observatories (11 km) and 91% - 97% for balloonborne observations (at 20 km and 30 km high respectively).

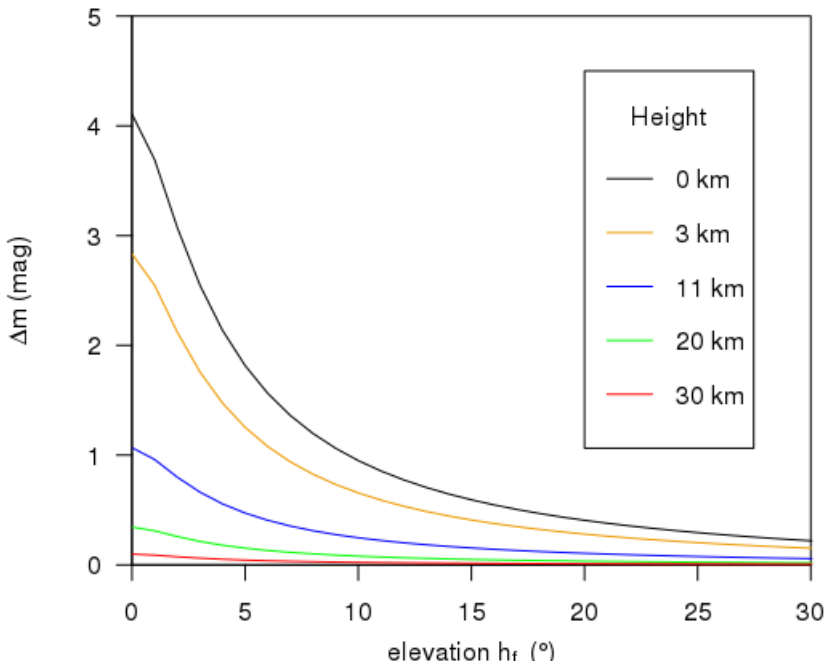

Figure 3.5: Magnitude difference Δm due to the extinction as a function of the elevation of the field of view for different heights.

3.2.3.1 Validation

In order to validate the method and the implementation into code we reproduced results from literature, in this case using data kindly provided by Dr. Peter Brown (UWO). The method that he used is described in Brown et al. (2002). He provided raw meteor counts per camera N and all the observational parameters T, vlm, h_f, r . We have used a FoV divided in 10000 tiles. The others parameters and input used are exactly the same.

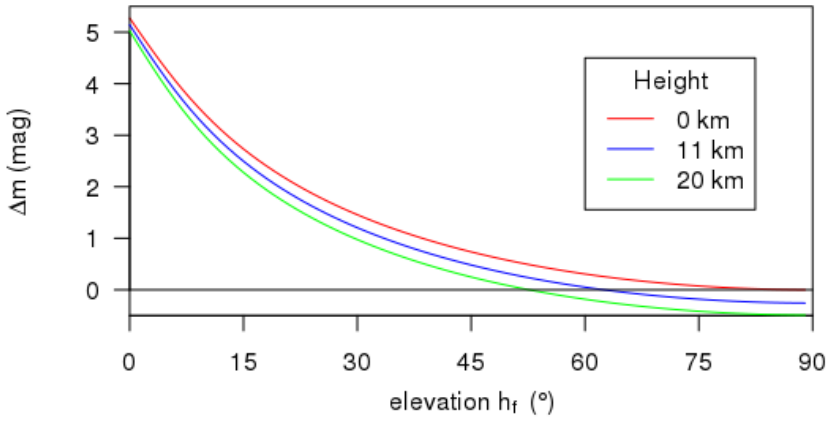

Figure 3.6: Magnitude difference Δm due to the distance as a function of the elevation of the field of view for different heights. This the correction to convert from relative to absolute magnitude. Note that for $h_b = 0$ km at zenith the distance d=H=100 km and therefore the correction Δm is zero by definition (see equation 3.3). Negative values are possible for $h_b > 0$ as the observer could be closer to the meteor layer.

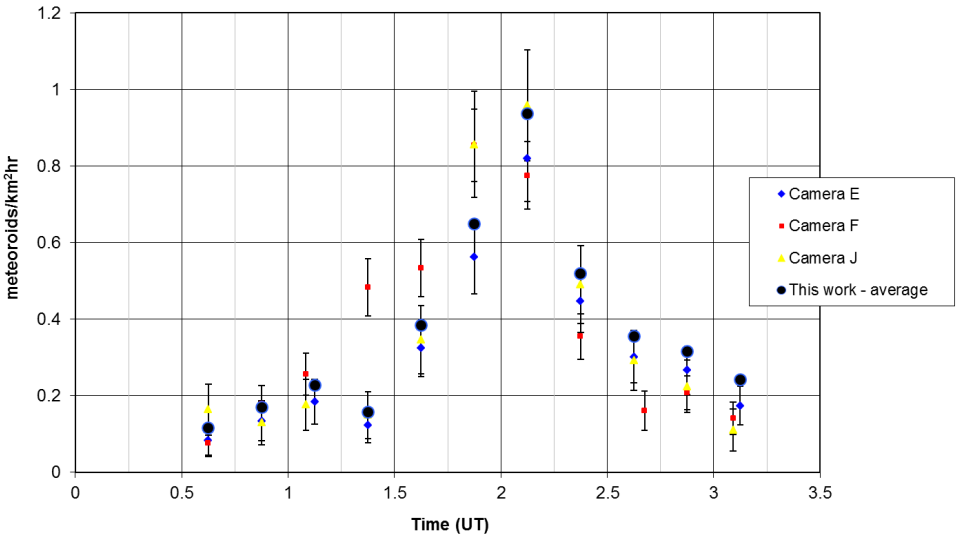

Figure 3.7: Comparison of the flux values calculated by Brown et al. for the cameras E, F, G. In a black and blue dot we overplot the average flux obtained using the method of this work.

The differences between the results of both algorithms are quite small (<10%), in the range of the uncertainties (figure 3.7). The variations are due to the different collective area given by each method. Our areas are systematically smaller than those of Brown which results in higher spatial number densities, because of the different assumptions made in the mathematical development.

Besides in section 3.2.4 we reproduce the values from the original implementation of the method by Bellot-Rubio. In the next chapter (section 4.2.4) our results agree with the the published literature.

3.2.4 Maximising the meteor detection

The use of the method described above allows us to evaluate the performance of difference instrumental setups and understand the role and influence of each parameter.

We start with a standard camera field of $39.6^\circ \times 27.0^\circ$, which corresponds to a lens with f = 50 mm on a film of 36 mm $\times$ 24 mm. We calculate the reduced areas A_{red} as a function of r and the elevation of the centre of the FoV h_f for H = 100 km and for elevations between 15 and 90 degrees. This expands the table from Bellot Rubio (1994b) to values for the centre of the field of view below 45 degrees of elevation (table 3.2). Note that the values are different from the ones of the Table 4 of Bellot Rubio (1994b) because he uses a simple approximation for airmass and extinction calculation. We are able to reproduce his results using a larger extinction coefficient ($k_V \sim 0.25$).

Table 3.2 shows that the loss of magnitude is compensated by the increment of the geometric area monitored when pointing at low elevations only if the population index r is small enough ($r < 2.5$). It is evident that when the meteor shower is composed mainly by dim meteors, the magnitude loss associated is going to overcome the gain of the area surveyed (see figure 3.8).

In order to study the behaviour of A_{red} at low elevations, we change the standard film camera for a smaller camera with a field of view of 1 degree by 1 degree (see figure 3.9). For all the usual values of the population index there is a turning point where the extinction loss overpowers the increment of the geometric area observed.

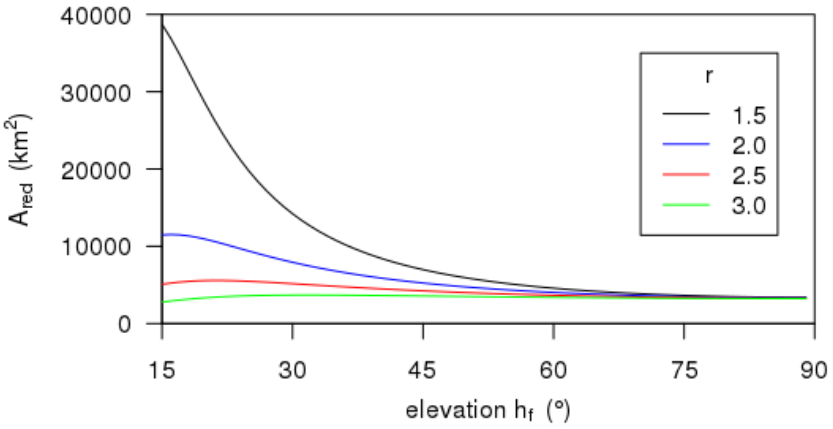

Figure 3.8: Effective area A_{red} of a standard film camera as a function of the elevation of field of view h_f for different values of the population index r.

As meteors appear distributed across the sky, the aim of the observer in order to maximise the number of meteors detected is to increase the effective area monitored. To analyse the equation 3.18 we expand vZHR and A_{red} and express the density flux Q as a function of all the variables:

$$Q(N, T, \gamma, h_R, vlm, A_i, d_i, \varepsilon_i) = \frac{\frac{N+1}{T} \sin^{-\gamma} h_R \cdot r^{6.5-vlm}}{\sum_i A_i \cdot r^{5 \log \frac{H}{d_i} - \varepsilon_i}} \tag{3.21}$$

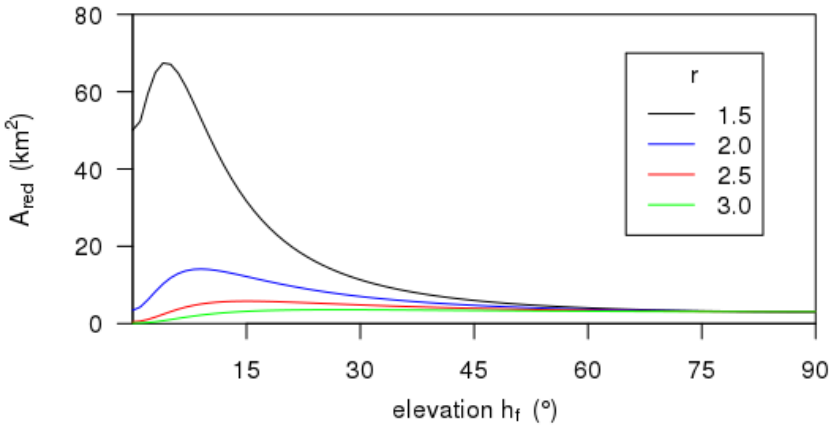

Figure 3.9: Effective area A_{red} of a standard $1^\circ \times 1^\circ$ camera as a function of the elevation of field of view h_f for different values of the population index r.

r	h_f														
	15	20	25	30	35	40	45	50	55	60	65	70	75	80	90
1.5	38726.7	28400.2	19718.9	14209.9	10754.6	8503.8	6977.2	5906.3	5136.1	4573.1	4158.9	3856.1	3640.3	3495.6	3384.4
1.6	28927.6	22714.7	16609.2	12430.1	9680.5	7827.8	6538.7	5616.3	4942.3	4443.3	4072.5	3799.1	3603.1	3471.0	3369.0
1.7	22221.8	18501.2	14172.0	10978.5	8778.1	7246.6	6154.8	5358.6	4768.0	4325.4	3993.3	3746.6	3568.7	3448.2	3354.7
1.8	17482.4	15310.0	12229.9	9778.9	8011.6	6742.2	5815.9	5127.9	4610.2	4217.7	3920.5	3698.0	3536.6	3426.9	3341.2
1.9	14037.8	12846.5	10659.8	8775.6	7354.0	6300.8	5514.5	4920.1	4466.5	4118.8	3853.1	3652.8	3506.7	3406.9	3328.6
2.0	11472.4	10912.2	9373.7	7927.7	6784.8	5911.6	5244.7	4731.8	4335.0	4027.5	3790.5	3610.6	3478.6	3388.1	3316.6
2.1	9520.4	9370.3	8308.1	7204.5	6288.4	5566.1	5001.8	4560.3	4214.2	3943.0	3732.1	3571.0	3452.2	3370.3	3305.3
2.2	8006.8	8124.4	7415.8	6582.2	5852.3	5257.5	4782.0	4403.5	4102.6	3864.4	3677.5	3533.8	3427.2	3353.5	3294.6
2.3	6813.4	7105.3	6661.6	6042.8	5466.7	4980.4	4582.1	4259.3	3999.2	3791.0	3626.3	3498.8	3403.7	3337.6	3284.4
2.4	5858.2	6262.6	6018.6	5571.9	5123.9	4730.3	4399.5	4126.3	3903.0	3722.3	3578.1	3465.7	3381.3	3322.4	3274.7
2.5	5083.6	5558.7	5466.2	5158.2	4817.3	4503.6	4232.1	4003.3	3813.4	3657.9	3532.7	3434.3	3360.1	3308.0	3265.4
2.6	4447.8	4965.3	4988.2	4792.6	4541.9	4297.1	4078.0	3889.0	3729.5	3597.2	3489.7	3404.5	3339.8	3294.2	3256.5
2.7	3920.3	4461.0	4571.9	4467.8	4293.3	4108.5	3935.7	3782.6	3650.8	3540.0	3448.9	3376.1	3320.5	3281.0	3248.0
2.8	3478.3	4029.1	4207.1	4177.8	4068.0	3935.4	3803.9	3683.2	3576.9	3485.9	3410.2	3349.1	3302.0	3268.4	3239.8
2.9	3104.9	3656.6	3885.7	3917.8	3863.1	3776.1	3681.4	3590.1	3507.2	3434.7	3373.4	3323.3	3284.4	3256.3	3232.0
3.0	2786.7	3333.2	3601.1	3683.6	3676.0	3629.1	3567.3	3502.8	3441.4	3386.1	3338.3	3298.7	3267.4	3244.7	3224.4
3.1	2513.5	3050.8	3347.8	3471.8	3504.6	3493.0	3460.8	3420.6	3379.1	3339.8	3304.8	3275.0	3251.1	3233.5	3217.1
3.2	2277.6	2802.8	3121.4	3279.6	3347.2	3366.6	3361.1	3343.2	3320.1	3295.8	3272.8	3252.4	3235.5	3222.7	3210.1
3.3	2072.4	2583.9	2918.1	3104.6	3202.0	3249.0	3267.6	3270.1	3264.0	3253.8	3242.1	3230.6	3220.4	3212.3	3203.3
3.4	1893.0	2389.8	2735.1	2944.7	3068.0	3139.4	3179.6	3200.9	3210.7	3213.7	3212.7	3209.7	3205.9	3202.2	3196.7

Table 3.2: Reduced areas A_{red} as a function of r and the elevation of the centre of the FoV h_f for H = 100 km. The FoV is the one of a 'standard' camera, 39.6° of width and 27.0° of height. Therefore it is an update version of the Table 4 of Bellot Rubio (1994b).

Some of the parameters are characteristic on the meteor stream or the meteor physics (N,T, r, γ, H) but others are relative to the observing place (h_R, d_i) or the observatory conditions and instrument (ε_i, A_i). We can investigate what are the best settings to maximise the flux detection.

– $\mathbf{h_R}$ – the elevation of the radiant
It is dependent on the geographical position. The best possible option would be observing from the sub-radiant point (the radiant point projected in the Earth's surface). Nevertheless this point moves up to 1600 km/h and its tracking would be only possible on-board of a supersonic plane.

– $\mathbf{vlm}$ – the limiting magnitude
It is directly related to the instrumental capability to collect photons and to deal with noise and background sources. However fast-moving objects (average speed of degrees per second) spread their signal over several detection elements. The video limiting magnitude is therefore the magnitude of the dimmest meteor recorded by the system and it suffers from a magnitude loss regarding the star limiting magnitude, as they are static objects. This is critical in order to select the pixel size of the system. This magnitude loss depends on the meteoroid stream speed V_∞, the geometric conditions of the encounter and the pixel size (Gural, 2002):

$$\Delta m = 2.5 \log \frac{\omega}{\omega_0} \tag{3.22}$$

where ω is the angular speed of the meteors of the stream in a location of the sky at a distance from the radiant $D_{radiant}$:

$$\omega = V_\infty \frac{\sin D_{radiant}}{d_i} \tag{3.23}$$

and ω_0 is the maximum angular speed for an object to stay in the same resolution element during the exposure time:

$$\omega_0 = \frac{\text{resolution element (radians)}}{\text{integration time(s)}} \tag{3.24}$$

The resolution element is the pixel size in systems that undersample the images and the FWHM of the PSF in systems where that value is larger than the pixel size.

– $\mathbf{A_i}$ – the geometrical area
The area covered by each element of the field of view of the instrument depends essentially by the angle of elevation. It is obvious that the farther from the zenith, the largest is the area surveyed.

– $\mathbf{d_i}$ – the distance to the meteor
The distance to the meteor depends basically on the height of the observer and the elevation over the horizon of the field of view. For low pointings the elevation h_f is the main source of magnitude loss (figure 3.6), as the height $h_b << d$ (e.g., h_b is between 20 to 30 km for a balloon-borne mission, while the distance at $h_f = 0$ is $\approx 1000km$).

– $\varepsilon_\mathbf{i}$ – the extinction
The extinction produces a loss of magnitude that is significant for observations at lower elevations. For the usual values of r, there is an elevation when extinction overcomes the effect of monitoring larger area. In the case of balloonborne observations, the extinction is considered negligible (figure 3.5) and the lack of extinction at 20 km implies that the increase of geometric area is translated into a gain of effective area A_{red} (figure 3.10). That is true only for values $r < 2.5$, over that value of population index the magnitude loss due to the distance is larger than the increase of geometric area (figure 3.11).

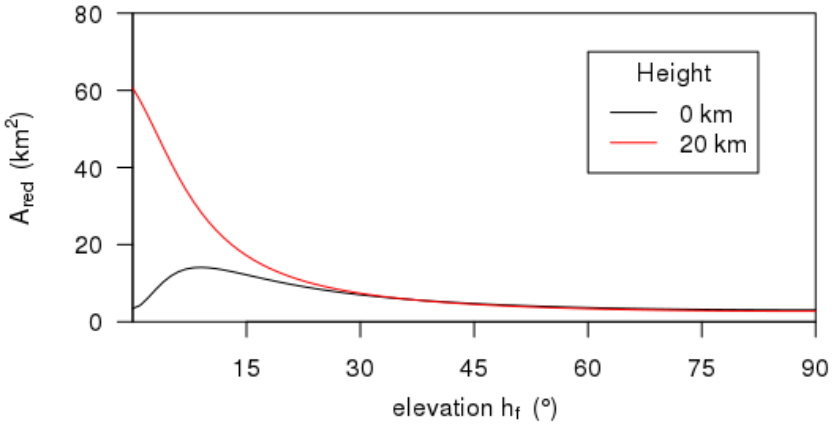

Figure 3.10: Effective area A_{red} of the 1 deg^2 camera as a function of the elevation of field of view h_f for two different observing heights h_b, with $r = 2$. The lack of extinction at 20 km implies that the increase of geometric area is translated into a gain of effective area A_{red}.

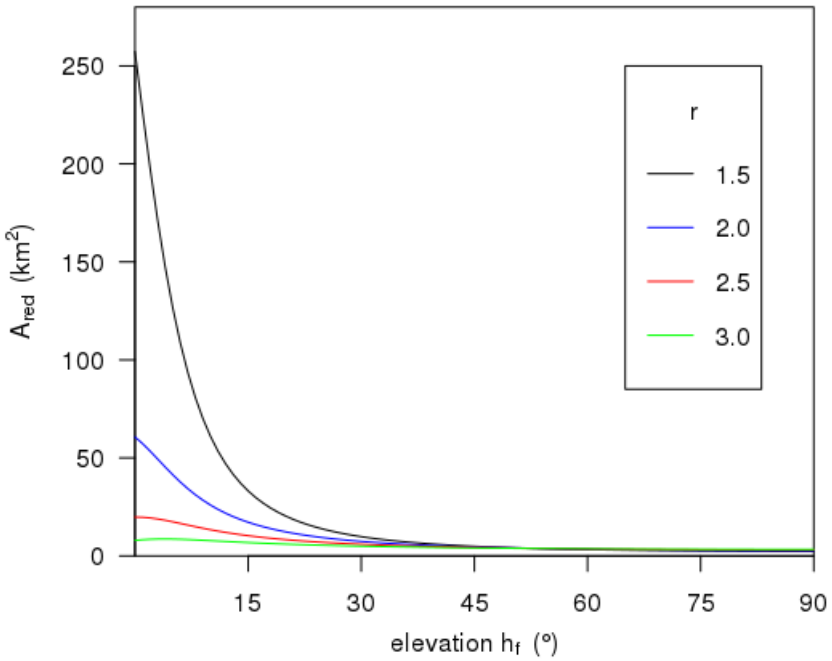

Figure 3.11: Effective area A_{red} of the 1 deg^2 camera as a function of the elevation of field of view h_f for different values of population index r, for an observer with h_b =20 km. Only for values larger than 2.5 the magnitude loss due to the distance is larger than the increase of geometric area.

Therefore we can improve the determination of meteoroid flux, increasing the number of meteors detected N or the effective area surveyed A_{red}:

- Maximising the coverage of area surveyed using large field of view optical designs. E.g., wide-field low-light sensitivity videocameras.
- Maximising the effective area A_{red} avoiding the extinction of the lower layers of the atmosphere. E.g., balloonborne wide-field camera. Pointing to the horizon increases the detection efficiency as the apparent meteor angular speed ω decreases towards the horizon.
- Increasing the limiting magnitude of the meteors detected vlm with an instrument of large aperture and moderate field of view. E.g., wide-field telescope. Moreover the long focal length prevents too much sky background addition per pixel, increasing the detection efficiency.

3.2.5 Error budget analysis for flux determination

The number N of meteors is one of the major sources of error when N is low (from Poisson statistics the error is $\sqrt{N}$). N depends always on the time step used, but the goal should be to reach a good time resolution during major showers similar to that previously obtained in Leonid meteor storms by separated teams. Unless otherwise noticed, the error calculation applied for the fluxes in the next section is based only in the poissonian nature of the distribution of the meteors. A complete review of the uncertainties of all these parameters can be found in Blaauw et al. (2016). We don't include these uncertainties as they are mainly systematic or come from parameters which values are not derived from the data of this research work. The errors does not come from the method itself, but from our knowledge of meteoric science and the use of light proxies to infer the actual meteoroid properties.

On the other hand some assumptions are done only for the general development of the method. Bellot Rubio (1994b); Blaauw et al. (2016) find that assuming H =100 km introduces in general less than 10% of error, but could be up to 40% in extreme cases like May Camelopardalids. The meteor layer height H depends on several parameters and is therefore different for each shower, so we use the actual value from literature when available.

Some other parameters need further research. For review and open topics see Gural (2002). One of the most relevant parameters is the gamma exponent in the radiant elevation correction, which can lead to a systematic uncertainty of more than 40% under unfavourable conditions of radiant height and observers possible location. There has been some theoretical investigations about the topic, with meteoroid models that are useful to understand the physics under the gamma exponent (Bellot Rubio, 1994a). In any case observations with radiant close the zenith are strongly encouraged.

Another large component of the error is that derived from the limiting magnitude correction. Scaling fluxes to +6.5 is done for ease of comparison. The general suggestions for the observers in order to minimize the uncertainties is, obviously, to observe in the best possible conditions, with the FoV as much homogeneous as possible with regard to limiting magnitude, meteor angular speed, etc.

3.3 Characterisation of meteors: meteor spectroscopy

3.3.1 Theory of emission for meteors

When an approaching meteoroid gets closer than 300 km to the Earth's surface it starts heating. It eventually reaches 900 K and spallation starts. The material then sublimates when it reaches 2200 K and heating stops because most of the kinetic energy is consumed by the ablation. The evaporated gas is mainly composed by excited metallic atoms, which emit light when de-excited.

According to the theory of emission for meteors, their spectra show strong emission lines, some molecular bands and weak blackbody continuum. They are emitted by an optically thick plasma that is out of equilibrium, but the theory is developed under the assumption of chemical and thermal equilibria in the whole radiating volume. Using these simplifications, the radiative transport equation is solved and a comprehensive model is built (Borovička, 1994; Jenniskens, 2007).

Under those assumptions we can use a a Boltzmann distribution for the level populations of those atoms. The concentration of atoms with level i populated, n_i , is :

$$n_i = \frac{n}{U(T)} g_i e^{\frac{E_i}{KT}} \tag{3.25}$$

where n is the concentration of all the atoms for a given element, U is the partition function, g_i is the statistical weight of the level, E_i is the energy level, T is the temperature and k is the Boltzmann constant.

With this Boltzmann distribution, the source function becomes the Planck function $B_\nu(T)$ and the equation of radiative transfer can be integrated under the assumption of constant temperature in the whole volume of the meteor, getting the following solution for the intensity at frequency ν:

$$I_\nu = B_\nu(T)(1 - e^{-\tau_\nu}) \tag{3.26}$$

where τ_ν is the optical depth. This depth is function of the column density of the element N (cm^{-2}) and the damping constant Γ:

$$\tau_\nu = N\sigma H(\Gamma) \tag{3.27}$$

where H is the Voigt function, and σ is a compilation of atomic data for the element:

$$\sigma = \frac{\pi^{1/2} e^2}{m\, e\, U} \left(\frac{m_a}{2KT}\right)^{1/2} \lambda\, g_1\, f\, e^{\frac{E_i}{KT}} \left(1 - e^{\frac{-h\nu}{KT}}\right) \tag{3.28}$$

Combining the dependencies from equations 3.26, 3.27 and 3.28 we can say that the intensity I_ν is only function of T, N and Γ. We can use several lines to find the value of the 3 unknowns.

Note that the natural width of these emission lines is too small to be resolved by the spectrographs used for meteor spectroscopy (usually $\frac{\lambda}{\Delta\lambda} \equiv R < 2000$), therefore the spectra are fitted with an instrumental gaussian profile (with width Δ, peak intensity $\Im_0$) and there is no line-shape physical information extracted, but just the intensity Im_λ integrated along the whole line $d\lambda$ (Borovička, 1994):

$$\Im = \int Im_\lambda \, d\lambda = \pi^{1/2} \Delta \Im_0 \tag{3.29}$$

The analysis of meteor spectra with these models (Borovička, 1994; Jenniskens, 2007) leads to the finding of two components in the plasma, the main one at $T = (4300 \pm 300)$ K and a hot one strongly dependent on the meteor speed, from $T = (10000 \pm 1000)$ K for the slow ones (20 km/s) up to $T = (14500 \pm 1000)$ K for the fastest ones (70 km/s). Both components represent two different positions around the meteoroid, and apparently they are separated, with no intermediate temperature zones (Jenniskens, 2007).

This procedure was developed in the 1990's, however in the literature we can find no more than some tens or hundreds of spectra, while published meteoroid orbits are in the range of thousands. The reason for this is the difficulty to analyse the spectra and automatise the process described before. As meteors appear in random time and location, even spectra extraction is manual. And reduction is done in case-by-case basis (figure 3.12). This is the starting point for our proposal of narrowband photometric system to extract this line information in a sort of low- resolution spectroscopy covering the most interesting lines.

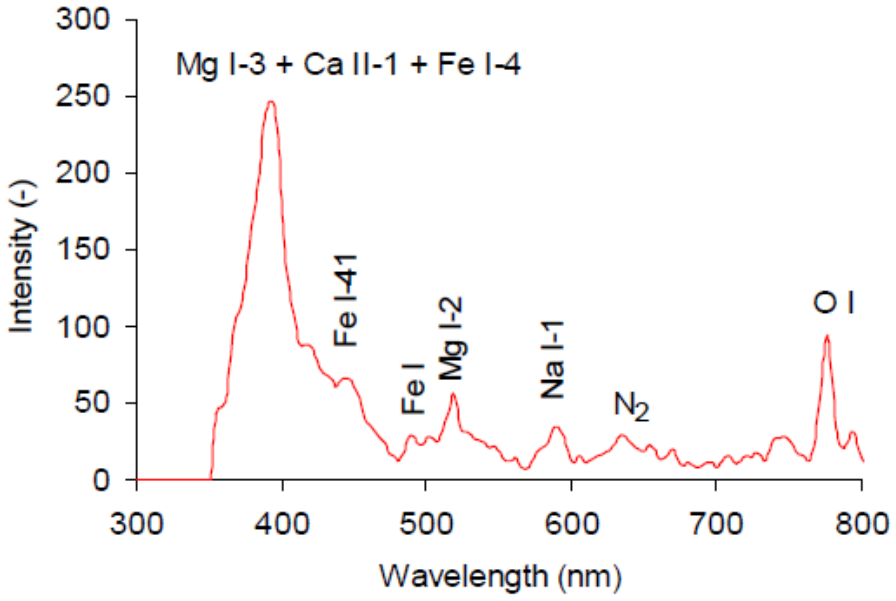

Figure 3.12: Calibrated emission of the -7 ± 1 Perseid bolide recorded by one of the nodes of SPMN on August 7 2012 at 02:44:04.3 UT (SPMN code 070812). Figure from Ocaña et al. (2013). One of the UCM cameras also has a diffraction grating to record the spectra of meteors. As mentioned in the text the analysis is complex and is done in the frame of the SPMN by J.M. Madiedo (Madiedo, 2014).

3.3.2 Narrowband-photometry filters set for meteor properties determination

Narrow-band filters have been used in astrophysics to characterise different kinds of objects according to composition, temperature and other physical properties. Several authors have studied the radiative emission of meteors to understand and measure the observed spectra. The narrow-band photometry measures total intensity $\Im$ for the line or multiplet. When the continuum is considered non-negligible, we can use other narrow-band filters to estimate the blackbody emission in parts of the spectrum where line contribution is small.

In meteor physics some research groups have already performed narrow-band observations. Taylor et al. (2000) used a 10-nm filter centred at 518 nm for high resolution imaging of different features. On the other hand, simultaneous multiband observations have been done with the `ALIS` system (Brändström et al., 2001), which was designed for wide-field imaging of auroral emission. Two other filters were added for meteor observation: Na I at 589 nm and Fe I + Mg I at 423 nm. The equipment was not optimised for meteors, but Pellinen-Wannberg et al. (2004) detected H_2O^+ and $H_{\alpha,\beta,\gamma}$ emissions .

The author proposed a multiband photometric system optimised for meteor physics for his final year research project (Ocaña, 2011). It was a proof of concept, with a theoretical development and a pipeline simulation: background + sky + object (using a fireball spectrum from the literature), with different filter bandwidths and running central wavelength. The main goal of that project was to increase the detection level at the Observatorio UCM, where they were running a Fireball Detection Station (Ocaña et al., 2011).

The concept is being tested with some experimental set-ups. In 2011 we installed at Observatorio UCM a videorecording system with commercial narrow-band interferometric 10-nm filters and Watec 902 H2 Ultimate cameras. Preliminary results for a very limited amount of examples were analysed in Ocaña et al. (2012). In 2015 a narrow-band system was designed and built for the American Meteor Society by Gural (2015). It partially matches our system as the design follows similar trade-offs, what reinforces the narrow-band photometry concept we analyse in this work. Similarly, in the Meteoroids 2016 conference, K. Bloxam and M.D. Campbell-Brown presented the results for a multi-camera system with bands that are also partially coincident to the system we proposed.

Colour indexes have been used to characterise meteors since 1950s as addressed by Davis (1963) (and references therein), using instrument response as the definition of the band. Nevertheless, to our knowledge, the system introduced in this paper is the first one based on narrow-band filters. The design of the system is science-driven, founded on the premise of maximising the scientific output, in a sort of low-resolution spectroscopy with filters covering bands of interest.

The bands are selected to cover relevant emission lines, molecular bands and continuum, considering the continuum background where the emission lines are weaker in the spectrum. The lines to be observed are from both hot and main components in the optical range, between the Ca II lines and 800 nm. The target chemical species are Ca, Cr, Fe, Mg, Mn, N, Na and Si, but the system is focused and referred to the determination of the iron abundance N_{Fe}. When possible the elements should be observed in different excitation states.

In order to make the system realistic in the sense of an affordable observational setup, the design considers the system to be modular, and the scientific case defines the number of bands needed. For most of the results in this work, we use 4 filters. According to these criteria, the bands (see figure 3.13 and table 3.3) were selected using the lines listed in Borovička (1994); Jenniskens (2007).

As a feasibility study we have not focused on the availability of commercial components for the development of an instrumental solution, although we did not have much difficulties to find them for our observational setup (Ocaña et al., 2012). The bandwidth and central wavelength were selected after a trade-off considering light pollution lines, airglow lines and the inclusion/exclusion of the lines and multiplets that were from the same and different species (Ocaña, 2011).

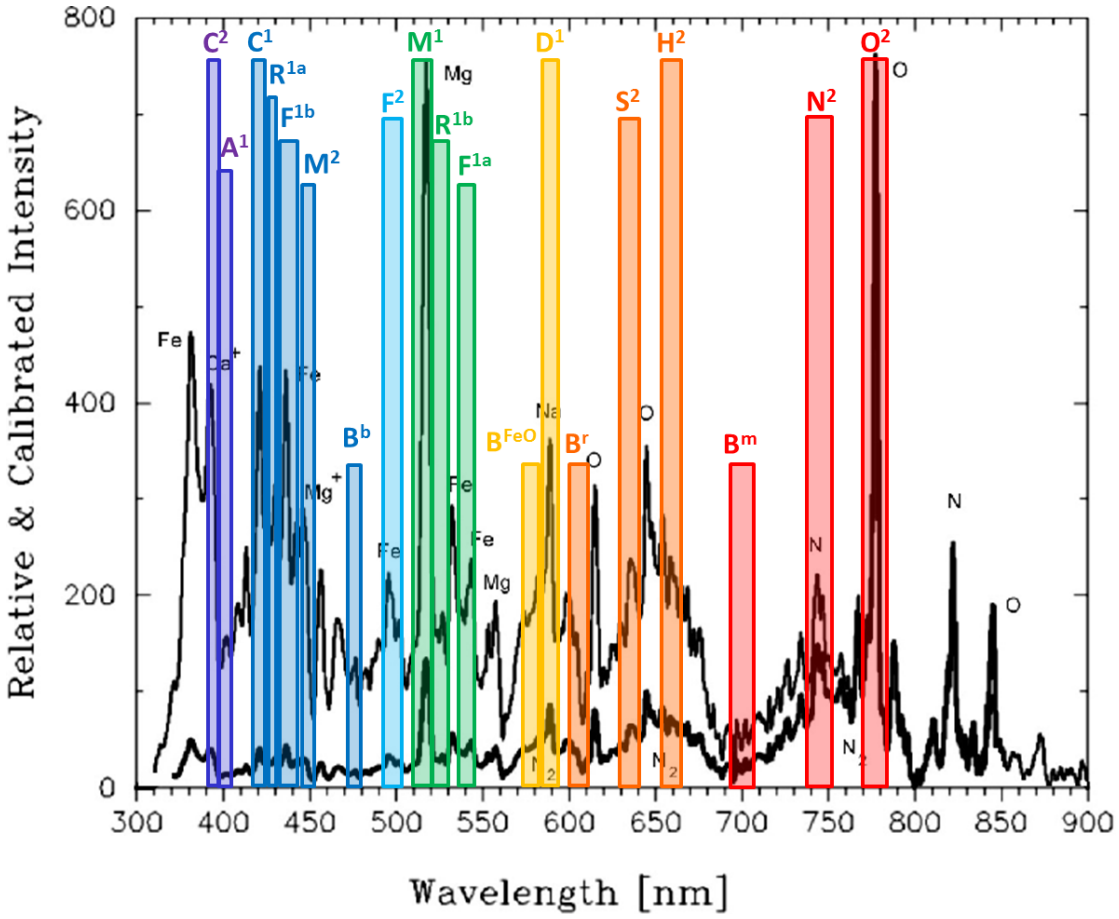

Figure 3.13: Proposed photometric system based on narrow-band filters, represented over a sample of fireball spectrum from Abe et al. (2000), where the thin line (top) is the calibrated flux and thick line (bottom) is the detected flux. Note that line width is the instrumental one, and natural line width is at least 10 times less. Figure after Ocaña (2011).

The resulting system (table 3.3) consists of 20 bands, rectangular with transmission $\tau = 1$, between 7 to 15 nm of width, equivalent to a resolution of $R \sim 50$. They cover approximately 150 nm of the 380-800 nm range. Bands are named after the initial of the element/line and the component as superindex (1 for hot, 2 for main component), adding a letter when needed to avoid repetition.

The filters covering the molecular bands and continuum are named with a B and superindexes referring to the part of the spectrum, as they are designed to estimate the 'background'. We can use them to fit a power-law continuum, usually a blackbody one, though we can simplify it to a polynomial (Pascual et al., 2007). In this work we use a simpler approximation and consider it constant for a small part of spectrum (no more than 100 nm). The use of this kind of background level estimation works in the calculation in the O/Mg line intensity ratio with O^2 and M^2 colours, where M^2 is corrected with the closest B band. However it is not needed for other lines/bands that are closer in the spectrum, and therefore have the similar blackbody contribution.

Band	Band characteristics			
	λ_{centre} (nm)	Width (nm)	Hot component	Main component
C^2	395.0	7	CaII(1)	CaII(1)
A^1	403.0	8	MnI(2)+FeI(43)	
C^1	420.5	8	CaI(2)+FeI(sev)	
R^{1a}	427.0	5	CrI(1)+FeI(152)	
F^{1b}	437.0	11	FeI(2)+FeI(41)	
M^2	448.0	8		MgII(4)
F^2	497.0	12	FeI(318)+FeII(42)	
M^1	515.0	9	MgI(2)+FeI(37) +CrI(7)	
R^{1b}	524.5	10	CrI(18)+FeI(sev)	
F^{1a}	541.5	10	FeI(15)	
D^1	589.5	10	NaI(1)	
S^2	636.0	12		SiII(2)
H^2	657.0	12		HI(1)
N^2	744.0	16		NI(3)
O^2	777.0	15		OI(1)
B^b	475.0	8	'**B**lack body' **b**lue part	
B^{FeO}	580.0	10	max. bands FeO	
B^r	605.0	12	bands N_2^+, FeO	
B^m	700.0	15	**m**ax '**B**lack body'	

Table 3.3: Bands of the photometric system proposed. Bands are defined as rectangles centred at λ_{centre}.The last two columns include the lines, multiplets and molecular bands most relevant within the band from the hot component and main components. Multiplet numbers refer to the system from Moore (1945). Table adapted from Ocaña (2011).

In the case when the filter covers several lines of different elements (e.g., A^1 or M^1), we can use information from other filters and assume ratios between lines to separate the contribution from different elements (Pascual et al., 2007). This will not always be possible, but the use of different colour-colour diagrams combined to known properties extracted from spectroscopy could overcome this problem.

Therefore this technique has limitations for quantitative analysis, but is very convenient for statistical purposes. Meteoroid populations with a wide variety of Fe and Na compositions, even for the same stream, were found employing statistical analysis (Borovička et al., 2005). Moreover extending the meteoroid properties research to fainter ranges could lead to the discovery of populations with different properties and these groups could be more abundant than previously thought (Campbell-Brown, 2015). The application to fainter targets could improve the research on meteor ablation in fainter stages or for dimmer meteors, specially in the differential ablation process (Abe et al., 2000), as current spectrographic instruments do not have access to these dim meteors.

3.3.2.1 Advantages of narrow-band photometry

Narrow-band photometry has some clear advantages regarding traditional slitless spectroscopy used for meteors. It does not require the use of an order blocking filter and the sky background is reduced with decreased light pollution or atmospheric lines contributions.

Moreover slitless meteor spectroscopy still suffers from large inconveniences, like the loss of photons in the orders not observed or the differential focus along the spectrum. Besides the transmission of the prism/grating varies widely along the observed range or with the angle of incidence of light.

Along the whole meteor track the narrow-band photometric system can monitor differential extinction due to the atmosphere. That is a correction term usually neglected or simplified, however it is important for meteors as they change their zenithal angle really fast. For instance, in normal conditions (extinction coefficients $k_B = 0.4$ and $k_V = 0.2$) moving from 30° to 60° of zenithal angle yields a differential absorption between the blue and red ends of more than 30% (e.g., in that 30-degree travel in the B band the absorption increases for 37% when in R band it is only an 8%).

The design of the observational setup could be focused also on an optimisation of the detection. The detector characteristics (sensor technology, gain, dynamic range) can be selected for each band, and the background is therefore reduced. The overall result would be a significant increase of the dynamic range.

Besides, the processing part is easier, as photometric pipelines are already widely used and automated for meteors (Weryk et al., 2008; Madiedo and Trigo-Rodríguez, 2008). Image calibration is easier too, as there is no need to use lamps, but tens of stars can be used as calibration standards for each image.

3.3.2.2 Synthetic photometry

We have used a synthetic photometry tool from the Spanish Virtual Observatory (SVO). The tool is described in Bayo et al. (2008) and can be reached at http://svo2.cab.inta-csic.es/theory/myspec/. This technique is applied in many fields to make absolute calibration of a spectrum, comparing absolute photometry with convolved spectra (see a full description of the synthetic photometry method in Straizys (1996)). In our case we make use of the tool as part of the research to show the feasibility of the narrow-band photometric system proposed. We convolve observed meteor spectra in the bandpasses described in table 3.3 (figure 3.14). Using Vega spectrum Rieke et al. (2008) we calculate the zero-points of the proposed narrow-band filter system. The input for the SVO tool is a column ASCII file: first wavelength in Ångströms and intensity (a.u.).

For this work we have used the filters described in the previous section and the spectra catalogue from Vojáček et al. (2015) as the input data for the synthetic photometry. The 'Catalogue of representative metor spectra' (Vojáček et al., 2014) was downloaded from the VizieR database of astronomical catalogues (Ochsenbein et al., 2000). It comprises the spectra of 84 meteors (54 sporadics and 30 shower members) covering the range 370 nm-880 nm with a dispersion $\sigma \sim$ 1.5-3.0 nm taken with video techniques. Apart from the reduced and calibrated spectra, the catalogue includes total intensities of multiplets Mg I-2, Na I-1, and Fe I-15, that are obtained by fitting the lines to different components.

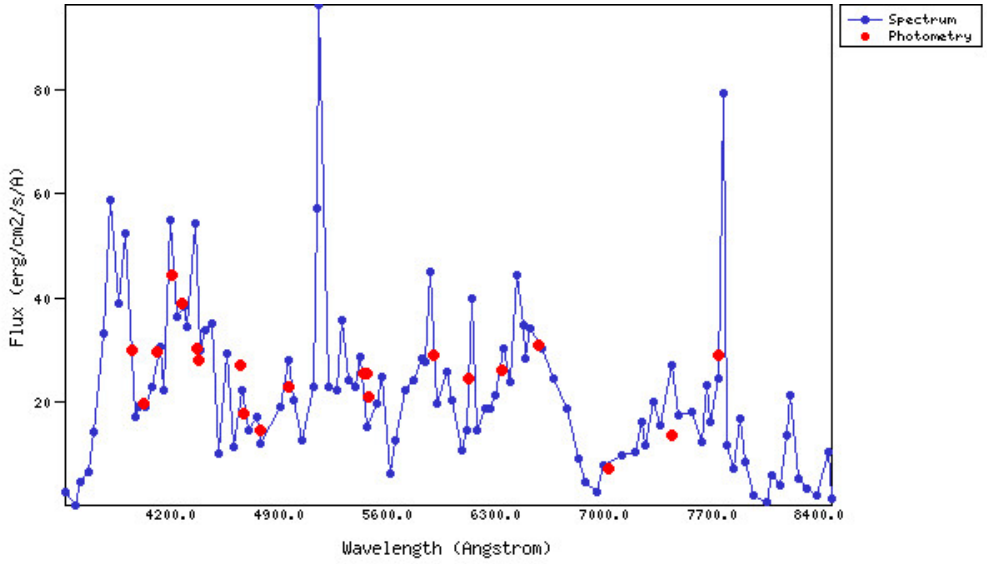

Figure 3.14: Fireball spectrum (blue) with photometric points obtained after convolution with the photometric system proposed in this work (red). It shows how these points contain much of the information of the spectrum. We consider narrow-band photometry equivalent to low-resolution spectroscopy, in this case with $R \sim 50$.

We have used their tabulated data to compare with the intensities measured with our synthetic photometry over bands covering the same multiplets. Some of the spectra are incomplete and consequently the fluxes of all the bands could not be calculated.

3.3.2.3 Results

The narrow-band photometric system is designed to derive meteoroids properties from photometry, and we have used synthetic photometry over a spectra catalogue to measure some basic properties as a showcase. Moreover we have worked on other colour-related issues in the meteoric science, like the limiting magnitude determination or the speed-colour bias in detection.

In the next three subsections we try to reproduce some of the results of spectral classification based on Borovička et al. (2005) and performed in Vojáček et al. (2015). We use colour diagrams with bands centred on the relevant multiplets. For the Na/Mg ratio we show that some colours need a background correction, but they are still a good approximation. For the O/Mg ratio we show the use of this background correction (combination of blackbody emission and nitrogen bands).

We conclude with results of BVR photometry and show how the difference between the meteor colours and the stars used as references affect the estimation of the limiting magnitude and consequently the flux determination.

– Spectral classification based on Na-Mg-Fe lines

  Optical meteor spectra show emission lines coming at least from these 4 elements: Fe, Mg, Ca and Na. Although they are not the main components of the meteoroids, they can be used to classify them (Borovička et al., 2005). We use filters F^{1a}, M^1 and D^1 to cover multiplets Fe I(15), Mg I(2) and Na I(1) respectively. However the colour ternary diagram does not classify the meteors as expected (figure 3.15). Note that the failure on the classification

on the meteoroids using this ternary diagram is not due to a limitation of the narrow-band system itself, but the application of the synthetic photometry on spectra that have not enough resolution. In this case the lines are blended, and/or part of the flux is taken out of the filter. The filter M^1 is 9-nm wide and centred in 515 nm, when the Mg I(2) multiplet is in 518.2 nm. With higher resolution spectra, we could reproduce the colour diagram $F^{1a} - M^1 - D^1$ and make a similar classification. The contribution of Fe I(37) in the band M^1 may force the use of a correction or change it for the band M^2.

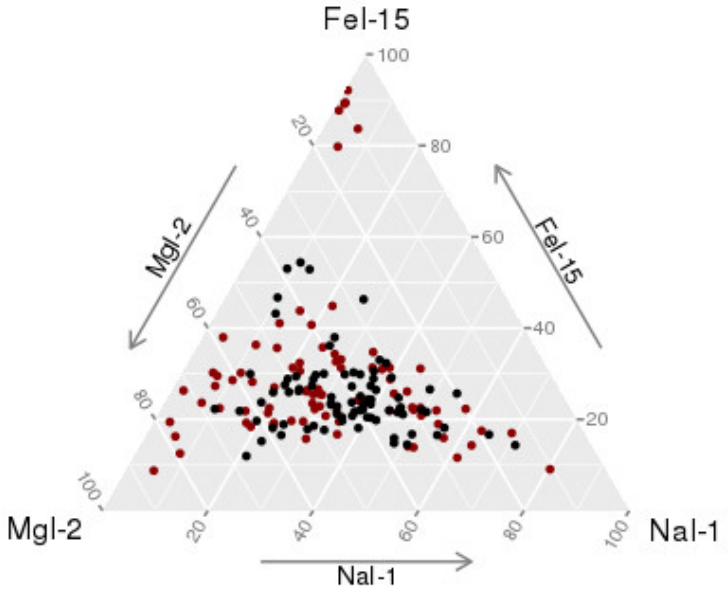

Figure 3.15: Ternary diagram showing in red dots the line intensities from Fe I(15), Mg I(2) and Na I(1) as tabulated in Vojáček et al. (2015) and in black dots the $F^{1a} - M^1 - D^1$ colours. These colours do not reproduce well this spectral classification, mainly because the spectral input data does not have enough resolution and some lines are blended with iron ones in the band F^{1a}.

– Na/Mg lines intensity ratio

The ratio of Na/Mg lines intensity is used by the spectral classification from Borovička et al. (2005) to discriminate between Na-poor and Na-free meteoroids. We use filters F^{1a} and D^1 to cover multiplets Fe I(15) and Na I(1) respectively.

In the colour diagram (figure 3.16) with F^{1a} and D^1 bands we also found that the Na/Mg ratio increases for speeds below 35 km/s. For higher speeds the ratio is velocity independent. However the Na-free meteors ($log\frac{Na}{Mg} < -1$) are not found. It is due to the continuum being non-negligible and comparable in flux to the Na line in the band D^1 for these sodium poor meteoroids. This a good example of the need of background subtraction and for this diagram it has not been possible. For the O/Mg ratio we show how the use of background corrects it.

– O/Mg lines intensity ratio

The ratio of the O/Mg lines intensity increases with meteor speed, as fast meteors are dominated by light coming from atmospheric lines. We use filters O^2 and M^1 to cover multiplets O I(1) and Mg II(4) respectively. In this case we need to apply a background correction, so we call Mg* the magnesium line intensity already corrected. This colour index reproduces

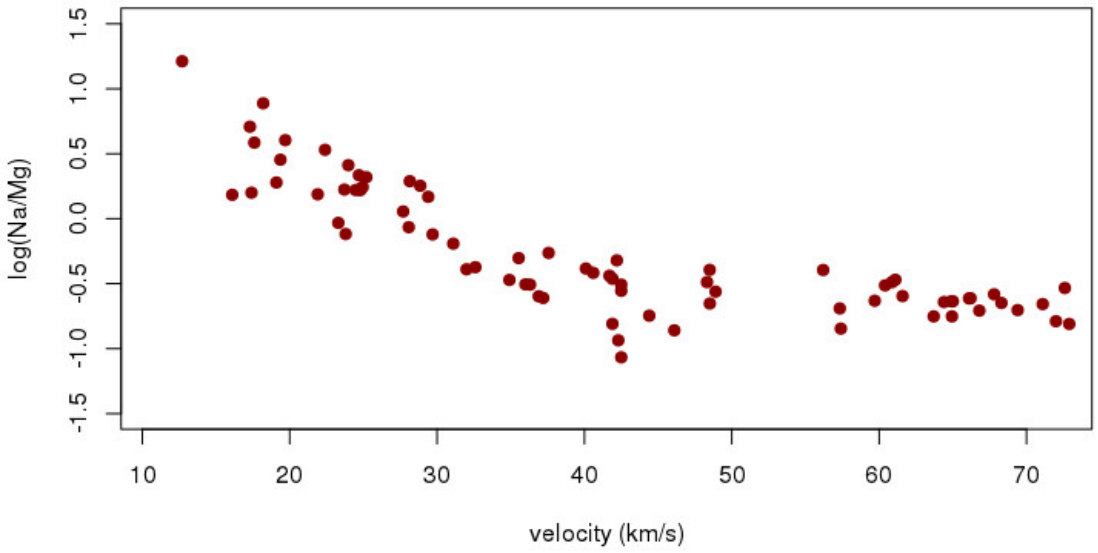

Figure 3.16: Intensity ratio of the Na/Mg lines, calculated as the ratio of bands D^1/M^1.

well the O/Mg ratio distribution from Vojáček et al. (2015), although Mg flux is still overestimated in 0.5 dex(figure 3.17). Apart from the continuum there may be another line that contributes to the flux in the band M^1 .

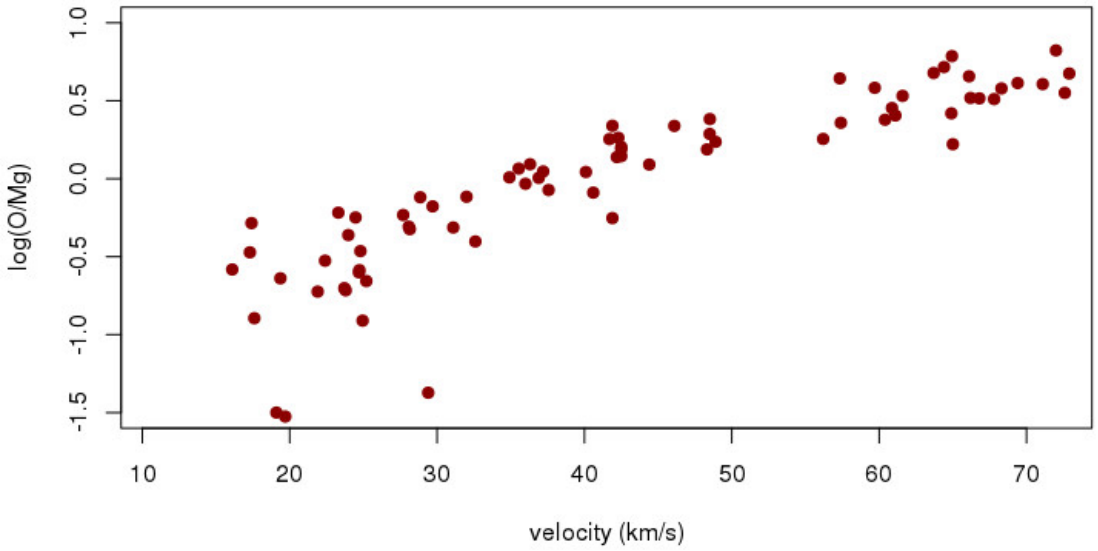

Figure 3.17: Intensity ratio of the O/Mg* lines, calculated as the ratio of colours from bands O^1 and the band M^1 corrected with the background.

– BVR photometry

Johnson-Cousins UBVRI photometric system was designed as a wide band photometric system for classifying stars but it is still a popular standard, and many fields in astrophysics still use these bands as references. Moreover many research works provide transformation equations to it from other systems, like Gunn-Thuann `uvgriz` or Sloan `u′g′r′i′z′`.

We have calculated V band and R band photometry for the whole dataset. Unfortunately B band photometry was not possible due to the high uncertainty of the meteor spectra in this region. Preliminary results using the same technique with fireballs spectra from other sources show that average values are around B-V=0.8 for slow ones, and goes bluer down to B-V=0.0 for faster ones, mainly due to Ca II lines from the hot spectral component.

V band is dominated by Fe I and Mg I lines, while R band includes N_2 bands and a stronger continuum. Both bands include with similar weight the D line of Na I. We find that V-R magnitude is dependent on the velocity for meteors faster than 35 km/s (figure 3.18), reproducing the behaviour of the Na/Mg ratio. The outliers ($V - R < -1$) are slow iron meteoroids and some Na-free or Na-poor meteoroids, which due to their lack of Na and atmospheric lines experience low brightness in R band. The V-R colour dependence on speed and composition implies a significant bias in detection for the broadband instruments.

Similar results were obtained by Weryk et al. (2008) comparing very-broad-band photometric observations comparing panchromatic film band and the one resulting from HAD CCD, were fast meteors appear dimmer in the chips compared to the film.

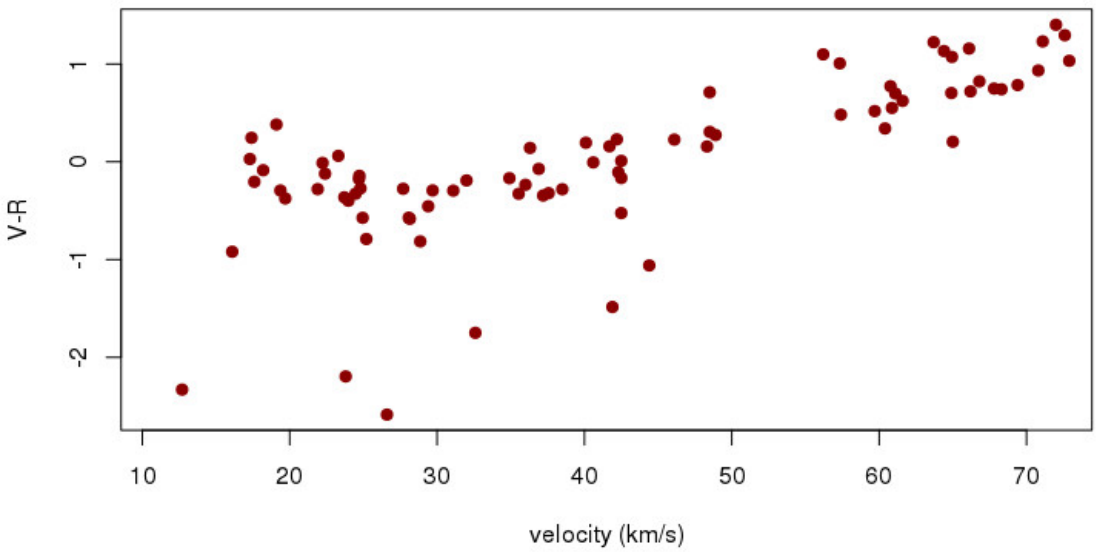

Figure 3.18: V-R colour index is dependent on the speed for meteors faster than 35 km/s.

From these results we conclude that the use of wide band unfiltered systems, such us low-light videocameras (e.g., Watec) or intensifiers, leads to a big colour detection bias depending on the meteor speed. Fast meteors include hot component and atmospheric lines that increase brightness mainly in B and R bands. This leads to a double bias because on the one hand stars are mainly red (average ∼B-V=1.0 and ∼V-R=0.5) for the visual range (brighter than magnitude +6) and in the other the V and R magnitudes are usually taken as a reference for limiting magnitude estimation for wide band unfiltered systems with silicon-based detectors. The colour-speed detection bias is present even when using synthetic photometry of stars in a wide arbitrary band, as noted by Weryk et al. (2008).

The use of the proposed photometric system allows the estimation of the limiting magnitude and extinction in several bands. For stars down to magnitude 11 we can find their spectral classification from Tycho-2 catalogue (Høg et al., 2000). Spectral libraries are available for

each stellar class, therefore the band magnitudes for each star are easy to calculate using synthetic photometry.

V and R magnitudes could be considered good approximation for G and R Bayer-matrix filters respectively, however each digital single lens reflex camera (DSLR) model has different transmission curves, which must be calculated for each one. We propose its application to the meteors detected with DSLR cameras by the astronauts from the International Space Station (Sánchez de Miguel, 2015).

3.3.2.4 Conclusions

In order to derive meteoroids properties from photometry we have used synthetic photometry over a spectra catalogue with a narrow-band photometric system. We have as well worked on other colour-related issues in the meteoric science, like the limiting magnitude determination or the speed-colour bias in detection.

Further research would benefit from spectra with better resolution in order to have a better correspondence between the synthetic photometry and the real photometry with filters. Despite this limitation we have proved the equivalence of narrow-band photometry to low-resolution spectroscopy. We have used it for a meteoroid spectral classification case. When the flux in a band was contaminated with other sources, we have improved the result using a close background band. Besides the system could help to minimise some limitations of spectroscopy, and extend the range of meteors under research to fainter magnitudes.

4

Optical instrumentation for maximising meteoroid flux determination

4.1 Introduction

In the previous section we have introduced the flux density Q as a characteristic of the meteoroid streams that Earth encounters. We have analysed all the factors involved in the calculation of that flux density and how to maximise the scientific output designing the proper instrument and observational setup. In this section we develop those conclusions and design some cost-effective setups for the study of the interplanetary matter that collides with our planet. The goal is to design versatile instruments that allow detection and characterisation of meteors across a wide range of brightness, but bearing in mind the restrictions in budget and location that we are subject to.

In the first part (section 4.2) we design an instrumental system to participate in the monitoring of the Iberian Peninsula for the Spanish Meteor Network (SPMN) from the Observatorio UCM, located under a heavily light polluted sky. The system is complemented with a mobile station that can be moved to darker skies. As a showcase of this design we present the flux density determination for the outburst of the Draconids 2011. As part of the work in the design of the instrumentation for Observatorio UCM, we have calibrated in the laboratory two of the videocameras used for meteor research (appendix A). Apart from the results presented in this dissertation, the observatory and the author, as a node of SPMN, have contributed to many scientific works (Madiedo et al., 2014a,b,c, 2013; Trigo-Rodríguez et al., 2013).

According to the conclusions of the previous chapter, we can increase the detection avoiding the extinction with a ballonborne mission and wide-field video cameras on-board. In section 4.4 we evaluate the feasibility of these missions and present the results for the campaign of the Geminids 2016.

To conclude we have considered also another of the conclusions from the previous chapter, increasing the aperture of the instrument in order to detect more meteors and also try to detect meteoroids with less mass the than the ones detected with wide-field videocameras. In this case we evaluate the performance for meteor research of the TBT telescopes, described in section 2.2 and the possibility of exploitation of data archives from large surveys.

4.2 Optical ground-based videodetection of meteors

Since the work of Benzenberg and Brandes (1800) the observation in double-station has been widely used for meteor research. The observation from two places located several kilometres apart and the use of parallax allow the researcher to calculate the trajectory of the meteor and consequently the orbit of the meteoroid. The introduction of photography increased the precision of the method and permitted studying the dynamic properties of the meteoroids and their parent bodies.

As meteors are fast moving objects, the use of photography was rapidly complemented with electro-optical detection devices to increase the temporal resolution, like vidicon, SEC and SIT tubes. By far the most popular ones are the video sensors with image intensifier, that has been use from the 70's till today (Hawkes and Jones, 1973; Hawkes, 1993; Koschny et al., 2004; Vítek et al., 2016). However their price prevented its use in networks were several cameras at several locations were needed. Nevertheless the mass-production of video CCDs brought a low-cost device to use in these networks. Video monochrome CCDs have been used from early 80's (Hawkes and Jones, 1986) for the detection of meteors. Nowadays it is the most used sensor, sometimes combined with the image intensifier (see review of the different techniques applied for meteors by Hawkes (1990)).

Currently there are several video meteor observing networks around the world (e.g., (Molau, 2001; Weryk et al., 2008; SonotaCo, 2009; Trigo-Rodríguez et al., 2004)). The characteristics of each one is different according to the scientific goals they pursue. Some of them are only devoted to the detection of new streams, while others are focused on measuring meteoroid fluxes or recording only fireballs in order to recover meteorites. Indeed NASA (Cooke and Moser, 2012) and ESA (Koschny et al., 2013) have their networks to provide input for their models. In our case we are going to introduce the design of a meteor detection station at Observatorio UCM to be integrated as a node of the Spanish Meteor and Fireball Network (SPMN) with an end goal to survey the atmosphere over the Iberian Peninsula and recover any possible meteorite falling in the country.

4.2.1 Design of a meteor detection station: Observatorio UCM case

The astronomical observatory of the *Universidad Complutense de Madrid* (Observatorio UCM) is located in *Ciudad Universitaria* campus which is an urban area of Madrid (40° 27' 04"N , 03° 43' 34"W, 640m, MPC Code I86). UCM Observatory is the urban teaching observatory of Universidad Complutense de Madrid. With two 4.5-m domes equipped with small-sized telescopes (Celestron 11" and a Meade LX 200 12") and some adjacent labs at the top of the physics building, the observatory is mainly used for teaching and outreach purposes, and also some researching activities. Most of the research is carried out as trainee projects by undergraduated students, supervised by the astrophysics professors.

We have designed a fireball detection station for the Fireball Research Group at Observatorio UCM as a node of the SPanish Meteor and Fireball Network (SPMN). The Fireball Research Group is part of the Group of Extragalactic Astrophysics and Astronomical Instrumentation (GUAIX) (Gallego et al., 2011). We obtained additional funds from the Spanish Science Ministry to set up a complete station to cover the whole sky.

These are the high-level scientific requirement that have driven the design of the station:

– Global coverage and meteorite recovery

  The station should cover the whole sky seen from the observatory in order to detect the maximum number of meteors, and especially the possible meteorite-dropper fireballs.

– Orbit calculation

  One of the goals of the SPMN is to recover a meteorite and link it to the parent body. The astrometric precision required for the orbit calculation is in the order of arcminutes, taking for granted that there is enough number of stars for the plate solving of the image. This requirement should be addressed in the trade-off between field size and the star limiting magnitude. Besides timing is crucial for the orbit calculation, and the precision should be 1/30 s.

– Meteor flux determination

  The station should observe at least during night hours and as many nights as possible. Apart from the specific campaigns during major meteor showers, the station could detect at any moment any unexpected outburst.

The interpretation of these requirements has been done according to the budget available and the astronomical quality of the observatory. Another functional requirements were included after the analysis of the global environment:

– Automation

  Although the station is not going to be located in a remote area, the availability of personnel to operate the station is very limited. Ideally the station should run in a completely unattended way for long periods. House-keeping tasks or data analysis could be programmed or done remotely.

– Data processing and data storage

  The volume of data foreseen is huge with several hours per night covered at a resolution of arcminutes covering the whole sky. Therefore the processing should be done on real-time and only real meteor detections should be recorded in order to optimise the data storage.

– Integrated system based on available off-the-shelf components

  The station shall comprised an integrated system with on-site monitoring, detection and archiving in real-time. All the elements should be COTS in order to be cost-effective and allow its replication in a network.

As it is an urban observatory, it suffers from a very heavy light polluted sky, with a zenithal sky background brightness of around 17.2 mag/arcsec^2 in the Johnson V band. It is not surprising that part of our research is focused on astronomical characterization of the night sky in order to fight and control light pollution (Sánchez de Miguel and Zamorano, 2010). Some simple devices and wide field cameras were developed to measure the night sky brightness and photometric constants

in the past years. It also hosts an all-sky camera (AstMon-UCM) which monitors continuously the whole sky in the B, V and R Johnson bands.

Since 2001 some of the researchers at the group have been collaborating in the SPanish Meteor and Fireball Network (SPMN) observing campaigns. Following the Puerto Lápice fireball, astrophysics professors and students participated in the meteorite recovery with success (Madiedo et al., 2008; Trigo-Rodríguez et al., 2009). In 2009 we started as a node of the SPMN network setting-up a small station with our first video camera at Observatorio UCM.

4.2.2 Videodetection Station at UCM

Following the high level requirements explained in the introduction, we have designed the station to cover the whole sky with high resolution, following the goal of the SPMN to cover the Iberian Peninsula skies in order to record fireball trajectories with precision enough to recover the possible meteorites dropped (Madiedo et al., 2009). Madrid is a key node since it is roughly at the centre of the Iberian Peninsula, with the possibility of performing double station observation with another 5 SPMN nodes.

The baseline design is one with six cameras to cover the whole sky at night. Five cameras, pointing at an elevation of 25 degrees, with FoV $72^\circ \times 54^\circ$ covering all azimuths of the horizon and the sixth camera is aimed to the zenith. With this arrangement a plate scale of 7 arcmin/pixel is achieved, enough to meet the SPMN quality standards for the astrometric measurements (see figure 4.1).

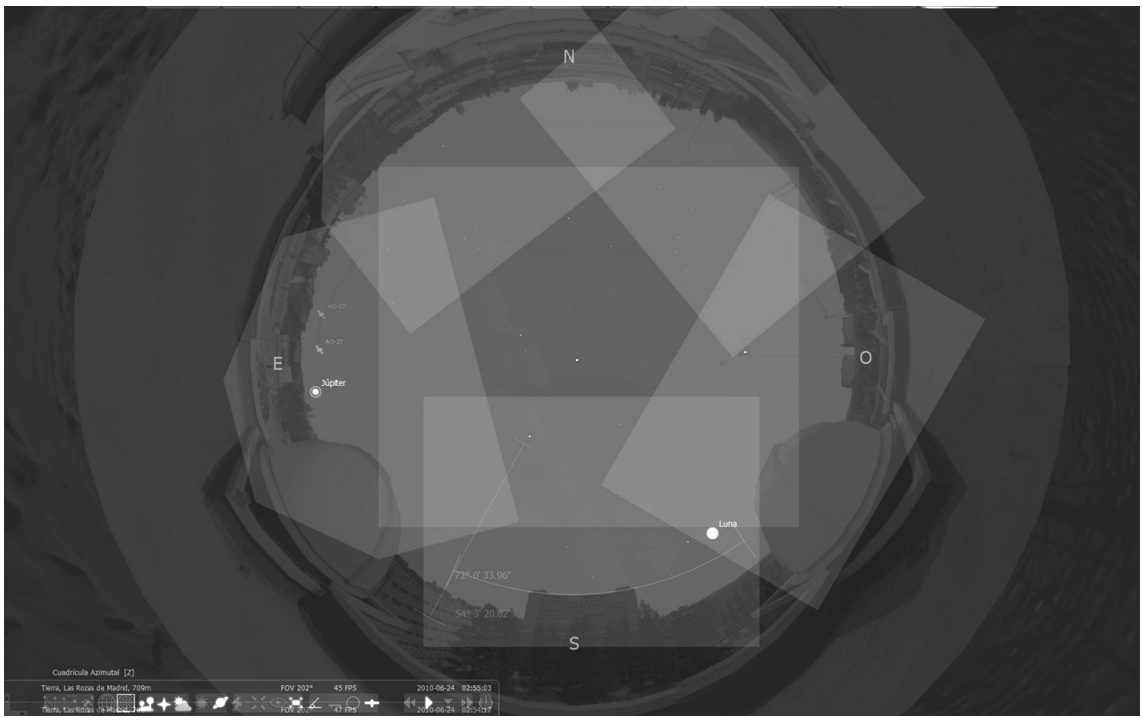

Figure 4.1: Ideal coverage of the sky from Observatorio UCM domes. Please note that over the local horizon there are several building and light pollution sources. Figure from Manjavacas (2010).

However the local horizon from the rooftop is not free from obstacles, therefore we increased the average elevation to 35 degrees. Consequently, we can decrease the FoV size in order to avoid

necessary overlapping and improve the resolution. This process is done individually, setting each camera at different elevation and azimuth to avoid obstructions, ensuring the fully coverage and prioritising the pointing for double-station observation with other nodes (table 4.1). The system is duplicated with cameras to be used during the day, for detection of superfireballs.

Name	FoV (deg^2)	True area (10^3 km^2)	Direction
Bol02	69×52	10.6	SW
Bol03	64×48	11.2	NW
Bol04	64×48	11.8	NE
Bol05	59×45	6.9	E
Bol06	60×45	7.8	SE
Bol07	140×105	~ 60	All-Sky

Table 4.1: Observational parameters and values for each camera. Total geometrical area of the cameras is $\sim 70,000$ km^2. Note that Bol07 partially overlaps with the other camera fields.

In order to cover the sky as described before, we selected cameras and lenses according to the budget. In the appendix A there is a full description of the selection and characterisation of the cameras and sensors. Please find here a brief overall description of the instrumentation, based on low-light CCTV cameras with auto-iris lenses. The selection of the lenses has been based on several reviews, and our experience with different models in the same price range, under ∼100€. We have mainly evaluated the stellar PSF (average and across the field). A review of different wide-field lenses used for meteor astronomy can be found in Wisniewski et al. (2005).

For nighttime detection we are using B&W high sensitivity CCTV cameras, manufactured by Watec, Japan. Watec 902 H2 Ultimate has a 1/2" chip, which allows covering the FoV required with a lens of 4.7mm of focal length. The lens chosen is the Tamron 12VG412ASIR, which is a fast f/1.2 varifocal 4-12mm IR corrected aspherical lens. We have used different cheap Fujinon zoom lenses with good results, but this Tamron lens gives the best image quality among all the lenses tried and has an affordable price ∼100$.

We fitted the zenith camera with an all-sky lens to cover the sky above 55 degrees in elevation with one camera, this is very useful to look for bright events spending just a couple of minutes every morning. The fish-eye lens is the Pentax C70100, varifocal 1.6mm to 3.4mm, quite fast f/1.4, with aspherical elements. Although it is not cheap, ∼400$, we chose this lens because it is noticeably better than other lens we have tested (Rainbow L163VDC4P ∼150$ or Fujinon 1/3" 1.4-3.1mm ∼125$). The three lenses are for 1/3" chips, but Pentax and Rainbow images almost fill the 1/2" chip with slight vignetting. To extend the detection to daytime, we are using colour CCTV cameras Samsung SCC B1331P. It is a cheap, multipurpose CCTV camera with standard daytime sensitivity enough for detecting fireballs at daytime. A light-sensor relay switches between daytime and nighttime cameras (figure 4.4).

All the cameras have been mounted inside Pelco enclosures at the top of the Physics building next to the Observatorio UCM domes (figure 4.2), are fed with 12 V and output an analogue video cable. As an addition to these cameras installed in the rooftop of the faculty, the group has also developed a movable station to cover the major showers and specific campaigns, in order to achieve better geometric conditions for orbit determination or detection efficiency. The station consists of a small notebook with 10 h battery autonomy. It controls up to two high sensitivity CCTV camera,

as described above, fed by a small 12 V DC battery. The station weighs less than 5kg (tripod included) and can be installed in less than 10 minutes.

Figure 4.2: Actual appearance of the cameras mounted close to the Observatorio UCM domes. The cameras were distributed in three poles to avoid the appearance of the domes in the FoV.

Apart from the cameras mentioned, the researchers of the group installed some cameras to complement the station at the observatory. In Madrid, Jaime Izquierdo deployed DSLR cameras with wide-angle lenses for high-resolution images of fireballs during the maxima of meteor showers. Moreover J. Zamorano installed an extra station in Villaverde del Ducado (Guadalajara), also as a node of the SPMN, with an adequate baseline for double station observation with Observatorio UCM.

4.2.3 Control and operation of the station

One of the main characteristics of this station is its automatic operation, so daily maintenance is not necessary. An electronic system switches on and off the cameras and also changes between day and more sensitive night cameras according to amount of light. Each pair of night and day cameras feed one framegrabber connected to a PC computer alternatively. Therefore the control system consists of 6 computers for detection and a server which holds the network, makes a backup

of all the detections and runs the analysing scripts (figure 4.3). Absolute timing is very important for orbital determination, thus the server is synced using a NTP service and the control computers retrieve time from it.

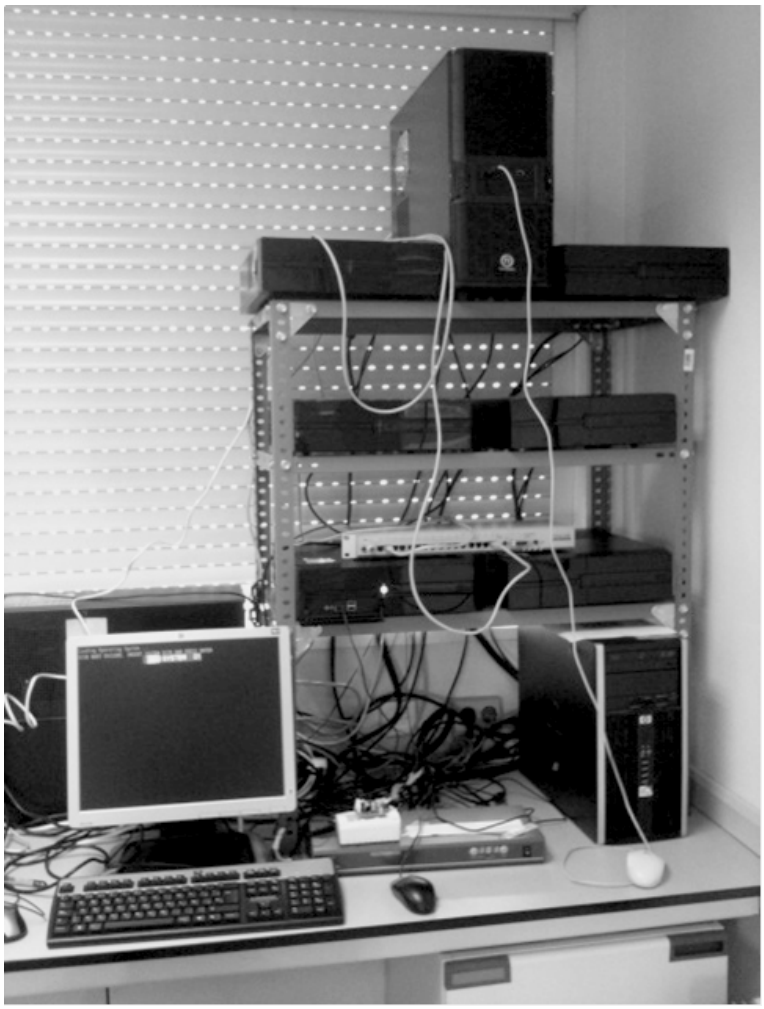

Figure 4.3: Current status of the control system: 1 server and 6 computers fed with video signal, light sensor and rain sensor data.

The operation of the station is quasi-automatic, being able to run for 3 or 4 weeks without human intervention. Moreover the operator could work remotely through VNC remote desktop protocol. Using a switch for the camera electricity supply controlled by a rain sensor, the system stops the cameras when rain is present to prevent the recording of lots of false detections caused by the rain (figure 4.4). Moreover the lenses chosen has an auto-iris that prevents the sensors to get damaged by direct sunlight.

The video analogue signal fed to the computers is digitalised by 8-bit USB framegrabbers that allows us to achieved the astrometric precision required. The software UfoCapture by SonotaCo is used for detection, in accordance to most of the stations of SPMN network. For a comparison of the software packages available and their characteristics see Molau and Gural (2005). UfoCapture is a real-time processing software that identifies changes in the field of view and discriminates meteors from satellites, planes or birds.

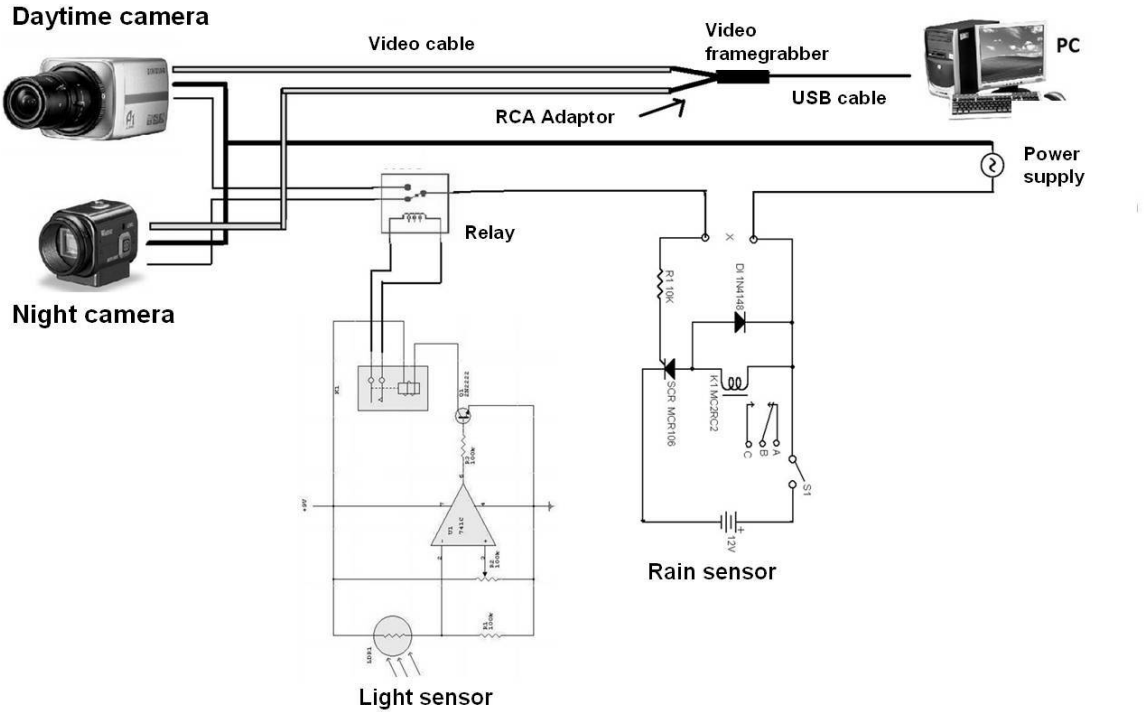

Figure 4.4: Scheme of the electrical circuit that controls all the system performance in day/night changes and rain situations, as designed by J. Izquierdo (UCM). Figure from Zamorano et al. (2010).

All the files associated to each meteor detected are copied to the server, where different scripts are running. One of them sends an email each morning to the operators with the poststamp images of the fireballs detected. Another script makes a cross-checking between the different UCM stations looking for fireballs recorded in double station. Our longest baseline is ∼110 km between UCM stations and we have recorded some fireballs in double station with SPMN nodes as far as 500 km. UCM cameras survey more than 60000 km^2 of atmosphere surface at 100 km height. The most interesting events are quickly preanalysed by the operators, uploaded to the SPMN server and they alert other networks members to check their detections.

4.2.4 Analysis of the results: Density flux calculation for Draconids 2011

Since the installation of the cameras, the Fireball Detection Station at Observatorio UCM has produced several TB of data. As a sample of the capabilities of the Observatorio UCM station here we have selected one of the cases that combines data from the fixed cameras at Madrid and the ones from the movable station.

An outburst of Draconids took place on the 8th of October, with the maximum at $\sim$ 20h UT as forecast. The GUAIX (UCM group of Extragalactic Astrophysics and Astronomical Instrumentation) prepared a dedicated observing campaign to complement the continuous monitoring at Observatorio UCM (Madrid). The scientific objective of the campaign was to obtain flux density and astrometric recordings of the Draconids in a well placed location with good weather and optimal radiant elevation conditions.

The highlight was the launch of a high-altitude helium balloon with a scientific payload for recording the Draconids. This was done in collaboration with Proyecto Daedalus that had successfully launched other balloons. The payload consisted of a netbook recording the signal coming from a Watec high-sensitivity video camera. See section 4.4 for the description of this mission.

Part of the group (J. Izquierdo, J. Zamorano and the author) went to the Sierra Nevada Observatory (OSN) of the Instituto de Astrofísica de Andalucía (IAA) at 2900 m high in Sierra Nevada (Granada) (figure 4.5). More than a hundred Draconids were recorded. Some fireballs were observed in multiple station by several nodes of the SPMN (SPanish Meteor Network). The analysis presented here was lead by the author and is part of the undergraduate research project *'Dungeons & Draconids (&Fellows!)'*. M. F. Palos, B. Muñoz-Ibáñez and A. Santamaría are undergraduate Physics students and take part in this program as an introduction to scientific research (Ocaña et al., 2013).

4.2.4.1 Equipment and method

The 2011 Draconids were recorded using Watec 902 H2 Ultimate cameras and wide-field lenses covering down to magnitude +3 and all-sky lenses down to +1. There were 7 cameras at Observatorio UCM (Madrid) and 5 cameras at OSN (Granada). High resolution images were taken with DSLR cameras from OSN in double station with other SPMN nodes in order to calculate precise orbits. The Draconid flux was calculated using video data from the UCM cameras at OSN and UCM observatories (table 4.2) . We use the method explained in section 3.2.

Figure 4.5: Equipment deployed at the Observatorio de Sierra Nevada by J. Izquierdo, J.Zamorano and the author. We acknowledge the support of Instituto de Astrofísica de Andalucía (IAA-CSIC) for their support carrying out the observations.

The video limiting magnitude for meteors is determined using the dimmest meteor detected by each camera. We use 2.3 as a constant value for the population index (Trigo-Rodríguez et al. (2013)) and the zenith exponent γ is assumed to be 1. The beginning height H value used is 105 km (Suzuki et al., 1999; Koten et al., 2007).

4.2.4.2 Observation and data

The data used is divided in 12-minute bins in order to have at least 10 meteors per bin during the FWHM of the outburst. We have calculated the effective collecting area for each camera and counted the number of meteors. We use the sum of all the cameras to calculate a single value of flux density.

Name	FoV (deg^2)	vlm	True area (km^2)	Effective area (km^2)	Meteors
Bol02	69×52	2.3	10584	125872	20
Bol05	59×45	2.8	6941	882533	18
Bol06	60×45	2.6	7786	37976	41
OSN01	39×29	2.7	3131	418323	8
OSN05	71×54	2.7	10843	340279	54

Table 4.2: Observational parameters and values for each camera. Total geometrical area of the cameras used was $\sim 39 \cdot 10^3$ km^2, and the total effective area A_{red} for the Draconids with r=2.3 and H=105km was $\sim 1.8 \cdot 10^6$ km^2.

All cameras were working from civil twilight until 00h UT. We analyse here the data of 5 cameras at OSN and UCM observatories from 18h48m UT to 23h00m UT. We discarded the other 3 cameras that were aimed for double station observations (section 4.2.4.3). Weather was fine during the observation apart from some thin high clouds by the end of the observing period.

Main source of uncertainties is the small number of meteors per bin (from statistics the error is $\sqrt{N}$). The uncertainties on the zenith exponent γ and the population index are considered to be systematics, and not included in our calculation. Our main concern is the error associated to the computation of the video limiting magnitude for meteors (vlm). A systematic error of -0,5 magnitude means an increase of +50% value of flux (using r=2.3). Therefore we use the N meteors detected by the 5 cameras to minimise the uncertainty for the fluxes calculated. Although we are aware that the systematics could be larger.

4.2.4.3 Double station observations

The UCM group was running 12 videocameras from 3 different stations (table 4.3). At least 6 fireballs were detected simultaneously by Observatorio UCM and Villaverde del Ducado (Guadalajara) cameras. We recorded also several events by our cameras and others SPMN stations, which are analysed in Trigo-Rodríguez et al. (2013).

Observatory	Coordinates	# Cameras	Others
Observatorio UCM	40°27′04″ N, 03°43′34″ W	5 cameras	
Villaverde del Ducado	41°00′08″ N, 02°29′25″ W	4 cameras	Equipped with gratings
Observatorio Sierra Nevada	37°03′51″ N, 03°23′05″ W	3 cameras	Also DSLR

Table 4.3: UCM group observing stations for the Draconids 2011 outburst.

4.2.4.4 Discussion and results

The flux density is calculated using 141 meteors from 18h48m to 23h00m UT. The total collecting area of the cameras was $\sim 39 \cdot 10^3$ km^2 (equivalent to an effective area of $A_{red} \sim 1.8 \cdot 10^6$ km^2), with an average limiting magnitude of 2.6. The population index value used is 2.3 and assumed to be constant along the outburst. Also we assumed the zenith exponent γ to be 1.

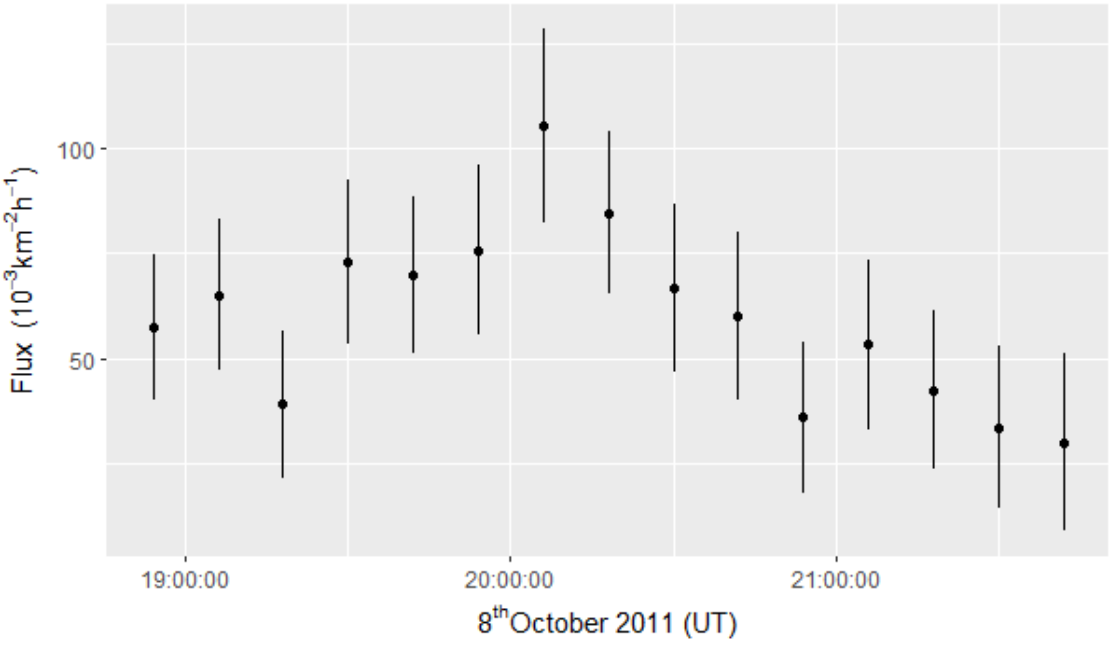

Figure 4.6: Draconid flux profile for meteoroids with mass >5mg (meteors brighter than magnitude 6.5).

Even using a 12-minute bin the profile is noisy (see figure 4.6). We obtain a maximum flux density of $(105 \pm 23) \cdot 10^{-3}$ meteoroids km^{-2}h^{-1} producing meteors brighter than magnitude 6.5 (mass $>$ 5 mg). The maximum took place at around 20h06m UT. It had a FWHM of ∼80 minutes, and shows a clear asymmetry, with a strong decay after the maximum. This is the result of the addition of peaks from 1907 and 1900 (forecast at 19h36m and 20h01m UT respectively by Vaubaillon et al. (2012)).

Our result is in good agreement with other results published. SPMN calculations use $r = 2.3$ and get a flux of $(102 \pm 13) \cdot 10^{-3}$ meteoroids km^{-2}h^{-1} at 20h08m UT (Trigo-Rodríguez et al., 2013). IMONET gets similar results with a flux density of $(118 \pm 10) \cdot 10^{-3}$ meteoroids km^{-2}h^{-1} (Molau and Barentsen, 2014).

4.3 Telescopic detection of meteors

According to one of the conclusions of the previous chapter, the density flux determination was strongly affected by the limiting magnitude, as the meteoroid distribution in mass (with an index *s*) and therefore in brightness (with an index *r*) follows a power law. Besides the increase of geometrical monitoring area was always badly affected by the increment of the distance, and the magnitude loss was always significant (see figure 3.6).

Therefore we consider than increasing the aperture of the instrument in order to detect more meteors and also try to detect meteoroids with less mass the than the ones detected with wide-field videocameras. There has been already instrumental developments in this direction, like the super-Schmidt cameras (Hawkins and Upton, 1958; Hoffmeister, 1950) and it is not the purpose of this work to investigate in new optical configurations, but rather in using the data acquired by current wide-field telescopic surveys. In this case we evaluate the performance of the TBT telescopes, described in section 2.2 and in the possibility of exploitation of data archives from large surveys.

Meteors have been widely observed with the use of telescopes (Henize et al., 1993), but in the vast majority of the cases these are serendipitous detections (Jenniskens et al., 2004; Iye et al., 2007). Nevertheless identifications could be an issue in wide-field telescope images. Fortunately these telescopes usually have focal lengths large enough to show meteors (at 100 km height) out of focus (Jenniskens et al., 2004; Iye et al., 2007). Also low-earth orbit satellites are easily discarded taking images only when the Sun is not illuminating these orbits (usually within 2 hours after or before the twilight). Due to their nature meteors within the hundredths of micron range are monitored using radar sensors. Most optical meteor surveys observe meteor down to magnitude 6 (millimetres range), however smaller meteoroids are able to produce meteors as they suffer ablation down to 100 microns (Bronshten, 1983). For the sake of simplicity, we assume they have similar luminous efficiencies and there is constant mass index (s) in the range of the meteors detectable by wide-field survey telescopes (magnitude < 10). To determine the number of meteors N_m detectable by the telescope we need to calculate the flux of meteoroids in the detection range of the telescope, it is the integral down to the limiting magnitude lm of the meteor luminosity function $F(m)$. Therefore these meteors are observable in the optical range with the use of silicon devices (i.e., CCDs) and the aid of large collection area optical devices.

$$F(m)\mathrm{d}m = \mathrm{d}N_m \approx m^{-s}\mathrm{d}m \tag{4.1}$$

Inputs for this study are the sporadic meteoroid fluxes detected in the visual range (down to magnitude +6) by IMONET (Molau et al., 2013) and in the radar range for fainter meteors (Blaauw et al., 2011).

4.3.1 Average sporadic meteor

We define some 'standard' values to simplify the problem. They are educated guesses to get a rough order of magnitude of the detectable meteors, although the best approximation for such a problem would be a proper simulation with real population and conditions. The limiting magnitude for meteor detection depends on the sky brightness, the time of integration and the speed of the meteor. Then the photons reaching a certain pixel coming from a meteor should be numerous enough over the photons coming from the sky during the whole time of integration. As the distribution is close

to potential, the 'radar' meteors would be the most numerous. For this range the sporadic flux is well above the meteor shower flux. Thus we can assume some average properties (i.e., 30 km/s speed), an average elevation of the FoV of 50 degrees and a mean radiant distance to the sporadic sources of 45 degrees. This leads to an average apparent speed of $8^{\circ}/s$.

The area is the projected FoV at 100 km high, the average beginning height of meteors at this magnitude range. Therefore we would calculate the number of meteors starting in the FoV, but not the ones crossing it. Consequently we consider the meteors being 10 degrees long to include all the meteors crossing the FoV.

4.3.2 Meteor detections by telescopes: estimations

Once the flux of meteoroids down to a certain mass/size is known, we can evaluate the performance of these systems (meteor rate) as the product of the flux of meteoroids by the atmospheric area A monitored by the telescope.

$$\text{meteor rate} = A \cdot \int_{-\infty}^{lm} F(m)\mathrm{d}m \tag{4.2}$$

However as we mentioned is the previous chapter, there is a magnitude loss due the light of the object spread across several pixels that we described in equations 3.22 to 3.24. In this case integration time t_{exp} is much larger than the time the image of the meteor is in each pixel t_0. Therefore we can compare the limiting meteor magnitude *vlm* to the stellar limiting magnitude *lm* in terms of times:

$$\Delta m = vlm - lm = 2.5 \log \frac{t_0}{t_{exp}} \tag{4.3}$$

where $t_0 = \frac{\text{meteor speed}}{\text{pixel size}}$.

In this thesis we use as a reference for the telescopic meteor observation the telescope discussed in the previous chapter of this work, as a sample of a future network with several telescopes around the globe. The Test-Bed Telescope (TBT) project will procure a validation platform for an autonomous optical observing system in a realistic scenario, consisting of two telescopes located in Spain and Chile, to collect representative test data for precursor SSA services. They are 56-cm telescopes with a 2.5×2.5 deg^2 FoV taking short exposure images during clear nights all year round. TBT telescopes have a plate scale of 2.2 arcsec/pixel. For a meteor at $8^{\circ}/sec$, the light will be over the pixel for only 0.08 ms. Therefore the relationship between plate scale and meteor speed is the main constraint for the limiting magnitude. For a typical exposure of 2 s, the stellar limiting magnitude for TBT telescopes will be around 18, however it would be no more than 7 for our average meteor. This leads to a value of only 0.06 meteors starting in the field per hour, and around 1 meteor per hour through the field. The result of this study for the TBT telescopes with ca. 12 deg^2 of FoV is the detection of sporadic meteors around 1 per hour and telescope. Low-noise CCD read-out, short exposures and dark sky are essential to increase the SNR of meteors and the subsequent detection probability. Else the limiting magnitude is diminished rapidly due to the short time the meteor spends over a pixel compared to the constant photon flux from the sky background.

System	Diameter (cm)	FoV (deg^2)	Meteor lm vlm	Meteor rate (h^{-1}) Estimated	Observed
TBT	56	6.25	7	1	
SuperWasp	20	482	8	10	
MiniMegaTortora	8.5	900	8	25	27
HINWO/ACR	3.5	557	6	5	~ 5

Table 4.4: Comparison of theoretical numbers with real data from IMONET (videocamera ACR operated by Wolgang Hinz) (Molau et al., 2013) and MiniMegaTORTORA (Karpov et al., 2016).

In the literature we can only compare our estimations to an experimental test with a CMOS sensor at the 1.05-m Kiso Schmidt, and they get results in the range expected (Watanabe et al. (2014). In order to complete this work we include two different surveys, with smaller aperture sizes. The SuperWASP survey is covering 482 deg^2 with a plate scale of 13.7 arcsec/pixel. The same 'average' meteor will spend 0.5 ms over each pixel. For its typical exposure of 30 s, the stellar limiting magnitude for SuperWASP is 18, however it would be only 8 for meteors. This leads to a value of around a tenth of meteors per hour through the field.

We can also apply our estimations to the MiniMegaTORTORA survey (Karpov et al., 2012). It is an observatory with nine 8.5-cm camera lenses covering 300 deg^2 that is focused on fast-transient events, so it uses faster image rate (6 fps) and has a smaller aperture when compared to the general-purpose astronomical survey telescopes we were referring to. In Table 4.4 it can be seen that a system like SuperWasp or MiniMegaTortora could achieve a similar detection rate that a dedicated meteor detection videocamera.

4.3.3 Conclusions

Meteor detection rates to be achieved with the future wide-field survey telescopes are similar to the ones for current video networks. Therefore meteors detected as byproducts in these surveys will be a new source of meteoric data. For this purpose survey images should be analysed by meteors scientists using survey archives or even dedicated algorithm in their processing pipelines. All these telescopes will sum up thousands of square degrees, observing each night. The combined detecting area at 100 km high will be more than 10000 km^2, similar to some of the videosystems devoted to meteor detection. However large survey telescopes, like TBT are not especially competitive. Short exposures are very important for increasing meteor detection rate, what could be the case for time-domain surveys. Common general-purpose telescopes have small plate scale and most scientific cases lead to employ large integration times, what plays against meteor detection.

4.4 Balloon-borne meteor observations

As an application from the results obtained in previous chapter, we have explored the observation of meteors from high elevation above the ground. Over the troposphere the extinction is very limited, what allows us to increase the area surveyed and to maximise the detection rates. In order to reach the stratosphere we study balloonborne missions and the expected meteor detection performance in order to select the adequate instrumentation.

Since the end of the 18th century astronomers have been involved in balloon-borne observations. The first observations were casual stargazing without instruments. And therefore one of the first phenomena to be observed were meteors and fireballs. The first account of meteor sighting is as early as 1807 (Forster, 1832; Beech, 1999), while the first observational campaigns were organised for the forecast storm of the Leonids 1899 (Beech, 1999). Almost one hundred years later, the Leonids 1998 outburst was observed from a balloon with modern instruments (Jenniskens et al., 1998). Apart from balloonborne campaigns, meteor storms have been studied in several airborne campaigns (Millman, 1973; Murray et al., 1999; Vaubaillon et al., 2015), but the cost of these is some orders of magnitude larger than low-cost balloon flights and still suffer from some extinction (Gural and Jenniskens, 1998).

In this section we reproduce the schema as before, from the theoretical calculation to an instrumental implementation:

- Application of the method for the calculation of A_{red} for balloon-borne observations in an extinction-free environment for different meteoroid population indexes.

- Instrumental design for optimising the meteor detection. The design of the payload has been driven by science and technology development, and based on COTS components.

- Performance of balloonborne meteor observations in collaboration with Proyecto Daedalus[1]. Daedalus started as an amateur high-altitude balloon launching team, for outreach and technology development. In the framework of this thesis, Alejandro Sánchez de Miguel and the author added astronomical payloads for nighttime missions for the research areas of our group (meteors and light pollution).

In the last 6 years we have participated in a total of 11 nighttime missions. The scientific payloads for these stratospheric flights were designed for light pollution and meteor research. The first of these nighttime flights, Daedalus 2, took place in 2010 as an instrumental test to monitor light pollution. The same year a second flight over the city of Jaén successfully took the first images for scientific use (Sánchez de Miguel et al., 2011). In 2014 the project was repeated over the city of Madrid, acquiring images of quality comparable to the ones from airborne instruments with a hundredth of the cost. The data of some of these missions for light pollution were used in the thesis of Sánchez de Miguel (2015).

The other scientific objective of these night flights was the estimation of meteoroid influx at Earth through the observation of meteor showers. Observing meteors from the stratosphere improves detection efficiency thanks to much lower extinction and less background brightness. Other teams had already demonstrated the benefits of airborne observations for these objects. Thanks to the low cost of balloons and high-sensitivity cameras there is already a number of other groups using stratospheric balloons to record meteors (Moser et al., 2013; Koukal et al., 2016).

Since 2016 the payloads have flown on-board the ORISON Pathfinder missions. ORISON is a H2020 project to study feasibility of innovative astronomical research infrastructure based on stratospheric balloons (López-Moreno et al., 2016).

[1] http://www.proyectodaedalus.com/

4.4.1 Meteor detection from the stratosphere

In section 3.2.4 we showed that the maximisation of the detection of meteors could be achieved surveying a big area at low elevation in an environment free of extinction. We consider a mission with a nominal flight altitude of 20 km and start the analysis with a 1 deg^2 FoV. At h_b =20 km the meteor layer is closer to the observer, which reduces the geometric area monitored (the sensor projected onto the meteor layer), especially while pointing close to the zenith. On the other hand the meteors are closer (figure 3.6) and the extinction is lower (figure 3.5), increasing the apparent brightness of the meteors (figure 4.7). They compensate each other and the effective area A_{red} at the zenith is similar for the cases from ground and at 20 km height (figure 3.10).

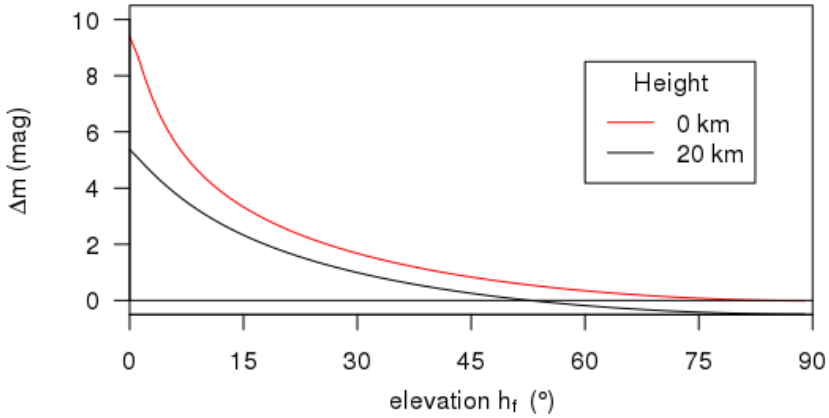

Figure 4.7: Total magnitude loss Δm due to the distance and extinction as a function of the elevation of the field of view for different heights. Main contributor to the difference is the extinction. Distance accounts for a maximum of $\Delta m = 0.25$ magnitudes.

Therefore the main difference between the ground and flight levels is the extinction, and at larger zenithal angles the effective area A_{red} is maximised for balloonborne observations. Observing from the stratosphere yields larger effective area (table 4.5) in comparison to ground level (table 4.6) for all the usual values of the population index r. The analysis of these data confirms our hypothesis, that the largest effective areas are surveyed from the stratosphere while pointing from the horizon up to 5 degrees of elevation. In order to select the instrumentation we take into account the other constraints that arise from the observational platform.

4.4.2 Description of the platform, mission stages and systems operation

Proyecto Daedalus has been launching high-altitude balloons since 2009. They offered their platform to include astronomical payloads for night-time missions. We describe the platform here in order to evaluate the constrains imposed for the instrument selection. For further detail of the platform developed by Proyecto Daedalus, the current status and the evolution path followed, see Ocaña et al. (2016a).

The platform is a passive craft, with basic stabilisation and 3-hour length nominal mission. Current design has up to 4 observational ports, three at the sides of the square-shaped probe and one aiming at nadir for Earth Observation (figure 4.8). We have used the side ones, with elevation $h_f = 0$ for our instruments in order to increase the detection according to the table 4.6. The

r	h_f														
	0	5	10	15	20	25	30	35	40	45	50	60	70	80	90
1.5	49.35	66.60	48.59	31.59	21.26	15.12	11.31	8.84	7.16	5.98	5.13	4.04	3.44	3.14	3.05
1.6	27.40	45.06	36.70	25.48	17.95	13.21	10.16	8.11	6.68	5.67	4.92	3.96	3.41	3.13	3.05
1.7	15.77	31.22	28.20	20.82	15.31	11.64	9.18	7.48	6.27	5.39	4.74	3.87	3.38	3.13	3.05
1.8	9.36	22.09	22.00	17.21	13.18	10.33	8.34	6.93	5.90	5.14	4.57	3.80	3.35	3.12	3.05
1.9	5.72	15.93	17.39	14.37	11.44	9.22	7.62	6.44	5.57	4.92	4.42	3.73	3.33	3.11	3.05
2.0	3.59	11.68	13.91	12.12	10.00	8.29	6.99	6.02	5.28	4.71	4.27	3.67	3.30	3.11	3.05
2.1	2.30	8.69	11.25	10.30	8.80	7.48	6.44	5.64	5.01	4.53	4.14	3.61	3.28	3.10	3.05
2.2	1.51	6.56	9.19	8.82	7.79	6.79	5.96	5.30	4.77	4.36	4.02	3.55	3.26	3.10	3.05
2.3	1.00	5.01	7.58	7.61	6.93	6.19	5.53	4.99	4.55	4.20	3.91	3.50	3.24	3.09	3.05
2.4	0.68	3.88	6.30	6.60	6.20	5.66	5.15	4.72	4.35	4.05	3.81	3.45	3.22	3.09	3.05
2.5	0.47	3.03	5.28	5.76	5.57	5.20	4.81	4.47	4.17	3.92	3.71	3.40	3.20	3.08	3.05
2.6	0.33	2.39	4.45	5.06	5.02	4.79	4.51	4.24	4.00	3.79	3.62	3.35	3.18	3.08	3.05
2.7	0.23	1.90	3.78	4.46	4.55	4.42	4.23	4.03	3.84	3.68	3.53	3.31	3.16	3.07	3.05
2.8	0.17	1.53	3.22	3.95	4.14	4.10	3.98	3.84	3.70	3.57	3.45	3.27	3.14	3.07	3.05
2.9	0.12	1.23	2.77	3.52	3.77	3.81	3.75	3.66	3.56	3.47	3.38	3.23	3.13	3.07	3.05
3.0	0.09	1.01	2.39	3.14	3.45	3.55	3.55	3.50	3.44	3.37	3.31	3.19	3.11	3.06	3.05
3.1	0.07	0.83	2.07	2.82	3.17	3.31	3.36	3.35	3.32	3.28	3.24	3.16	3.10	3.06	3.05
3.2	0.05	0.68	1.80	2.53	2.91	3.10	3.18	3.21	3.21	3.20	3.17	3.12	3.08	3.06	3.05
3.3	0.04	0.57	1.58	2.29	2.69	2.91	3.02	3.08	3.11	3.12	3.11	3.09	3.07	3.05	3.05
3.4	0.03	0.47	1.39	2.07	2.49	2.73	2.88	2.96	3.01	3.04	3.05	3.06	3.05	3.05	3.05

Table 4.5: Reduced areas A_{red} in km^2 as a function of r and the elevation of the centre of the FoV h_f for H = 100 km and $h_b = 0$ km. The FoV is 1 deg^2. Effective area increases towards the horizon until a point where the extinction overcomes it. That turnover point depends on the population index r.

structure is a styrofoam box with an anchorage point for the balloon/s. The probe uses up to 3 meteorological sounding balloons to get out of the troposphere. The probe usually rises to 30 km of altitude, where the largest balloon burst and then descends in free-fall with a parachute or slowed down by the moderate lifted of the remaining balloon/s. The probe has GSM, RF and GPS beacons and some missions had also bidirectional communication. During the flight the probe is chased from ground using the beacons in order to recover it as all the data is stored locally.

The platform is equipped with several sensors that provide information about the flight and environment. Accelerometers, magnetometers, thermometer, hygrometer are used to analyse the flights. These values constrain the characteristics of the experiments that are qualified to fly. The analysis of the data from accelerometers in the 3 axis permits us to identify different flight phases: launch and troposphere with average acceleration up to 3 m/s^2. The flight in the stratosphere is very stable, with an average of 1 m/s^2 for the 3 axis. While falling the probe is not stabilised at all, registering average values over 4-5 m/s^2 in all of the axis (figure 4.9). Maximum values registered in the missions are up to 15 m/s^2, which imposes constrains for fragile instruments and wires.

The temperature is also a constraint for the instruments, the power budget of the mission and the length of the flight. The probe is not pressurised, consequently the air flows out during the ascent. Therefore the temperature decreases slowly until the burst of the balloon. During the fall the cold air flows in and battery voltage drops significantly, but they have never frozen. On the other hand humidity has never become a problem. Optical instruments have shown some water drops after going through clouds, but they have evaporated soon after. Only one launch has been performed under the rain. However the lenses were not fogged after some minutes over the clouds.

r	h_f														
	0	5	10	15	20	25	30	35	40	45	50	60	70	80	90
1.5	241.07	126.34	60.92	33.09	20.25	13.59	9.79	7.45	5.92	4.87	4.14	3.21	2.71	2.46	2.38
1.6	175.57	98.25	50.25	28.54	18.08	12.47	9.19	7.12	5.75	4.79	4.11	3.25	2.77	2.53	2.46
1.7	130.36	77.58	41.94	24.84	16.25	11.50	8.65	6.82	5.59	4.72	4.09	3.28	2.83	2.60	2.53
1.8	98.45	62.09	35.37	21.79	14.70	10.66	8.18	6.55	5.44	4.65	4.07	3.31	2.89	2.67	2.60
1.9	75.49	50.30	30.10	19.25	13.36	9.92	7.75	6.31	5.30	4.58	4.05	3.34	2.94	2.73	2.67
2.0	58.68	41.19	25.83	17.12	12.21	9.26	7.37	6.09	5.18	4.52	4.03	3.37	2.99	2.80	2.73
2.1	46.17	34.06	22.33	15.31	11.21	8.68	7.02	5.88	5.06	4.46	4.01	3.40	3.04	2.86	2.80
2.2	36.74	28.41	19.44	13.76	10.33	8.16	6.71	5.69	4.96	4.41	3.99	3.43	3.09	2.92	2.86
2.3	29.54	23.90	17.03	12.43	9.55	7.69	6.42	5.52	4.85	4.36	3.98	3.45	3.14	2.97	2.92
2.4	23.97	20.25	15.00	11.27	8.86	7.26	6.15	5.35	4.76	4.31	3.96	3.48	3.19	3.03	2.98
2.5	19.61	17.27	13.28	10.27	8.25	6.88	5.91	5.20	4.67	4.26	3.95	3.50	3.23	3.09	3.04
2.6	16.18	14.82	11.81	9.38	7.70	6.53	5.68	5.06	4.59	4.22	3.93	3.52	3.28	3.14	3.10
2.7	13.44	12.80	10.56	8.61	7.21	6.21	5.48	4.93	4.51	4.18	3.92	3.55	3.32	3.19	3.15
2.8	11.24	11.11	9.47	7.92	6.76	5.91	5.28	4.80	4.43	4.14	3.90	3.57	3.36	3.24	3.21
2.9	9.46	9.69	8.53	7.31	6.36	5.64	5.10	4.69	4.36	4.10	3.89	3.59	3.40	3.30	3.26
3.0	8.01	8.49	7.71	6.76	5.99	5.39	4.93	4.58	4.29	4.06	3.88	3.61	3.44	3.35	3.31
3.1	6.82	7.47	6.99	6.27	5.65	5.16	4.78	4.47	4.23	4.03	3.87	3.63	3.48	3.39	3.37
3.2	5.84	6.60	6.36	5.83	5.35	4.95	4.63	4.37	4.16	3.99	3.86	3.65	3.52	3.44	3.42
3.3	5.02	5.86	5.80	5.44	5.06	4.75	4.49	4.28	4.11	3.96	3.84	3.67	3.55	3.49	3.47
3.4	4.33	5.21	5.31	5.08	4.81	4.56	4.36	4.19	4.05	3.93	3.83	3.69	3.59	3.54	3.52

Table 4.6: Reduced areas A_{red} in km^2 as a function of r and the elevation of the centre of the FoV h_f for H = 100 km and $h_b = 20$ km. The FoV is the one of a 1 deg^2 camera. For $r > 2.9$, the largest effective area is achieved at the horizon level.

Nevertheless the water affects the latex and the balloon went off prematurely for that mission.

This work summarises the results from a total of 11 nighttime missions between 2010 and 2016 (see table 4.4.2). All of them were recovered, and the scientific programme was completed or partially completed in 7 of them. Every mission comprises several stages when part or all the subsystems are working. In this section we describe the fundamental parts of the mission, the operation of the systems involved and the impact they have on the scientific goals.

The first stage of a mission is the planning. It usually starts weeks ahead the launch. Planning includes the design of the flight, the integration of the craft and instrument, and the request of flight permit when needed. The starting point of the mission is the definition of the scientific requirements for the specific campaign. For the demonstration campaigns we have always chosen the peaks of annual meteor showers. The hour of the launch is when the radiant is well above the horizon, as the number of meteors is proportional to $\sin h_r$. Main constraint for the design of the flights is the recovery in an easy-access area, far from the seaside. The launch location is always in the centre of the Iberian Peninsula, where part of the team is located. Other members of the team are based on locations from NW to SE Spain, consequently the logistics for the assembly are complex. The flight is simulated following a protocol including different scenarios (balloon lift $\pm$ 10%, premature balloon burst, payload weight $\pm$ 10% and others). The implementation of the evaluation of the scenarios is one of the lessons learnt from some difficult recoveries.

The launch is the longest stage of a mission. It includes the countdown for the release of the balloon and the testing of all systems, using checklists and protocols inspired by the ones of the European Cooperation for Space Standardisation (ECSS). The lift is provided by commercial

Figure 4.8: Detail of the bottom part of the probe for Daedalus 19 mission. The nadir port hosts a GoPro camera for light pollution research. Image provided by ORISON project.

weather balloons, which weight from 400 g to 2000 g. The nominal mass of the probe is 4 kg, and the balloons are filled with 9 m^3 of helium, yielding a lift slightly over 7 kg. Therefore the standard mission reaches a burst-altitude of 30 km after 80 minutes. After the burst the probe enters in free-fall phase and few seconds later the parachute opens and starts breaking the assembly as the atmosphere gets thicker. One of the current developments to increase the control of the flight is the addition of a "cut&down" system, that cuts off the balloon rope. Probes Daedalus 18 (D18) and 19 (D19) were equipped with this system. The Wolfram filament was damaged in D18 and it did not work. For the D19 it worked well, but the cut rope got rolled with the parachute, not releasing the balloon. Daedalus Team members are currently working on a new design to solve this problem.

We have used the data from magnetometers and accelerometers to study the rotation of the probe. It depends on the configuration of the balloons and the mass distribution within the craft. After Daedalus 17 mission, all the probes include passive stabilisation based on a mass distribution optimised to increase inertia momentum (see figure 4.10).

Tracking is essential for the recovery of the probe. The default mode of the probe is uncontrolled, with unidirectional communication. This option was chosen after several designs in order to keep the simplicity. The use of bidirectional communication was tested in some missions but the ground segment needs more operators and more hardware. Currently only the option of active control of the probe in the case of the "cut&down system" is considered. The probe is currently equipped with different trackers and beacons: GPS, mobile network GSM and radiofrequency (RF). The recovery team has always at least two people, the driver and the operator. The operator receives positioning through satellite/internet, GSM and RF receivers. In case the probe lands in an area where the recovery is difficult, the systems may run out of battery before the team arrives. In that case the probe is searched during the following day. The probe always has a tag with contact information for the fortuitous discoverers (figure 4.11).

Date	Code	Objective	Success	Instruments	Stab.	# Balloons
2010/09/18	D2	LP	Yes	Cam+Rec	No	2
2011/10/08	D4	DRA	No	W+PC	No	2
2011/10/14	D5	LP	Partial	LX7	No	1
2012/08/24	D11	LP	Partial	Gopro	No	1
2012/12/12	D12	GEM	Yes	W+Rec+PC	No	2
2014/05/24	DX1	CAM & LP	Yes	W+Rec & LX7	No	1
2015/12/13	D17	GEM	No	SA7S	Pas	3
2016/01/04	D18	QUA	Yes	SA7S	Pas	1
2016/04/23	D19	LYR	Yes	SA7S & Go4	Pas	2
2016/08/13	D20	PER	Yes	SA7S & Go4	Pas	3
2016/12/13	D21	GEM	Yes	SA7S	Pas	3

Table 4.7: Nighttime missions from 2010 to 2016. Participants were always Daeadalus Team, UCM group and for last three times, the Instituto de Astrofísica de Andalucía (IAA, in the frame of the Pathfinder for ORISON project). The abbreviations used are: D#, for the codename of Daedalus mission. For the scientific goal we have used LP: light pollution and the IMO code for meteor showers DRA-Draconids, QUA-Quadrantids, LYR-Lyrids and GEM-Geminids. For the equipment PC: detection PC, W:Watec 902 H2 Ultimate, Go4: GoPro 4, LX7: Panasonic Lumix 7, SA7S: Sony α7S, Rec: videorecorder. For stabilisation we use Stab. and we refer to passive one as Pas.

4.4.3 Instrument selection and characterisation

The overview of the characteristics of the platform available for the instruments already establishes some high-level constraints for the design of the instrument:

- The pointing of the instrument is not going to be fixed. We expect movements in all directions, mainly periodic, in low and high frequencies.
- During the flight level the density of the air is going to change from usual sea-level to almost vacuum. The instrument should not be very focus sensitive. And the temperature control of the instruments should not be based on convection or fan-forced airflow.
- The weight budget is limited, $\sim 2\,\mathrm{kg}$ are available for the detection and recording system.
- The risk of loss of the instrument is a limit for the cost. The selected component should be COTS, allowing a fast acquisition phase for each mission.
- The instrument should consider a recording system for the data as there is no downlink to the ground station.
- Balloons will obstruct the FoV around the zenith, while observing ports are available at nadir and sides of the probe.

For the analysis we combine the constraints already explained for the scientific case to be covered, in this case the flux density determination. This is a justified description of the characteristics for the selection of the instrument:

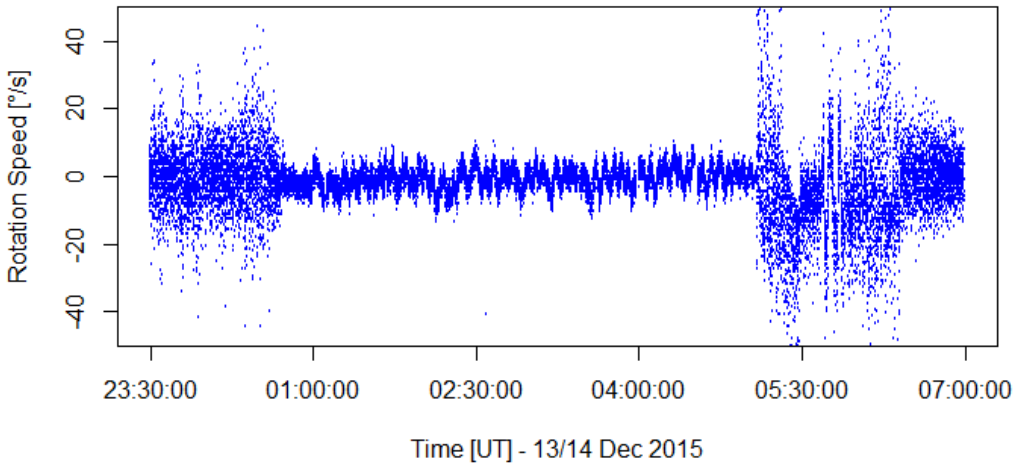

Figure 4.9: Rotation rates, in degrees per second, for the Geminids 2015 mission. The 3 stages of the mission are easily identified, with an unstable tropospheric ascent, a long pleasant stratospheric flight and a wobbling free fall after the balloon burst. The long ascent happened because one of the balloons exploded prematurely and the lift was dramatically reduced. Figure adapted from Ocaña et al. (2016a).

- The instrument will have a large FoV (tenths of degrees) in order to ensure that the desired pointing is achieved despite the movements. The first flights would be tests to determine the amplitude of the movements.

- The plate scale should minimise the spread of the light due to the movements of the pointing direction, therefore rotation speed of the probe should be in the range of the meteor relative speed. For the analysis we use the equations 3.22 and 3.23. We calculate an average values for ω considering an average speed V_∞ = 45 km/s and $D_{radiant}$ =45 ° at 20 km and for an elevation of 0 ° over the horizon, which gives us $\omega \sim 0.03\ s^{-1}$.

  From equation 3.23 for the usual video rate of 25 fps the resolution element should be $\sim$ 4 arcmin. For 50 fps it would be $\sim$ 2 arcmin. Therefore the resolution element (pixel size or PSF) should be larger than those values to avoid trailing losses because of the light spreading. For fast short-focal lenses the PSF is going to be in the range of arcminutes as well, therefore the pixel size should be in the range of the PSF.

- At the same time the plate scale should be enough to allow accurate astrometric analysis. As for the cameras from Observatorio UCM we set the goal in the order of 7 arcmin/pixel, and at least better than 10 arcmin/pixel.

These requirements were compared and matched to the available commercial instruments. The first instruments on-board were B&W high-sensitivity low-resolution videocameras, like the Watec 902 H2 Ultimate. We used the same lenses that are in use for the Observatorio UCM, the Tamron 12VG412ASIR. As a varifocal lens for 4-12 mm we could test the results with different FoV. The best results were with the widest FoV: focal lenght 4 mm, FoV $92° \times 69°$, plate scale 9 arcmin/pixel, limiting magnitude 3.

Figure 4.10: Probe configuration before launch of Daedalus 19, ready to attach the balloons. The probe has a long rod and the mass is distributed to increase the moment of inertia. Image provided by ORISON project.

A sample of preliminary results with the combination of Watec 902 H2 Ultimate can be found in figure 4.13, in section 4.4.4 and in Sánchez de Miguel et al. (2013). We tested all the equipment and we were able to detect meteors in the stratosphere. But as we have calculated the number of meteors was not enough for analysis, so we decided to increase the sensitivity of the instrument for the following campaigns.

We explored the Electronic Viewfinder with Interchangeable Lens (EVIL) cameras. We could use the Sony α7S, with a backlit sensor recording full-HD colour frames, at 30 fps, 1/50 s exposure time and 60000 ISO. It recorded up to magnitude 6.5 for stars, or 21.5 magnitudes per arcsecond^2 for sky brightness (see figure 4.12). As important as the sensor, the optics are chosen to be fast (low f/ number) and covering the full sensor. For Quadrantids 2016 the lens used was a Sigma 30 mm f/1.4, producing slight vignetting in the corners of the full-format chip. For Lyrids 2016, Perseids 2016 and Geminids 2016 the lens was a Samyang 24 mm f/1.5.

As discussed in the scientific requirements, we need a video stable up to the angular speed of the meteors $\omega \sim 0.03\ s^{-1}$. The result for this configuration is that we consider it stable when the rotation rate of the balloon is under 1 rotation every 6 minutes (i.e., 1 deg/s or $\omega \sim 0.017\ s^{-1}$). Note that there is no available software to automatically process the video data even for airborne videos, as the detection algorithms are based on the detection of changes in consecutive images. Several rounds of visual inspection proved to be the most effective way to count the number of meteors detected (Jenniskens, 1999a).

In the design of the system the option of downloading the data was discarded due to the nature of the experimental setup. For meteors and light pollution studies, the data consists of videos of 18 MB/s for the Watec camera and 6 MB/s for the Sony one thanks to compression. That download bandwidth was not affordable with standard RF equipment, and with the cost or mass budgets for the probe and the tracking team. Therefore we needed a recording system, as all the data generated by the instruments is stored locally and not uploaded to the tracking station. In the first missions we used a videorecorder but the compression algorithm constrained the scientific

Figure 4.11: Geminids 2015 probe was recovered by Salvamento Marítimo (maritime rescue) floating on the Mediterranean Sea 10 miles off-coast thanks to the GPS and RF beacons.

use of the images. For the mission D4 we used a notebook but the system failed when exiting the troposphere as the rare air caused high temperatures in the processor. For the mission D12 we increased the radiative heat dissipation, but the computer was switched off accidentally before reaching the stratopause. The introduction of new detection systems (cameras Panasonic Lumix LX7 for light pollution and Sony α7S for meteors) changed the approach as the instruments had internal storage for the data.

Another important part of the detection and recording system is the control part. For the first missions the detection system was activated during the countdown before the launch, but that reduces the lifetime of the mission. In the last four missions the camera Sony α7S was controlled using two different systems. For the Geminids 2015, the camera was controlled using WiFi communication messages sent by a Raspberry Pi (a credit card-sized board computer). However the WiFi suffered from interference and the system failed. For Quadrantids, Lyrids and Geminids in 2016 we used a cable trigger commanded by an Arduino micro-controller that decides the moment to start recording.

Figure 4.12: Sony α7S imaging Scorpio and Sagittarius constellation, showing stars up to magnitude 6.5. Galactic centre is also visible.

4.4.4 Results

In 2011 we sent a low-light video camera to observe the Draconids 2011 outburst (Ocaña et al., 2013). The scientific payload consisted of a notebook (Samsung NF 210), a Watec 902 H2 Ultimate camera, a framegrabber and a 18000 mAh battery (XPAL Power) with a total weight over 3 kg. As a consequence Daedalus platform could not fly all the usual sensors, which impacts the quality of the ancillary flight data and the flight performance. Unfortunately the recording system failed and the experiment had to be redesigned. The balloon was launched in Daimiel (Ciudad Real) and it landed 200 km away, after a 4-hour flight. It reached a level of 29 km and descended slowly to a place close to Jaén.

The post-mission analysis showed that the control and recording computer stopped working after 30 minutes, when it was at around 11 km height. Previous launches by Daedalus had shown that the balloon remains stable only after crossing the tropopause (about 15 km high). Therefore the video is wobbly and shows stars up to only magnitude 2, and no Draconid was recorded during this period. The malfunction was due to the very high ($> 85^{\circ}$C) temperature reached by the CPU. This failure was completely unexpected as CPUs had already been launched and reached 30 km without any problem. However the CPU load is maximum when running the detection software. We consider that the problem was probably caused by this high CPU load and the decrement of the dissipation power of the air due to the rarefaction, or maybe by the obstruction of the ventilation duct with the isolation foam.

In order to avoid future problems with the CPU and fit better in the probe weight budget, we modified the scientific payload. The commercial notebook was changed for a fanless board-computer, less prone to overheating. Moreover we added a backup digital video recorder (DVR). For Geminids 2012 (Sánchez de Miguel et al., 2013) we tested this configuration. The weight was still over the nominal limit and the probe was not equipped with all the sensors. Because

of a human error, the recording computer was turned off 8 minutes after the launch. The backup recording system worked perfectly and we could analyse the data. The DVR compresses the video signal and most of the photometric information is lost. However we finally got meteors detected from the stratosphere (see figure 4.13).

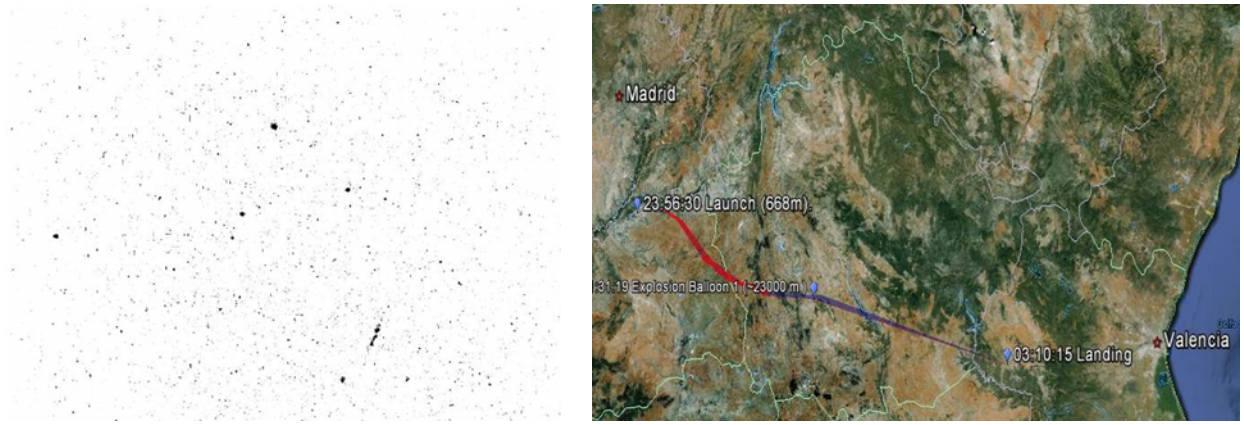

Figure 4.13: Left: Trace of a SPO meteor on a registered and stack image (inverted colours) during the maximum of Geminids 2012. When the probe is stable, the stacking of tens of images is possible. Right: Ground track of the Daedalus 12 (D12) mission. The launch was in the province of Toledo and landed in the province of Valencia. The total length was 210 km and was 3 hours and 14 minutes long. Figure adapted from Sánchez de Miguel et al. (2013).

For Camelopardalids 2014 the scientific payload was fitted to the 2 kg budget and only the DVR could fly. The forecast outburst was not as strong as expected, and the number of Camelopardalids was not enough for a statistically significant analysis. We considered this two flights (Geminids 2012 and Camelopardalids 2014) as a successful proof-of-concept, thus we decided increase the sensitivity to pursue the end goal of the experiment: meteoroid flux determination.

In 2016 we started to collaborate with ORISON project, and they provided new hardware. The B&W low-light 1/2" CCD video camera was replaced by a full-frame colour CMOS videocamera with better sensitivity, a Sony α7S (formally Sony ILCE-A7S). The colour information provides basic spectral information from the objects (Ocaña et al., 2012). The Sony α7S is an EVIL (Electronic Viewfinder with Interchangeable Lens) camera with a backlit CMOS sensor and a self-recording system included. The first lens for the camera was a Sigma with a focal length of 30 mm and f number 1.4.

The camera hosts a full-frame format (35.6 mm$\times$23.8 mm Exmor^{TM} CMOS sensor with a total of 12.2 megapixels and a pixel size of 8.4 μm) and a sensitivity up to 409600 ISO. The nominal configuration we use for the record of meteors is full-HD-1080p colour frames (1920 x 1980 pixels = 2 Mpix), at 30 fps with 1/50 s exposure time and sensitivity of 60000 ISO (over that value the noise increases with no apparent increase of sensitivity). The video is stored in clips of 1m44s with a data rate of 50 Mbps, and a total filesize of 650 MB. The format of the video is MPEG-4 Part 14 (international standard ISO/IEC 14496-14:2003), using the Sony proprietary codec for professional videos XAVC S.

The new colour sensitive video payload was launched for the Geminids 2015 (Sánchez de Miguel et al., 2016c). According to our previous experience and the analysis of the video data it was needed to decrease the rotation rates of the probe. The new probe design included active

(gyroscopes) and passive (weight distribution to increase inertia momentum) stabilisation systems. All the instruments worked flawlessly but the flight did not follow the original plan. The ascent was 4 times longer (figure 4.9), and the storage for scientific data was full before the probe could reach any stable layer, thus the video was wobbly and had no meteors. The use of gyroscopes was discarded for further missions because they took a large portion of weight and energy budget.

We repeated the test 3 weeks later. The same probe configuration and scientific payload was launched for the Quadrantids 2016. The weather was very bad in the Iberian Peninsula, so the balloon observation could provide unique information. The launch took place at 01h42m UT of the 4th of January, under moderate wind and drizzle. Unfortunately the mission ended prematurely due to a balloon malfunction, probably caused by the rain becoming ice and damaging the balloon. The flight was only 90 minutes long and the ground track was 150 km. Maximum height was 22 km, and the stable phase of the mission was limited to 7 minutes. Preliminary results confirm that 12 QUAs were recorded in these 7 minutes in the magnitude range from +1 to +6 (Sánchez de Miguel et al., 2016; Sánchez de Miguel et al., 2016b). Despite the reduced lenght of the period (according to mission plan it should be between 40 to 60 minutes), we could analyse the performance of the new colour full-HD data. The limiting magnitude of the frames was 6.5. More than 400 stars were detected, providing enough references for an astrometric resolution $\sim$ 1 arcmin.

In April 2016 and August 2016 we carried out another two missions to record the Lyrids meteor shower (Sánchez de Miguel et al., 2016a) and Perseid meteor shower respectively. The missions were successful and the analysis lead to some improvements of the instrument settings. For the peak of Geminids 2016 we carried out the last mission to the date and we have analysed in detail the meteors recorded (section 4.4.4.1).

4.4.4.1 Geminids 2016

Geminids annual meteor shower has been observed since mid-1860s and is a very interesting stream because of its parent body: the asteroid 3200 Phaethon. Moreover its level of activity in the last decades made it the most active of the annual showers, and therefore one of the better studied (Rendtel, 2004). The meteoroids have larger bulk density than average, and the lightcurves of Geminids agree with the single-body theory. The mechanism for the release of meteoroids from the asteroid surface is not completely understood, but thermal-fracture model and/or thermal decomposition of surface minerals when near perihelion are the most probable (Li and Jewitt, 2013). The flux density time profile was the main input to calculate the meteoroid stream mass in the 10^{16} to 10^{18} g range (Ryabova, 2017). The flux density profile feeds the models to estimate the age and evolution of the stream (Ryabova, 2016). Moreover Geminid stream is considered a potential meteorite-dropper stream (Madiedo et al., 2013) and therefore is monitored in detail by SPMN.

Geminids have a broad maximum centred at solar longitude 262.2°, at 2h UT for the 14th December 2016. The mission was designed to observe at the maximum elevation of the radiant (located at $\alpha = 112^{\circ}$, $\delta = 33^{\circ}$). Ground-based observing conditions for the peak of Geminids in 2016 were bad because of the scattered moonlight (Moon illuminated fraction >95%). This atmospheric scattering is produced by air-molecules and aerosols, consequently a balloon-borne mission is practically not affected by the moonlight.

The instrument used for this mission was the Sony α7S in video mode recording full-HD-1080p colour frames (1920 x 1080 pixels), at 30 fps with 1/50 s exposure time and sensitivity of 60000 ISO. The lens is a Samyang with a focal length of 24 mm and f/ number1.5, that produces a slight vignetting in the corners of the full format chip.

We have analysed the astrometry of the image splitting the video in all the frames, and each frame in the R, G, B channels. Using the suite `astrometry.net` (Lang et al., 2010) we calculated the plate constants. The plate scale of the system in video mode is 153 arcsec/pixel. Measured PSF for the stars in the FoV has a FWHM of 460 arcsec on average, in the range of a critical sampling frequency according Nyquist theorem. The field of view is $82^\circ \times 46^\circ$ with the centre at $hf = 0^\circ$.

In the beginning we mentioned that Geminid meteoroids penetrate more than other showers, and it indeed has a lower average middle point for meteors, on average it is H=92 km (Koten et al., 2004) but it is highly dependent on the absolute magnitude of the meteor. We calculate the average apparent magnitude of our meteors in order to estimate the expected middle point height. For a population with a population index r=2.2 and a limiting magnitude lm=6.5, we obtain an average magnitude of 2.3 (Arlt, 2003). The absolute average magnitude, considering the meteors are at $d \sim 1000$ km is -0.2. For that value in the literature we find middle point height in the range 80-90 km, so we chose H =85 km.

The launch took place at 23h17m UT the 13$^{\text{th}}$ December 2016 and the burst took place at 01h50m UT. In total the mission lasted 276 minutes as the probe landed at 03h55m UT. The first visual inspection of the video shows stable and unstable phases. We have used the date from the 3-axis accelerators to identify these phases using the Lomb method for frequency analysis (Lomb, 1976; Ruf, 1999). Along the whole mission we find a constant 1-second vertical tilt and 3 to 8-second roll movement (partial rotation along the optical axis). The other movement present is the rotation around the vertical axis of the probe, that results in a panning movement of the camera along the whole range of azimuth (figure 4.14). The period of this movement changes during the different phases, and we define the stable phases when it is larger than 6 minutes, that corresponds to a movement of 1°/s. This selection yields a useful period of 5 consecutive clips, for a total of 8 minutes and 40 seconds, from 01h40m UT on.

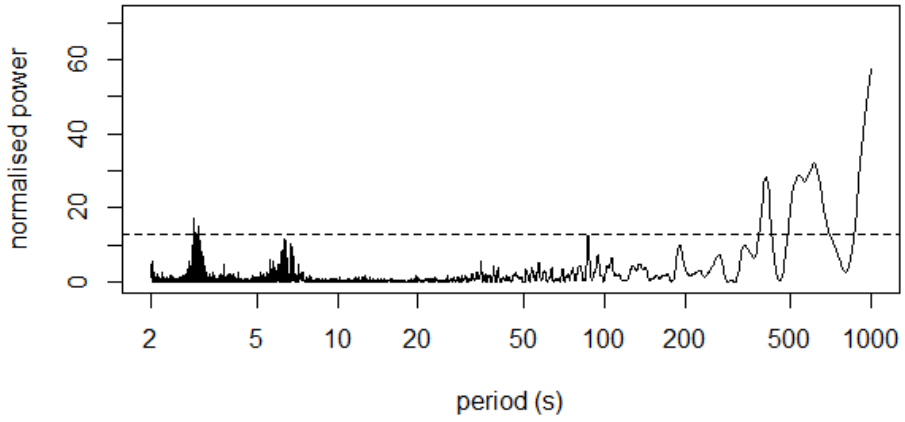

Figure 4.14: Lomb periodogram for the acceleration measured in the 3 axis for the third hour of the flight until the burst of the largest balloon. The visual inspection of the videos show that there is a field rotation with periods of ∼2.9 s and ∼6.2 s. We find that periods over 60 s are related to the rotation of the probe around its vertical axis. We defined stable conditions when the rotation period is longer than 360 seconds.

The video is analysed by visual inspection and only the upper half of the frame is considered (elevation$> 0\,^{\circ}$), yielding an effective field of view of $82\,^{\circ} \times 23\,^{\circ}$. For the meteor count we have followed the visual analysis method as described in Jenniskens (1999a). As Jenniskens states the researcher only detects 70% $\pm$ 30% during the first visualisation, and up to 3 viewings were needed for our video clips. Star limiting magnitude was calculated measuring frames in G band with V magnitudes from catalogue, and meteor magnitudes were derived by visual comparison with stars. The star limiting magnitude is 6.0 for the period analysed, and we get the same value for the meteor video limiting magnitude vlm as the magnitude loss due to the meteor speed is < 0.1 magnitudes thanks to slow speed of meteors when pointing to the horizon.

We used the algorithm introduced in this thesis to calculated the density flux. The area monitored was 525729 km^2 and the correction factors yielded an effective area A_{red} =26110 km^2. For the full period we get an average value of $(15 \pm 3) \cdot 10^{-3}$ meteoroids km^{-2}h^{-1} producing meteors brighter than magnitude 6.5 (meteoroid mass > 0.6 mg). There are no published results available for Geminids 2016, but the shower is stable through years and we can compare with other values from literature for solar longitude 261.1°, that range between 15 to 60 meteoroids km^{-2}h^{-1} (Molau et al., 2013; Blaauw et al., 2014; Neslušan, 2015; Blaauw, 2016). Therefore our results for Geminids 2016 from balloon-borne observations are in agreement with the values from previous years.

5

Conclusions

In this dissertation we have carried out a detailed and comprehensive analysis of the detection of two optical proxies for the determination of interplanetary matter properties in the Earth's neighbourhood, especially the size frequency distribution. As an initial approach to this complex problem we built a telescope for observing the light reflected by these objects. Considering the expected detection rates, we find a lower limit beyond which they are rarely detected by ground-based telescopes. Hence for smaller bodies we observe them when they enter into the atmosphere and emit light as meteors, and we have designed a couple of instrumental setups for the meteoroids flux estimation.

In chapter 2 we focused on the asteroids in the Earth's neighbourhood. We consider the Near-Earth Objects as a probe of the general asteroid population for dynamics models. Moreover we focus on them for their hazard to our planet. We build a fully-robotic observatory for the European Space Agency for the survey and follow-up of these objects. The main conclusions of that work are:

1. The design and development of the TBT project has yielded an efficient instrument for NEO detection based on commercial off-the-self (COTS) components.

2. The simulation of the long-term TBT telescopes performance shows it will be a very competitive NEO survey instrument. In the Southern Hemisphere currently there are no dedicated instruments for this task so the second TBT telescope could cover this niche area.

3. The results after the commissioning of the Cebreros TBT telescope show that it fulfils all the design requirements. Cebreros observatory has now the MPC Code Z58 and is ready for asteroid observation. It also proved to be successful for artificial satellite observations, including objects beyond the requirements, like the Exomars probe.

4. All in all, Cebreros TBT telescope, as a prototype of a future network, is a reliable robotic system for NEO observation. As the observatory design is scalable, a robotic network is feasible. The test of the two prototypes working together will take place by the end of 2017.

While the SFD of asteroids is studied based on the detection of the light reflected by these bodies, the objects smaller than 1 m are not detected by optical telescopes yet. We observe them as meteors and we define a method to estimate the influx of meteoroids using low-light CCD video cameras and extend the observation to altitudes above the troposphere. In chapter 3 important results arose from that study:

1. The spatial number density is a basic parameter of a meteoroid stream, or of the sporadic background component. It is necessary in order to estimate the stream mass, and study the stream evolution and the global impact in our environment. Video observations are a good input for calculating meteoroid fluxes. The algorithm presented generalises the method for video observations from ground to stratospheric observations. The method presented here is an accurate approach to flux calculation, allowing a deep look inside the different parameters used for calculation.

2. We analysed the dependence of the observed meteor flux to the different parameters concluding that the optimisation could be done from different approaches. One is the coverage of the full-sky, pertinent for large meteoroids. We also researched the use of large optical apertures and conclude that telescopic meteor observations in the astronomical-survey era are possible as a by-product from other scientific programs.

3. Balloon-borne observations maximise the meteor detection. According to the theoretical approach described, the observation from the stratosphere benefits from no extinction and higher detection rates.

4. Narrow-band photometry of meteors is suitable for meteoroid characterisation equivalent to low-R spectroscopy. We propose a filter set for the characterisation of meteors and reproduce the classification of meteors using synthetic photometry over a spectra catalogue. We conclude that unfiltered or broadband detection systems suffer a bias in speed and composition of meteoroids.

We then shifted our main subject of interest that is the design of the instrumental setups for the scientific cases presented: all-sky coverage from single observatory for meteor showers; telescopic detection of meteors and balloon-borne meteor observation. The most relevant conclusions reached in that analysis are the following:

1. In general, wide-field cameras maximise the meteor surveillance from a single observatory. The design and instrumental solution proposed here allow an optimal coverage with an astrometric precision good enough for orbit determination and meteorite recovery. The station built is a node of the SPMN network and the data is analysed in that framework. In this work we present the results for the Draconids 2011 campaign and the results for the density flux determination are in good agreement to the published literature.

2. Telescopic detection of meteors compensates the small area surveyed with larger fluxes thanks to the power-law that describes the meteoroid SFD. However when applying our method to the TBT telescopes, as an example of a survey telescope, we find that detection rates will be low due to long exposures and trailing losses. Therefore meteors are not going to be a common by-product from standard astronomical long-exposure surveys, but from fast transients surveys (range of seconds), e.g., MiniMegaTortora or LEO satellites surveys.

3. Balloon-borne observations have proven to be an excellent solution for meteoroid flux determination, overcoming troposphere handicaps like weather or extinction. We have studied the practical implementation of the idea. First with a low-cost B&W camera that proved the concept and played the role of test-bed for our instrumental development for the stratosphere. And then with a professional camera that allowed us to calculate the meteoroid flux. The lack of stabilisation in the platform prevents the automatic analysis of the data and furthermore, it deteriorates the quality of the data when the rotation angular speed is larger than meteor angular speed, causing trailing losses. We have designed and tested instrumentation for balloon-borne missions, and analysed the most stable part of the video of the Geminids 2016 campaign, providing for the first time flux density values from a balloon-borne instrument.

Concluding remarks

In brief, interplanetary matter distribution models will benefit from more flux determination at different mass ranges from 1 AU and the results of this work constitute an important contribution to the instrumentation for this field. NEOs and meteoroids have usually very short observation periods over constrained geographical areas and thus the research in that field require a distributed effort. We have analysed the SFD of the interplanetary matter and designed instrumental solutions for asteroids and meteors. These solutions are cost-effective, based on COTS and therefore ready for reproduction in global networks.

The instrumental setups designed for meteors have been tested in real scenarios and have been used to calculate the particle fluxes for showcases. In the case of the filter set for narrow-band low-res spectroscopy, the concept have been validated against a catalogue of spectra using synthetic photometry, but there are already some research groups using instruments to test the concept. For asteroids we simulated the performance of the TBT telescopes with a realistic population, and found that it can contribute for discovery and follow-up of objects down to $\sim$400 m. The commissioning of the first TBT telescope proves the observatory fulfils the requirements and therefore it will be a powerful instrument when entering into operation.

Last, but not least, the testing of these instruments provided direct scientific outcome with flux determination for Draconids 2011 and Geminids 2016. Besides these outcome, there is a dataset generated that is ready to be further exploited. The Cebreros TBT telescope is ready to enter into operation and in the commissioning period has already observed hundreds of asteroids. Meanwhile the meteor observing station at Observatorio UCM has contributed to some SPMN works and have data from several meteor shower campaigns to be analysed.

6

Future work

6.1 TBT telescopes for NEO survey and follow-up

Based on the requirements from ESA, a telescope for NEO survey and follow-up has been designed, built, integrated and tested. The simulation of performance based on current models for NEOs concludes that TBT telescopes are competitive instruments. In order to evaluate the performance of the Cebreros TBT telescope it should enter in nominal phase of operations. The bias of the real observations and the simulated one would help to refine the model of NEO population, as shown by Granvik et al. (2016).

On the other hand, as part of the future work, we have the installation and commissioning of the second TBT telescope in Chile (foreseen for the second half of 2017). Thanks to the better observational conditions and the lack of dedicated telescopes in the Southern Hemisphere, this Chile TBT telescope could become the largest survey program under meridional skies.

6.2 Meteoroid influx detection and characterisation

A classical method for meteoroid influx estimation was adapted for video observations and observations at different altitudes. The calculation was simplified for elevations over the horizon ($h > 0^{\circ}$) but the method could be extended for elevations below the true horizon integrating the whole optical path. As this path could cross up to two times several layers of the atmosphere, the calculation needs real extinction input from photometric analysis of the observations.

On the other hand we propose a narrow-photometry filter set for meteor characterisation in order to overcome the intrinsic difficulties of meteor spectroscopy. This low-resolution meteor characterisation is also being developed by other groups using commercial elements. At Observatorio UCM we run a test with 2 cameras as a proof of concept and now we consider that it should be extended to at least 4 filters in order to evaluate the system proposed.

As part of future work we would like to analyse with synthetic photometry more meteor spectra when another catalogue with more resolution is published. In the meantime we can analyse the spectra available and transform our filters using narrower convolution kernels to take into account the spectrograph resolution (as if they had already been convolved by the instrument kernel).

6.3 Optical instrumentation for meteoroid flux estimation

As part of the work for this Thesis we designed and installed a meteor detection station at Observatorio UCM. We analyse the data from one of the campaigns, the Draconids 2011, as a demonstration to show the actual performance for meteoroid flux detection. The station have been gathering data for almost 5 years and some of the data has been analysed as part of the network SPMN. However the rest of the data can be analysed, especially combining data for several years that is now available.

In section 2.4 we have considered the TBT telescopes as detectors for estimating the meteoroid influx and we conclude that these telescopes are not going to observe many meteors due to the combination of CCD long exposures and the large trailing losses. However the same telescope with fast-reading large-pixel CMOS camera would be a suitable instrument for meteoroid influx determination (similar to the MiniMegaTORTORA). Those instruments are currently on development for LEO satellite observations, e.g, Yanagisawa et al. (2016).

The most promising results were obtained with the instrumentation development for balloon-borne mission. We used Geminids 2016 as a showcase but we are already working in the next missions. The goal is to include the camera in a stabilised balloon mission in order to have data of more quality.

Besides we are working on the analysis of superfireballs (Zamora et al., 2015), events produced by the collision of small asteroids, in the range between meteoroids and the asteroids that can be detected with telescopes. As this events are extremely scarce we analyse the record of the last 150 years using newspapers as a source.

A

Appendix: Cameras characterisation: Watec 902 H2 Ultimate and Watec 910 HX

The use of wide-field optical cameras with high temporal resolution CCD sensors developed mainly in the 90´s with the first commercial video devices. The technique was fast applied for meteor detection and several research groups around the world started networks for nighttime coverage, based mainly in the cost-effective high-sensitivity cameras from Mintron Enterprise Co., Ltd and Watec Co. Ltd. (Madiedo et al., 2009). According to the market prices and the model availability, the best option was the Sony ICX429ALL hosted in the camera Watec 902 H2 Ultimate (Koschny, 2004; Jähne, 2007). During the development of the station, Watec released a new model that according to vendor specifications could be competitive with our selected model, the 902 H2 Ultimate. The new Watec 910 HX model is a 0.5 MPix multipurpose video camera with up to x256 frames integration capability.

We present a sensitivity and spectral characterisation for both models done at Universidad Complutense de Madrid instrument laboratory (LICA)[1]. Besides we have carried out a field test to show the performance of this camera for meteor observation. With respect to the similar model 902 H2 Ultimate, the new camera has additional setup controls that are important for the scientific use of the recordings.

The Watec 902 H2 Ultimate is the model chosen for the Observatorio UCM station. It is a low-light level video camera that hosts a 1/2 inch interline transfer CCD, with a pixel size of 9.8 (vertical) $/times$ 8.4 (horizontal) μm. The output is a composite 640 $\times$ 480 pixel interlace PAL video. And for the mode selected the shutter speed is 1/60 s.

For the model 910 HX Watec claims it is sensitive up to 0.0001 lux. It is a multipurpose camera with up to x256 frames integration capability, similar to Watec 120N (Koschny, 2004). The information provided by the manufacturer is difficult to compare between cameras, being sometimes adimensional or lens-dependent. Therefore we have measured the Watec 910 HX characteristics and analysed its meteor detection performance in comparison with the Watec 902 H2 Ultimate.

[1]This work was presented by the author in the International Meteor Conference in Poznan (Poland) on August 2013. The text written here is an adaptation of the one published in the conference proceedings (Ocaña et al., 2014).

A.1 Experimental set-up and data

Both cameras have multiple parameters that can be modified by the user. We selected them in order to assure the repeatability and scientific meaning of the measures. For both cameras the shutter speed was at $1/50$ s, background light correction (BLC) was off, gain was set in manual control (MGC) and gamma value was 1.

Moreover Watec 910 HX camera has an advanced electronic module for frame integration and noise suppression. These are not desirable for the scientific recording of meteors and were disabled (sense-up off, 3DNR off, WDR off, sharpness 0).

A.1.1 First setup: laboratory

At the Laboratory for Scientific Advanced Instrumentation (Laboratorio de Instrumentación Científica Avanzada, LICA) (Zamorano, 2013) we used the optical calibration facilities, with a monochromator Oriel Cornerstone 260. It is a dual grating instrument, set up to cover the whole range from UV (350 nm) to IR (1000 nm) and a resolution of 1.4 nm. The source of light is a tungsten filament Oriel 50 W lamp, and the calibration to absolute values is done with a Si photodiode Hamamatsu S2281.

The measurements at LICA were taken by Carlos Tapia and the author, using a USB framegrabber (chipset Silan SC8113) to digitalise the signal in PAL format: 25 fps 720 x 576 pixels (CCIR cameras). For each data series a dark current value was measured (in ADUs). For each one of the spectral response measurements the intensity of the lamp was modified to benefit from the whole dynamic range of the chips.

A.1.2 Second setup: field test

An observational campaign was carried out to evaluate the performance of the camera for the observation of meteors. Both Watec cameras, 902 H2 Ultimate and 910 HX were installed in identical setups running UfoCapture with the same parameters to compare their capabilities for meteor recording. The observations were performed in Villaverde del Ducado (figure A.1). It is a dark observing site, node of the SPMN network operated by UCM researchers. The observation took place during a night with waning moon to study the effect of the different sky brightnesses. The 910 HX gain was set in 41 dB, the maximum value. However the 902 H2 has a rough manual control. The gain was set in a middle value as a trade off between noise and sensitivity, based on our previous experience with several of these cameras.

A.2 Spectral response and linearity

The monochomator was set to move along the 380-950 nm wavelength range in 10 nm steps. The intensity was measured absolutely by the photodiode and relatively in ADUs by the cameras. The plot of the normalized intensity (maximum is the unity) against the wavelength show the spectral response curves of the chips (see Figure A.2). These curves were determined within the linearity range of the chips.

Figure A.1: Field test setup with both cameras using same lenses, framegrabbers and settings, and pointing to the same field of view.

The Watec 910 HX curve peaks at 520 nanometres, while the Ultimate's peak is shifted towards the red to 560 nm. The enhanced blue sensitivity of 910 HX (and other cameras with similar chips) could lead to a bias in a favoured detection of fast meteors, as mentioned in section 3.3.2.3.

According to these curves and the information available from the Sony CCIR chips (Thompson, 2012), we tentatively identify the 910 HX chip as the Sony ICX419ALL one. It is the one that the Watec 120N uses. And it is already known to be less sensitive than the ICX429ALL that the Watec 902 H2 U hosts[2].

A.2.1 Watec 910 HX linearity issue

While taking the spectral responses curves it was noticed that 910 HX may have some linearity issues not seen in the tests of the 902 H2 Ultimate. We carried out a linearity test for the range from the bias to the saturation levels. The wavelength was fixed in 600 nm. The number of ADUs from the camera/digitiser and light received by the photodiode were measured simultaneously. The 910 HX showed a lack of linearity above ≈ 200 ADUs (dark current subtracted) (figure A.3). We carefully checked that all the 'special' features were set off (see Section A.1) to keep the image as raw as possible.

This test was repeated for 902 H2 Ultimate with good linearity up to the saturation level. Although for both chips Sony specification sheets claim for "excellent antiblooming characteristics" that feature may still be responsible for the problem, as Watec 910 HX is intended for internal stacking (longer exposures) and may have a stronger saturation correction.

[2]EIA versions for Watec 910 HX and Watec 902 H2 Ultimate are ICX418ALL and ICX428 all respectively

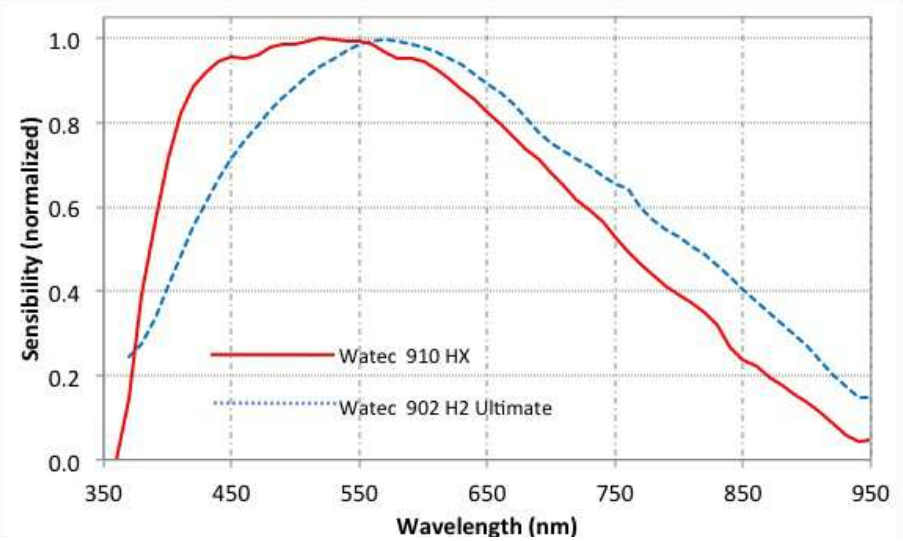

Figure A.2: Watec 910 HX and 902 H2 Ultimate relative response curve comparison. Both curves are scaled according to sensitivity values published by chip manufacturer (Table A.3).

A.3 Sensitivity and conclusions

Tests in the laboratory were not successful in determining the sensitivity of the cameras, specially with regard to meteor observation performance. For low gain (4dB), the Watec 902 H2 Ultimate was detecting light (monochromatic - 600nm) down to $6 \cdot 10^{-10}$A, while Watec 910 HX only reached the value of $3 \cdot 10^{-9}$A .

However it was not possible to set accurate intermediate gain values for 902 H2 Ultimate. At the maximum gain value (41dB for both), the Watec 902 H2 Ultimate is so noisy that it was not possible to measure properly its sensitivity.

An observational campaign was carried out with cameras and software running in parallel using the same parameters. At first sight 902 H2 Ultimate shows a better image quality and slightly more sensitivity. 910 HX shows black rings around objects, similar to those observed previously in the cameras Mintron 12Vx (Koschny, 2004).

The result of the night of observation was surprising. The Watec 910 HX outperformed slightly the Watec 902 H2 Ultimate, with 25% more meteors detected. Although the realtime video of the Watec 902H2U showed more stars. We think that the method using the same detection parameters for both cameras was not correct as they show very different noise levels. Also software could be playing an important role with regard to trigger/noise level evaluation.

Sony provides some basic sensor performance data measured under standard imaging conditions at 60°C (see Table A.3). These values are in good agreement with the results presented here. And it supports that ICX419ALL is a good candidate to be the chip of Watec 910 HX.

We tentatively identify the Watec 910 HX chip as the Sony ICX419ALL one, based on the spectral response and the datasheet published by the manufacturer. This camera is therefore very similar to the Watec 120N, and consequently less sensitive than the Watec 902 H2 Ultimate, as we have measured. Though our field test results are not in good agreement with this statement, we suspect it was a matter of software and experiment design. Therefore Watec 902 H2 Ultimate is

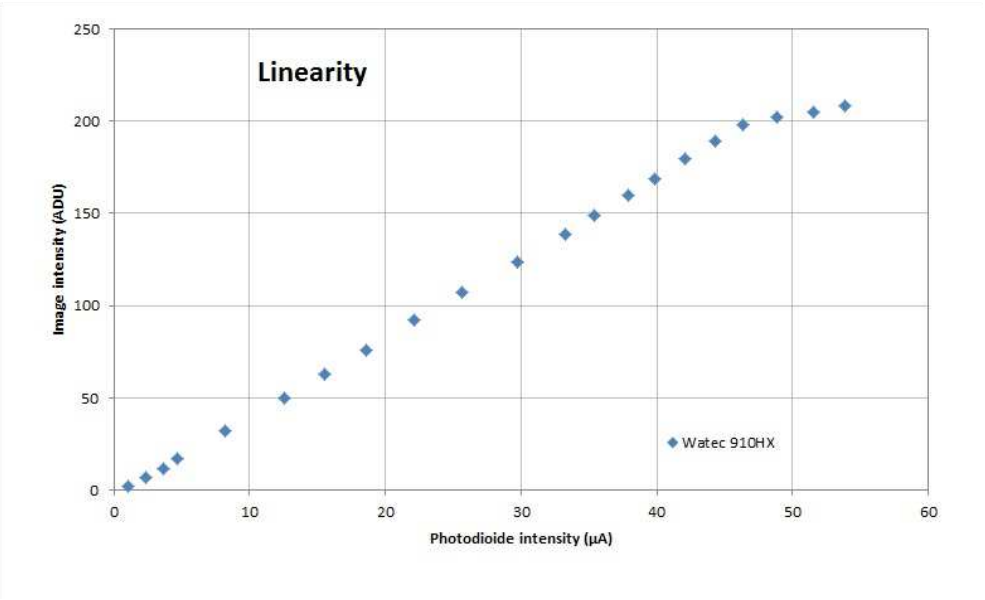

Figure A.3: Watec 910 HX linearity test. Saturation is reached at $\approx$ 200 ADUs (dark current subtracted).

Camera	Chip	Sensitivity	Dark current	Saturation
Watec 910 HX	ICX419ALL?	1100mV	2mV	1000mV
Watec 902 H2 U	ICX429ALL	1400mV	2mV	1100mV

Table A.1: Sensitivity data for Sony chips measured under standard imaging conditions at 60°C. From manufacturer datasheet.

more suitable for meteor observation at Observatorio UCM than Watec 910 HX, especially when the price difference is almost a factor of 3 (from 260€ to 700€). Moreover, we suspect of a non-linear zone in the response of the Watec 910 HX camera. This should be checked and further studied as it could lead to wrong photometry. Similar situation could happen with Watec 120N.

Acronyms

ADU Analog-to-Digital Unit.

ASAP Asteroid and Satellite Automatic Processor.

AU Astronomical Unit.

CCD Charge Coupled Device.

CCTV Closed-Circuit TeleVision.

CDR Critical Design Review.

CMOS Complementary Metal–Oxide–Semiconductor.

COTS Commercial Off-The-Shelf.

CTE Charge Transfer Efficiency.

DC Direct Current.

Dec Declination.

DSLR Digital Single Lens Reflex.

ESA European Space Agency.

ESAC European Space Astronomy Center.

ESOC European Space Operations Center.

ETC Exposure Time Calculator.

FAT Factory Acceptance Test.

FITS Flexible Image Transport System. Standard image format used in astronomy.

FoV Field of View.

FWHM Full Width at Half Maximum. Measurement of the width of a function.

GEO Geosynchronous Equatorial Orbit.

GSP Global Positioning System.

GSTP General Studies and Technology Programme.

HAD Hole Accumulation Diode.

IAA Instituto de Astrofísica de Andalucía.

IDP Interplanetary Dust Particle.

IAU International Astronomical Union.

IMC Intermediate Mars-Crossing.

JFC Jupiter-Family Comet.

JPL Jet Propulsion Laboratory.

LEO Low Earth Orbit.

LICA Laboratorio de Instrumentación Científica Avanzada.

LPC Long Period Comet.

MEO Medium Earth Orbit.

MFD Mass Frequency Distribution.

MOID Minimum Orbit Intersection Distance.

MPC Minor Planet Centre.

NASA National Aeronautics and Space Administration.

NEA Near-Earth Asteroid.

NEO Near-Earth Object. It comprises asteroids and comets.

NEOPOP Near-Earth Object Population Observation Program.

NTP Network Time Protocol.

OGS Optical Ground Station.

OSN Observatorio de Sierra Nevada.

PDR Preliminary Design Review.

PID Proportional–Integral–Derivative.

PHO Potentially Hazardous Object.

PSF Point Spread Function. Image of a point source yielded by an optical system.

QE Quantum Efficiency.

RA Right Ascension.

RMS Root Mean Square.

RTS2 Remote Telescope System 2.

SAT Site Acceptance Test.

SFD Size Frequency distribution.

SIP Simple Imaging Polynomial.

SNR Signal-to-Noise Ratio.

SPMN SPanish Meteor and fireball Network.

SSA Space Situational Awareness.

SST Space Surveillance and Tracking.

TBT Test-Bed Telescopes.

TCA Time of Closest Approach.

TNO TransNeptunian Objects.

TOTAS Teide Observatory Tenerife Asteroid Survey.

TNT Trinitrotoluene.

UCM Universidad Complutense de Madrid.

UPS Uninterrupted Power Supply.

UT Universal Time.

VMO Virtual Meteor Observatory.

VNC Virtual Network Computing.

vZHR video Zenithal Hourly Rate.

WCS World Coordinate System.

ZHR Zenithal Hourly Rate.

Bibliography

S. Abe, H. Yano, N. Ebizuka, and J.-I. Watanabe. First Results of High-Definition TV Spectroscopic Observations of the 1999 Leonid Meteor Shower. *Earth Moon and Planets*, 82:369–377, 2000.

C. H. Acton. Ancillary data services of NASA's navigation and ancillary information facility. *Planetary and Space Science*, 44(1):65–70, 1996.

E. Anders. Pre-biotic organic matter from comets and asteroids. *Nature*, 342(6247):255–257, 1989.

R. Arlt. Bulletin 19 of the International Leonid Watch: Population index study of the 2002 Leonid meteors. *WGN, Journal of the International Meteor Organization*, 31:77–87, 2003.

R. Arlt and G. Barentsen. Bulletin 21 of the International Leonid Watch: Global analysis of visual observations of the 2006 Leonid meteor shower. *WGN, Journal of the International Meteor Organization*, 34:163–168, Dec. 2006.

D. Asher. The Leonid meteor storms of 1833 and 1966. *Monthly Notices of the Royal Astronomical Society*, 307(4):919–924, 1999.

D. J. Asher and S. V. M. Clube. An Extraterrestrial Influence during the Current Glacial-Interglacial. *Quarterly Journal of the RAS*, 34:481–511, Dec. 1993.

A. Bayo, C. Rodrigo, D. Barrado Y Navascués, E. Solano, R. Gutiérrez, M. Morales-Calderón, and F. Allard. VOSA: virtual observatory SED analyzer. An application to the Collinder 69 open cluster. *Astronomy & Astrophysics*, 492:277–287, Dec. 2008. doi: 10.1051/0004-6361:200810395.

M. Beech. Halley's meteoric hypothesis. *Astronomy Quarterly*, 7(1):3–18, 1990.

M. Beech. The Makings of Meteor Astronomy: Part XVIII. *WGN, Journal of the International Meteor Organization*, 27:45–51, Feb. 1999.

M. Beech and D. Steel. On the definition of the term meteoroid. *Quarterly Journal of the Royal Astronomical Society*, 36:281, 1995.

M. Beech, P. Brown, and J. Jones. The Potential Danger to Space Platforms from Meteor Storm Activity. *Quarterly Journal of the RAS*, 36:127, June 1995.

L. R. Bellot Rubio. Dependence of the population index on the radiant zenithal distance. *WGN, Journal of the International Meteor Organization*, 22:13–26, Feb. 1994a.

L. R. Bellot Rubio. Spatial number densities and errors from photographic meteor observations under very high activity. *WGN, Journal of the International Meteor Organization*, 22:118–130, Aug. 1994b.

C. Benn. Signal. *GEMINI Newsletter Royal Greenwich Observatory*, 35:20, 1992.

J. F. Benzenberg and H. W. Brandes. Versuch die Entfernung, die Geschwindigkeit und die Bahn der Sternschnuppen zu bestimmen. *Annalen der Physik*, 6(2):224–235, 1800.

R. P. Binzel, A. S. Rivkin, J. S. Stuart, A. W. Harris, S. J. Bus, and T. H. Burbine. Observed spectral properties of near-Earth objects: results for population distribution, source regions, and space weathering processes. *Icarus*, 170(2):259–294, 2004.

D. S. Birney, G. Gonzalez, and D. Oesper. *Observational astronomy*. Cambridge University Press, 2006.

R. Blaauw. Mass Index and Mass of the Geminid Meteoroid Stream as Found with Radar, Optical, and Lunar Impact Data. *NASA Technical Reports Server*, 2016.

R. Blaauw, M. Campbell-Brown, and R. Weryk. Mass distribution indices of sporadic meteors using radar data. *Monthly Notices of the Royal Astronomical Society*, 412(3):2033–2039, 2011.

R. Blaauw, M. Campbell-Brown, and W. Cooke. Characteristics of the 2012 Geminids. *NASA Technical Reports Server*, 2014.

R. Blaauw, M. Campbell-Brown, and A. Kingery. Optical meteor fluxes and application to the 2015 Perseids. *Monthly Notices of the Royal Astronomical Society*, 463(1):441–448, 2016.

J. Borovička. The Chelyabinsk event. *Proceedings of the International Astronomical Union*, 11 (A29A):247–252, 2015.

J. Borovička, P. Spurnỳ, P. Brown, P. Wiegert, P. Kalenda, D. Clark, and L. Shrbenỳ. The trajectory, structure and origin of the Chelyabinsk asteroidal impactor. *Nature*, 503(7475):235–237, 2013.

J. Borovička. About the definition of meteoroid, asteroid, and related terms. *IAU General Assembly*, 22:2253831, Aug. 2015.

J. Borovička, P. Koten, P. Spurný, J. Boček, and R. Štork. A survey of meteor spectra and orbits: evidence for three populations of Na-free meteoroids. *Icarus*, 174:15–30, Mar. 2005. doi: 10.1016/j.icarus.2004.09.011.

J. Borovička. Two components in meteor spectra. *Planetary and Space Science*, 42:145–150, Feb. 1994. doi: 10.1016/0032-0633(94)90025-6.

W. F. Bottke, A. Morbidelli, R. Jedicke, J.-M. Petit, H. F. Levison, P. Michel, and T. S. Metcalfe. Debiased orbital and absolute magnitude distribution of the near-Earth objects. *Icarus*, 156(2): 399–433, 2002.

E. Bowell, B. Hapke, D. Domingue, K. Lumme, J. Peltoniemi, and A. W. Harris. Application of photometric models to asteroids. In *Asteroids II*, pages 524–556, 1989.

U. Brändström, B. Gustavsson, A. Steen, and A. Pellinen-Wannberg. ALIS (Auroral Large Imaging System) used for optical observations of the meteor impact process. In B. Warmbein, editor, *Meteoroids 2001 Conference*, volume 495 of *ESA Special Publication*, pages 331–336, Nov. 2001.

V. A. Bronshten. Physics of meteoric phenomena. *Fizika meteornykh iavlenii, Moscow, Izdatel'stvo Nauka, 1981 Dordrecht, D. Reidel Publishing Co., 1983, 372 p. Translation.*, 1983.

P. Brown, M. D. Campbell, R. L. Hawkes, C. Theijsmeijer, and J. Jones. Multi-station electro-optical observations of the 1999 Leonid meteor storm. *Planetary and Space Science*, 50:45–55, Jan. 2002. doi: 10.1016/S0032-0633(01)00112-X.

P. Brown, R. Spalding, D. ReVelle, E. Tagliaferri, and S. Worden. The flux of small near-Earth objects colliding with the Earth. *Nature*, 420(6913):294–296, 2002.

P. Brown, J. Assink, L. Astiz, R. Blaauw, M. Boslough, J. Borovička, N. Brachet, D. Brown, M. Campbell-Brown, L. Ceranna, et al. A 500-kiloton airburst over Chelyabinsk and an enhanced hazard from small impactors. *Nature*, 503(7475):238–241, 2013.

M. Buie. General analytical telescope pointing model, 2003.

M. Campbell-Brown. Directional variation of sporadic meteor activity and velocity. *Earth, Moon, and Planets*, 102(1-4):79–84, 2008.

M. Campbell-Brown. A population of small refractory meteoroids in asteroidal orbits. *Planetary and Space Science*, 118:8–13, Dec. 2015. doi: 10.1016/j.pss.2015.03.022.

R. M. Canup and E. Asphaug. Origin of the Moon in a giant impact near the end of the Earth's formation. *Nature*, 412(6848):708–712, 2001.

J. Carpenter, A. Abbey, R. Ambrosi, and A. Wells. Effects of micrometeoroid and space debris impacts in grazing incidence telescopes. In *SPIE Astronomical Telescopes+ Instrumentation*, pages 62663K–62663K. International Society for Optics and Photonics, 2006.

R. D. Caswell, N. McBride, and A. Taylor. Olympus end of life anomaly—a perseid meteoroid impact event? *International Journal of Impact Engineering*, 17(1):139–150, 1995.

Z. Ceplecha, J. Borovička, W. G. Elford, D. O. ReVelle, R. L. Hawkes, V. Porubčan, and M. Šimek. Meteor phenomena and bodies. *Space Science Reviews*, 84(3-4):327–471, 1998.

S. R. Chesley, P. W. Chodas, A. Milani, G. B. Valsecchi, and D. K. Yeomans. Quantifying the risk posed by potential Earth impacts. *Icarus*, 159(2):423–432, 2002.

C. F. Chyba, P. J. Thomas, L. Brookshaw, and C. Sagan. Cometary delivery of organic molecules to the early Earth. *Science*, 249(4967):366–374, 1990.

C. F. Chyba, P. J. Thomas, and K. J. Zahnle. The 1908 tunguska explosion: atmospheric disruption of a stony asteroid. *Nature*, 361(6407):40–44, 1993.

L. Cibin, M. Chiarini, A. Bertoli, F. Villa, L. Dimare, D. Farnocchia, F. Bernardi, A. Milani, G. Pinna, I. Zayer, et al. A dynamic observation concept as a key point for an enhanced SSA optical network. In *Proceedings of the European Space Surveillance Conference WPP-321*, pages 7–9, 2011.

W. J. Cooke and D. E. Moser. The status of the NASA All Sky Fireball Network. In *Proceedings of the International Meteor Conference, 30th IMC, Sibiu, Romania, 2011*, pages 9–12, Jan. 2012.

G. Daniels. A night sky model for satellite search systems. *Optical Engineering*, 16:66–71, 1977.

J. Davis. Photoelectric meteor observations and the colour indices and visual magnitudes of meteors. *Monthly Notices of the Royal Astronomical Society*, 126:445, 1963. doi: 10.1093/mnras/126.5.445.

F. DeMeo and B. Carry. The taxonomic distribution of asteroids from multi-filter all-sky photometric surveys. *Icarus*, 226(1):723–741, 2013.

F. DeMeo and B. Carry. Solar system evolution from compositional mapping of the asteroid belt. *Nature*, 505(7485):629–634, 2014.

V. Dikarev, E. Grün, J. Baggaley, D. Galligan, M. Landgraf, and R. Jehn. The new ESA meteoroid model. *Advances in Space Research*, 35(7):1282–1289, 2005.

R. Dogniaux. *Variations géographiques et climatiques des expositions énergétiques solaires sur des surfaces réceptrices horizontales et verticales: données d'application pour les latitudes comprises entre 0° et 60°, pour les facteurs de trouble compris entre 2 et 5 par ciel sans nuages, pour des conditions de ciel uniformément couvert*. Institut Royal Météorologique de Belgique, 1975.

ESA-SSA. Near-Earth Object Population Observation Program NEOPOP, 2015. URL `http://neo.ssa.esa.int/neo-population`. NEOPOP webpage.

D. Farnocchia, F. Bernardi, and G. B. Valsecchi. Efficiency of a wide-area survey in achieving short-and long-term warning for small impactors. *Icarus*, 219(1):41–47, 2012.

O. Fors, J. Núñez, J. L. Muiños, F. J. Montojo, R. Baena-Gallé, J. Boloix, R. Morcillo, M. T. Merino, E. C. Downey, and M. J. Mazur. Telescope Fabra ROA Montsec: A New Robotic Wide Field Baker-Nunn Facility. *Publications of the Astronomical Society of the Pacific*, 125(927):522, 2013.

T. Forster. *Annals of Some Remarkable Aërial and Alpine Voyages, Including Those of the Author*. Keating and Brown, 1832.

J. L. Galache, C. L. Beeson, K. K. McLeod, and M. Elvis. The need for speed in Near-Earth Asteroid characterization. *Planetary and Space Science*, 111:155–166, 2015.

J. Gallego, N. Cardiel, J. Zamorano, J. Gorgas, A. Castillo-Morales, M. C. Eliche-Moral, A. Gil de Paz, S. Pascual, P. G. Pérez-González, R. Guzmán, G. Barro, C. Díaz, N. Espino, J. Izquierdo, E. Mármol-Queraltó, J. C. Muñoz-Mateos, F. Ocaña, L. Rodriguez, A. Sánchez de Miguel, E. Toloba, V. Villar, and M. Abelleira. UCM Group of Extragalactic Astrophysics and Astronomical Instrumentation, 2011. URL `http://guaix.fis.ucm.es/fireball`. GUAIX webpage.

M. Granvik, A. Morbidelli, R. Jedicke, B. Bolin, W. F. Bottke, E. Beshore, D. Vokrouhlickỳ, M. Delbò, and P. Michel. Super-catastrophic disruption of asteroids at small perihelion distances. *Nature*, 530(7590):303–306, 2016.

M. Granvik, A. Morbidelli, D. Vokrouhlický, W. F. Bottke, D. Nesvorný, and R. Jedicke. Escape of asteroids from the main belt. *Astronomy & Astrophysics*, 598:A52, Jan. 2017. doi: 10.1051/0004-6361/201629252.

E. Grün, R. Srama, M. Horanyi, H. Kruger, R. Soja, V. Sterken, Z. Sternovsky, and P. Strub. Comparative Analysis of the ESA and NASA Interplanetary Meteoroid Enviroment Models. In *6th European Conference on Space Debris*, volume 723 of *ESA Special Publication*, page 36, Aug. 2013.

J. Gumbel and L. Megner. Charged meteoric smoke as ice nuclei in the mesosphere: Part 1—a review of basic concepts. *Journal of Atmospheric and Solar-Terrestrial Physics*, 71(12):1225–1235, 2009.

P. Gural. The American Meteor Society's filter bank spectroscopy project. In J.-L. Rault and P. Roggemans, editors, *Proceedings of the International Meteor Conference Mistelbach, Austria, 27-30 August 2015*, pages 16–23, Jan. 2015.

P. S. Gural. Meteor Observation Simulation Tool. In M. Triglav, A. Knöfel, & C. Trayner, editor, *Proceedings of the International Meteor Conference*, pages 29–35, 2002.

P. S. Gural and P. Jenniskens. Leonid storm flux analysis from one Leonid MAC video AL50R. *Earth, Moon, and Planets*, 82:221–247, 1998.

A. W. Harris and G. D'Abramo. The population of near-Earth asteroids. *Icarus*, 257:302–312, 2015.

R. Hawkes and J. Jones. An inexpensive meteor observing system. *The Observatory*, 93:233–235, Dec. 1973.

R. L. Hawkes. Constructing a video-based meteor observatory. *WGN, Journal of the International Meteor Organization*, 18:145–151, Aug. 1990.

R. L. Hawkes. Television meteors (Invited). In J. Stohl and I. P. Williams, editors, *Meteoroids and their Parent Bodies*, page 227, 1993.

R. L. Hawkes and J. Jones. Electro-optical meteor observation techniques and results. *Quarterly Journal of the RAS*, 27:569–589, Dec. 1986.

G. S. Hawkins and E. K. Upton. The Influx Rate of Meteors in the Earth's Atmosphere. *The Astrophysical Journal*, 128:727, 1958.

E. F. Helin and E. M. Shoemaker. The Palomar planet-crossing asteroid survey, 1973–1978. *Icarus*, 40(3):321–328, 1979.

K. G. Henize, J. F. Stanley, C. A. O'Neill, and B. S. Nowakowski. Detection of orbital debris with GEODSS telescopes. In *Optical Engineering and Photonics in Aerospace Sensing*, pages 76–84. International Society for Optics and Photonics, 1993.

M. E. Hervig, L. E. Deaver, C. G. Bardeen, J. M. Russell, S. M. Bailey, and L. L. Gordley. The content and composition of meteoric smoke in mesospheric ice particles from sofie observations. *Journal of Atmospheric and Solar-Terrestrial Physics*, 84:1–6, 2012.

C. Hoffmeister. Investigations concerning fundamental problems of meteoric astronomy. *The Observatory*, 70:70–76, 1950.

E. Høg, C. Fabricius, V. V. Makarov, S. Urban, T. Corbin, G. Wycoff, U. Bastian, P. Schwekendiek, and A. Wicenec. The Tycho-2 catalogue of the 2.5 million brightest stars. *Astronomy and Astrophysics*, 355:L27–L30, 2000.

R. Hueso, S. Pérez-Hoyos, A. Sánchez-Lavega, A. Wesley, G. Hall, C. Go, M. Tachikawa, K. Aoki, M. Ichimaru, J. Pond, et al. Impact flux on jupiter: From superbolides to large-scale collisions. *Astronomy & Astrophysics*, 560:A55, 2013.

D. W. Hughes. P/Halley dust characteristics - A comparison between Orionid and Eta Aquarid meteor observations and those from the flyby spacecraft. *Astronomy & Astrophysics*, 187:879–888, Nov. 1987.

S. Imoto and I. Hasegawa. Historical Records of Meteor Showers in China, Korea, and Japan. *Smithsonian Contributions to Astrophysics*, 2:131, 1958.

M. Iye, M. Tanaka, M. Yanagisawa, N. Ebizuka, K. Ohnishi, C. Hirose, N. Asami, Y. Komiyama, and H. Furusawa. Suprimecam observation of sporadic meteors during perseids 2004. *Publications of the Astronomical Society of Japan*, 59:841–855, 2007.

B. Jähne. Data acquisition by imaging detectors. In *Springer Handbook of Experimental Fluid Mechanics*, pages 1419–1436. Springer, 2007.

R. Jedicke, M. Granvik, M. Micheli, E. Ryan, T. Spahr, and D. Yeomans. Surveys, astrometric follow-up, and population statistics. *Asteroids IV*, pages 795–813, 2015.

P. Jenniskens. Activity of the 1998 Leonid shower from video records. *Meteoritics & Planetary Science*, 34(6):959–968, 1999a.

P. Jenniskens. Update on the Leonids. *Advances in Space Research*, 23:137–147, 1999b.

P. Jenniskens. The I.A.U. meteor shower nomenclature rules. *WGN, Journal of the International Meteor Organization*, 34:127–128, Oct. 2006.

P. Jenniskens. Quantitative meteor spectroscopy: Elemental abundances. *Advances in Space Research*, 39:491–512, 2007. doi: 10.1016/j.asr.2007.03.040.

P. Jenniskens. Meteoroid streams that trace to candidate dormant comets. *Icarus*, 194(1):13–22, 2008.

P. Jenniskens. Meteor showers in review. *Planetary and Space Science*, 2017.

P. Jenniskens and J. Vaubaillon. Minor planet 2008 ED69 and the Kappa Cygnid meteor shower. *The Astronomical Journal*, 136(2):725, 2008.

P. Jenniskens, M. De Lignie, H. Betlem, J. Borovicka, C. Laux, D. Packan, and C. Kruger. Preparing for the 1998/99 Leonid storms. *Earth, Moon, and Planets*, 80(1-3):311–341, 1998.

P. Jenniskens, E. Jehin, R. A. Cabanac, C. O. Laux, and I. D. Boyd. Spectroscopic anatomy of a meteor trail cross section with the european southern observatory very large telescope. *Meteoritics & Planetary Science*, 39(4):609–616, 2004.

P. Jenniskens, Q. Nénon, J. Albers, P. Gural, B. Haberman, D. Holman, R. Morales, B. Grigsby, D. Samuels, and C. Johannink. The established meteor showers as observed by CAMS. *Icarus*, 266:331–354, 2016.

P. M. M. Jenniskens. *Meteor showers and their parent comets*. Cambridge University Press, 2006.

J. Jones. Meteoroid Engineering Model–Final Report. *NASA. Technical report, MSFC internal report SEE/CR-2004*, 400, 2004.

J. Jones and T. Kaiser. The effects of thermal radiation, conduction and meteoroid heat capacity on meteoric ablation. *Monthly Notices of the Royal Astronomical Society*, 133(4):411–420, 1966.

S. Karpov, G. Beskin, S. Bondar, A. Perkov, G. Greco, A. Guarnieri, and C. Bartolini. Wide and fast. Status update on FAVOR project and MegaTORTORA system. In *Astronomical Society of India Conference Series*, volume 7 of *Astronomical Society of India Conference Series*, page 219, 2012.

S. Karpov, N. Orekhova, G. Beskin, A. Biryukov, S. Bondar, E. Ivanov, E. Katkova, A. Perkov, and V. Sasyuk. Meteor observations with Mini-MegaTORTORA wide-field monitoring system. *arXiv preprint arXiv:1602.07977*, 2016.

R. Koschack and J. Rendtel. Determination of spatial number density and mass index from visual meteor observations (I). *WGN, Journal of the International Meteor Organization*, 18:44–58, Apr. 1990.

D. Koschny. Comparing two potential meteor cameras - the Mintron and the Watec 120N. In M. Triglav-Čekada and C. Trayner, editors, *Proceedings of the International Meteor Conference, 22nd IMC, Bollmannsruh, Germany, 2003*, pages 59–63, 2004.

D. Koschny and M. Busch. The Teide Observatory Tenerife Asteroid Survey. *Planetary and Space Science*, 118:305–310, 2015.

D. Koschny and J. Zender. Comparing Meteor Number Fluxes from Ground-Based and Airplane-Based Video Observations. *Earth Moon and Planets*, 82:209–220, 2000.

D. Koschny, J. D. Del Rio, R. Piberne, M. Szumlas, J. Zender, and A. Knöfel. Radiants of the Leonids 1999 and 2001 obtained by LLTV systems using automatic software tools. *Earth, Moon, and Planets*, 95(1-4):255–263, 2004.

D. Koschny, F. Bettonvil, J. Licandro, J. Mc Auliffe, H. Smit, H. Svedhem, F. de Wit, O. Witasse, J. Zender, et al. A double-station meteor camera set-up in the Canary Islands–CILBO. *Geoscientific Instrumentation, Methods and Data Systems*, 2(2):339–348, 2013.

P. Koten, J. Borovička, P. Spurnỳ, H. Betlem, and S. Evans. Atmospheric trajectories and light curves of shower meteors. *Astronomy & Astrophysics*, 428(2):683–690, 2004.

P. Koten, J. Borovička, P. Spurnỳ, and R. Štork. Optical observations of enhanced activity of the 2005 draconid meteor shower. *Astronomy & Astrophysics*, 466(2):729–735, 2007.

J. Koukal et al. STRATO 02/2015 – The Perseids 2015 stratospheric balloon mission. *WGN, Journal of the International Meteor Organization*, 44, Feb. 2016.

P. Kubánek. RTS2: Lessons learned from a widely distributed telescope network. *Astronomische Nachrichten*, 329(3):271–274, 2008.

P. Kubánek. RTS2—the remote telescope system. *Advances in Astronomy*, 2010, 2010.

P. Kubánek, M. Jelínek, M. Nekola, M. Topinka, J. Strobl, R. Hudec, T. d. J. M. Sanguino, A. d. U. Postigo, and A. J. Castro-Tirado. RTS 2- Remote Telescope System, 2 nd Version. In *Gamma-Ray Bursts: 30 Years of Discovery*, volume 727, pages 753–756, 2004.

D. Lang, D. W. Hogg, K. Mierle, M. Blanton, and S. Roweis. Astrometry. net: Blind astrometric calibration of arbitrary astronomical images. *The astronomical journal*, 139(5):1782, 2010.

S. Larson, E. Beshore, R. Hill, E. Christensen, D. McLean, S. Kolar, R. McNaught, and G. Garradd. The CSS and SSS NEO surveys. In *Bulletin of the American Astronomical Society*, volume 35, page 982, 2003.

M. Laurance and D. Brownlee. The flux of meteoroids and orbital space debris striking satellites in low earth orbit. *Nature*, 323(6084):136–138, 1986.

H. F. Levison, A. Morbidelli, L. Dones, R. Jedicke, P. A. Wiegert, and W. F. Bottke. The mass disruption of oort cloud comets. *Science*, 296(5576):2212–2215, 2002.

J. Li and D. Jewitt. Recurrent perihelion activity in (3200) Phaethon. *The Astronomical Journal*, 145(6):154, 2013.

N. R. Lomb. Least-squares frequency analysis of unequally spaced data. *Astrophysics and space science*, 39(2):447–462, 1976.

J. J. López-Moreno, J. L. Ortíz, R. Duffard, J. Wolf, K. Schindler, T. Müller, L. Berenguer, and J. Baztarrica. ORISON un proyecto de instrumentación astronómica estratosférica, May 2016. URL `https://doi.org/10.5281/zenodo.53051`.

S. Love and D. Brownlee. A direct measurement of the terrestrial mass accretion rate of cosmic dust. *Science*, 262(5133):550–554, 1993.

J. M. Madiedo. Robotic systems for the determination of the composition of solar system materials by means of fireball spectroscopy. *Earth, Planets and Space*, 66(1):70, 2014.

J. M. Madiedo and J. M. Trigo-Rodríguez. Multi-station Video Orbits of Minor Meteor Showers. *Earth Moon and Planets*, 102:133–139, June 2008. doi: 10.1007/s11038-007-9215-x.

J. M. Madiedo, J. M. Trigo-Rodriguez, J. Llorca, J. Borovička, J. Zamorano, J. Izquierdo, and F. Ocaña. The Puerto Lapice Eucrite Fall Phenomenon. In *Lunar and Planetary Institute Science Conference Abstracts*, volume 39 of *Lunar and Planetary Institute Science Conference Abstracts*, page 1815, Mar. 2008.

J. M. Madiedo, J. M. Trigo-Rodriguez, J. Alonso, J. Zamorano, F. Ocaña, J. A. Docobo, P. Pujols, and J. Lacruz. The Spanish Meteor Network (SPMN): full coverage of the Iberian Peninsula by means of high-sensitivity CCD video devices. In *European Planetary Science Congress 2009*, page 560, Sept. 2009.

J. M. Madiedo, J. M. Trigo-Rodríguez, J. L. Ortiz, and N. Morales. Robotic systems for meteor observing and moon impact flashes detection in spain. *Advances in Astronomy*, 2010, 2009.

J. M. Madiedo, J. M. Trigo-Rodríguez, A. J. Castro-Tirado, J. L. Ortiz, and J. Cabrera-Caño. The Geminid meteoroid stream as a potential meteorite dropper: a case study. *Monthly Notices of the Royal Astronomical Society*, 436(3):2818–2823, 2013.

J. M. Madiedo, J. M. Trigo-Rodríguez, J. Zamorano, J. L. Ortiz, A. S. de Miguel, F. Ocaña, J. Izquierdo, A. J. Castro-Tirado, N. Morales, D. Galadí, E. de Guindos, J. Lacruz, F. Organero, L. Ana-Hernández, F. Fonseca, M. Tapia, F. Gallego, and J. Cabrera-Caño. Analysis of a superbolide from a damocloid observed over Spain on 2012 July 13. *Monthly Notices of the Royal Astronomical Society*, 436:3656–3662, Dec. 2013. doi: 10.1093/mnras/stt1845.

J. M. Madiedo, J. L. Ortiz, J. M. Trigo-Rodríguez, J. Zamorano, N. Konovalova, A. J. Castro-Tirado, F. Ocaña, A. S. d. Miguel, J. Izquierdo, and J. Cabrera-Caño. Analysis of two superbolides with a cometary origin observed over the Iberian Peninsula. Icarus, 233:27–35, May 2014a. doi: 10.1016/j.icarus.2014.01.031.

J. M. Madiedo, J. M. Trigo-Rodríguez, J. Zamorano, L. Ana-Hernández, J. Izquierdo, J. L. Ortiz, A. J. Castro-Tirado, A. Sánchez de Miguel, F. Ocaña, S. Pastor, J. A. de los Reyes, D. Galadí, E. de Guindos, F. Organero, F. Fonseca, and J. Cabrera-Caño. Trajectory, orbit, and spectroscopic analysis of a bright fireball observed over Spain on April 13, 2013. *Astronomy & Astrophysics*, 569:A104, Sept. 2014b. doi: 10.1051/0004-6361/201322120.

J. M. Madiedo, J. M. Trigo-Rodríguez, J. Zamorano, J. Izquierdo, A. S. de Miguel, F. Ocaña, J. L. Ortiz, F. Espartero, L. G. Morillas, D. Cardeñosa, M. Moreno-Ibáñez, and M. Urzáiz. Orbits and emission spectra from the 2014 Camelopardalids. *Monthly Notices of the Royal Astronomical Society*, 445:3309–3314, Dec. 2014c. doi: 10.1093/mnras/stu1990.

A. Mainzer, J. Bauer, T. Grav, J. Masiero, R. Cutri, J. Dailey, P. Eisenhardt, R. McMillan, E. Wright, R. Walker, et al. Preliminary results from NEOWISE: An enhancement to the wide-field infrared survey explorer for Solar System science. *The Astrophysical Journal*, 731(1):53, 2011.

E. Manjavacas. Estación de videodetección de bólidos del Observatorio UCM. *UCM e-prints http://eprints.ucm.es/11458/*, July 2010.

J. Mathews. Sporadic e: current views and recent progress. *Journal of Atmospheric and Solar-Terrestrial Physics*, 60(4):413–435, 1998.

J. A. M. McDonnell, N. McBride, and D. J. Gardner. The Leonid Meteoroid Stream: Spacecraft Interactions and Effects. In B. Kaldeich-Schuermann, editor, *Second European Conference on Space Debris*, volume 393 of *ESA Special Publication*, page 391, 1997.

R. S. McMillan. Spacewatch preparations for the era of deep all-sky surveys. *Proceedings of the International Astronomical Union*, 2(S236):329–340, 2006.

H. McNamara, R. Suggs, B. Kauffman, J. Jones, W. Cooke, and S. Smith. Meteoroid Engineering Model (MEM): A meteoroid model for the inner solar system. In *Modern Meteor Science An Interdisciplinary View*, pages 123–139. Springer, 2005.

R. H. McNaught and D. J. Asher. Leonid dust trails and meteor storms. *WGN, Journal of the International Meteor Organization*, 27:85–102, 1999.

P. M. Millman. Meteor News. *Journal of the RASC*, 55:265, Dec. 1961.

P. M. Millman. Meteor News: Airborne Observations of the 1972 Giacobinids. *Journal of the RASC*, 67:35, Feb. 1973.

S. Molau. The AKM video meteor network. In *Meteoroids 2001 Conference*, volume 495 of *ESA Special Publication*, pages 315–318, Nov. 2001.

S. Molau and G. Barentsen. Real-Time Flux Density Measurements of the 2011 Draconid Meteor Outburst. *Earth, Moon, and Planets*, 112(1-4):1–5, 2014.

S. Molau and P. S. Gural. A review of video meteor detection and analysis software. *WGN, Journal of the International Meteor Organization*, 33:15–20, Feb. 2005.

S. Molau et al. Monthly Reports of the AKM/IMO Video Meteor Network, 2013. URL `http://www.imonet.org/reports/`. IMONET website.

F. Montojo, O. Fors, J. Muinos, J. Nunez, R. López-Morcillo, R. Baena, J. Boloix, T. López-Moratalla, and M. Merino. The Fabra-ROA Telescope at Montsec (TFRM): A Fully Robotic Wide-field Telescope for Space Surveillance and Tracking. *arXiv preprint arXiv:1109.5918*, 2011.

C. E. Moore. A Multiplet Table of Astrophysical Interest. Revised Edition. Part I - Table of Multiplets. *Contributions from the Princeton University Observatory*, 20:1–110, 1945.

A. Morbidelli and D. Vokrouhlickỳ. The Yarkovsky-driven origin of near-Earth asteroids. *Icarus*, 163(1):120–134, 2003.

D. Morrison. The Spaceguard Survey: Report of the NASA International Near-Earth-Object Detection Workshop. *NASA STI/Recon Technical Report N*, 92:34245, 1992.

D. Morrison, C. R. Chapman, D. Steel, and R. P. Binzel. Impacts and the public: communicating the nature of the impact hazard. *Mitigation of hazardous comets and asteroids*, pages 252–390, 2004.

D. E. Moser, R. M. Suggs, W. J. Cooke, and R. C. Blaauw. The 2012 Lyrids from non-traditional observing platforms. 2013.

I. S. Murray, R. L. Hawkes, and P. Jenniskens. Airborne intensified charge-coupled device observations of the 1998 Leonid shower. *Meteoritics & Planetary Science*, 34(6):949–958, 1999.

N. Myhrvold. Comparing NEO Search Telescopes. *Publications of the Astronomical Society of the Pacific*, 128(962):045004, 2016.

W. M. Napier. The influx of comets and their debris. In *Accretion of Extraterrestrial Matter Throughout Earth's History*, pages 51–74. Springer, 2001.

National Research Council. *Limiting Future Collision Risk to Spacecraft: An Assessment of NASA's Meteoroid and Orbital Debris Programs*. National Academies Press, 2011.

L. Neslušan. A summary of the research of Geminid meteoroid stream. *Contrib. Astron. Obs. Skalnaté Pleso*, 45:60–82, 2015.

D. Nesvornỳ, P. Jenniskens, H. F. Levison, W. F. Bottke, D. Vokrouhlickỳ, and M. Gounelle. Cometary origin of the zodiacal cloud and carbonaceous micrometeorites. implications for hot debris disks. *The Astrophysical Journal*, 713(2):816, 2010.

H. A. Newton. Abstract of a memoir on shooting stars. *American Journal of Science*, (116): 193–207, 1865.

F. Ocaña. Optimización de técnicas de detección de bólidos y meteoros, jul 2011. URL `http://eprints.ucm.es/13292/`. UCM e-prints.

F. Ocaña, J. McAuliffe, and D. Koschny. Meteoroid spatial number density and flux calculation with video meteor observation. i. In *Proceedings of the International Meteor Conference, 29th IMC, Armagh, Northern Ireland, 2010*, pages 76–80, 2011.

F. Ocaña, J. Zamorano, A. Sanchez de Miguel, J. Izquierdo, E. Manjavacas, P. Ramirez-Moreta, and R. Ponce. Setting-Up a Fireball Detection Station at UCM Observatory. In *Proceedings of the International Meteor Conference, 29th IMC, Armagh, Northern Ireland, 2010*, pages 81–86, Jan. 2011.

F. Ocaña, J. Zamorano, and J. Gallego. Narrow-band photometry of meteors. In *Proceedings of the International Meteor Conference, 30th IMC, Sibiu, Romania, 2011*, pages 48–52, Jan. 2012.

F. Ocaña, J. M. Madiedo, J. M. Trigo-Rodríguez, J. Zamorano, J. Izquierdo, and A. Sánchez de Miguel. Physico-Chemical Properties of 109P/Swift-Tuttle Debris. In *Lunar and Planetary Science Conference*, volume 44 of *Lunar and Planetary Science Conference*, page 1159, Mar. 2013.

F. Ocaña, J. Zamorano, A. S. de Miguel, J. Izquierdo, J. Gallego, M. Palos, B. Muñoz-Ibáñez, G. Rodríguez-Coira, R. García, A. Santamaría, et al. First scientific results of the Fireball Detection Station at UCM Observatory. In *Proceedings of the International Meteor Conference, 31st IMC, La Palma, Canary Islands, Spain, 2012*, volume 1, pages 178–181, 2013.

F. Ocaña, J. Zamorano, and C. E. Tapia Ayuga. Performance of Watec 910 HX camera for meteor observing. In M. Gyssens, P. Roggemans, and P. Zoladek, editors, *Proceedings of the International Meteor Conference, Poznan, Poland, 22-25 August 2013*, pages 47–49, Jan. 2014.

F. Ocaña, M. F. Palos, J. Zamorano, A. Sanchez de Miguel, J. Izquierdo, B. Munoz-Ibanez, A. Santamaria, and J. Gallego. The 2011 Draconid outburst: UCM group preliminary results from Spain. In *Proceedings of the International Meteor Conference, 31st IMC, La Palma, Canary Islands, Spain, 2012*, volume 1, pages 70–73, 2013.

F. Ocaña, M. Castillo, E. Uranga, J. Ponz, T. Consortium, et al. A test-bed configuration: Toward an autonomous system. In *Astronomical Data Analysis Software an Systems XXIV (ADASS XXIV)*, volume 495, page 227, 2015.

F. Ocaña, A. S. de Miguel, and A. Conde. Low cost multi-purpose balloon-borne platform for wide-field imaging and video observation. In *SPIE Astronomical Telescopes+ Instrumentation*, pages 99061X–99061X. International Society for Optics and Photonics, 2016a.

F. Ocaña, A. Ibarra, E. Racero, Á. Montero, J. Doubek, and V. Ruiz. First results of the test-bed telescopes (tbt) project: Cebreros telescope commissioning. In *SPIE Astronomical Telescopes+ Instrumentation*, pages 990666–990666. International Society for Optics and Photonics, 2016b.

F. Ochsenbein, P. Bauer, and J. Marcout. The VizieR database of astronomical catalogues. *Astronomy and Astrophysics Supplement Series*, 143:23–32, Apr. 2000. doi: 10.1051/aas:2000169.

J. Ortiz, P. Sada, L. B. Rubio, F. Aceituno, J. Aceituno, P. Gutierrez, and U. Thiele. Optical detection of meteoroidal impacts on the moon. *Nature*, 405(6789):921–923, 2000.

S. Pascual, J. Gallego, and J. Zamorano. A Contribution to the Selection of Emission-Line Galaxies Using Narrowband Filters in the Optical Airglow Windows. *Publications of the Astronomical Society of the Pacific*, 119:30–49, Jan. 2007.

A. Pellinen-Wannberg, E. Murad, B. Gustavsson, U. Brändström, C.-F. Enell, C. Roth, I. P. Williams, and Å. Steen. Optical observations of water in Leonid meteor trails. *Geophysical Research Letters*, 31:L03812, Feb. 2004. doi: 10.1029/2003GL018785.

J. M. Plane. Cosmic dust in the Earth's atmosphere. *Chemical Society Reviews*, 41(19):6507–6518, 2012.

P. Pravec and A. W. Harris. Fast and slow rotation of asteroids. *Icarus*, 148(1):12–20, 2000.

D. Rabinowitz. Detection of earth-approaching asteroids in near real time. *The Astronomical Journal*, 101:1518–1529, 1991.

E. Racero, A. Ibarra, F. Ocaña, S. de Lis, J. Ponz, M. Castillo, and M. Sánchez-Portal. Toward an autonomous telescope network: the tbt scheduler. In *Astronomical Data Analysis Software an Systems XXIV (ADASS XXIV)*, volume 495, page 231, 2015.

M. Rapp and F.-J. Lübken. Polar mesosphere summer echoes (PMSE): Review of observations and current understanding. *Atmospheric Chemistry and Physics*, 4(11/12):2601–2633, 2004.

Í. Rapp-Arrarás and J. M. Domingo-Santos. Functional forms for approximating the relative optical air mass. *Journal of Geophysical Research: Atmospheres*, 116(D24), 2011.

V. Reddy, J. A. Sanchez, W. F. Bottke, A. Thirouin, E. G. Rivera-Valentin, M. S. Kelley, W. Ryan, E. A. Cloutis, S. C. Tegler, E. V. Ryan, et al. Physical characterization of 2 m diameter near-earth asteroid 2015 tc25: A possible boulder from e-type asteroid (44) nysa. *The Astronomical Journal*, 152(6):162, 2016.

J. Rendtel. Evolution of the Geminids observed over 60 years. *Earth, Moon, and Planets*, 95(1-4): 27–32, 2004.

G. H. Rieke, M. Blaylock, L. Decin, C. Engelbracht, P. Ogle, E. Avrett, J. Carpenter, R. M. Cutri, L. Armus, K. Gordon, R. O. Gray, J. Hinz, K. Su, and C. N. A. Willmer. Absolute Physical Calibration in the Infrared. *The Astronomical Journal*, 135:2245–2263, June 2008. doi: 10.1088/0004-6256/135/6/2245.

G. D. Roth, H. J. Augensen, and W. D. Heintz. Compendium of practical astronomy. *Volumes 1-3. Springer-Verlag Berlin Heidelberg New York*, page 153, 1994.

A. E. Rubin and J. N. Grossman. Meteorite and meteoroid: New comprehensive definitions. *Meteoritics & Planetary Science*, 45(1):114–122, 2010.

T. Ruf. The Lomb-Scargle periodogram in biological rhythm research: analysis of incomplete and unequally spaced time-series. *Biological Rhythm Research*, 30(2):178–201, 1999.

G. Ryabova. A preliminary numerical model of the Geminid meteoroid stream. *Monthly Notices of the Royal Astronomical Society*, 456(1):78–84, 2016.

G. Ryabova. The mass of the geminid meteoroid stream. *Planetary and Space Science*, 2017.

A. Sánchez de Miguel. Variación espacial, temporal y espectral de la contaminación lumínica y sus fuentes: Metodología y resultados. 2015.

A. Sánchez de Miguel and J. Zamorano. Light Pollution in Spain: A European Perspective. In J. M. Diego, L. J. Goicoechea, J. I. González-Serrano, & J. Gorgas, editor, *Highlights of Spanish Astrophysics V*, page 535, 2010. doi: 10.1007/978-3-642-11250-8_164.

A. Sánchez de Miguel, A. Conde, F. Ocaña, F. Ortuño, D. Mayo, M. A. Gómez Sánchez-Tirado, R. Raya, and P. León. Daedalus 2 - NS1b - XIX CEA - High sensitivity camera, Mar. 2011. URL `http://dx.doi.org/10.5281/zenodo.52562`. https://youtu.be/GVBCrusKgK0.

A. Sánchez de Miguel, F. Ocaña, F. Ortuño, D. Mayo, M. A. Gómez Sánchez-Tirado, A. Conde, T. Ortuño, J. Zamorano, J. Izquierdo, R. Raya, and P. León. Geminids from the Daedalus 12, Feb. 2013. URL `http://dx.doi.org/10.5281/zenodo.52570`. https://youtu.be/4eIXx8egqsA https://youtu.be/t0MKkoR3yVQ.

A. Sánchez de Miguel, F. Ocaña González, J. M. Madiedo, F. Ortuño, A. Conde, P. León, M. Á. Gómez Sánchez-Tirado, D. Mayo, R. Raya, J. Zamorano Calvo, et al. The 2012 Geminids Balloon-Borne Misson Over Spain. In *Lunar and Planetary Institute Science Conference Abstracts*, volume 44, page 2202, 2013.

A. Sánchez de Miguel, M. A. Gómez Sánchez-Tirado, P. Maier, D. Mayo, and A. Conde. Lyrids Mission: ORISON pathfinder, May 2016a. URL `http://dx.doi.org/10.5281/zenodo.52775`.

A. Sánchez de Miguel, M. A. Gómez Sánchez-Tirado, C. E. Tapia Ayuga, F. Ocaña, D. Mayo, and A. Conde. Video of Quadrantids 2016 from the Stratosphere, Jan. 2016b. URL `http://dx.doi.org/10.5281/zenodo.52630`.

A. Sánchez de Miguel, F. Ocaña, M. A. Gómez Sánchez-Tirado, and A. Conde. Light pollution from Daedalus 17, May 2016c. URL `http://dx.doi.org/10.5281/zenodo.52574`. https://youtu.be/kdVdmg2JFfQ.

A. Sánchez de Miguel, F. Ocaña, C. Tapia Ayuga, J. Madiedo, J. Zamorano, J. Izquierdo, M. Gómez Sánchez-Tirado, F. Ortuño, D. Mayo, R. Raya, et al. The 2016 Quadrantids Balloon-Borne Mission Over Spain: Full HD and Colour Videorecording. In *Lunar and Planetary Science Conference*, volume 47, page 2637, 2016.

E. Schunová-Lilly, R. Jedicke, P. Vereš, L. Denneau, and R. J. Wainscoat. The size-frequency distribution of H> 13 NEOs and ARM target candidates detected by Pan-STARRS1. *Icarus*, 284:114–125, 2017.

F. Selsis, M. T. Lemmon, J. Vaubaillon, and J. F. Bell. Extraterrestrial meteors: A martian meteor and its parent comet. *Nature*, 435(7042):581–581, 2005.

D. L. Shupe, M. Moshir, J. Li, D. Makovoz, R. Narron, and R. N. Hook. The SIP convention for representing distortion in FITS image headers. In *Astronomical Data Analysis Software and Systems XIV*, volume 347, page 491, 2005.

R. H. Soja, M. Sommer, J. Herzog, R. Srama, E. Grün, J. Rodmann, P. Strub, J. Vaubaillon, A. Hornig, and L. Bausch. The Interplanetary Meteoroid Environment for eXploration–(IMEX) project. In *Proceedings of the International Meteor Conference, Giron, France, 18-21 September 2014*, pages 146–149, 2014.

SonotaCo. A meteor shower catalog based on video observations in 2007-2008. *WGN, Journal of the International Meteor Organization*, 37:55–62, Apr. 2009.

E. J. Spillar, D. Dumbrill, G. Grasdalen, and R. Howell. The Wyoming infrared observatory telescope software system. *Publications of the Astronomical Society of the Pacific*, pages 616–624, 1993.

S. M. Stanley. *Earth system history*. Macmillan, 2005.

G. H. Stokes, J. B. Evans, H. E. Viggh, F. C. Shelly, and E. C. Pearce. Lincoln near-Earth asteroid program (LINEAR). *Icarus*, 148(1):21–28, 2000.

V. Straizys. The method of synthetic photometry. *Baltic Astronomy*, 5:459–476, 1996.

D. Subasinghe, M. Campbell-Brown, and E. Stokan. Luminous Efficiency Estimates of Meteors-I. Uncertainty analysis. *Planetary and Space Science*, 2017.

S. Suzuki, T. Akebo, T. Yoshida, and K. Suzuki. TV Observations of the 1998 Giacobinid Outburst. *WGN, Journal of the International Meteor Organization*, 27:214–218, 1999.

M. J. Taylor, L. C. Gardner, I. S. Murray, and P. Jenniskens. Jet-Like Structures and Wake in Mg I (518 nm) Images of 1999 Leonid Storm Meteors. *Earth Moon and Planets*, 82:379–389, 2000.

J. Thompson. A survey of ccd's used in astro-video cameras. `http://karmalimbo.com/aro/reports/old_AstrovideoCameraCCDSurvey.pdf`, 2012. Abbey Road Observatory webpage.

J. L. Tonry. An early warning system for asteroid impact. *Publications of the Astronomical Society of the Pacific*, 123(899):58, 2011.

P. Tricarico. The near-Earth asteroid population from two decades of observations. *Icarus*, 284: 416–423, 2017.

Trigo-Rodríguez.

J. M. Trigo-Rodríguez, A. J. Castro-Tirado, J. Llorca, J. Fabregat, V. J. Martínez, V. Reglero, M. Jelínek, P. Kubánek, T. Mateo, and A. D. U. Postigo. The Development of the Spanish Fireball Network Using a New All-Sky CCD System. *Earth Moon and Planets*, 95:553–567, Dec. 2004. doi: 10.1007/s11038-005-4341-9.

J. M. Trigo-Rodríguez, J. Borovička, J. Llorca, J. M. Madiedo, J. Zamorano, and J. Izquierdo. Puerto Lápice eucrite fall: Strewn field, physical description, probable fireball trajectory, and orbit. *Meteoritics and Planetary Science*, 44:175–186, Mar. 2009. doi: 10.1111/j.1945-5100.2009.tb00726.x.

J. M. Trigo-Rodriguez, J. M. Madiedo, I. P. Williams, and A. J. Castro-Tirado. The outburst of the κ Cygnids in 2007: clues about the catastrophic break up of a comet to produce an Earth-crossing meteoroid stream. *Monthly Notices of the Royal Astronomical Society*, 392:367–375, Jan. 2009. doi: 10.1111/j.1365-2966.2008.14060.x.

J. M. Trigo-Rodríguez, J. M. Madiedo, I. Williams, J. Dergham, J. Cortés, A. J. Castro-Tirado, J. L. Ortiz, J. Zamorano, F. Ocaña, J. Izquierdo, et al. The 2011 October Draconids outburst–I. Orbital elements, meteoroid fluxes and 21P/Giacobini–Zinner delivered mass to Earth. *Monthly Notices of the Royal Astronomical Society*, 433(1):560–570, 2013.

J. Vaubaillon, J. Watanabe, M. Sato, S. Horii, and P. Koten. The coming 2011 Draconids meteor shower. In *Proceedings of the International Meteor Conference, 30th IMC, Sibiu, Romania, 2011*, volume 1, page 39, 2012.

J. Vaubaillon, P. Koten, A. Margonis, J. Toth, R. Rudawska, M. Gritsevich, J. Zender, J. McAuliffe, P.-D. Pautet, P. Jenniskens, et al. The 2011 Draconids: the first European airborne meteor observation campaign. *Earth, Moon, and Planets*, 114(3-4):137–157, 2015.

P. Vereš, R. Jedicke, R. Wainscoat, M. Granvik, S. Chesley, S. Abe, L. Denneau, and T. Grav. Detection of Earth-impacting asteroids with the next generation all-sky surveys. *Icarus*, 203(2): 472–485, 2009.

F. Verniani. Meteor masses and luminosity. *Smithsonian contributions to astrophysics*, 10:141–195, 1967.

F. Verniani. An analysis of the physical parameters of 5759 faint radio meteors. *Journal of Geophysical Research*, 78(35):8429–8462, 1973.

S. Vítek, P. Páta, P. Koten, and K. Fliegel. Long-term continuous double station observation of faint meteor showers. *Sensors*, 16(9):1493, 2016.

V. Vojáček, J. Borovička, P. Koten, P. Spurný, and R. Štork. VizieR Online Data Catalog: Catalogue of representative meteor spectra (Vojacek+, 2015). *VizieR Online Data Catalog*, 358, Sept. 2014.

V. Vojáček, J. Borovička, P. Koten, P. Spurný, and R. Štork. Catalogue of representative meteor spectra. *Astronomy & Astrophysics*, 580:A67, Aug. 2015. doi: 10.1051/0004-6361/201425047.

U. von Zahn. The total mass flux of meteoroids into the Earth's upper atmosphere. In *17th ESA Symposium on European Rocket and Balloon Programmes and Related Research*, volume 590, pages 33–39, 2005.

B. D. Warner and A. W. Harris. Using sparse photometric data sets for asteroid lightcurve studies. *Icarus*, 216(2):610–624, 2011.

J. Watanabe, T. Kasuga, T. Terai, S. Miyazaki, K. Ohta, F. Murooka, T. Ohnishi, T. Yamasaki, H. Mito, T. Aoki, et al. Faint meteor observation by large-format CMOS sensor with 1.05-m Kiso schmidt telescope. *Meteoroids 2013*, 1:325–328, 2014.

L. Weinek. Beobachtungen auf der kk Sternwarte in Prag. *Astronomische Nachrichten*, 114(24): 408–412, 1886.

R. J. Weryk, P. G. Brown, A. Domokos, W. N. Edwards, Z. Krzeminski, S. H. Nudds, and D. L. Welch. The Southern Ontario All-sky Meteor Camera Network. *Earth Moon and Planets*, 102: 241–246, June 2008. doi: 10.1007/s11038-007-9183-1.

F. L. Whipple. A comet model. I. The acceleration of Comet Encke. *The Astrophysical Journal*, 111:375–394, 1950.

F. L. Whipple. A Comet Model. II. Physical Relations for Comets and Meteors. *The Astrophysical Journal*, 113:464, 1951.

P. Wiegert, J. Vaubaillon, and M. Campbell-Brown. A dynamical model of the sporadic meteoroid complex. *Icarus*, 201(1):295–310, 2009.

M. Wisniewski, A. Olech, M. Krasnowski, K. Zloczewski, K. Mularczyk, P. Kedzierski, and W. Jonderko. CCTV lenses for video meteor astronomy. *WGN, Journal of the International Meteor Organization*, 33:23–29, 2005.

T. Yanagisawa, H. Kurosaki, and O. Hiroshi. Detection of LEO Objects Using CMOS Sensor. *Transactions of the Japan Society for Aeronautical and Space Sciences, Aerospace Technology Japan*, 14(ists30):Pr_51–Pr_55, 2016.

Q.-Z. Ye, P. G. Brown, and P. Pokornỳ. Dormant comets among the near-Earth object population: a meteor-based survey. *Monthly Notices of the Royal Astronomical Society*, 462(4):3511–3527, 2016.

S. Zamora, F. Ocaña, A. Sánchez de Miguel, and M. Mole. On the frequency of the superfireballs: more than 150 years of reports. In *Proceedings of the International Meteor Conference, Mistelbach, Austria, 27-30 August 2015, Eds.: Rault, J.-L.; Roggemans, P., International Meteor Organization, ISBN 978-2-87355-029-5, pp. 187-191*, volume 1, pages 187–191, 2015.

J. Zamorano. Laboratory for scientific advanced instrumentation, 2013. URL `http://guaix.fis.ucm.es/lica`. GUAIX webpage.

J. Zamorano, F. Ocaña, A. Sánchez de Miguel, J. Izquierdo, E. Manjavacas, R. Ponce, García, and Sáez. Estación de detección de bólidos de la universidad complutense: montaje, automatización y primeros resultados. Poster Session: Spanish Society of Astronomy Meeting 2010, 2010.

J. Zamorano, A. Sánchez de Miguel, D. Martínez Delgado, and E. Alfaro Navarro. Proyecto NixNox disfrutando de los cielos estrellados de españa. *Astronomía*, (142):36–42, 2011.

J. Zvolankova. Dependence of the observed rate of meteors on the Zenith distance of the radiant. *Bulletin of the Astronomical Institutes of Czechoslovakia*, 34:122–128, Mar. 1983.